Liquid micro-junction surface sampling and MALDI imaging of small and large molecules in human liver disease.

by

Joscelyn Sarsby

A thesis submitted to the University of Birmingham
for the degree of Doctor of Philosophy.

School of Chemistry
University of Birmingham

September 2015

Abstract

Liquid extraction surface analysis (LESA) mass spectrometry is an emerging direct surface sampling technique. In this thesis, LESA has been coupled to an Orbitrap Velos ETD (Thermo), a TSQ Vantage (Thermo) and a Synapt G2-S (Waters) mass spectrometers, for the analysis of lipids and proteins from human liver. The aim was to develop analytical methods that would ultimately be used in the study of non-alcoholic liver disease. Initial investigations assessed the capabilities of using LESA for imaging and optimised sampling protocol for lipids and proteins. Analysis of the fatty acid binding protein was explored further, in particular to the identification of a single amino acid substitution that is associated with non-alcoholic steatohepatitis, a potentially fatal liver disease. Both top-down and bottom-up proteomics techniques were employed. Bottom-up resulted in over 300 proteins being detected and identified, including several other known biomarkers for liver disease, however failed to distinguish between two proteins with a single amino acid substitution. Top-down approach was employed to identify these two proteins. Field asymmetric ion mobility spectrometry (FAIMS) analysis was coupled with LESA to enhanced the quality of intact protein mass spectra and doubled the number of proteins detected. FAIMS analysis was able to separated lipids and proteins that are extracted simultaneously as well as removing background noise from large unresolvable ions. To fully appreciate that data that was

acquired using the FAIMS visualisation software was developed. In addition to FAIMS, traveling wave ion mobility spectrometry (TWIMS) was also coupled to LESA via the Synapt G2-S. In addition to the separation of lipids from proteins, several lipids also showed a separation in drift. MS/MS of one of these lipids revealed that the composition of the two drift peaks differed. The ability to separate isobaric lipids made this technique particularly useful for imaging. MALDI imaging was performed on the Synapt G2-S with TWIMS, to show the isolation of specific lipid species using MS/MS imaging and TWIMS imaging. The MALDI gives a complementary approach to LESA for tissue analysis.

Declaration

I hereby declare that the work presented in this thesis is entirely my own, except where indicted by reference in the text.

I also declare that this thesis has not been submitted for a degree at any other institution.

Work presented in chapter 4 has been published in:

Sarsby, J., Martin, N.J., Lalor, P.F., Bunch, J., and Cooper, H.J., Top-down and bottom-up identification of proteins by liquid extraction surface analysis mass spectrometry of healthy and diseased human liver tissue. *J Am Soc Mass Spectrom*, 2014. **25**(11): p. 1953-1961.

Work presented in chapter 5 has been published in:

Sarsby, J., Griffiths, R.L., Race, A.M., Bunch, J., Randall, E.C., Creese, A.J., and Cooper, H.J., Liquid Extraction Surface Analysis Mass Spectrometry Coupled with Field Asymmetric Waveform Ion Mobility Spectrometry for Analysis of Intact Proteins from Biological Substrates. *Anal Chem*, 2015. **87**(13): p. 6794-6800.

Acknowledgements

I would like to start by thanking my supervisors who have supported and guided me throughout my studies. I would like to thank the Bunch group with whom I started my research, particularly Alan Race and Rian Griffiths, who have been constant companions providing valuable insight and knowledge. I finished my research in the Cooper group who welcomed me warmly to their group with particular thanks to Andrew Crease and Nick Martin, who have supported me with their expertise and guidance. There are many people of the 5th Floor of Bioscience who have contributed to me finishing by being available to chat and helping my motivation levels over cup of tea and a piece of cake. It is not just in the office where I have been supported I would also like to give particular thanks Lindsey Van Gemeren, Max Harris and my mum, Jan a who have been there and understood when I get home. And Finally to my dad, Alan who's expert knowledge of Microsoft word has helped guide me in creating this thesis.

Abbreviations

AGC	Automatic gain control
CID	Collision inducted dissociation
CF	Continuous flow or Compensation field
DAG	Diacylglyceride
DF	Dispersion field
EI	Electron impact
ESI	Electrospray ionisation
ETD	Electron transfer dissociation
FABP1	Liver Fatty acid binding protein
FAIMS	High-Field asymmetric ion mobility spectrometry
HCD	Higher energy collision dissociation
HOBP	2-hydroxy-4-octyloxybenzophenone
LC	Liquid chromatography
LESA	Liquid extraction surface analysis
LIT	linear ion trap
LMJ	Liquid micro-junction
MALDI	Matrix-assisted laser desorption/ionisation
MS	Mass spectrometry
MS/MS	Tandem mass spectrometry
m/z	mass to charge ratio
NASH	Non-alcoholic steatohepatitis
NCE	Normalised collision energy
QqQ	Triple Quadrupole
QToF	Quadrupole Time of Flight
QTrap	Quadrupole ion trap
PC	Glycerophosphatidylcholine
PE	Glycerophosphatidylethanolamine
PEG	Polyethylene glycol
PTM	Post Translational modification
RF	Radio Frequency
SIMS	Secondary ion mass spectrometry
SM	Sphingomyelin
SRM	Single reaction monitoring
TAG	Triacylglycerides
TLC	Thin layer chromatography
TWIG	Traveling wave ion guide
TWIMS	Traveling wave ion mobility spectrometry
UltraFAIMS	Ultra-high field asymmetric ion mobility spectrometry

Table of Contents

Table of Figures

List of tables

Chapter 1: Introduction

1.1 Origins of Mass spectrometry

In 1803, a theory put forward by John Dalton that described matter as a composition of various different atoms was one of the first steps in bringing understanding to molecular compositions. Dalton's theory was based on four assumptions:

- Matter is composed of elements consisting of solid indivisible atoms.
- The elements are indestructible.
- The number of different types of atoms corresponds exactly to the number of chemical elements.
- Each element has fixed and measurable properties.

This theory started the process of the development of mass spectrometry as an instrument to measure atoms and elements. [1, 2]

The discovery of cathode rays in the late 19th century started the development of the first mass spectrometer. It was noticed that this ray was made of particles that could be deflected by strong magnetic or electrical fields, and that the degree of the deflection was related to their charge to mass ratio, which was measured at 1/1800th of a hydrogen atom. This was the discovery of the

electron for which J.J. Thomson and G.J. Stoney were awarded the Noble prize for physics in 1906. [1, 2]

Meanwhile Eugen Goldstein hypothesised that if negatively charged particles were traveling in one direction then positively charged particles must be traveling in the opposite direction. He was able to prove these particles were indeed traveling in the opposite direction but could not prove that they were positively charged as this would require stronger magnetic fields than were available to Goldstein. It was Weilhelm Wien, a student of Goldstein's, who was able to demonstrate the production of positive ions. He used a combination of magnetic and electrical fields to deflect ions. These deflections were detected on a photographic plate and characteristic parabolas were observed with lighter ions being deflected more than heavier ions. Wien used this equipment to calculate the mass to charge ratio of a proton by calculating the degree of deflection. Larger ions that were analysed were difficult to interpret because the resolution was very poor. Thompson and Francis W. Aston developed the technique to enhance the clarity of the results by removing the air that was causing interference. The first mass spectrometer produced images of parabolas the width and height of which were specific to an ion. J. J. Thomson further developed methods for ion detection: Instead of all ions being detected at the same time, single ion types were detected in turn by tuning the magnetic field so that ions sequentially passed through a parabola shaped slit in a metal sheet, producing a spectrum.

Mass spectrometers and mass spectrometry have progressed since the work of J. J. Thomson. Several Nobel prizes have been won for contributing to the design and methodology that have enabled mass spectrometry to become an instrument that is used in several scientific disciplines. The individuals that have won or shared the Nobel prize are [3];

- In 1922 Francis W. Aston won the Nobel prize for chemistry by identifying 212 natural occurring isotopes using Thomson's mass spectrometer [4]
- In 1939 Ernest O. Laurence was awarded the Nobel prize for physics for the Invention of the Cyclotron [5]
- Wolfgang Paul and Hans Dehmelt (quarter each) shared the Nobel prize in physics in 1989 for the invention of the ion trap techniques [6, 7]
- In 2002 John Bennett Fenn and Koichi Tanaka shared (quarter each) the Nobel Prize in chemistry for the development of soft ionisation techniques for the analysis of biological macromolecules. [8, 9]

1.2 Modern mass spectrometers

There are a wide variety of mass spectrometers available, each used for a different purpose. All mass spectrometers have a similar configuration as outlined in Figure 1.

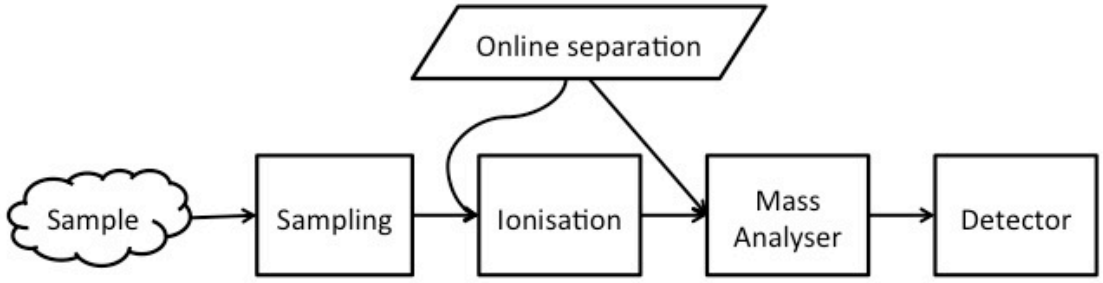

Figure 1: Generalised schematic of mass spectrometers. Online separation is optional.

The sample, sampling method, and ionisation techniques are directly related to each other, because the sample needs to be introduced to the instrument in a suitable manner. In addition, online separation techniques such as liquid chromatography or ion mobility (see section 1.4) are sometimes used to enhance the quality and quantity of the data.

1.2.1. Ionisation Techniques

Molecules are converted to ions in the ionisation source. The hardness of the ionisation technique is a measure of how fragmented the analytes are after ionisation. Hard ionisation techniques such as electron ionisation (EI), result in extensive fragmentation. The advantage of EI is that the fragmentation is very predictable and mass fingerprinting and quantification is possible [10, 11], however the intact mass of the precursor ion is sometimes lost. The intact mass can be obtained by using softer ionisation methods. Soft ionisation techniques produce less fragmentation and are able to ionise larger molecules. The softest ionisation technique is matrix-assisted laser desorption/ionisation (MALDI), and is capable of ionising large molecules of over 100,000 Da as a singly charged ion [12]. This characteristic is ideal for the simplicity of the mass

spectrum however only the time of flight mass analyser (see section 1.3.1) is capable of analysing ions of this size. Electrospray Ionisation (ESI) is also a soft technique. It can still analyse large molecular weight compounds however typically produces a series of multiply charged ions for each molecular species. [13] The advantage of multiply charged ions is that there is a reduction in the mass to charge (*m/z*) ratio of the detected ions and so a wider choice of mass analysers is available.

Ionisation techniques can be split into two categories, low-pressure ionisation (in a vacuum) and atmospheric pressure ionisation. A sub category of atmospheric pressure ionisation is ambient ionisation, where ionisation occurs at room pressure. The most widely used ambient ionisation technique is electrospray ionisation, and is discussed in more detail in section 1.2.1.2. Low-pressure ionisation MALDI (with the exception of atmospheric pressure MALDI [14]) is one of the main vacuum based ionisation technique. The research presented here uses the soft ionisation techniques of MALDI and ESI. A few examples of ionisation techniques in each of these categories are shown in Table 1-1.

Table 1-1: Catagories of ionisation techniques

Technique	Low pressure ionisation	Atmospheric ionisation	Ambient ionisation
Secondary ion mass spectrometry [15]	✔		
Matrix assisted laser desorption ionisation [16]	✔		
Atmospheric pressure MALDI [14]		✔	
Atmospheric pressure chemical ionisation [17]		✔	
Atmospheric pressure photo ionisation [18]		✔	
Electrospray ionisation [19]		✔	✔
Desorption electrospray ionisation [20]		✔	✔
Laser desorption ionisation [21]		✔	✔

1.2.1.1 Matrix-assisted laser desorption/ionisation

MALDI is a combined sampling and ionisation technique that was first reported in 1987 for the ionisation of non-volatile compounds [16]. This method incorporates a matrix compound to coat or suspend the sample. The matrix then absorbs the energy from the laser causing desorption and ionisation. The matrix choice is very important and some important considerations:

- A good absorbance at the wavelength of the laser; [22]
- Be soluble in a solvent that is suitable for the sample (exception of dry coating techniques); [23-25]
- Not cause too much interference of analyte peaks in the spectrum,
- Be stable under a vacuum (except AP-MALDI), especially true for liquid matrices [26]

- Form smaller crystals than the spatial resolution required (specific to imaging);
- Results in homogeneous analyte inclusion;
- Be able to be dispensed evenly across a surface (specific to imaging);
- Promote ion formation;

The relationship between the matrix and the sample is very complex. The ratio between the number of matrix molecules and number of analyte molecules can affect the intensity and type of species detected [27]. This can be easily controlled when using pure standards however in complex samples where the composition of analytes changes through out the sample it can be more difficult to control. Some commonly used matrices are;

Table 1-2: Examples of matrices and their uses.

Matrix	**Used for***	**References**
2,5-Dihydrobenzoic acid	Positive mode, Lipids and polymers.	[28, 29]
α-cyano-hydroxycinannic acid	Positive mode Lipids, proteins and peptides	[28, 30]
Sinapinic acid	Positive mode, proteins	[31, 32]
2,4,6-Trihydroxyacetophenone	Positive and negative mode, Carbohydrates oligonucleotides, Lipids	[33-35]
9-Aminoacridine	Negative mode, Lipids and small molecules.	[36-38]

* This is not an exclusive nor exhaustive list.

Matrix application is important. Some factors that affect the quality of the data are:

- Collection and Storage
- Washing
- Matrix
- Matrix application

Collection and Storage are critical aspects of MALDI sample preparation, some molecules will degrade quickly others will degrade slowly. [39] To prevent degradation 3 methods can be employed, Snap freezing, chemical treatment such as formalin fixation, and heat treatment. [40-42]

Tissue washing is an important aspect of MALDI sample preparation. The advantages of tissue washing are that it removes salts and competitive molecules that could prevent the ionisation of the target molecules. However, there is the risk of delocalising the molecules that are being targeted, which for imaging, results in misleading images. It is possible to reduce the degree of delocalising during washing by choosing wash solutions that do not dissolve the target molecules. [43-45]

There are two considerations when choosing a matrix for MALDI imaging, the compatibility of the matrix with the target molecules and the crystal size of the matrix when it dries. There are many matrices used in MALDI, 2,5-

Dihydroxybenzoic acid, a-Cyano-4-hydroxycinnamic acid and 2,4,6-Trihydroxyacetophenone, are common. [46] There are many more, the use of nano-particles and ionic compounds as matrices are expanding areas.[47, 48]

The matrix needs to be applied in such a manor that there is a uniform distribution across the surface. There are a number of methods to do this. Spraying is possibly the most popular method. This can be done relatively cheaply by hand using an airbrush, but this is very user specific. To make the process more repeatable inkjet printers can be used, but plastic tubing often does not last long with some organic solvents. Specially designed automatic sprayers and spotters are available on the market. Other methods include sublimation, and dry coating. [49, 50]

1.2.1.1.1 MALDI ionisation

Ionisation occurs when a laser pulse impacts the sample. The exact mechanism is still unclear however there is a wide range of theories. These theories can be separated into primary and secondary ion formation models. Primary ion formation is the direct ionisation caused by the laser and is typically matrix or matrix related molecules. Where by a matrix molecule (M) looses and electron to become a radically charged ion ($M^{+\cdot}$) [51]

$$M \rightarrow (h\nu) \rightarrow M^{+\cdot} + e^{-}$$

It has been proposed that when the matrix molecule (M) is excited by the laser (*hv*) the excited molecule exists for sufficient length of time to then further react with molecules within close proximity, possibly ionising with analyte molecules (A). This is known as the excited state proton transfer.

$$M \rightarrow (hv) \rightarrow M^* + A \rightarrow n(hv) \rightarrow [M\text{-}H]^- + [A+H]^+$$

Other primary ionisation processes include thermal ionisation are outlined in Zenobi and Knochenmuss [51]

Secondary ionisation processes is the interaction between two ions where the charge is transferred from an ion to form another. [11, 51] For example,

$$M \rightarrow (hv) \rightarrow M^* + M \rightarrow n(hv) \rightarrow [M\text{-}H]^- + [M+H]^+$$

Followed by

$$[M+H]^+ + A \rightarrow M + [A+H]^+$$

Overall, desorption and ionisation occurs when the laser interacts with the sample. A plume of molecules and ions form over the sample prior to the extraction of either positive or negative ions this process is shown in Figure 2.

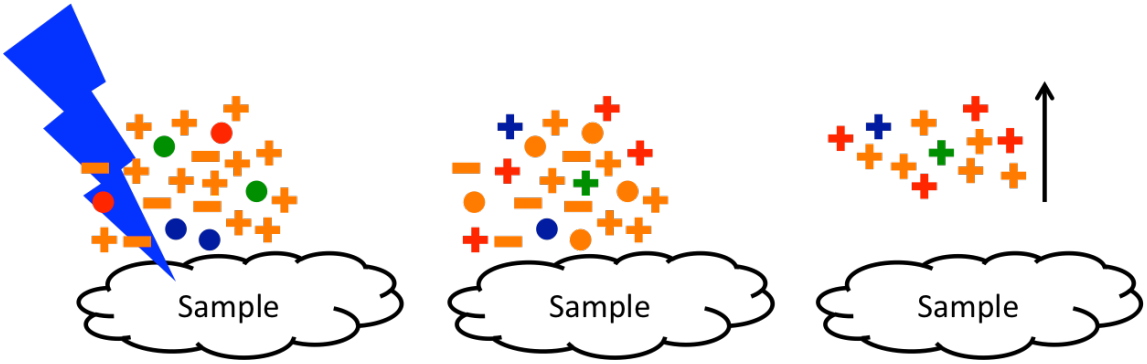

Figure 2: Schematic of MALDI sampling. Laser causing desorption and ionisation (orange matrix molecules in their charge state). Secondary ionisation processes occur to ionise analyte molecules (red, blue and green). Positive ions are then extracted for analysis.

MALDI is currently used for a wide range of analytes and purposes in a biological context. MALDI is used for the analysis of lipids, [52] proteins, [53] metabolites, [54] drug molecules [55]and DNA [56], from tissue[57], urine [58]and bacteria [59] to name a few. For MALDI there is a large emphasis on sample preparation, which is key to the success of the results, especially within MALDI imaging [41].

1.2.1.1.2 MALDI Imaging

MALDI images are maps of ion distribution across a surface. They are produced by the sequential MALDI analysis over a sample area. The spectra acquired retain the spatial location enabling the intensity of specific *m/z* to be plotted. (Figure 3) The laser is often focused to under 200 µm in diameter and can be down to a few µm. This means that the sampling is spatially localised

and recent advances are achieving subcellular resolution [60, 61]. The first mass spectrometry images were first reported in 1994 by Short [62] who imaged spots acetylcholine and its MS/MS product ions from dry filter paper. The first biological sample was analysed by Caprioli in 1997, [63] where a selection of peptides and small proteins were imaged from human buccal mucosa cells.

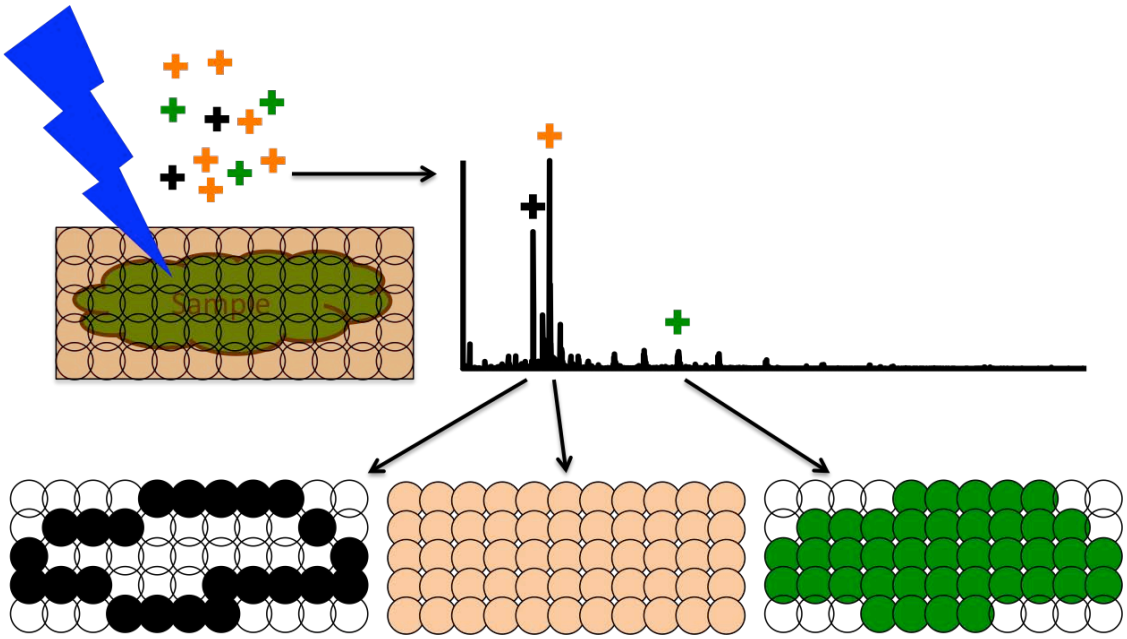

Figure 3 Schematic of MALDI imaging. Laser ablates a localised position on the sample. The spectrum is collected and the intensity of a particular *m/z* is displayed as a map.

The spatial resolution can be increased by over-sampling. Oversampling involves reducing the step size between pixels to smaller than the diameter of the laser. This is possible because when the laser ablates an area it ablates the matrix. When the laser is moved to the next pixel, only the region where matrix is present will induce ionisation. A consequence of this is the first row and column may be more intense than the all the remaining pixels. [64]

MALDI and MALDI imaging is not the only way to analyse biological molecules and to view their distribution on tissue. Electrospray ionisation is capable of ionising these molecules and a number of ambient sampling/ionisation methods have been developed that would be suitable for imaging.

1.2.1.2 Electrospray ionisation

Electrospray ionisation (ESI) is an atmospheric ionisation technique that was developed by Whitehouse et al. in 1985, in-order to couple liquid chromatography with mass spectrometry. [19] In ESI, a liquid sample is passed through a capillary and a voltage is applied between the end of the capillary and the entrance to the mass spectrometer, resulting in the production of charged droplets.

Three models are proposed for the ionisation of species via ESI (Figure 4). [65, 66] The first is the ion evaporation model (IEM), whereby as the charge density on the droplet increases individual ions are ejected. IEM is the suggested mechanism for small, low charge state ions. The second model is the charge residue model (CRM) in which a large biomolecule is encompassed in a droplet and as the solvent evaporates the charge is transferred to the analyte resulting in a highly charged ion. The third is the chain ejection model whereby as the droplet evaporates a polymer chain gradually detaches from the droplet. As the polymer detaches charged residues reduce the charge density in the droplet. [65]

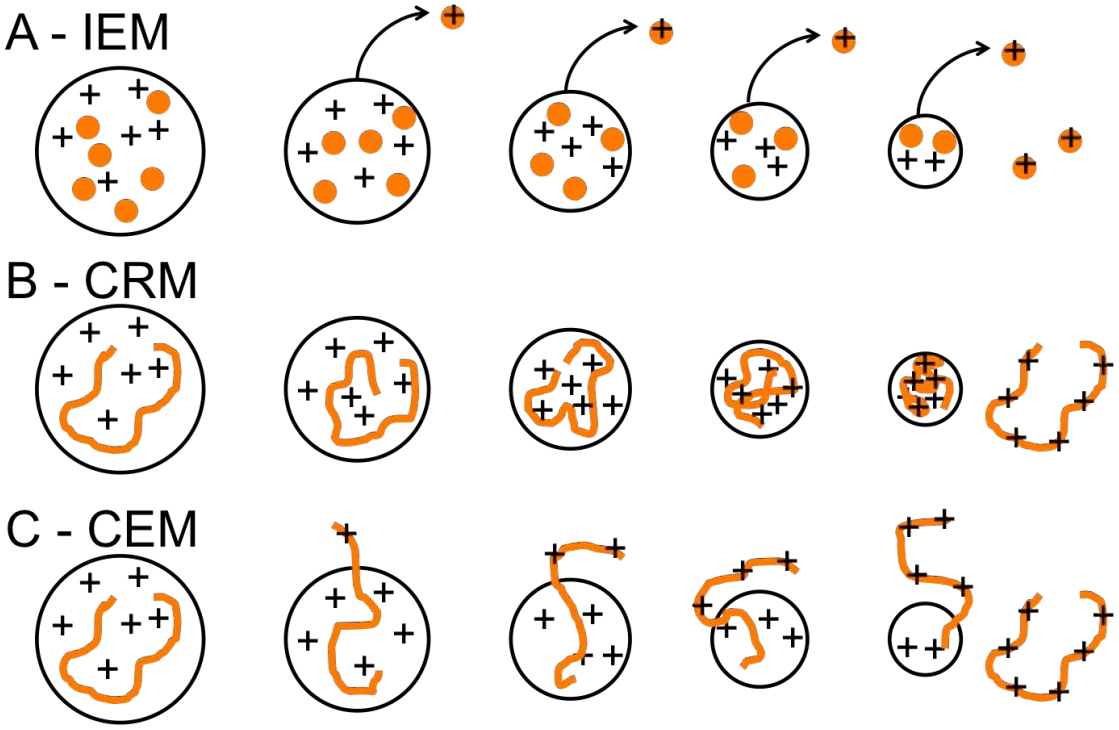

Figure 4: Three models of ionisation for ESI. A) ion ejection model, B) chain residue model C) chain ejection model. Orange circles and lines are analyte molecule obtaining a postive chare.

Factors that will affect the ability of ESI to be effective include,

- The organic content of the solution
- Solubility of the sample in the solution
- Salt content of sample

Organic solvents have a higher vapour pressure than water and evaporate more readily. A combination of organic solvent and water is typically used for biological samples. The one exception is analysis of proteins in their native state where organic solvents are not used as they denature the protein. [67] The sample needs to be a solution rather than a suspension; this includes any biological matter that might have been picked up during sampling. This is

because the electrospray nozzle can be very narrow especially for nano-ESI.[68] Nano-ESI follows the sample principles as ESI, however the flow rates at which the sample is introduced are in the region of nanoliters per minute rather than millilitres per minute for standard ESI. Salt content can also affect the ionisation: salts are naturally ionic and stabilise the charge of other molecules, including water, neutralising or reducing the charge of other species.

1.2.1.3 Liquid micro-junction surface analysis

Liquid micro-junction (LMJ) surface analysis is a newly emerging technique where micro-litre liquid droplets connect to a surface and a sampling probe. There are two types of LMJ surface analysis platforms available commercially: the continuous flow (CF-) LMJ sampling platform, produced by Prosolia and known as the flowprobe, and a discrete position LMJ analysis platform produced by Advion called the NanoMate TriVersa which performs liquid extraction surface analysis (LESA).

The CF-LMJ sampling technique was first reported by Wachs and Henion (2001) [69], who described a process whereby a solution was fed from a reservoir onto a sample and then the enriched solution was led away via an internal tube into an ESI source. The first instance of use of the liquid micro-junction sampling technique was the CF-LMJ sampling of TLC plates in 2002. [70]. Since then this technique has been demonstrated on SPE cards [71], and drug tablets [72] and has been used to show a selection of analytes including

active pharmaceutical ingredients and dyes [70, 72-75]. The fluid dynamics has also been investigated using dyes and a transparent sampling probe [76, 77].

The LESA approach, developed by Kertesz and Van Berkel (2009) [78], involves aspiration of a predetermined volume of electrospray solution from a reservoir into a probe, relocation to the required position above the substrate and lowering of the pipette to just above the surface. A set volume of the solution is dispensed so that there is contact between the probe and the surface, i.e., formation of a liquid-microjunction. A short pause allows molecules from the surface to diffuse into solution before the sample is re-aspirated into the probe. The sampling probe relocates and rotates 90^{o} to makes contact with the nano-ESI chip. This chip has 400, 10 μm (I.D.) capillaries through it, and becomes the ESI source. (Figure 5)

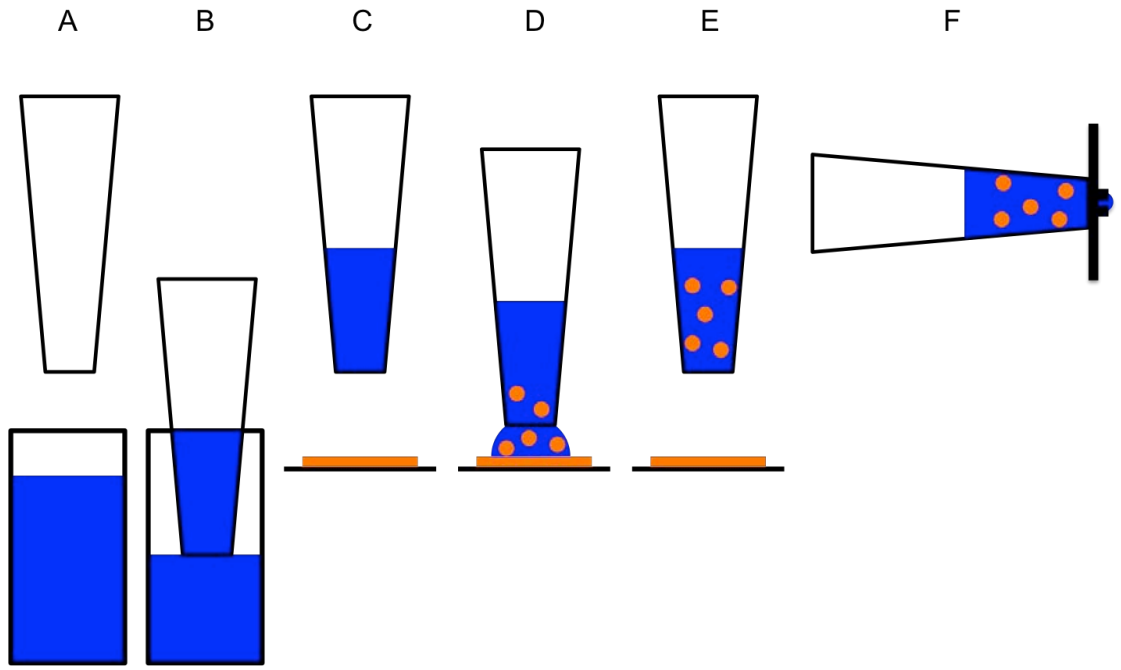

Figure 5: Schematic of LESA protocol. A and B) LESA tip decendes into solvent well and draws up some solution, C) LESA tip relocates over sample (orange), D) LESA tip descends to just above the sample and dispences some of the solution. E) Enriched solution is reasiprated. F) The tip relocates to the capillary chip for nano-ESI.

The LESA approach has been used to analyse a wide range of tissue sections including arterial plaque [79], whole body rat [78, 80], porcine ear [81], rat liver [82] and formalin fixed mouse brain [45]. Other complex biological samples have been analysed such as dried blood spots[83-85], bacterial colonies [86]and single cells printed onto glass[87].

In most cases the tissue has been dosed with a drug and investigations have shown the detection of the drug or its metabolites. However Stegemann et al. demonstrated the possibility of detecting endogenous lipid species directly from tissue by LESA and compared the approach with the Folch extraction, a method of extracting and purifying total lipids from tissue sections [79, 88]. The first demonstration of the analysis of intact proteins by LESA coupled to mass

spectrometry was the detection of haemoglobin variants from dried blood spots [83, 84]. Intact endogenous proteins have also been detected in bacterial colonies [86]. The first example of intact proteins from tissue is presented here in chapter 3.

Both these techniques have advantages and disadvantages. CF-LMJ is able to spray for a long time but because of the continual sampling the extraction is liable to change over the analysis time whereas in LESA, a specific volume is collected. This finite volume is homogenous and therefore long experiments can be conducted without the risk of the sample composition changing. In addition there is no contamination using the LESA system as every analysis uses a fresh probe and chip position whereas the CF-LMJ uses the same probe for all analyses meaning the approach is prone to contamination between samples.

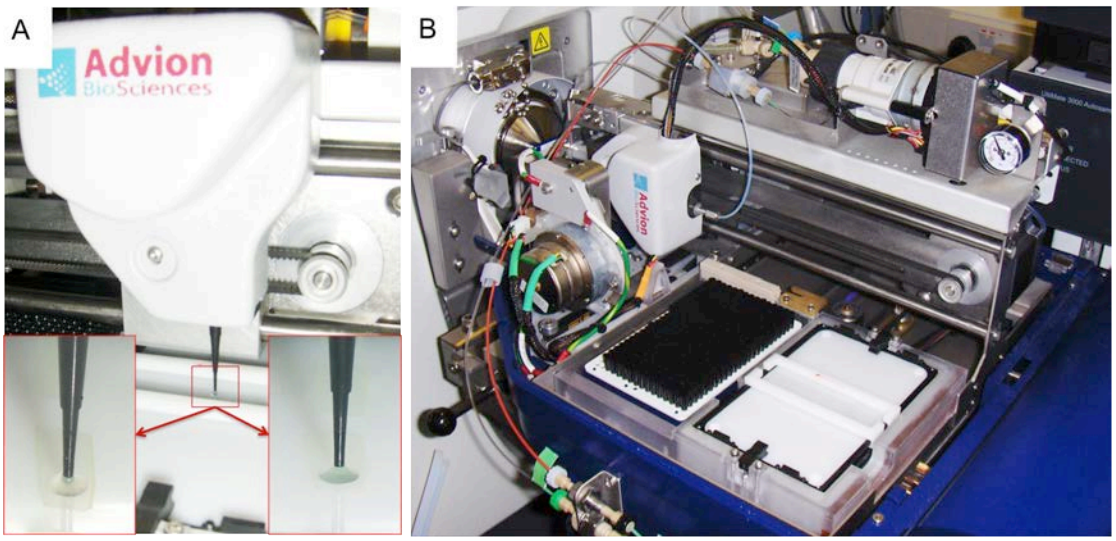

Figure 6: A) Photograph of the NanoMate TriVersa sampling from tissue using a liquid microjunction, B) Advion NanoMate TriVersa in the spray position.

1.2.1.3.1 Liquid micro-junction imaging

Liquid microjunction sampling is also an imaging modality. The sampling is limited in both the x and y directions, therefore the results from a particular analysis are spatially localised. LESA imaging has been used demonstrated by Eikel et al who profiled terfenadine, a pharmaceutical drug from dosed mouse brain [80]. These images were produced using an SRM method and therefore targeted to a specific *m/z*. Other reported instances of LESA imaging are single line evaluations [81]. Although neither study displayed the data as what might be considered a typical image (one as a bar chart and the other as a line graph) both have conducted spatially sequential analysis of pharmaceuticals from tissue. A SRM study was conducted to show the distribution of drug metabolites over a section of rat kidney. The other study on porcine tissue used a QToF however only reported the intensity of product ions [81, 89].

The spatial resolution of these two techniques is very similar. LESA reports a step size between pixels as 1-2 mm [82, 90]. Reported literature for CF-LMJ imaging via the FlowProbe uses discreet spot locations. That displayed the distribution of three *m/z* that registered with the three tissue types found in diseased rabbit lung tissue [91]. The flow probe has the capability for raster mode imaging however this has yet to be demonstrated.

1.2.2. Other ambient sampling and ionisation methods

Ambient ionisation is often confused with atmospheric pressure ionisation. To be defined as ambient ionisation a techniques must adhere to the following four conditions [92]:

1. Minimal sample pre-treatment,
2. Ionisation conducted in open air.
3. Not be specific to a particular mass analyser.
4. Soft ionisation or sample must be between the ionisation source and the inlet.

The first condition, minimal sample pre-treatment, puts an emphasis on direct ionisation from a sample and excludes on and off-line purification methods such as chromatographic methods or other purification/separation techniques.

The second condition, ionisation is conducted in open air, is the key difference to atmospheric pressure ionisation, which is conducted in an enclosure at atmospheric pressure. This condition also means that ambient ionisation should be able to sample any object regardless of size and shape without need to section the object, as there would be no physical constraints. This is not strictly true in all cases as some manufacturers include sample holders that limit the size and shape of the sample, however, it is not the technique per se that is the limiting factor.

The third condition is that the ionisation source is independent from the mass analyser, i.e., the ionisation source should be interchangeable with other mass analysers that have an atmospheric pressure compatible inlet.

The fourth condition is to enable the analysis of a wide range of molecules from complex samples. Soft ionisation can be hard to define: In this case, the limit is equal to or softer than ESI, i.e., able to ionise large molecules intact, with the potential to produce multiply charged species.

Even taking into account these four points, there are still many ambient pressure techniques that have been reported in literature. There are over 40 ambient ionisation methods, several of which are very similar, and recent reviews have further subdivided ambient ionisation into groups based on their method of sampling and ionisation. [92, 93]

1. Solid-Liquid Extraction Based
2. Plasma Based
3. Two step Non-Laser,
4. Acoustic Desorption
5. Two Step Laser Desorption/Ablation
6. Other and Multimodal

Solid-Liquid extraction based sampling techniques is a group of two-step sampling –ionisation sources. It is in this group that liquid-micro junction

techniques such as LESA are located [78]. Other techniques in the group include the CF-LMJ [69], the SSSP [94], and nano-DESI [95] (see table for acronym description).

Plasma based techniques are techniques that use plasma beams for the desorption/ablation and ionisation of the sample. [96-98]

Two-step Non-Laser techniques are a mix of acoustic, thermal and mechanical extraction techniques. There are two acoustic methods that use vibrations created by either radio frequency (RADIO) [99] or a pulsed laser through foil (LAID-ESI) [100] to vibrate the sample from a surface. An ESI plume then picks up the vaporised sample where molecules are ionised. Thermal methods such as APTDI [101] or APTD-ESI [102] heat the sample causing volatile molecules to vaporise. The vaporised sample then meets the ESI spray and induces ionisation of the sample.

Two-step Laser ablation/desorption techniques are all very similar. The main differences are the types of laser used, and a difference in the extraction mechanism, either desorption or ablation. LADESI [103] and LDESI [104] both use IR-lasers to desorbed/ablate the sample the former used Er:YAG and the latter CO_2. Also in this category is MALDIESI [105] similar to the two previous techniques, MALDIESI uses a UV laser (Nd:YAG) and a matrix is applied to the sample. In all cases an electrospray source is positioned so that the ESI spray

and the plume created by the laser intermingle. The electrospray droplets pick up some of the desorbed/ablated molecules and ionisation occurs via ESI.

The five subcategories listed contain most of the ambient techniques, the remaining few including swiFerr [106] and REIMS [107] are unique enough to not have any other technique similar to them and do not form a definable category by altogether, and so this category is defined as other techniques.

Table 1-3: Ambient techniques in alphabetical order based on their abbreviation

Technique	Brief Description	First reported
Ambient micro-hollow cathode discharge ionisation (ambient MHCD)	A plasma stream formed from a micro-hollow cathode, was directed over the sample interacting at a 45°C angle causing desperation and ionisation.	[108]
Atmospheric pressure thermal desorption ionisation (APTDI)	Heated nitrogen is directed onto a surface, desorbed ions are analysed	[101]
Atmospheric pressure thermal desorption-ESI (APTD-ESI)	Sample is heated — emissions are then captured by ES resulting in ionisation.	[102]
Beta electron-assisted direct chemical ionisation (BADCI)	b-emitting radioactive source ionises nitrogen gas stream that flows over sample	[109]
Desorption atmospheric pressure chemical ionisation (DAPCI)	Plasma induces ionisation of atmospheric water molecules ionising the sample.	[110]
Desorption atmospheric pressure photo-ionisation (DAPPI)	Jet of nebulised solvent desorbs sample, ultra-violet lamp is used to ionise the sample.	[111]
Direct analysis in real time (DART)	A stream of a reagent gas (He or N) is excited and projected onto the sample at an angle causing desorption/ionisation.	[112]
Dielectric barrier discharge ionisation (DBDI)	Alternating current between two electrodes separated by glass slide containing the sample produced plasma, for desorption and ionisation.	[113]

Technique	Brief Description	First reported
Desorption corona beam ionisation (DCBI)	A coronal beam is created from a stream of helium gas. Beam is directed onto a surface causing desorption and ionisation	[114]
Desorption electro-flow focussing ionisation (DEFFI)	A jet of solvent surrounded by a flow of nitrogen gas is directed at the sample. desorption then chemical induced metastable ionisation occurs.	[115]
Desorption electrospray/metastable-induced ionisation (DEMI)	A jet of solvent directed at the sample desorption occurs, desorbed molecules mingle with charged ions causing metastable – induced ionisation.	[116]
Desorption electrospray ionisation (DESI)	A high velocity jet of electrospray solution aimed at sample extracts analyte molecules from a surface. Secondary droplets are formed from the impact of the original jet. Ionisation occurs similar to that of ESI.	[20]
Desorption ionisation by Charge exchange (DICE)	Conducted in a similar manor to DESI using toluene as a spray solvent	[117]
Electrode-assisted DESI (EADESI)	An electrode positioned on close to the outlet for the jet of electrospray, Charged droplets desorbed analytes from the surface and form secondary droplets. Ionisation occurs similar to ESI.	[118]
Easy ambient sonic-spray ionisation (EASI) also known as Desorption sonic spray ionisation (DeSSI)	A supersonic nebulising gas carries a jet of solvent to the sample. Desorption and ionisation occur without heat or voltage applied.	[119]
Electrospray assisted laser desorption ionisation (ELDI)	Pulsed nitrogen laser beam ablates sample, plume mingles with ES creating ions.	[120]
Flowing atmospheric pressure afterglow (FAPA)	Ions formed by the collision of helium gas and electrons. This ion beam desorbs and ionises sample.	[121, 122]
Infrared laser ablation metastable induced chemical ionisation (IR-LAMICI)	IR-lasers ablate sample the plume is ionised by excited helium and nitrogen gas that flows to the MS inlet.	[123]
Laser ablation atmospheric pressure photoionisation (LAAPPI)	IR laser ablates sample, the plume is caught by heated toluene from a nebuliser. At the intersect of plume and spray a UV lamp causes ionisation.	[124]
Laser assisted desorption electrospray ionisation (LADESI)	Er:YAG IR laser desorbs the sampling the plume is caught and ionised using ESI.	[103]
Laser ablation electrospray ionisation (LAESI)	Nd:YAG UV laser ablates the sample and the resulting plume is caught in the electrospray spray where the sample is ionised.	[125]
Laser desorption electrospray ionisation (LDESI)	CO_2 IR laser desorbs the sampling the plume is caught and ionised using ESI. Requires Aqueous based sample.	[104]

Technique	Brief Description	First reported
Laser desorption ionisation (LDI)	CO_2 or Nd:YAG lasers are used to desorbed the sample, tubing then transfers the ions from the sample to the instrument.	[21]
Laser induced acoustic desorption/atmospheric pressure chemical ionisation (LIAD/APCI)	Laser is directed at the reverse side of aluminium foil containing the sample, causing desorption, desorbed species are ionised using chemical ionisation.	[126]
Laser induced acoustic desorption electrospray ionisation (LIAD-ESI)	Laser desorbs sample from silica/aluminium foil substrate via vibrational energy. Desorbed species are then captured by the ESI spray.	[100]
Surface sealing sampling probe (SSSP)	A sampling probe with blade around the tip. The probe makes contact with the sample forming a seal. Liquid is then dispensed into this sealed area and re-aspirated to be ionised via ESI.	[94]
Low temperature plasma probe (LTP)	Stable 30 ^oC plasma discharge is focused onto a surface causing desorption and ionisation.	[98]
Laserspray ionisation (LSI)	The spraying capillary is irradiated with an IR laser inducing ionisation. Later versions us a CO_2 laser.	[127]
Matrix assisted laser desorption electrospray ionisation (MALDESI)	Matrix is applied to a surface a laser induces desorption the ion plume is then picked up in an ESI spray.	[105]
Micro-fabricated glow discharge plasma (MFGDP)	A glowing plasma discharge is produced at the end of a probe. Sample is introduced at close proximity to the probe and the MS inlet.	[128]
Neutral desorption extractive electrospray ionisation (ND-EESI)	A nitrogen stream is directed onto a sample, the resulting aerosol is heated and combines with an ES for ionisation.	[129]
Plasma-assisted desorption ionisation (PADI)	A low temperature plasma is desorbs and ionise a sample close to the mass spectrometry	[96]
Probe electrospray ionisation (PESI)	A solid probe pricks the sample and then moved to point into the inlet, a voltage is then applied to the probe and ions are ejected.	[130]
Plasma assisted multi wavelength laser desorption ionisation (PAMLDI)	PADI using a tuneable laser.	[97]
Paper spray ionisation (PSI)	A liquid sample is dispensed onto paper, a voltage is applied to the paper and induces a ionising spray.	[131]
Radio-frequency acoustic desorption and ionisation (RADIO)	Sample on a quartz crystal microbalance is subjected to and RF of 10.1Mhz. Plume is captured and directed into mass spectrometer by sprayed solvent stream.	[99]
Rapid evaporative ionisation mass	A heated probe vaporises and ionises the sample. Ions transferred to mass	[107]

Technique	Brief Description	First reported
spectrometry (REIMS)	spectrometer using nitrogen flow.	
Surface acoustic wave nebulization (SAWN)	Acoustic wave propagates along the surface and into the sample nebulizing and ionising the sample.	[132]
Switched ferroelectric plasma ionizer (SwiFerr)	A sample that is in aerosol form enters the ionisation chamber and passes over a ferroeletric material that emits plasma radiation.	[106]
Transmission mode DESI (TMDESI)	A high velocity jet of electrospray solution is passed through a mesh holding the sample.	[133]

1.2.2.1 Ambient imaging techniques,

Many of the techniques mentioned in the previous section have spatially localised sampling, making them suitable for imaging. The majority of these techniques are liquid micro-junction techniques and laser or plasma directed sampling such as DESI, LAESI or PESI. [134] To-date the resolution that is achievable via ambient imaging techniques does not yet match the subcellular resolution of vacuum-based techniques such as MALDI or SIMS. [60, 61, 135].

Nano-DESI is a direct relative of LESA. This technique supports a droplet between a solvent delivery tube and an extraction tube, and this extraction tube is also the ESI capillary. Images of rat brain tissue were acquired in raster mode, with a y-axis resolution of 200um and an x-axis resolution of 20um. Images show lipids specific to different regions of the brain. [136]

1.3 Mass analysers

There are a wide range of mass analysers, four are discussed here. A summary of the techniques are provided in Table 1-4

Table 1-4: – Comparison between mass analysers, data taken from vendor websites[137, 138]

Parameter	Time of Flight (Synapt G2)	Quadrupole (TSQ Vantage)	Orbitrap Velos
Mass resolution	20,000 at *m/z* 556 (in resolution mode)	7,500 at *m/z* 508	100,000 at *m/z* 400
Mass Accuracy	<1ppm using Lockmass between *m/z* 150-800	<5ppm between *m/z* 168 -1224	<3ppm external calibration, <1ppm internal calibration
Mass range	*m/z* 20-100,000 (in resolution mode)	*m/z* 10-1500	*m/z* 50-2000 or *m/z* 200-4000

1.3.1. Time of Flight

Time of flight instruments measure the time taken for an ion to travel from the source to the detector. Using known molecular mass standards the time of flight can be related to the *m/z* ratio of the ion.

Packets of ions are accelerated using an electrical potential gradient. (Figure 7) Ions are held between potentials (1) which are both equal (i=ii), for the extraction and acceleration, a potential gradient is formed (i>ii) (2), the potential at (iii) is neutral and therefore the same as the detector, insuring no further acceleration occurs during the flight path. Differences in the energy of

the ions starting point will be counteracted by this method for acceleration. Ions closer to the ion gate receive a stronger acceleration force than those further away. [11] This ensures that ions of the same *m/z* arrive at the detector at the same time.

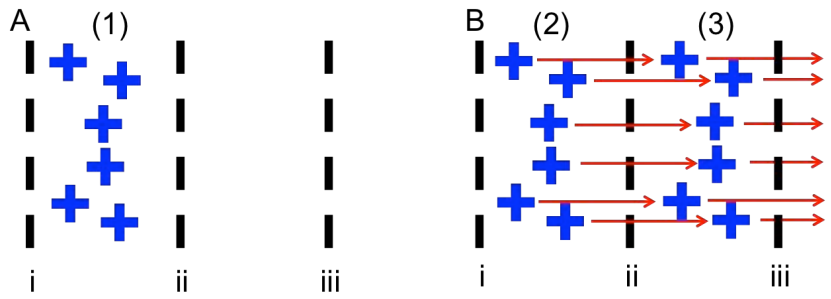

Figure 7 (1) Ions are contained between he sample plate (i) and the first ion gate(ii). (2) Ions are extracted when a potential gradient is applied (i>ii). (3) Ions are accelerated, the third ion gate insure there is no potential gradient between the source and the detector. (iii=d)

Ions of different mass to charge are separated because they have the same kinetic energy (KE) that they receive during acceleration (V_x). Therefore the velocity (v) of the ion is dependant on the mass (m) and charge (ze).

Equation 1

$$KE = \frac{mv^2}{2} = zeV_x$$

The velocity of an ion can be calculated by rearranging Equation 1.

Equation 2

$$v = \sqrt{(\frac{2zeV_x}{m})}$$

Ions will travel at a constant velocity for the length of the flight tube (*L*) and therefore the time the ion detected (*t*) is dependent on the mass to charge (*m/z*) ratio of the ion. A doubly charged ion will feel the accelerating force twice as strongly resulting in a velocity twice as fast, halving the time it would take a signally charged ion of the same mass to reach the detector.

Equation 3

$$t^2 = \frac{m}{z}\left(\frac{L^2}{2eV_x}\right)$$

The longer the flight path, the greater the separation in time, and the better the resolution. However the longer the flight path, the greater chance for ions to either be neutralised by hitting residual air molecules in the instrument or to be extracted by the vacuum pump this reduces the sensitivity of the approach. Longer flight paths also cause a broadening of the peaks caused by ions of the same *m/z* having subtlety different velocities. Even using pulsed extraction to accelerate the ions there can be subtle differences in the kinetic energy. The resolution can be improved by reflecting the ions using reflectrons, which reduces this variation.

Ions entering the reflector of the same *m/z* but differing slightly in their velocities penetrate into the reflector to differing degrees (*d*). Therefore the path length that the ions take is proportional to the velocity of the incoming ion. The depth the ion penetrates into the reflector is dependant on the electrical field (*E*)

of the reflector, which is in turn calculated by depth of the reflector (D) and the electrical field (V_y). Therefore the depth an ion penetrates into a reflector is calculated using Equation 4

Equation 4

$$d = \frac{KE}{qE} = \frac{qV_x}{q\,{V_y}/{D}} = \frac{DV_x}{V_y}$$

This process refocuses ions so that they reach the detector at the same time. This narrows the peak width and improves the resolution. [11, 139]

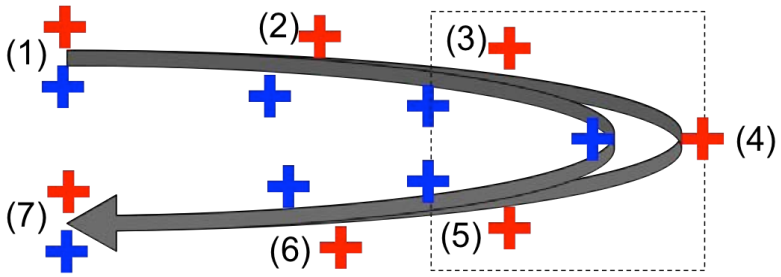

Figure 8: Reflectron are used to remove subtle difference in velocity between ions of the same mass. Two ions of the same *m/z* but have different energies (red and blue cross) (1) the higher energy red ion travels faster (2) the ion take different paths through the reflector, and ions refocus on the detector

There are three configurations of time of flight instruments:

- Linear: Straight line between source and detector (Figure 9 Green line)
- V mode: there is a V shaped flight path using one reflector. (Figure 9 Red line)
- W mode: there is a W shaped flight path using 3 reflectrons. (Figure 9 Blue line)

Linear is the most sensitive but has the lowest mass resolution whereas W mode has the highest mass resolution but the lowest sensitivity.

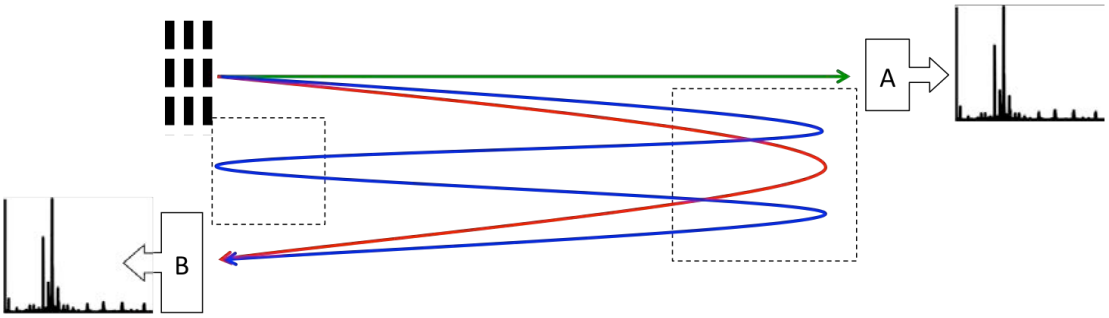

Figure 9: Schematic of the time of flight mass spectrometry illustrating 3 modes of use. Linear (green) detected at detector A. V mode (red) and W mode (blue) detected at detector B.

1.3.2. Quadrupole

The quadrupole is a mass filter as a low mass resolution mass analyser. Quadrupole mass analysers comprise four parallel rods to which oscillating electrical potentials are applied. Only ions that have stable trajectories are able to pass through the device; others are ejected out of the path (Figure 10). The arrangement is such that adjacent rods have opposite polarities. When ions pass through the quadrupole in each plane (vertical and horizontal) ions go through a cycle of focusing (when polarity is the same as charged particles) and defocusing (when the polarity is opposite to the charged particles). [11, 140, 141]

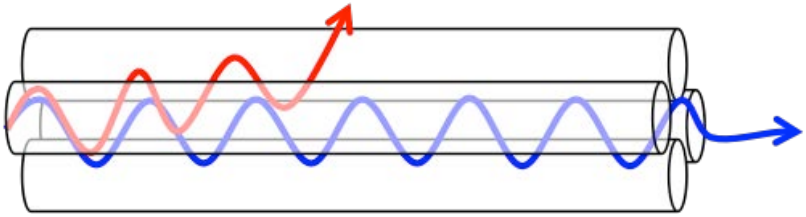

Figure 10: Schematic of a quadrupole, illustrating the ion path of a stable ion (blue) and an unstable ion (red)

In a single plane this causes ions to oscillate between the two poles; however, with two planes the motion is spiral. For any single ion there is a range of combinations of direct voltages and r.f voltages that can be used to stabilise the ions passage through the quadruple. To calculate the trajectory of an ion in a quadrupole, it is necessary to solve the following differential equations (Equation 5, Equation 6 and Equation 7) that relate to the x, y, and z planes of the quadrupole. [141]

Equation 5: x-plane

$$\frac{d^2x}{dt^2} + \frac{2zex}{mr_0^2}[U + Vcos(\varpi t)] = 0$$

Equation 6: y-plane

$$\frac{d^2y}{dt^2} - \frac{2zey}{mr_0^2}[U + Vcos(\varpi t)] = 0$$

Equation 7: z-plane

$$\frac{d^2z}{dt^2} = 0$$

Where V is the magnitude of the ac (RF waveform), U is the magnitude of the applied dc potential, t is time, r is the distance from the z axis to the surface of any electrode, ω is the angular frequency *m* is the mass of the ion and e is the charge. The solution can be represented an a-q stability diagram (Figure 11) where,

Equation 8

$$a = \frac{8zeU}{mr^2\omega^2}$$

Equation 9

$$q = \frac{4zeV}{mr^2\omega^2}$$

It is these equations that dictate the mass resolution and sensitivity of the instrument. The dc and ac potentials are applied to the quadrupole that satisfy these equations for each point along the scan line. Effective transmission of an ion of particular *m/z* only occurs when the stability diagram and the scan line intersect. Each mass to charge ratio has a similar stability diagram the peak of larger *m/z* has a higher 'a' and q value. Reducing the gradient of the scan line increases sensitivity but reduces mass resolution. [140, 141]

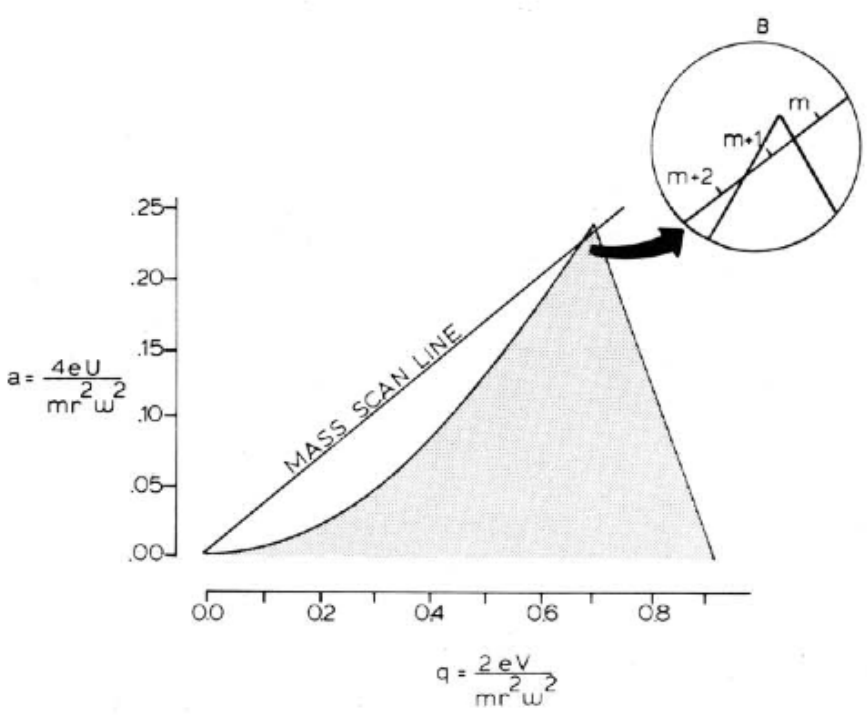

Figure 11: Graphical representation of the stability of an *m/z* ion in a quadruple. Figure taken from Miller et al (1986) [141]

The advantages of quadrupoles;

- Do not require a high vacuum, and therefore it is not necessary to have expensive turbo vacuum pumps.
- Can be used for transferring ions from atmospheric and ambient ion sources.
- Can be used to isolate one or more ions
- Only detects the target ion(s) by jumping through the frequencies.

Hexapoles are used in the Synapt G2-S (see section 1.6.2) and work on a similar principle to quadrupoles, however hexapoles have six parallel bars arranged in a hexagon pattern. Hexapoles are used to transport ions rather than analyse

them as they have a wider *m/z* transmission range and a lower focusing power. [11]

1.3.3. Linear ion trap

The linear ion trap (LIT) is similar to the quadrupole in that it comprises 4 parallel rods. The difference is that instead of the ions passing through the device, the ions are trapped within the device by ion lenses at either end to repel the ions back into the mass analyser. Using the same principles as quadrupoles, instead of stabilising a narrow range of *m/z* values, a much wider range of *m/z* are stable in the ion trap. This is achived by using *a* and *q* values in Figure 11 that would be more central in the stable region (greyed area) which overlap with the stability diagrams of other *m/z*. To detect and differentiate between ions of different *m/z*, the r.f values and direct voltages are scanned such that ions are destabilised sequentially. Ions can be ejected either axially or radially towards the detector. For radial ejection slits in the quadrupoles allow unperturbed transmission. LIT are also used as collision cells: a narrow range of *m/z* are selected and held in the LIT, the ions are then collided with a neutral gas causing the ions to fragment (see Section 1.5.1 for more information on CID). [11, 142]

1.3.4. Orbitrap

In an Orbitrap mass analyser ions rotate around a central barrel-shaped electrode. Ions rotate around this electrode in a radial direction (r) and travel

along the electrode transverse direction (q). The potential energy (U) of this field can be expressed using Equation 10. [143, 144]

Equation 10

$$U(r,q) = \frac{k}{2}\left(q^2 - \frac{r^2}{2}\right) + \frac{k}{2} \times (R_m)^2 \times \ln\left[\frac{r}{R_m}\right] + C$$

Where (r,q) are the cylindrical co-ordinates, k is the field curvature R_m is the radius and C is a constant. It is important to note there is no cross terms with r and z so these species are independent of each other. The motion of ions in transverse direction is calculated in radians per second and is dependant on the energy characteristics of the transverse direction (E_q), the mass (m) and the charge (z) of the ion and can be calculated using Equation 11 and Equation 12.

Equation 11

$$q(t) = q_0 \cos(\omega t) + \sqrt{\frac{2E_q}{k}} \sin(\omega t)$$

where

Equation 12

$$\omega = \sqrt{(z/m)k}$$

The motion of ions is determined by the mass to charge ratio and ions of similar *m/z* form a packet of ions. When these ions pass the detector they induce a

current. The amplitude of this current is representative to the number of ions in the packet.

By using the transverse motion rather than the radial motion ions stay in a tighter packet for longer increasing the spectral resolution. (Figure 12). [143-145]

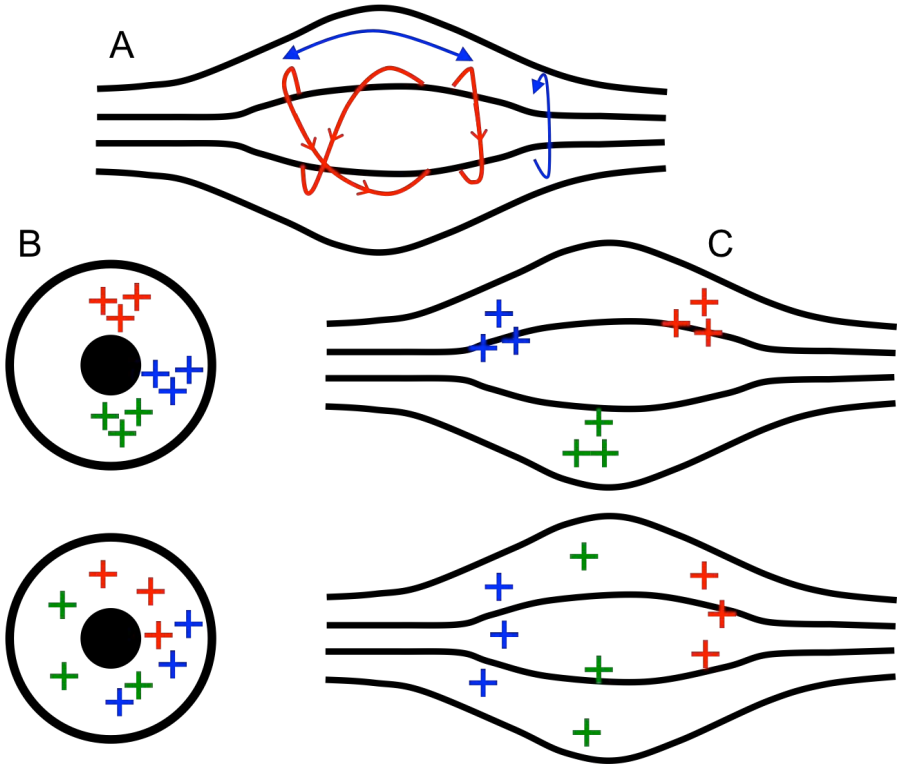

Figure 12: A) Obitrap mass analyser with the motion of ions idecated by the red line. Blue lines indicate Transverse and radial motion of ions. B and C) packets of ions (red green and blue crosses) degrading radially observed from the radial and transvers views.

Ion packets are measured multiple times as they pass the detector resulting in a time domain spectrum in which the waveform is comprised of the interfering frequencies for each *m/z*. The time domain spectrum can be converted to a frequency domain spectrum by means of Fourier transform. Subsequent

calibration of frequency for *m/z* results in a mass spectrum. If multiple ions are present the rate at which they rotate around the central electrode differs, inducing a detector response at different frequencies that when processed via Fourier transform, result in specific mass to charge ratios. In ion traps the direction of the motion that is detected is axial motion, i.e., the motion that rotate around control electrode. Developments of the ion trap reported by Alex Makarov, show that packets of ions of the same mass dissociate from each other axially very quickly, quicker than the decay of signal due to loss of ions and this limits the resolution that can be achieved with an ion-trap. Makarov goes on to show that packets of ions dissociate more slowly in the transverse direction and therefore significantly improve the resolution and sensitivity of the Orbitrap from other ion trap instruments. [144]

1.4 Separation techniques

Separation is used to enhance the quality of spectra and to reveal additional species and may be performed in the solution-phase or the gas-phase. Three separation techniques are used in this research, liquid chromatography (LC) and two forms of ion mobility. Ion mobility separation is a gas phase separation technique that there are several forms, two that will be discussed in this thesis are traveling wave ion mobility spectrometry (TWIMS)) and ultra-high field asymmetric ion mobility spectrometry (ultra-FAIMS).

1.4.1. Liquid Chromatography

Liquid chromatography is used to separate molecules on the interface of a stationary and mobile phase. The stationary phase is functionalised silica, typically with a C18 chain, that is packed into a column [146]. Variations in the carbon chain are used to target different molecules. Shorter chains such as C4 columns are used for intact proteins [147] and C30 columns used for small molecules. [148] The mobile phase is the solvent that carries the sample through the column. There are two forms: normal and reversed phase. Normal phase chromatography was developed first and comprises of a polar stationary phase and a non-polar mobile phase [149]. Reversed phase was developed second and uses a non-polar stationary phase and a polar mobile phase [150]. Proteomics typically uses reversed phase liquid chromatography because peptides have little affinity to a polar stationary phase, and peptides will not be retained or separated, in reverse phase the peptides have an affinity to the column enabling them to be separated. Occasionally normal phase chromatography is used for proteins because of the functionalised groups that they contain or if they are rich in hydrophilic amino acids, for this hydrophilic interaction liquid chromatography (HILIC) columns are used. [151]

Separation of proteins and peptides by LC occurs because of the affinity of the molecule to both the stationary and mobile phases. As the molecules travels through the column, an equilibrium is formed between the molecules on the stationary phase and the molecules in the mobile phase (Figure 13). As the

mobile phase is constantly moving the equilibrium is never reached causing the molecules to progress down the column. The composition of the mobile phase is often changed through the run to encourage slow moving analytes to elute from the column. [152]

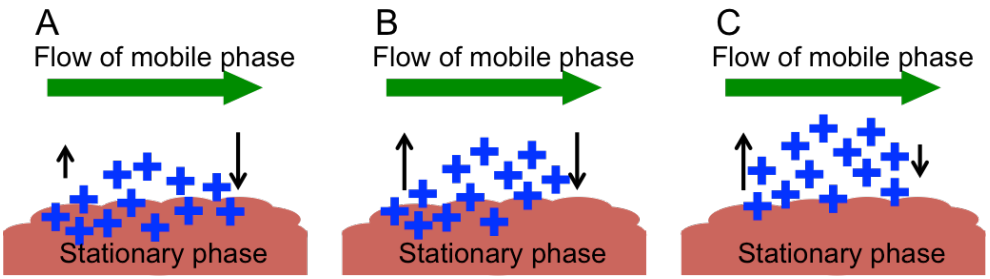

Figure 13: A) Molecules (blue crosses) have a strong affinity to the stationary phase resulting in a slow progression down the column. B) Molecules have an equal affinity to both the stationary and mobile phase. C) Molecules have a strong affinity to the mobile phase resulting in a fast elution.

The number of theoretical plates measures the efficiency of a column. The greater the number of theoretical plates, the greater the resolution. The number of theoretical plates can be calculated using Equation 13

Equation 13

$$Number\ of\ Plates = \frac{1}{plate\ height} \times Column\ length$$

To increase the number of plates either the column must be made longer or the plate height needs to be reduced. Increasing the pressure of the system can decrease the plate height, this is the strategy for high pressure and ultra-high pressure chromatography. [151] An alternative method for improving the separation is to conduct 2-dimentional liquid chromatography. Where LC is

conducted fractions of the eluent collected, then each fraction is run on an LC-MS/MS system for identification. This is particularly useful for extremely complex samples where the LC-MS/MS cannot identify peptides at a suitable rate for the identification of all detectable proteins in the sample. [153] When liquid chromatography is coupled to mass spectrometry by electrospray ionisation. The eluent of the LC from low flow rate systems can be directly coupled to the mass spectrometer, otherwise a splitter is used to redirect some of the sample to prevent the overloading the mass spectrometer.[154, 155]

1.4.2. Traveling wave ion mobility spectrometry

Traveling wave ion mobility spectrometry (TWIMS) separates ions based on the collisional cross section. [156, 157] Electrical potential waves are created by sequentially pulsing ring electrodes down a drift tube as a pulse occurs ions move down the potential gradient. (Figure 14 A) The expression that describes the effective potential generated (V^*), is;

Equation 14

$$V^*(r,z) = V_{max}\frac{[I_1^2(r,\delta)cos^2(z,\delta) + I_0^2(r,\delta)sin^2(z,\delta)]}{I_0^2(\rho,\delta)}$$

Where r and z describe the radial and axial co-ordinates, δ is the spacing between electrode. I_0 and I_1 are the zero and first order modified Bessel functions. V_{max} is;

Equation 15

$$V_{max} = \frac{qV_{RF}^2}{4m\omega^2\delta^2}$$

Where q is the charge of the molecule and m is the mass; V_{RF} is half the applied peak-to-peak voltage and ω is the angular frequency.[157, 158]

The wave is not completely efficient at driving the ions forward and occasionally an ion tumbles backwards rather than forward. The larger the ions the more likely this is to occur. This is because there is a relatively high pressure in the drift tube and larger molecules are more likely to collide with the gas molecules and tumble to the following wave. There is a direct relationship between the size of the ions and the rate in which they pass through the mobility chamber; this makes it possible to calculate the collisional cross section of a molecule. [159, 160]

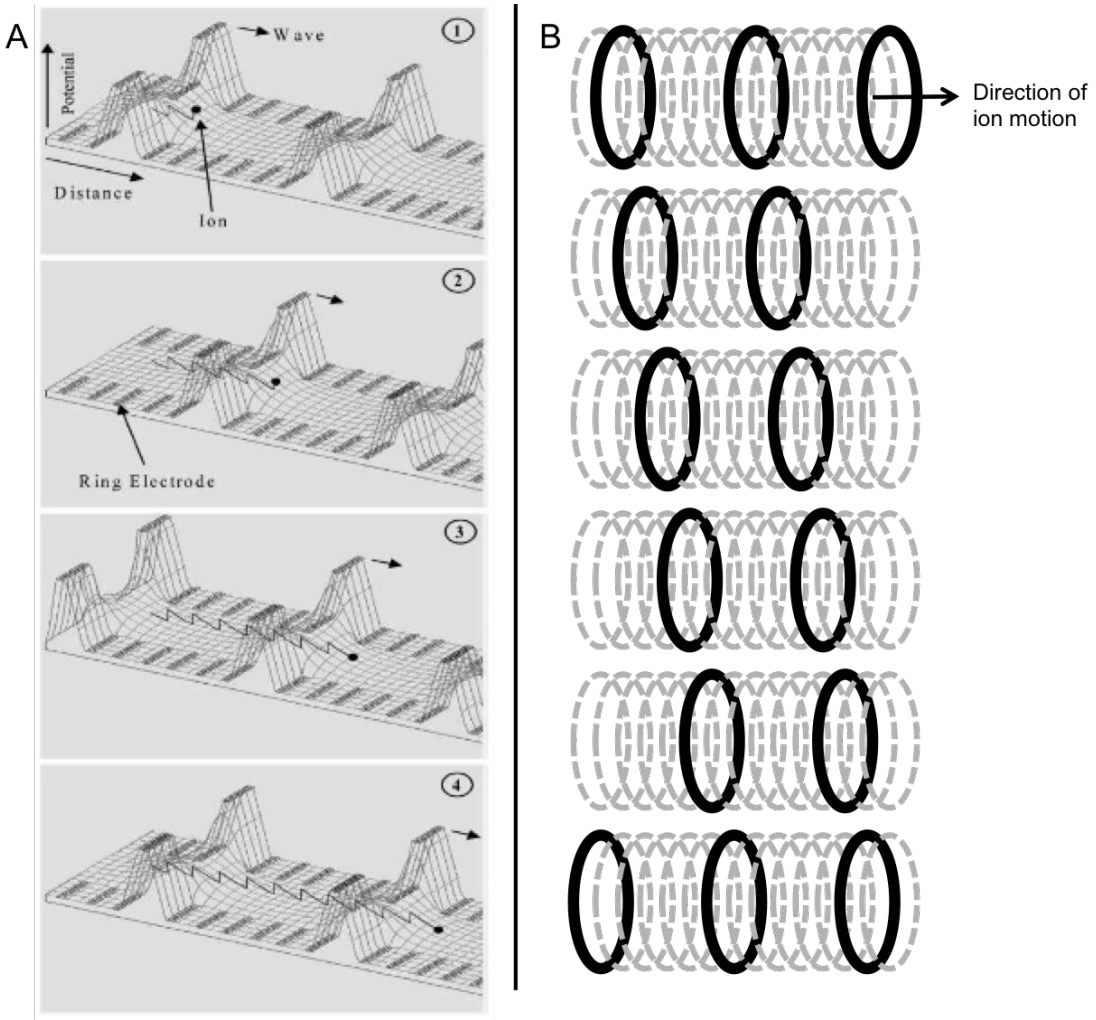

Figure 14: A) representation of TWIMS waves and the motion of an ion being affected by the wave. From Giles et al. 2004, [157], B) representation of sequentially pulsed ring electrodes that results in a wave. Black solid rings are the on with a high potential, grey dashed rings are in resting state with low potential.

1.4.3. Ultra-high field asymmetric ion mobility spectrometry

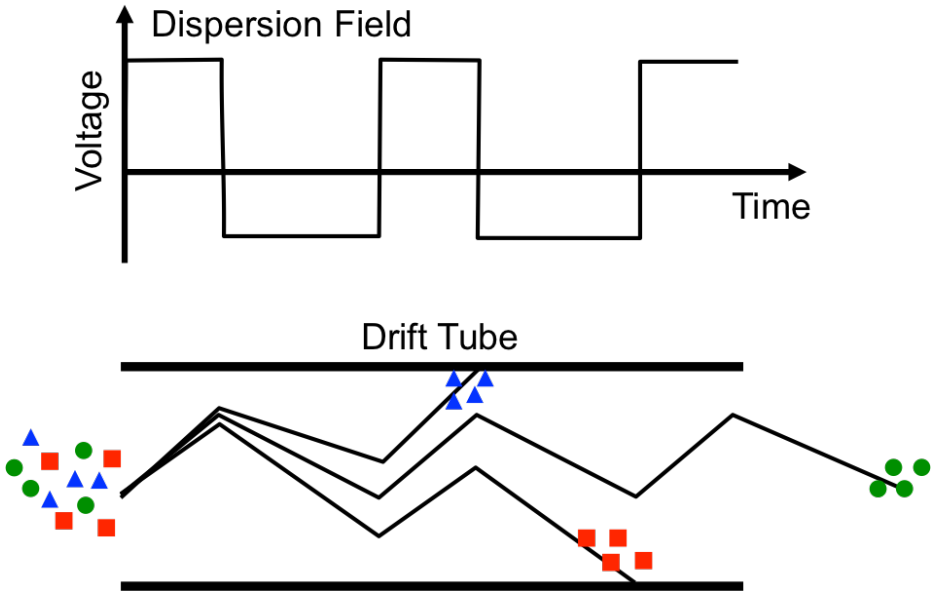

Figure 15: Top: Schematic of the dispersion field RF frequency showing an asymmetric waveform where the positive and negative parts would sum to zero. Bottom: Schematic of the drift of three theoretical ions using the dispersion field.

FAIMS separates ions on the basis of differences in their mobility in high and low electric fields. To disperse the ions a voltage is applied via a RF waveform. This attracts ions strongly to one plate for a short period of time and then the polarity switches and weakly attracts ions to the other plate for a longer period of time (Figure 15). The length of time each voltage is applied is such that the net field over one wave period is zero. If the mobilities in high and low electric field were equal, the displacement of an ion from its original trajectory is zero; however, this is not the case, a theory is that ions will change conformation in the high and low fields and therefore the mobility in each condition are different and as a result ions will drift away from their linear path.

The addition of a direct voltage (compensation voltage generating compensation field CF) between the two plates compensates for this drift. The compensation field (CF) is changed to allow specific ions to traverse the device. Until recently it has been believed that there is a limit to the resolving power (R). Exposing ions to the FAIMS field for longer is beneficial to a point. The relationship is proportional on the square root of time (t) the ions are subjected to the FAIMS field, therefore as time is extended the advantages gained get proportionally smaller. In addition FAIMS occurs in atmospheric conditions and therefore the longer ions are in the FAIMS device the weaker the ion signal will become. [161]

Equation 16

$$R \propto \sqrt{t}$$

Other factors that contribute to the resolution include the mobility (K_0) of a particular ion at a standard gas density (N_0), as this will affect the length of time an ion takes to pass through the drift tube. Another factor is the anisotropic diffusion (D_n) that causes peaks to broaden over a time period. The final factor affecting the resolution is the compensation field (E_C).

Equation 17

$$R = \frac{E_C K_0 N_0}{4N} \sqrt{\frac{t}{D_\Pi ln2}}$$

A recent development in FAIMS has reduced the path length that is required for the separation to occur. Shvartsburg et al. describe that increasing the E/N term in Equation 17, (by increasing the dispersion field) increases the resolution of FAIMS. Increasing the field strength was shown to have an additional benefit, as the resolution is less dependent on the mobility of an ion. [162] A chip based FAIMS device was developed by Owlstone Ltd. [161] , where the path length was only 700 μm, and there was not just one channel where a field is applied but many arranged in stacks along a chip (Figure 16A). In Figure 16 (B-D) the FAIMS chip is mounted into an adapted cone for the ESI inlet.

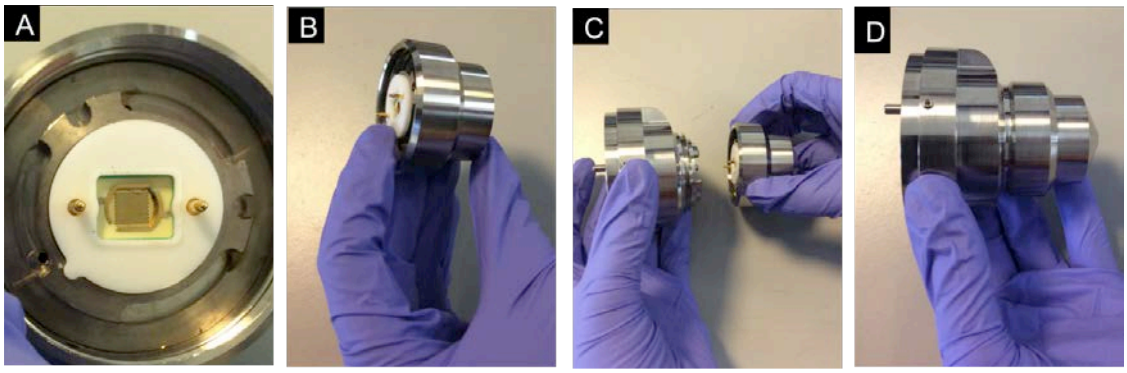

Figure 16: A) Photograph of the ultraFAIMS chip in the holder. B) Photograph of half of the ultraFAIMS cone, with the chip and electrodes visible C) Photograph of both halves of the ultraFAIMS cone not connected D) Photograph of the whole ultraFAIMS cone ready to be connected to the ESI inlet.

The first demonstration of the FAIMS chip was not in conjunction with mass spectrometry. The power of this technique was demonstrated with three ions that were known to have the same mobility with tradition FAIMS devices that operated at lower field strengths. At higher field strengths these three ions can be isolated using different compensation fields. [161]

A report published by the same group was the first to report the coupling of the FAIMS to a mass spectrometry. Analysis of leucine mixed with lab wastewater containing amino acids and peptide digests demonstrated the potential for this analysis. Leucine was separated from the near by peaks by tuning the dispersion field and the compensation field. [163] It should be noted that the units for the field strength in the ultraFAIMS is Townsends (Td). This is the ratio between the electric field and the gas number that was increased when developing the ultraFAIMS (Equation 18).

Equation 18

$$\mathrm{Td}=\frac{E}{N}=\frac{\mathrm{Vm^{-1}}}{\mathrm{m^{-3}}}=\ \mathrm{Vm^{2}}$$

Analysis of a standard peptide mix containing 5 peptides by Brown et al demonstrated that the ultraFAIMS device could separate peptides of the same *m/z*. [163] In a subsequent analysis singly and doubly charged peptides from a tryptic digest of alpha-1-acid-glycoprotein were separated using the ultraFAIMS. MS/MS analysis was conducted on the peptides demonstrating that this technique can be used for identification of small molecules. [163] Other work by the same group has looked at two isobaric species, polyethylene glycol (PEG) and 2-hydroxy-4-octyloxybenzophenone (HOBP). The ultraFAIMS separated these two compounds at different CV values. CID was also conducted on HOBP showing that there was a significant improvement in the MS/MS spectral quality when HOBP was isolated from PEG. [164]

In addition FAIMS coupled to in-source CID-MS was shown to improve the MS/MS spectra of HOBP due to the isolation of HOBP from PEG. [164]

1.5 Tandem mass spectrometry

Tandem mass spectrometry (MS/MS) enables structural characterisation of selected precursor ions. By fragmenting an intact ion it is possible to elucidate a structure, based on predictable bond cleavages.

Glycerol based lipids, such as triglycerides and phospholipids (see section 1.7.1) break along the glycerol and for phospholipids the phosphate group also cleaves (Figure 17). In addition lipids analysed from tissue often form salt adducts with the naturally occurring sodium and potassium, which readily dissociate upon fragmentation.

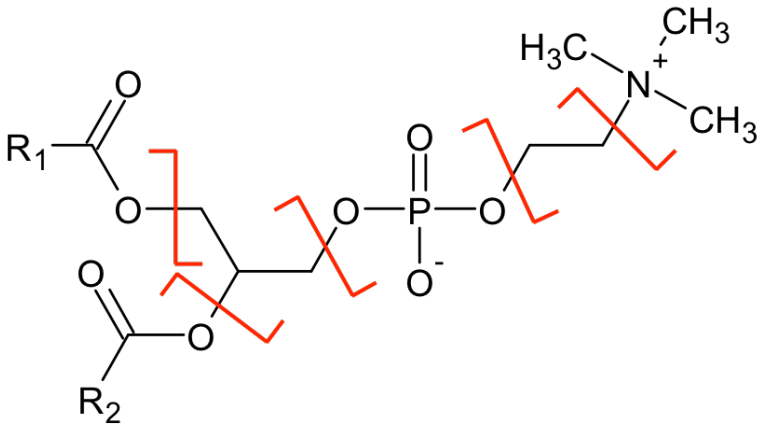

Figure 17: Phosphatidylcholine lipid. Where R_1 and R_2 represent an acyl chain. Red markers indicate common positions for fragmentation to occur

In contrast fragmentation of proteins typically occurs along the peptide backbone. (Figure 18) The fragments observed depend on the technique for fragmentation. CID and HCD fragmentation produces the b/y pair of product ions and an occasional a ion is also formed. With ETD fragmentation c/z pairs are produced and occasionally a,b or y ions

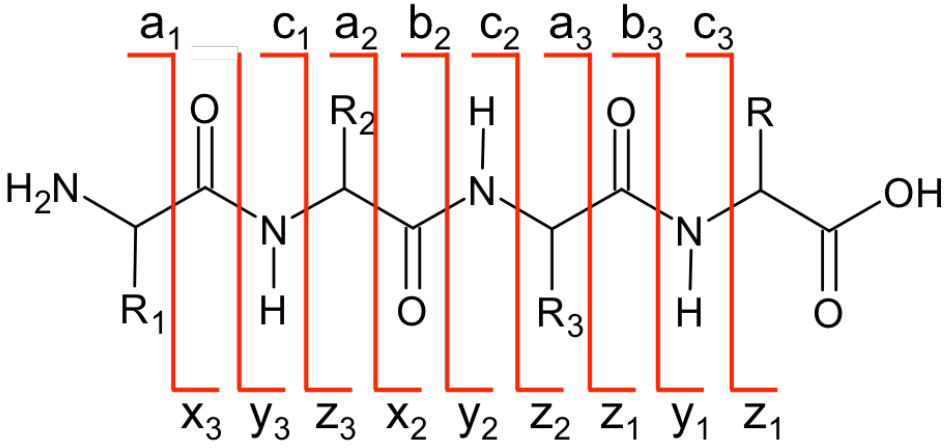

Figure 18: four amino acid long peptide, showing possible fragmentation. The letter indicates which bond is broken, and the number the number of residues along the chain the fragmentation has occurred. The b_1 ion is not labled because it cannot be formed.

Three different fragmentation methods are used in this research: collision induced dissociation (CID), higher energy collision dissociation (HCD) and electron transfer dissociation. (ETD).

The fragments observed are also dependant on the mass spectrometry used. If the fragmentation occurs in an ion trap then only ions down to 1/3rd of the mass of the precursor is stabled prior to mass analysis. However, if the fragmentation occurs in an quadrupole the full range if product ions can be detected. [165, 166]

1.5.1. Collision induced dissociation

Collision induced dissociation (CID) involves the inelastic collision of an ion (m_p^+) with an inert neutral molecule (N) such as nitrogen gas. The kinetic energy of the neutral molecules is converted into internal energy of the precursor ion, a uni-molecular degradation follows forming a fragment ion (m_f^+) and a neutral loss molecule (m_n). [11, 167]

$$m_p^+ + N \rightarrow m_p^{+*} \rightarrow m_f^+ + m_n$$

It is not necessarily a single collision event that occurs with CID. Multiple collisions with the inert neutral molecules may be necessary for the precursor ion to be activated sufficiently for fragmentation to occur

$$m_p^+ + N \rightarrow m_p^{+*} + N \rightarrow m_p^{+**} + N \rightarrow m_p^{+***} \rightarrow m_f^+ + m_n$$

Alternatively multiple fragmentation events may occur

$$m_p^+ + N \rightarrow m_p^{+*} \rightarrow m_{f1}^+ + m_n + N \rightarrow m_{f1}^{+*} \rightarrow m_{f2}^+ + m_n$$

1.5.2. High energy collision induced dissociation

HCD is the same principle as CID, the difference is that in CID ions held with a kinetic energy between 1-100 eV where as HCD the kinetic energy is several keV. [167] The larger kinetic energy involved means that there is more kinetic

energy to be transferred to internal energy, the internal energy for CID exhibits as rotational or vibrational where as for HCD it is electronic excitation. Ions with high internal energy give rise to fragmentation of stronger bonds, peptide side chains and fatty acid back bone fragments. [168] A reports suggest that HCD improves the fragmentation efficacy of peptides resulting in a higher score for identification. [169]

1.5.3. Electron transfer dissociation

ETD uses radical anions such as floranthene ($C_{16}H_{10}\cdot$) to transfer electrons to cations. The resulting ion becomes excited with the addition of an electron, this causes an electron cascade and the formation of c and z ions in peptides see Figure 19.

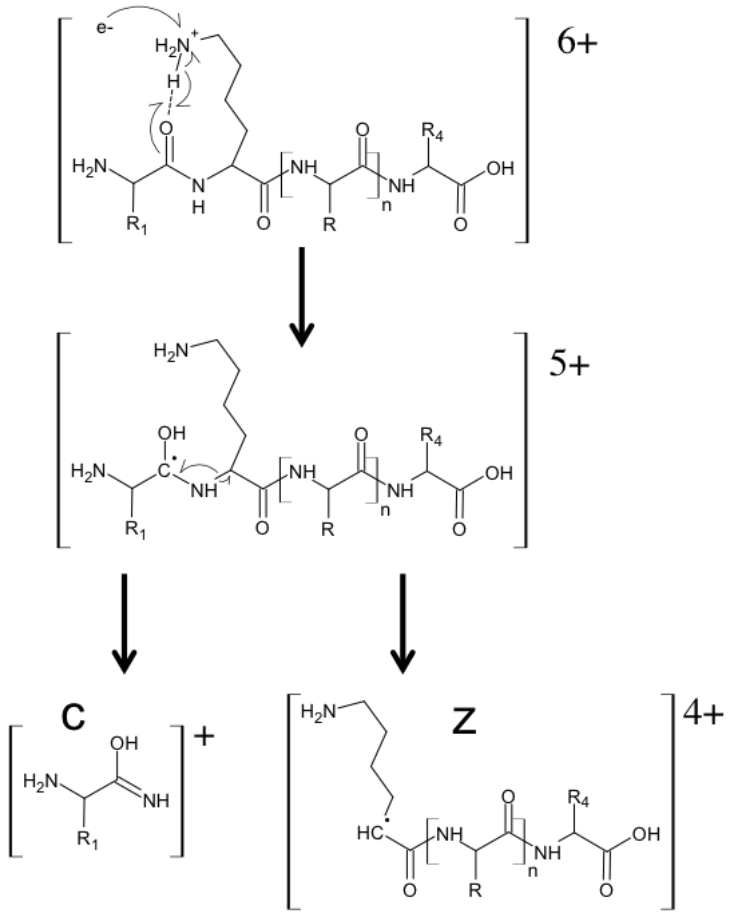

Figure 19: Formation of c and z ions via eletron transfer dissociation from a 6+ ion.

It is important to note that this method will only work with multiply charged ion. [170] Occasionally fragmentation does not occur and a charge-reduced species is detected, this is the precursor ion in a lower charge state than was initially selected.

1.6 Specific instrument set ups

The work presented has been conducted on three instruments, a Thermo Orbitrap Velos ETD, a Waters Synapt G2S, and a Thermo TSQ Vantage triple quadrupole The Orbitrap and triple quadrupole have a ESI source only and can

becoupled to the LESA platform or to liquid chromatography. The Synapt has been used with the Advion Triversa to allow LESA sampling and nano-ESI, and the MALDI source.

1.6.1. The Orbitrap Velos

The Orbitrap Velos ETD has two mass analysers and is capable of three fragmentation methods. A series of ion optics including a s-lens, a quadrupole and octopole transmit ions down from atmospheric pressure to a high vacuum and also as remove neutral molecules and solvent droplets. For MS analysis via Oribtrap, the ions are transmitted through the linear ion trap to the C-Trap where they accumulate prior to being injected into the Orbitrap. For MS/MS analysis the route of the transmitted ions differs for each fragmentation method. All MS/MS methods use the linear ion trap to isolate ions of a specific *m/z*;

For CID the ions are held in the LIT where they are bombarded with nitrogen. The product ions are then injected into the Orbitrap. Because the fragmentation occurs in the LIT product ions that are less than 1/3 of the precursor *m/z* are lost. For HCD the ions are transferred to the HCD collision cell, where they are fragmented using nitrogen. The product ions are then directed into the Orbitrap. This means that there are no restrictions on the lower *m/z* range enabling all ions to be detected. For ETD ions are held in the LIT and anions generated using the reagent ion source are injected causing fragmentation. Product ions are then analysed in the Orbitrap.

The Orbitrap can be operated in data-dependent mode. In this work a 'top 7' method was used: The method comprises a full scan survey spectrum is acquired followed by seven MS/MS events. The full scan spectra are acquired in the Orbitrap. Based on the survey spectrum, the seven most abundant precursor ions are sequentially isolated and fragmented in the ion trap. Product ions are detected in the Orbitrap. In this work CID induced fragmentation was used, however fragmentation via HCD and ETD are also possible with the instrumental set up. This configuration is used because it is fast and suitable for coupling with LC separation. The sample input is continuously changing therefore it is essential to increase the number of MS/MS events to maximise the number of identifications. Compared to direct infusion where the sample composition is constant and where more time can be taken for the MS/MS events.

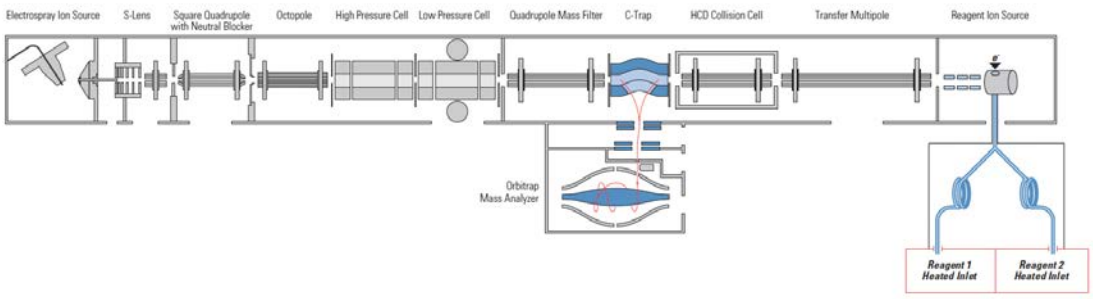

Figure 20: Schematic of an LTQ Orbitrap Velos ETD [171]

1.6.2. The Synapt G2-S

In this work the Synapt has been used with both the ESI source and MALDI source. Figure 21 below shows the ESI source. The MALDI source is positioned inline with the first ion gate prior to the step wave. A hexapole is used to transfer ions from the source to the ion gate. The StepWave ion guide is a filter to remove neutral molecules by changing the direction of the flow of ions. A quadrupole is used to transfer ions as well as isolate ions prior to the Triwave device. The Triwave comprises three travelling wave ion guides (TWIGs). The central TWIG is the ion mobility cell for TWIMS. A trapping cell is used to hold ions before pulsing the ions through the drift tube. The drift tube contains helium, to aid in the separation of molecules. The transfer tube extracts ions that have passed through the drift tube in packets for the time of flight mass analyser. Both the trapping and transfer cells can be used for CID. This allows investigations of the drift of fragments as well as the fragmentation of molecules with a specific drift time.

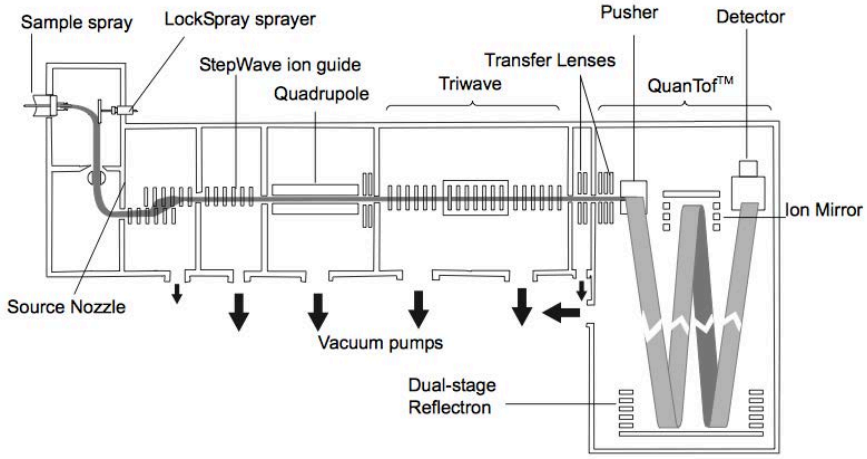

Figure 21: Schematic of an Synapt G2-S [172]

1.6.3. TSQ Vantage Triple Quadrupole.

The TSQ triple quadrupole (QqQ) is an instrument comprises of three quadrupoles. The first and the third are used as mass analysers whereas the second quadrupole is used as a transfer quadrupole and for fragmentation where necessary. In this thesis this instrument is has been used as mass analyser for full scan spectra.

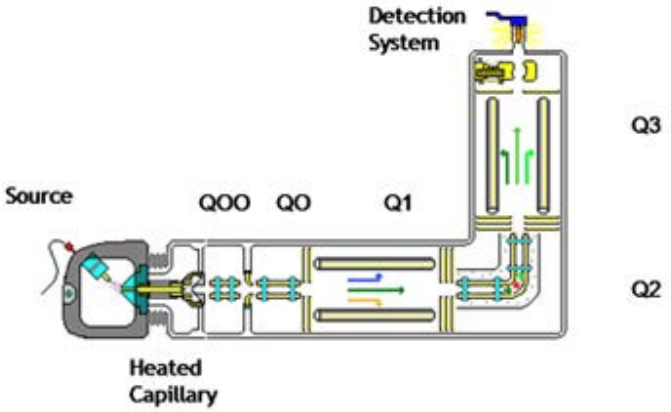

Figure 22: Schematic of an TSQ Vantage Triple Quadrupole [173]

1.7 The Human Liver

The liver is an organ that is fed by the hepatic vein and the portal artery. The hepatic vein carries blood that has picked up nutrients from the gut, and the portal artery is blood from the heart that is oxygen rich. Visually the liver is a relatively homogeneous, with arteries and veins for blood flow and the removal of bile. The main function of the liver is for metabolic reactions. This includes

the formation of enzymes and metabolites and the removal of toxins. In addition the liver also stores nutrients to ensure that the blood content remains stable. This means that diseases of the liver are often serious and can lead to fatalities as the whole body is affected.

One such disease is non-alcoholic steatohepatitis (NASH). NASH is an inflammatory condition of the liver that mimics the damage caused by alcohol without the consumption of large quantities of alcohol. Causes of the disease are not yet fully understood however both genetic predisposition and lifestyle choices are important [174].

The diseases progresses via fatty liver diseases that causes fibrosis, a localised reduction in cell function caused by the build up of collagen. If fibrosis is allowed to continue, cirrhosis develops. Cirrhosis is scaring of the liver that destroys the cellular structure causing cell death and ultimately liver failure. [175].

Serum biomarkers such as elevated amino transferases and a glutamyltransferase, are found in patients with NASH; however, these biomarkers are not specific to NASH. Furthermore, due to natural variation defining elevated levels of any protein or biomarker can be difficult. Initial reports suggest that the liver fatty acid binding protein (FABP1) [175-178] may be a suitable biomarker. The FABP1 comes from a family of fatty acid binding proteins that have three broad functions;

- Regulates specific enzymes of lipid metabolism
- Maintains the fatty acid levels in cellular membranes
- Regulates the expression of fatty acid-responsive genes

The FABP1 protein, like all FABPs, primarily binds to unsaturated and singly saturated fatty acids but is also capable of binding to other hydrophobic ligands such as heme. [179, 180]

Recent work by Peng et. al [181] has shown that two single nucleotide polymorphisms in the *FABP1* gene are associated with increased risk of developing non-alcoholic fatty liver disease. The first results in substitution of threonine for alanine at position 94 in FABP1, while the second is intrinsic. Increased risk of disease is linked to the two single nucleotide polymorphisms both individually and cumulatively, however the mechanisms by which these polymorphisms contribute to the disease process are unknown.

Potential biomarkers can present themselves in various forms. Here, lipids and proteins are investigated by mass spectrometry.

1.7.1. Lipids

Lipids are a class of small molecules that are not water-soluble, but instead are soluble in organic solvents. Lipids have a wide range of functions, these include

- Energy storage know as dietary fats,

- Cell structure, particularly the cell membranes
- Cell signalling.

There are eight subclasses of lipids, [182]

- Fatty acyls: hydrocarbon chain with an acyl group.
    - Used to functionalise proteins. [183]
    - Broken down during respiration. [184]
- Glycerolipids: Glycerol molecule with up to 3 fatty acids bonded to the hydroxyl groups
    - Used as fat storage. [185]
    - Cell signalling. [186]
- Glycerophospholipids: Glycerol molecule with a terminal hydroxyl group substituted for a phosphate group, with either one or two fatty acids on the remaining hydroxyl groups.
    - Used for to form cell membranes as they have hydrophobic and hydrophilic regions enabling them to self assemble into bilayers. [187]
- Polyketides: large cyclic molecules which large variety of functionalization.
    - Often have antibiotic and antifungal qualities. [188]
- Prenol Lipids: highly functionalised phenol molecules that is capable of polymerising.
    - Foundations of vitamins A, E and K. [189]

- Saccharolipids: sugar back bone with fatty acids functionalising the hydroxyl groups
    - Can form lipopolysaccharides chains found in gram negative bacteria, used for cell identification and communication [190]
- Sphingolipids: acyl chain with an amide and two alcohol groups, often found with substitutions of the amide and alcohol groups.
    - Used for cell recognition and signalling in mammalian cells [186]
- Sterol lipids: multi cyclic structures with typically a mix of cyclohexane and cyclopentane with a large verity of functional groups.
    - Used for cell signalling, specifically in the form of steroids to promote cell growth. [191]

Mass spectrometry is used to detect these species. Lipids typically have a mass between 220-1000Da, although some lipids are observed at higher masses. They are also usually observed as a singly charged ion. A number of approaches have been used to identify lipids from complex samples.

1.7.1.1 Analysis of lipids via mass spectrometry

MALDI mass spectrometry has identified lipids from a number of complex surfaces. These include plant and animal tissue. [52, 192]

In positive mode analysis the predominant species that have been detected is phosphatide choline. Other species have been detected using targeted approaches. Precurse ion scans enable the isolation of types of precursor ions

that produce a specific fragment and using optimised solvent extraction enables less detectable lipids to be identified including cholesterol esters, wax esters and ceramides. [87, 193]

Another method used to detect lipids is ESI. ESI requires a liquid sample, liquid extraction surface analysis is a new method that links a solid sample with ESI.

Electrospray analysis of lipids is common. A larger proportion of analysis is conducted on pre-prepared samples such that lipids are isolated and purified prior to analysis. A growing number of samples are now being analysed from the surface using techniques such as LESA.

LESA has been used to analyse lipids from a number complex samples, including a used contact lens, [193] a single living murine cell, [87] and atherosclerotic plaques [79]. In these examples a solvent composition of 1/2/4 chloroform:methanol:isopropyl alcohol with an ammonium acetate modifier was used (7.5 mM for atherosclerotic plaques and 20 mM for the contact lens and murine cell) with analysis being conducted on either a QqQ or a QTrap. The most wide spread detected lipids were phosphatidylcholines, sphingomyelin lipids and cholesterol esters with ceramide wax esters and phosphatidylethanolamines also being detected depending on sample type.

1.7.2. Proteins

Proteins are long chains of amino acids that are able to self assemble into a wide range of structures. There are 4 levels of structure to a protein. The first level is the amino acid sequence, the second is simple folding to form beta-pleated sheets and alpha helices, the third level is the arrangement of the beta-pleated sheets and alpha helices into a 3D conformation, and the fourth level is when 2 or more polypeptide chains come together to form a complex. The function of proteins is related to their structure.

Mass spectrometry is primarily used to identify the primary structure of a protein. Recent developments in analysis are allowing the analysis of native state proteins, providing insights to higher levels of structure. [194] In this report only the amino acid sequence is investigated.

1.7.2.1 Analysis of peptides and proteins

Proteins provide a wealth of information about health and disease. Since the invention of matrix-assisted laser desorption/ionisation[16, 195] and electrospray ionisation it has been possible to analyse proteins by mass spectrometry. With the ability to detect proteins it becomes necessary to identify the proteins detected. Two methods of identification are top-down and bottom-up.

Top-down describes the process of ionising the intact protein and then fragmenting the protein. The protein can be identified because the majority of

the product ions contain either the N-terminus or the C-terminus making it possible to search the measured *m/z* of the fragments against theoretical *m/z* of those from a proposed protein. This approach only works if there are proteins with which to compare the results. Generally, this means the genome has been sequenced. The measured masses are searched against protein databases using algorithms such as Prosight PTM, [196] and the output is a list of possible identifications. In some cases fragments between most or all the amino acid are observed, in theses cases it would be possible to construct the amino acid sequence using the mass difference between the fragments.

Top-down is the fragmentation of the protein backbone. Fragmentation produces two complementary ion pairs of the c-terminal and n-terminal ends of the amino acid sequence. The fragmentation can be induced in predictable ways, for example, collision induced dissociation (CID) produces primarily b/y ions, which is the breaking of the carbon-nitrogen bond between the carbonyl and the amide groups on the backbone, where as electron transfer dissociation (ETD) is likely to produce c/z ions which is the breaking of the carbon-nitrogen bond between the amide and the carbon attached to the side chain.

Identification of proteins using the top-down method relies either on a database of proteins such as, Prosight PTM 2.0, where fragmentation data can be imported, or for smaller and simpler proteins where there is a detected ion from each amino acid cleavage, build the amino acid sequence from sequential amino acids linkages. The former method often needs confirming by using a fragment

calculator such as Protein Prospector to improve sequence coverage. The later relies on efficient fragmentation between every amino acid in the sequence. Using top-down methods post translation modifications (PTM's), and variant amino acid sequences can be discovered and identified. Up until recently it has been necessary to purify the protein prior to analysis.

Detections of proteins via LESA mass spectrometry was first demonstrated by Edwards et al [83]. Analysis of haemoglobin and haemoglobin variants from dried blood spots demonstrated that LESA mass spectrometry was suitable for the top-down analysis of proteins. Later this was used to diagnosis unknown haemoglobin variants [84] (~15 kDa) in neonatal samples. A number of other neonatal blood disorders have also been analysed and diagnosed giving this the potential to be used in the clinic to screen for neonatal blood disorders. [197]

A continuous flow version of the LESA technology has been applied to the analysis of haemoglobin in dried blood spots from sheep. [198] LESA has also been applied to *E.coli* bacterial colonies, where 6 proteins (7kDa-15kDa) were identified. Here the LESA sampling was conducted by lowering the pipette tip into the colony rather than suspending the droplet on the surface. [86] Manual LESA was applied to sampling of intact proteins from thin tissue sections of bovine lens, and murine brain and kidney [199]. Proteins were extracted by LESA and then subjected to LC electron transfer dissociation MS/MS. Analysis of the lens samples resulted in the identification of a number of crystalline proteins (~21 kDa). Ten proteins (5-22 kDa) were identified from the brain

samples, and five (5-17 kDa) were identified in the kidney samples. It should be noted that the number of information-rich ETD MS/MS spectra was much greater than the number of identified proteins. This discrepancy reflect the difficulty in identify proteins on a large scale with top-down proteomics. The software often lacks the specificity and accuracy required to identify proteins. Despite these draw backs top-down is a growing field because analysis of intact proteins maintain post-translational modification,

Bottom-up proteomics is a technique that requires a proteolytic digestion step. This breaks the protein into smaller peptides. Most digestion enzymes cut the amino acid chain at specific amino acids. In this report trypsin is used as the digestion enzyme. Trypsin cleaves at the C- terminal side of lysine or arginine except when proline is the subsequent amino acid. [200] The peptides that are produced are often separated via liquid chromatography and the peptides detected using mass spectrometry. This requirement is due to the fact that a larger number of peptides can be produced from a relatively small number of proteins and adding a separation step prior to mass spectrometry analysis enables more peptides to be identified adding more confidence to the identifications. Peptides are identified using fragmentation methods and then a data base search is conducted on these fragments to identify possible proteins that they originated from.

In order for LESA to be coupled with bottom-up proteomics, a proteolytic digestion step needs to be introduced into the workflow. There are two approaches;

- Intact proteins are extracted by LESA prior to digestion. [85]
- An in-situ digestion is performed prior to liquid micro-junction extraction [201, 202].

The first approach has been applied to the analysis of dried blood spots, identifying over 100 proteins. The Advion Triversa Nanomate was used to extract the intact proteins via LESA and the solution was then deposited into a well of a 96-microtitre plate where the Triversa Nanomate proceeded to conduct an automated digestion procedure.

There are currently no automated processes for the digestion and extraction of peptides in the second approach. This is because a key issue is to prevent the evaporation of the trypsin solution. In-situ digestion was demonstrated for protein arrays (cytochrome C, myoglobin and bovine serum albumin) printed on a biomaterial substrate commonly used for cell culture [203]. Trypsin was deposited onto the protein spots and the array was transferred to a humidity chamber and incubated for 18 hours. The array was then analysed by LESA and data-dependent MS/MS. Quanico et al. [201] applied the in-situ digestion approach to the analysis of thin tissue sections from frozen rat brain. Trypsin solution was repeatedly deposited on the tissue surface throughout the

incubation period (1 hour). The resulting peptides were extracted via liquid microjunction sampling. Five extracts were pooled and analysed by LC MS/MS. This approach enabled the identification of ~1500 proteins per sample. The approach was subsequently applied to formalin fixed and paraffin embedded tissue sections from fallopian tube cancer biopsies [202].

1.8 Work Presented

In this thesis the LESA has been coupled to a LTQ Orbitrap Velos ETD (Thermo), a TSQ Vantage (Thermo) and a Synapt G2-S (Waters). In chapter 3, LESA sampling protocol to target lipids and proteins from human liver tissue has been investigated and the limitations of LESA spatial profiling have been explored. In chapter 4, analysis of proteins is taken further and *in-situ* proteins are extracted and identified using top-down and bottom up methods. Four intact proteins between 10,000 Da and 16,000 Da were fragmented from non-diseased and diseased tissue sections using either CID or ETD. Bottom-up methods identified over 300 proteins, several of which were known biomarkers for liver disease. A greater number of species are detected due to the separation techniques, however, LC analysis is quite time consuming. In chapter 5 FAIMS analysis was employed to enhance protein signal without increasing the analysis time. By applying FAIMS, lipids and proteins could be separated post sampling enhancing the spectral quality for both these species. MS/MS analysis showed that the FAIMS can be used as an exploratory technique to identify protein that had previously had a signal to noise ratio too low to detect. In

chapter 6, the LESA was coupled to the TWIMS. Similar to the FAIMS the TWIMS was able to separate lipids and proteins. In addition the TWIMS showed separation between isobaric species. This is particularly useful for imaging and spatial profiling as the LESA analysis has a poor spatial resolution and therefore MALDI was employed. MS/MS imaging and TWIMS imaging were used to separate isobaric species. Images produced showed separate spatial locations for several isobaric species.

Chapter 2: Materials and Methods

2.1 Materials

Methanol, ethanol and acetonitrile used in preparation of electrospray solvents were purchased from either Fisher Scientific (Leicestershire, U.K.) or acetonitrile J. T. Baker (The Netherlands). Water was purified by an ELGA Option 3 system (Marlow, UK). Formic acid (FA), lithium chloride and ammonium bicarbonate were purchased from Sigma-Aldrich Company Ltd. (Dorset, U.K.).

2.2 Sample Preparation

The work was approved by the NHS Walsall Local Research Ethics Committee (98/CA5192). All patient liver tissue was collected at The Queen Elizabeth Hospital in Birmingham with written informed patient consent. Non-diseased liver tissue was collected from donor material surplus to transplantation requirements or from resection margin specimens. Diseased liver specimens were collected upon transplantation surgery. All samples were rapidly processed and snap frozen in liquid nitrogen prior to storage at -80 °C.

Sections of normal human liver tissue of area approximately 1.5 cm^2 were obtained at a thickness of 10 μm using a CM1810 Cryostat (Leica microsystems, Wetzlar, Germany) and thaw mounted onto glass slides. Haematoxylin and

eosin (H&E, Leica UK) staining was performed according to standard protocols. [204, 205]

Liver and brain from wild-type mice (extraneous tissue from culled animals) were the gift of Prof Steve Watson (University of Birmingham). Organs were frozen on dry ice prior to storage at -80 °C. Sections of murine liver tissue and brain tissue of area ~ 1.5 cm^2 were obtained at a thickness of 10 µm using a CM1810 Cryostat (Leica Microsystmes, Wetzlar, Germany) and thaw mounted onto glass slides.

Glass slides were loaded onto a universal LESA adapter plate and placed in the TriVersa Nanomate chip-based electrospray device (Advion, Ithaca, NY) coupled to the Thermo Fisher Scientific Orbitrap Velos

2.3 Surface Sampling

Automated sample analysis was performed using the LESA Points software (Advion Ithaca, NY), which controls the TriVersa Nanomate. An image of the tissue section was acquired using an Epson Perfection V300 photo scanner. The LESA Points software (Advion) was used to select the location or locations on the tissue surface (x and y co-ordinates) and the z position, relative to the plate height, for sampling routines using the Nanomate probe. The LESA sampling routine involved the collection of a conductive tip from the Advion tip rack before moving to solvent well containing the electrospray solvent solution. The

Nanomate probe aspirated a pre-set volume into the conductive tip. The probe relocated to the predetermined location on the surface then descended to just above the surface. A schematic of the LESA stage is shown in Figure 23.

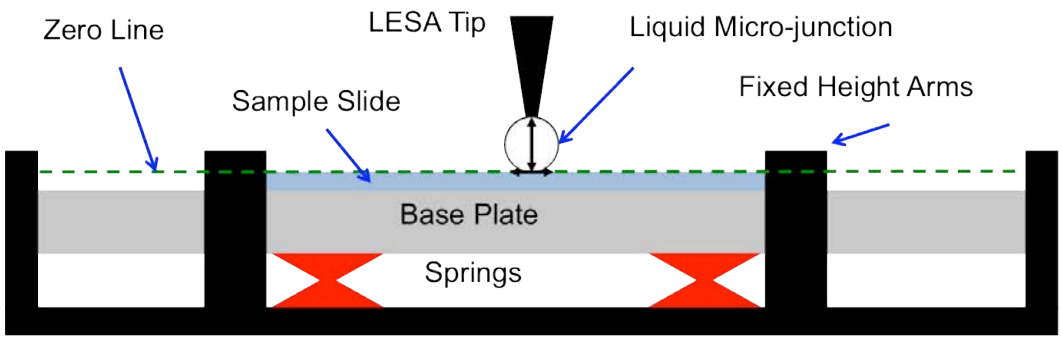

Figure 23: Schematic of the universal plate adaptor indicating that the sample slide is held in place between the base plate and the fixed height arms insuring that the height of the sample slide is the same for each analysis. The zero line is the fixed distance between the sample slide and the LESA tip. Not including the height of the sample on top of the sample slide.

The tip dispensed a proportion of the volume of the solution onto the sample forming a liquid micro-junction (LMJ) between the tip and the surface. The LMJ was maintained to allow sufficient time for analytes to be dissolved into the solution; the length of time varies depending on that analysis and is defined in more detail in specific methods later in this chapter. The solvent was then reaspirated into the tip. Finally the tip was rotated and engaged with the back of the ESI chip, and nanospray ionisation was initiated. The Triversa Nanomate was coupled with a Thermo Fisher Scientific LTQ Orbitrap Velos ETD mass spectrometer and a Waters Synapt G2-S. Values for the volumes, heights and length (time) of LMJ are recorded with specific experimental methods.

2.4 Mass Spectrometry.

2.4.1. LTQ Orbitrap Velos ETD analysis

LESA samples were introduced at a flow rate of ~80-150 nL/min with a gas pressure of 0.3 psi, a tip voltage of 1.75 kV and a capillary temperature of 250 °C. MS data were collected in full scan mode over a resolution of 100 000 at *m/z* 400 and in selected ion monitoring (SIM) mode, over selected *m/z* ranges. In experiments where the AGC target was used the target was $1x10^6$ with a maximum fill time of 2 s in full scan mode. Deviations from this, such as when the AGC is turned off, are described in the text for individual experiments.

2.4.2. TSQ Vantage analysis

LESA samples were introduced at a flow rate of ~80-150 nL/min with a gas pressure of 0.3 psi, a tip voltage of 1.75 kV. With a capillary temperature of 275 °C.

2.4.3. Synapt G2-S analysis

LESA samples were introduced at a flow rate of ~80-150 nL/min with a gas pressure of 0.3 psi, a tip voltage of 1.75 kV. The Synapt G2-S capillary voltage was set to 2.98 and temperature was set to 100 °C with a desolation temperature of 250°C.

Data was collected in resolution mode (W mode). TWIMS was conducted in the traveling wave ion mobility cell was operated using nitrogen at a pressure of 3.08 Torr.

2.4.4. UltraFAIMS analysis

FAIMS separation was carried out in positive ion mode using an NC chip (Owlstone) with trench length 78.1 mm, gap width 101.3 μm and total thickness 700 μm. The FAIMS device was operated either in 2D mode, in which both the dispersion field and compensation fields are varied, or in static mode, in which DF and CF are fixed.

2.5 Data processing

Data were analysed using either Xcalibur version 2.1.0.1139 software where the Xtract program was used to calculate monoisotopic masses, MATLAB version R2011a-student, MassLynx 4.1 or HDimaging 1.2.

2.5.1. Image construction

For LESA – Orbitrap image construction, data in the Thermo RAW format were converted to mzML using msconvert as part of ProteoWizard. [206, 207] Sequential spectra that corresponded to the same pixel (as determined by time from the total ion chromatogram) were summed together and outputted to mzML using a MATLAB script. The summed spectra were then converted to

imzML using imzMLConverter. [208] All further data processing was performed in MATLAB using in-house software.

For LESA- ESI - TWIMS image construction, the average mobilogram was calculated using the driftscope function in MassLynz. The total ion chromatogram was extracted for a specific *m/z* and drift time. Sequential spectra that corresponded to the same pixel as determined by time from the total ion chromatogram were summed together to determine the intensity of a peak at a given pixel.

MALDI images were constructed using Waters HDimaging software version 1.2.

2.5.2. UltraFAIMS data processing

In-house software was developed for the analysis of ultraFAIMS data. The software is described in detail in section 2.8.5.

2.6 Experimental methods for Chapter 3

2.6.1. Solvent Optimisation

Automated LESA experiments were conducted using electrospray solvents comprised of 40, 50, 60, 70 and 80% methanol, ethanol or acetonitrile prepared in water plus 0.1% (v/v) FA using the surface sampling procedure and the

experimental parameters outlined in Table 2-1. Additional solvent systems containing 30% methanol in water with 0.1% (v/v) FA or 70% methanol in water with 0.1 (v/v) FA were also used for LESA

2.6.2. LMJ delay

An automated LESA method was conducted using 70% methanol in water and 0.1% (v/v) FA and the surface sampling procedure and the experimental parameters outlined in Table 2-1. The sample was electrosprayed and mass spectra collected. AGC was turned off and the injection time set to 20 ms.

2.6.3. Height and volume

An automated LESA method was conducted using 70% methanol in water and 0.1% (v/v) FA and the surface sampling procedure and the experimental parameters outlined in Table 2-1. Each analysis was conducted on a fresh region of tissue. Both the dispensing volume and the dispensing height were varied.

2.6.4. Dilutions

An automated LESA method was conducted using 70% methanol in water and 0.1% (v/v) FA and the surface sampling procedure and the experimental parameters outlined in Table 2-1. The sample was electrosprayed and mass spectra collected. Each analysis was conducted on a fresh region of tissue using the parameters described in Table 2-1. AGC was turned off and an injection time of 50 ms was used.

2.6.5. Acid Concentration

An automated LESA method (outlined in section 2.3 and Table 2-1) was conducted using 70% methanol in water and 0.1% (v/v) FA, 1% FA (v/v), 2% FA (v/v) and 3% FA (v/v). Analysis was conducted using TSQ Vantage as described in section 2.4.2. Each analysis was conducted on a fresh region of tissue.

2.6.6. Tissue washing

An automated LESA method was conducted using 50% acetonitrile in water and 0.1% (v/v) FA was carried out with the method outlined in section 2.3 and Table 2-1. Bulk tissue washing was conducted by submerging the glass slide in 80% ethanol for 10 seconds and repeated up to twice more. The sample was electrosprayed and mass spectra collected on a TSQ Vantage (Thermo), using conditions outlined in section 2.4.2.

Localized washing was also conducted using the LESA protocol outlined in section 2.3, using 80% ethanol and 0.1% (v/v) FA at the same spatial location prior to analysis with 50% acetonitrile in water and 0.1% (v/v) FA. The sample was electrosprayed and mass spectra collected using the mass spectrometry conditions described in section 2.4.2.

2.6.7. Repeat Analysis Of A Single Location On Tissue

An automated LESA method was repeated at the same tissue location ten times. In this experiment single position surface analysis was conducted with a solvent system of 70% methanol in water and 0.1% (v/v) FA and parameters described in section 2.3 and Table 2-1. The electrosprayed sample was surveyed using the mass spectrometry conditions described for Orbitrap experiments section 2.4.1. AGC was turned off and the injection time set to 20 ms.

2.6.8. AGC tests

An automated LESA method was conducted using 70% methanol in water and 0.1% (v/v) FA. The sample was electrosprayed and mass spectra collected using the mass spectrometry conditions described in the surface sampling section 2.3 and Table 2-1. AGC was turned off and injection times of 1, 2, 3, 4, 5 ms were used.

2.6.9. Tissue Imaging

For imaging experiments LESA sampling was repeated using a solvent volume of 0.7 μL, dispensing 0.5 μL, re-aspirating 0.6 μL at sequential locations across the surface of the liver tissue, with x and y spacing of 1 and 2 mm (1 mm spaced image consisted of 60 pixels in 5 rows of 12, 2 mm spaced image consisted of 42 pixels in 6 rows of 7). MS data were collected for 3 minutes per extraction. The AGC was turned off and the injection time set to 20 ms.

2.6.10. Volume and height

An automated LESA method was conducted using 70% methanol in water and 0.1% (v/v) FA, using the surface sampling protocol in section 2.3 and the conditions described in Table 2-1. The sample was electrosprayed and mass spectra collected using the mass spectrometry conditions described in section 2.4.2.

Table 2-1: Experimental parameters for LESA analysis conducted in Chapter 3

Experiment	Total solvent	Height	Dispensing volume	LMJ Delay	Re-aspirated volume
Solvent Optimisation	2.5 µL	0.4 mm	1.3 µL	10 sec	1.7 µL
LMJ delay	3 µL	1.6 mm	1 µL	0, 5, 10, 15, 20, 30, 40 sec	1.3 µL
Height and Volume	0.5 µL more than dispensed	0.4, 0.8, 1.2, 1.6 mm	0.3 µL/0.5µL	15 sec	0.2 µL more than dispensed
Dilution	1, 2, 3, 4 µL	0.4 mm	0.5 µL	10 sec	0.7 µL
Acid Concentration	2 µL	0.4 mm	1 µL	10 sec	1.3 µL
Washing	2.5 µL	0.4 mm	1.4 µL	10 sec	1.7 µL
Repeat Extraction	5 µL	0.4 mm	4 µL	10 sec	4.5 µL
AGC tests	5 µL	0.4 mm	4 µL	10 sec	4.5 µL
1mm and 2 mm image	0.7 µL	0.4 mm	0.5 µL	10 sec	0.6 µL
Volume and area	5 µL	0.4 mm	0.5, 1, 2, 3 µL	10 sec	0.3 µL more than dispensed

2.7 Experimental methods for Chapter 4

2.7.1. Top-down LESA mass spectrometry of human liver tissue sections:

Sections of human liver thaw-mounted onto glass slides were washed in a solution of 80% ethanol prior to analysis. Using the LESA protocol in section 2.3 2 μL of 40% acetonitrile + 1% formic acid was aspirated from the solvent well. The robotic arm relocated to a position above the tissue section and descended to a height of approximately 1 mm above the surface. One μL of the solution was dispensed onto the tissue section to form a liquid microjunction. The liquid microjunction was maintained between the probe tip and the surface for 10 s. 1.3 μL was re-aspirated into the pipette tip. The dispense/reaspirate cycle was repeated 3 times. Full scan mass spectra (*m/z* 500-2000) were collected for 3 min. CID was performed in the ion trap at a normalized collision energy of 30% and the fragments detected in the Orbitrap (*m/z* 300-2000). The isolation width was 3 Th. AGC target was $1x10^6$ charges with a maximum injection time of 2 s. Each CID MS/MS scan comprised of 20 co-added microscans. Data were recorded for 10 min (~10 scans). ETD was performed in the ion trap and the fragments detected in the Orbitrap. The isolation width was 3 Th. AGC target was $1x10^6$ charges with a maximum injection time of 1 s. ETD activation time was 20 ms. Each ETD scan comprised of 20 co-added microscans. Data were recorded for 6 min (~9 scans). Number of scans for each experiment was determined by counting the scans after the analysis.

2.7.2. Bottom-up LESA mass spectrometry of human liver tissue sections:

Intact proteins were extracted from non-diseased human tissue via automated LESA: Samples were mounted onto a 96-well microtitre plate (Thermo Scientific, Loughbrough, UK) and placed in the Triversa Nanomate nanoelectrospray device (Advion Biosciences, Ithaca, NY). Three of the sample wells contained extraction solvents: one contained 50mM ammonium bicarbonate, one contained 50% methanol and one contained 70% methanol. A fourth well contained 0.1 mg/ mL trypsin (Trpysin Gold, Promega, Southampton, UK) in 50mM acetic acid. Surface sampling of the thin tissue section and trypsin digestion was performed by use of the advanced user interface. This involves the collection of a conductive tip from the Advion tip rack before moving to the well containing the extraction solvent to aspirate 2 µL from the solvent well. The arm relocated to a position above the tissue section and descended to a height of approximately 0.6 mm above the surface. One µL of the solution was dispensed onto the tissue section to form a liquid microjunction. The liquid micro-junction was maintained between the probe tip and the surface for 1 s. 1.3 µL were reaspirated into the pipette tip. The dispense-reaspiration cycle was repeated three times before finally dispensing into a clean well in the microtitre plate. The experiment was conducted using three extraction solutions: (a) 50% methanol, (b) 70% methanol, and (c) 50mM NH_4HCO_3. After extraction, the 50% and 70% methanol solutions were left for 30 min until dry to remove the organic content and the sample re-suspended in 10 µL 50mM NH_4HCO_3, using one mix cycle (repeat dispense/reaspiration) to promote re-suspension. For

each of the samples, 4.5 µL of trypsin solution was aspirated from the tryspin-containing well and dispensed into the sample well. The solutions were mixed by a single mix cycle (repeat dispense/reaspiration). The samples were incubated at 37 °C for 1 hour by use of the temperature control unit of the Triversa Nanomate. At 30 min and 1 h into the incubation, 7 µL of 50 mM NH_4HCO_3 was aspirated from the solvent well and added to the sample well in order to account for evaporation. The final volume was approximately 10 µL.

2.7.3. On tissue digestion for bottom-up mass spectrometry of human liver tissue

Using the advance user interface, 10 µL of 0.1 mg/ mL trypsin in 50mM acetic acid was aspirated from a well in a microtitre plate. The robotic arm relocated to a position above the tissue section and descended to a height of approximately 0.2 mm above the surface. All of the solution was dispensed onto the tissue section at a rate on 0.3 µL/min to form a liquid micro-junction. The liquid micro-junction was maintained between the probe tip and the surface for 30 min at which time any remaining solution is expelled from the pipette onto the tissue. This was repeated once more. The peptides were extracted using 10 µL 50 mM NH_4HCO_3 aspirated from a separate well in the 96-well microtitre plate. The robotic arm relocated to the same position above the tissue section and descended to the same height. 5 µL of the solution was dispensed onto the tissue section at a rate of 10 µL/min and re-aspirated at 10 µL/min. 5 µL were re-aspirated into the pipette tip and then the solution was dispensed into a clean well. This was repeated twice more, each time

dispensing the solution into a clean well in the microtitre plate. The sample was incubated at 35 °C for the length of the digestion and extraction process.

2.7.4. LC MS/MS

The microtitre plate was transferred to the HPLC autosampler (Ultimate 3000, Dionex Thermo Fisher Scientific Loughborough UK), which is coupled to an Orbitrap Velos ETD mass spectrometer (Thermo Fisher Scientific, Bremen, Germany) via the Triversa Nanomate. The proteolytic digests were each analysed in duplicate by LC-MS/MS. Five µL aliquots were injected onto a Pepmap 100, C_{18} 100 mm trap (Thermo Fisher Scientific Loughborough UK). The trap was treated with a 5 min wash cycle with 0.1 % formic acid prior to injection onto the analytical column (Pepmap 100 reversed phase C18 75 mm, 3 mm, 100 Å; Thermo Fisher Scientific Loughborough UK). Peptides were separated using a 30 min 3.2 % - 44 % acetonitrile (J.T Baker, Netherlands) gradient at a flow rate of 0.35 mL/min.

Samples eluted into the mass spectrometer via the Triversa Nanomate chip-based nano-electrospray device. Ionisation voltage was 1.4 kV, gas pressure was 0.3 psi and capillary temperature was 250 °C. Mass spectrometry analysis was performed via a 'top 7' method in which a survey scan was followed by MS/MS of the seven most abundant precursor ions. Survey scans were acquired in the Orbitrap with a *m/z* range 380–1800, an automatic gain control (AGC) target of 1×10^6 charges, a maximum fill time of 1 s and a resolution of

60,000 at *m/z* 400. CID was performed in the linear ion trap (AGC target: 30,000 charges) with helium gas and a normalized collision energy of 35 %. The width of the precursor isolation window was 2 Th and only multiply charged precursor ions were subjected to CID. The mass exclusion window was *m/z* ±0.05 and the exclusion list was set to 500. Dynamic exclusion was applied for 60s.

MS/MS data were searched against the SwissProt human database (downloaded Nov 2012), composed of 20203 sequences, using the Mascot and Sequest algorithms in Proteome Discoverer 1.4. The following parameters were applied: precursor ion mass accuracy 10 ppm, fragment mass tolerance 0.8 Da, methionine oxidation was allowed as a dynamic modification, up to 2 missed cleavages in the digestion. Data were filtered to a false discovery rate of 1% by including only high confidence peptides. The protein grouping algorithm was applied which grouped all non-unique peptides to the highest scoring protein.

2.8 Experimental methods for Chapter 5

2.8.1. Surface sampling

For LESA analysis 6 µL of 70% methanol + 0.1% formic acid (mouse liver) or 50% acetonitrile +1% formic acid (mouse brain) was aspirated from the solvent well. The robotic arm relocated to a position above the tissue section and descended to a height of approximately 0.2 mm above the surface. Three µL of

the solution was dispensed onto the tissue section to form a liquid micro-junction. The liquid micro-junction was maintained between the probe tip and the surface for 10 s, 3.5 µL was re-aspirated into the pipette tip. Mouse brain were prewashed by LESA sampling with 80% ethanol, using the same method described above (Section 2.3).

2.8.2. Mass spectrometry

Full scan (*m/z* 400-2000) data was collected at a resolution of 100, 000 at *m/z* 400. AGC target was set at $1x10^6$, with a maximum fill time of 1000ms. Each scan was composed of 1 microscan. Samples were introduced into the mass spectrometer via the TriVersa NanoMate, with gas pressure 0.3 psi, a tip voltage of 1.75 kV, and a capillary temperature of 250°C.

2.8.3. UltraFAIMS

ESI-FAIMS-MS was conducted in positive ion mode using the UltraFAIMS device (Owlstone, Cambridge, U.K.) mounted onto the Thermo Orbitrap Velos. The NC chip was employed with a trench length of 78.1 mm and a gap of 101.3 µm and a thickness of 700 µm.

For 2-D FAIMS analyses, FAIMS separation was carried out at eight discrete dispersion fields (DFs) between 130 Td and 270 Td with step size 20 Td. At each DF, the compensation field was varied between -1 to +4 Td over a time period of 180 s.

For static FAIMS analyses, optimal DF and CF conditions for the transmission of ions of interest were selected from the 2D FAIMS analyses. For the detection of lipids from mouse liver the conditions used were DF = 130 Td, CF=0.30 Td. For the detection of proteins from mouse liver the conditions used were DF = 270 Td, CF=2.62 Td. For the detection of proteins from mouse brain the conditions used were DF=270 Td, CF=2.60 Td.

2.8.4. Fragmentation

Two peaks were isolated for MS/MS analysis, *m/z* 1021.54 and *m/z* 952.63, with an isolation width of 3 Th. CID, ETD and HCD were conducted on the precursor ions. Each MS/MS spectrum was comprised of 5 microscans. Data were recorded for 2-3 mins in each case.

CID was carried out in the linear ion trap at normalised collision energy of 30%, and product ions were detected in the Orbitrap at a resolution of 100,000 at *m/z* 400. AGC target was 1 x 10^6 charges (mouse tissue samples) with maximum inject time of 1s.

HCD experiments (NCE 30%) were recorded at a resolution of 100,000 at *m/z* 400. AGC target was 1 x 10^6 charges (mouse tissue samples) with maximum inject time of 1 second.

ETD was performed with fluoranthene ions. AGC target for precursor ions was 1 x 10^6 charges with maximum inject time 1s. AGC target for fluoranthene ions

was 1 x 10^6 charges (maximum inject time 1s). Precursor ions were activated for 30 ms.

2.8.5. Data processing

The monoisotopic masses were calculated by using the Xtract function in Xcalibur software (Thermo Scientific). The .raw files of the extracted masses and the original data were converted to .mzml using msconvert as part of ProteoWizard conversion software. The .mzml files were then converted to .imzml files using imzMLConverter to produce two image data sets one of the raw data the other of the monoisotopic data. [208]. Heat maps of DF vs. CF and *m/z* vs. CF were produced using in house software. This software is described in detail in section 5.4.1.

2.9 Experimental methods for Chapter 6

2.9.1. Lithium Analysis

Automated LESA experiments were conducted using electrospray solutions comprised of 0, 0.1, 0.5, 1, 5 10, 15, 20, 25, and 30 mg/mL lithium chloride in 80% ethanol prepared in water plus 0.1% (v/v) FA. Using the surface sampling procedure in section 2.3, 5 µL was aspirated into the LESA pipette tip of which 2 µL was dispensed on to the surface then 2.5 µL was re-aspirated after a 10 second delay.

2.9.2. CID/HCD Comparison

An automated LESA method was conducted using either 25 mg/mL LiCl in 80% ethanol prepared in water plus 0.1% (v/v) FA for all MS/MS of Lithium adducts, or 70% methanol prepared in water plus 0.1% (v/v) FA for $[M+H]^+$, $[M+Na]^+$, and $[M+K]^+$ ions. The LESA protocol in section 2.3 was used with a total solvent volume of 5 µL aspirated into the LESA pipette tip of which 2 µL was dispensed on to the surface then 2.5 µL was re-aspirated after a 10 second delay.

HCD optimisation was conducted at normalised collision energies of 20%, 22%, 25%, 30%, 35%, 40%, 45% and 50%.

A 'top 7' method was conducted the same as previous with the addition of a HCD (at normalised collision energy of 40%) scan immediately following the CID scan so that the top 7 peaks were analysed by CID and HCD in adjacent scans. All other parameters were kept the same.

2.9.3. Data dependent analysis

An automated LESA method was conducted using either 25 mg/mL LiCl in 80% Ethanol prepared in water plus 0.1% (v/v) FA, using a total solvent volume of 5 µL aspirated into the LESA pipette tip of which 2 µL was dispensed on to the surface then 2.5 µL was re-aspirated after a 10 second delay.

Analysis was conducted using a 'top 7' method. Where by a survey scan is acquired and MS/MS is conducted on the top 7 most intense ions. Survey scans were acquired at a resolution of 60,000 at *m/z* 400 from *m/z* 400-1500 in the Orbitrap. CID was performed in the linear ion trap with helium gas at a normalised collision energy of 35%. Ions were detected in the Orbitrap at a resolution of 60,000 at *m/z* 400. Automatic gain control was set to 1×10^6, with a maximum fill time of 1000 ms. The precursor isolation window was set at 1 Th. Dynamic exclusion was applied for the duration of the analysis (15min), with a mass exclusion of ± 0.05, independent of charge states.

2.9.4. Liquid extraction surface analysis MS/MS imaging

For MS/MS imaging experiments a solvent volume of 1.5µL, dispensing 0.5µL, re-aspirating 1µL after a 10 second delay at sequential locations across the surface of the liver tissue, with x and y spacing of 2mm the image consisted of 48 pixels in 6 rows of 8. Data were collected for 4.18 minutes per extraction. Each injection was subdivided into 16 events the 1st and 16th event was a full scan event (*m/z* 400-1000), MS data was acquired for 0.28 min (5 scans). The 2nd to 15th event were a MS/MS event, 14 ions (*m/z* 764.58, 601.54, 722.55, 729.61, 502.35, 445.34, 774.54, 812.59, 814.59, 770.53, 90.59, 762.57) were isolated with a width of 1 Th and subjected to HCD analysis at a normalised collision energy of 40%. MS/MS spectra were acquired from *m/z* 50 to 10 Da above the precursor ion. All spectra were comprised of 4 co-added micro scans (~0.22min) The AGC

was turned off and the injection time set to 20 ms for full scan data and 40 ms for MS/MS data.

2.9.5. LESA Synapt Surface sampling

For LESA analysis, 3 μL of 70% methanol + 0.1% formic acid was aspirated from the solvent well. The robotic arm relocated to a position above the tissue section and descended to a height of approximately 0.8 mm above the surface. Two μL of the solution was dispensed onto the tissue section to form a liquid micro-junction. The liquid micro-junction was maintained between the probe tip and the surface for 10 s. 2.5 μL was re-aspirated into the pipette tip.

2.9.6. ESI-TWIMS

The TriVersa Nanomate (Advion) was mounted onto a Synapt G2-S. The source temperature was set to 30°C and the cone voltage was set at 45 V. All data were acquired in resolution mode with traveling wave ion mobility.

The traveling wave ion mobility cell was operated using nitrogen at a pressure of 3.08 Torr. A wave height of 40 V was used for all experiments. IMS separation was carried out at four wave velocities between 300 m/s and 450 m/s with step size 50 m/s.

For LESA experiments, the scan time was 0.5 sec and *m/z* range was 50–2000. Data were acquired for 12 sec in full scan mode

2.9.7. Fragmentation of ions using LESA coupled to TWIMS

Three peaks were selected for MS/MS analysis, one observed at *m/z* 764.5 (drift bins 82-89) and two observed at *m/z* 792.6 (drift bins 79-86 and drift bins 123-125) using a wave velocity of 350 m/s. Ions at *m/z* 764.2 were isolated in the quadrupole, prior to the Triwave, using a low mass resolution of 12.4 and a high mass resolution of 18.0. Ions were subjected to CID using an optimized, normalized collision energy of 35 %, in both the trap and transfer cell in separate experiments. Ions detected at *m/z* 792.6 were isolated using a low mass resolution of 10 and a high mass resolution of 20. Ions were subjected to CID using an optimized, normalized collision energy of 35 %, in the transfer cell. Data were acquired for 10 s and recorded between *m/z* 50-1200.

Data were analysed using Mass Lynx software (ver. 4.1, Waters).

2.9.8. ESI – TWIMS imaging

LESA imaging experiments were conducted using volume of 1.5 μL, dispensing 0.5 μL, re-aspirating 0.7 μL, after a delay of 5 seconds at sequential locations across the surface of the liver tissue, with x and y spacing 2 mm consisting of 56 pixels in 7 rows of 8. MS data were collected for 5 minutes per extraction. IMS separation was carried out at a wave velocity of 500 m/s.

2.9.9. MALDI Sample preparation

Sections of non-diseased and NASH human liver tissue, of area approximately 1.5 cm^2, were obtained at a thickness of 10 mm using a CM1810 Cryostat (Leica microsystems, Wetzlar, Germany) and thaw mounted onto glass slides. A matrix solution of 20 mg/mL CHCA in 85% MeOH +0.1% TFA was sprayed onto the tissue section (~15 mL) using an artist airbrush (Draper, Hampshire, UK) propelled by dry N_2. Glass slides were placed onto MALDI imaging plate holder, and loaded into the MALDI source. For MS/MS analysis sections were fixed using 0.154 M LiCl in 4% formaldehyde solution for 30 min prior to matrix application. [45]

2.9.10. MALDI MS/MS imaging

MALDI MS/MS analysis was performed on a Synapt G2-S, using a Nd:YAG laser (355 nm) firing at a 1000Hz with a normalized laser energy of 300. The image was acquired using a sampling spacing of 100 μm. Spectra were produced from 500 laser shots per location. Fragmentation of *m/z* 792.5 was conducted in the transfer cell using a normalized collision energy of 30. Isolation of ions occurred in the quadrupole, and optimised so that only ions relating to peak *m/z* 792.5 were transmitted. Image was produced using in house software.

2.9.11. MALDI TWIMS

MALDI TWIMS data were acquired from mouse liver extract using spot mode analysis. Lipids were extracted using the Folch extraction method and stored at -80^{o}C until required. [88] Samples were left at room temperature to defrost, and mixed with 25 mg/mL CHCA at a ratio of 1:1. 1 µL was spotted onto a 96 well MALDI spot target plate. Spot samples were interrogated in a spiral pattern using a normalized laser energy of 300 at a rate of 50 Hz. TWIMS was implemented in both static and variable mode. For static TWIMS analysis IMS separation was carried out at 6 wave velocities between 300 m/s and 800 m/s with step size 100 m/s. For variable TWIMS the wave velocities were changed at a linear rate during each duty cycle of the TWIMS nine gradients were implemented, 600-100 m/s, 700-100 m/s, 800-100 m/s, 900-100 m/s, 900-200 m/s, 900-300 m/s, 900-400 m/s, 900-500 m/s, and 900-600 m/s. A wave height of 40 V was used for all experiments. Spectra were acquired every 1 sec (50 scans per spectrum). Data were acquired for 10 second per sample spot at a mass range of *m/z* 50-2000.

2.9.12. MALDI TWIMS imaging

MALDI TWIMS MS/MS analysis was performed on a Synapt G2-S, using a ND:YAG laser (355 nm) firing at a 1000 Hz. The image was acquired at a resolution of 100 µm using a normalised laser energy of 300. Spectra were summed from 500 laser shots per location. A variable wave velocity of 900-300 m/s and a constant peak height of 40 V was used for imaging. The mobility cell

was operated at a pressure of 3.08 Torr and contained nitrogen. Images were reconstructed using Waters HDImaging software.

Chapter 3: Optimization of liquid extraction surface analysis for analysis and imaging of lipids and proteins in thin tissue sections

3.1 Introduction

Liquid extraction surface analysis (LESA) is a relatively new technique. It is based on the liquid-solid extraction of analytes, however it is the automation and the ability to link this technique to a mass spectrometer, which makes this technique so powerful.

LESA is the process of dispensing a droplet of ESI solution onto a surface. Molecules will dissolve into the ESI solution. Re-aspiration collects the enriched solution and robotics position the tip to connecting it to the nano-ESI source. The nano-ESI source is a chip with capillaries running through it. Backpressure is applied to the solution encouraging it to flow through the capillary, voltages applied to the capillary causes ionisation.

This chapter will describe optimisation of this process, with the aim of using the LESA technique as an imaging system.

3.2 Results and Discussion

Representative full scan mass spectra acquired following LESA of human liver sections are presented in Figure 24. Use of a solvent solution containing ~70% methanol resulted in detection of both singly and multiply charged ions (panel A). Inspection of an enlarged spectral region from *m/z* 900-1600 revealed peaks corresponding to several species in various charge states (panel B). The most abundant species were found to be phospholipids, detected as singly charged ions between *m/z* 700-820 (shown in panel C with accompanying inset of *m/z* 620-750), some lipids are shown in Table 3-1.

Table 3-1: Selection of abundant phospholipids from human liver tissue.

Measured *m/z*	**Theoretical *m/z***	**Error (ppm)**	**Identification**
732.5547	732.5538	-1.23	$[PC(32:1)+H]^+$
758.5704	758.5538	-1.32	$[PC(34:1)+H]^+$
796.5464	796.5454	-1.51	$[PC(34:2)+K]^+$
798.5418	798.5410	-1.00	$[PC(34:1)+K]^+$
820.5266	820.5253	-1.58	$[PC(36:4)+K]^+$

The effect of altering the organic composition of the electrospray solvent used for the liquid extraction surface analysis and ESI routine can be seen by comparing spectra presented in Figure 24 panels A, D and E. Reducing the percentage of methanol in the solution to ~50% resulted in a dramatic increase

in the relative abundance of multiply charged species, as shown in panel D. Singly charged ions were still detected between *m/z* 600-800 but spectra obtained were dominated by peaks corresponding to multiply charged ions. Further reduction of the methanol content to ~30% resulted in poor quality spectra as presented in panel E, indicating either poor extraction of molecules from the tissue surface or poor ionisation of extracted species during electrospray, or both. While extraction and ionisation of species from tissue are decoupled in LESA-ESI-MS, the most efficient routines in terms of throughput require the process to be achieved without the extracted sample being dried and re-dissolved in an alternative solvent prior to ESI-MS.

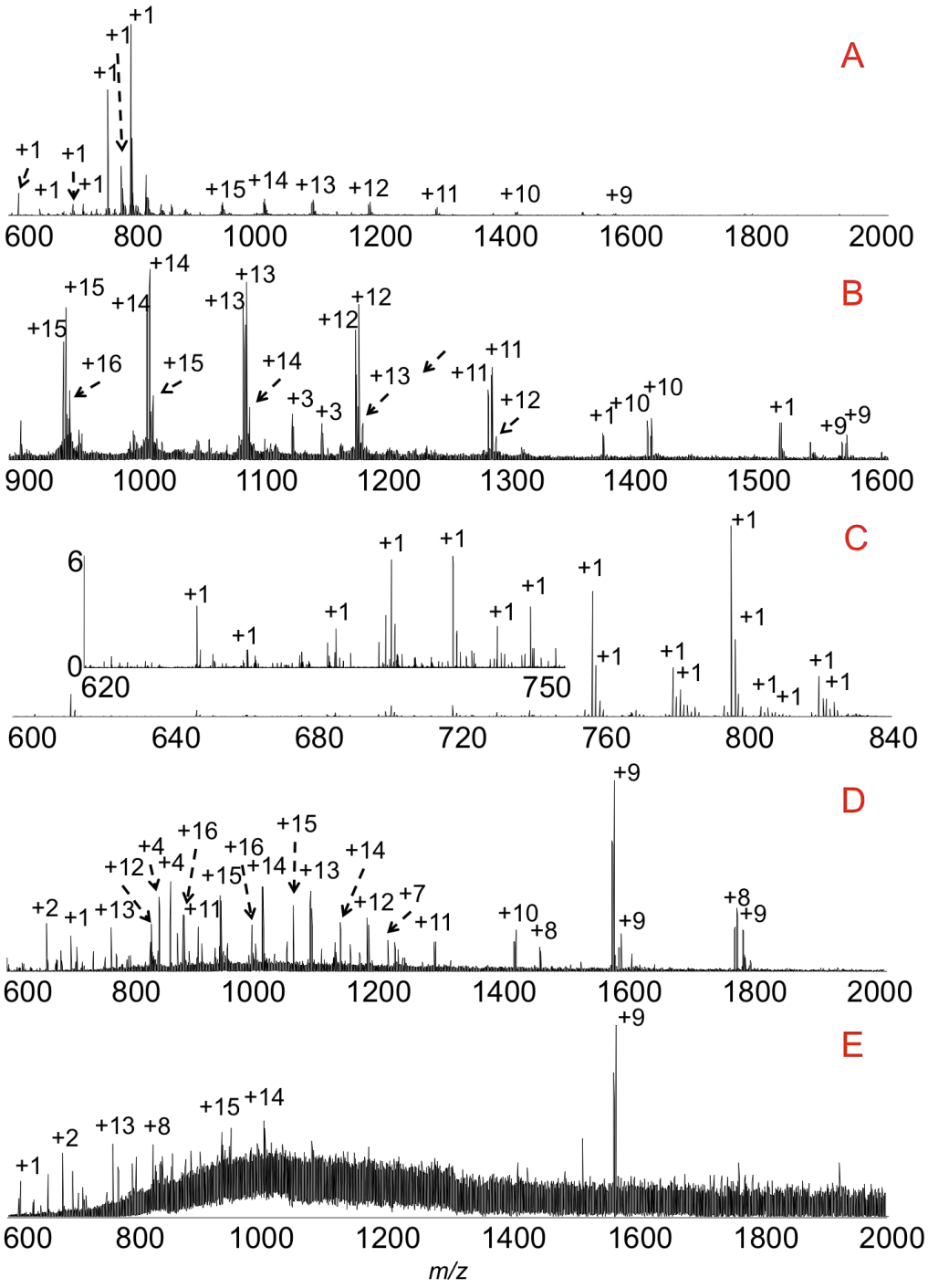

Figure 24: A) Spectrum acquired using 70% Methanol +0.1 % FA as the solvent in a LESA protocol of non-diseased human liver tissue. Enlarged region of this spectrum, are presented in B (protein region) and C (lipid region), D) Spectrum observed using 50% Methanol + 0.1 % FA as the solvent, E) Spectrum observed using 30% Methanol + 0.1 % FA as the solvent.

Using varying percentages of methanol, ethanol and acetonitrile prepared in water and FA confirmed that solvent selection should be carefully considered with respect to the scope of analytes detected by mass spectrometry. Whilst all solvent solutions assessed were compatible with maintenance of a liquid micro-junction, the solvent used altered the nature of analytes detected. Thus optimum solvent compositions for detection of multiply charged ions of peptides and proteins were found to contain ~40-50% acetonitrile. For analysis of lipids a solvent composition of ~80% ethanol yielded the richest spectra, and the most appropriate solvent solution for surveying both lipids and proteins comprised ~70% methanol. Representative spectra and a table summarising the most abundant species detected in LESA experiments using these solvent preparations are presented in Figure 25 and Table 3-2. In general solvent solutions containing a higher proportion of water resulted in superior detection of peptides and proteins and those with a higher organic content were found to be more useful for lipid analysis.

Table 3-2: Summary of pecies detected with differing solvent extractions

Organic Content	**Methanol**	**Ethanol**	**Acetonitrile**
80%	Lipids and Proteins	Lipids	Lipids and Proteins
70%	Lipids and Proteins	Proteins	Proteins
60%	Proteins	Proteins	Proteins
50%	Proteins	Proteins	Proteins
40%	Proteins	Proteins	Proteins

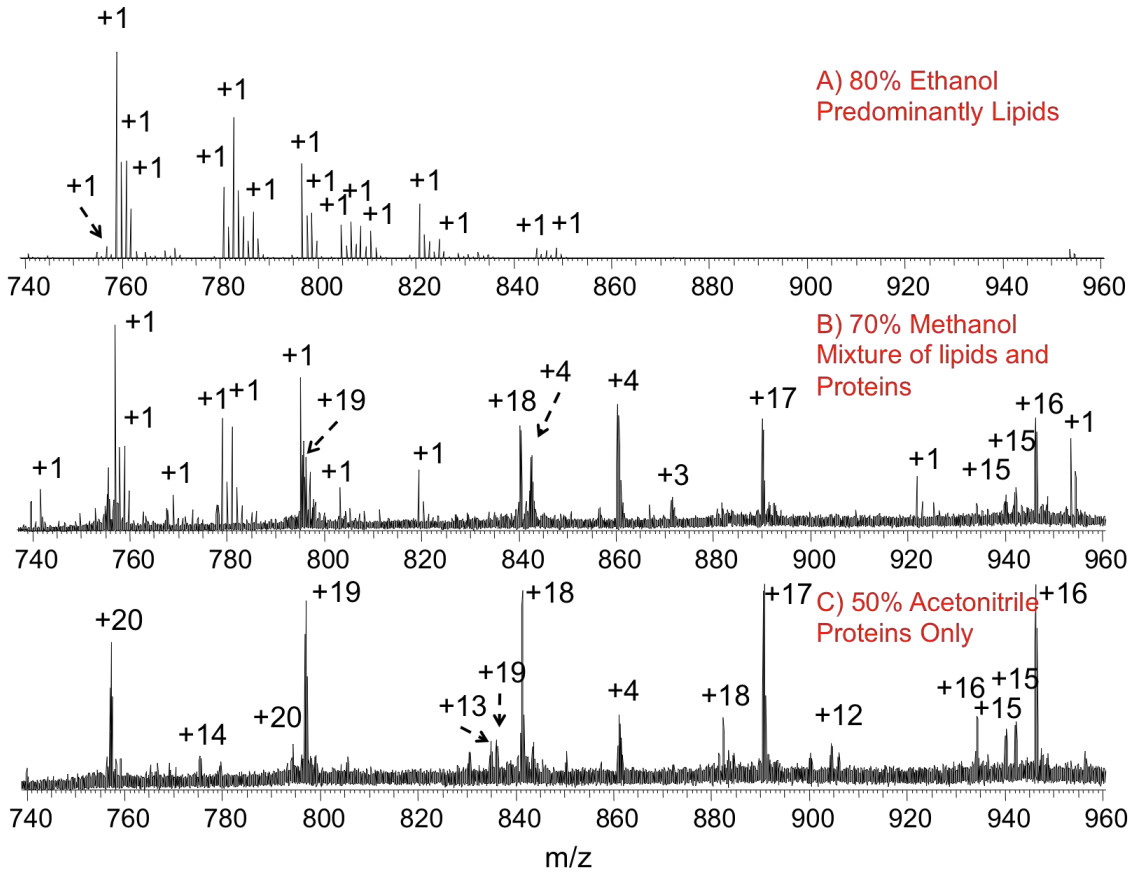

Figure 25: A) Enlarged region of a spectrum acquired using 80% Ethanol +0.1 % FA as the solvent in a LESA protocol of non-diseased human liver tissue. B) Enlarged region of a spectrum observed using 70% Methanol + 0.1 % FA as the solvent, C) Enlarged region of a spectrum observed using 50% Acetonitrile + 0.1 % FA as the solvent.

3.2.1. LMJ delay

The delay determines the length of time the LMJ is maintained. It was observed that lipids and proteins have different optimum extraction times. Lipids are observed at their most intense using a 10 sec LMJ, where as the optimum for proteins is a 30 sec LMJ. (Figure 26A and B)

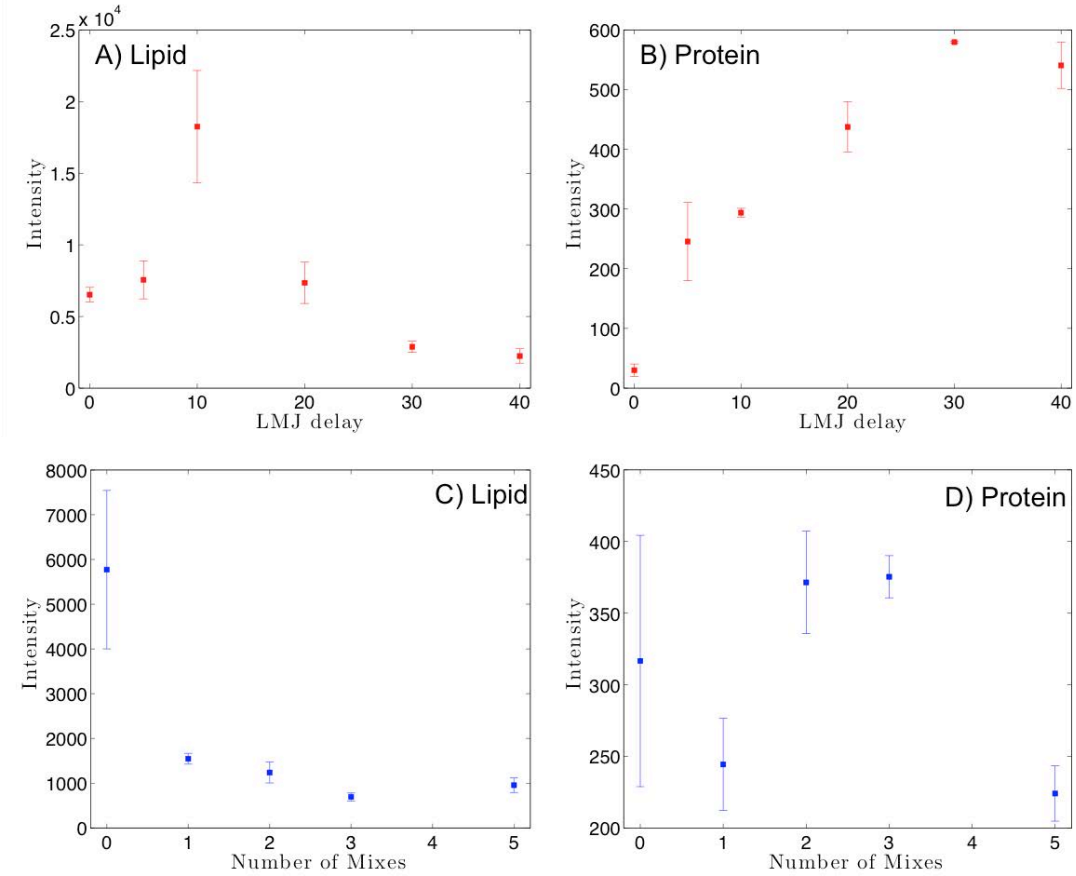

Figure 26: Graphs display the intensity of specific ions at increasing LMJ delays (A and B) and using increasing number of 5 sec mixes (C and D). A and C) Singularly charged ion was detected at *m/z* 758.54 and identified as $[PC34:2+H]^+$, B and D) Ion in +15 charge state, most abundant ion detected at *m/z* 942.23 identified as the +15 charge state of liver fatty acid binding protein. Error bars are 1 standard deviation from 3 repeats.

A solvent system comprising 70% methanol was used in this experiment. Lipids are very soluble in organic solvents where as proteins are less so. Under these conditions both lipids and proteins are soluble however lipids dissolve faster than proteins and spectra collected with short LESA extraction times were typically dominated by peaks associated with lipid species. Even still for optimum lipid analysis, a LMJ of 10 seconds was necessary to allow for the lipids to dissolve into the LMJ, but short enough before the protein concentration became too high.

In these experiments, the only movement of solvent occurs during the process is the dispensing and aspirating stages. Common practice when trying to dissolve compounds is to include a degree of agitation during the process. To increase the agitation during LESA, multiple dispensing and aspiration cycles were conducted each with a 5 second delay. 0, 1, 2, 3 and 5 repeats were investigated. Zero repeats mean that a single 5 second long LMJ was conducted. One repeat refers to two five second LMJ equating to a total LMJ time of 10 seconds, and 5 repeats equates to a 30 second LMJ, in 6 parts. The results show that there is a drop in intensity for the lipids when using the repeat cycles (Figure 26C). In the previous experiment 10 seconds was found to be the optimum delay time. This is equivalent to using 1 repeat, (2 x 5 sec), where there is a dramatic reduction in the intensity. Increasing the number of repeated cycles resulted in lower ion intensities for detected lipid species. The protein signal is not affected by the degree of agitation (Figure 26D), and it can be concluded that increasing the agitation by repeated mixing does not help improve the signal intensity of lipids or proteins.

Without using any agitation the length of the LMJ delay can significantly affect the ions observed in the spectra. The spectra produced using a signal LMJ with increasing junction delays are shown in the mass spectra presented in Figure 27. Increasing the delay between 5 and 30 seconds resulted in detection of more multiply charged species. A delay time of 40 seconds did not result in any further improvement. In future experiments a time of 20 seconds was used

because increasing the length of the delay allows significant evaporation of the solvents reducing the volume that is recovered and increasing the likely hood of the LMJ breaking prior to recovery resulting in poor analysis of the sample.

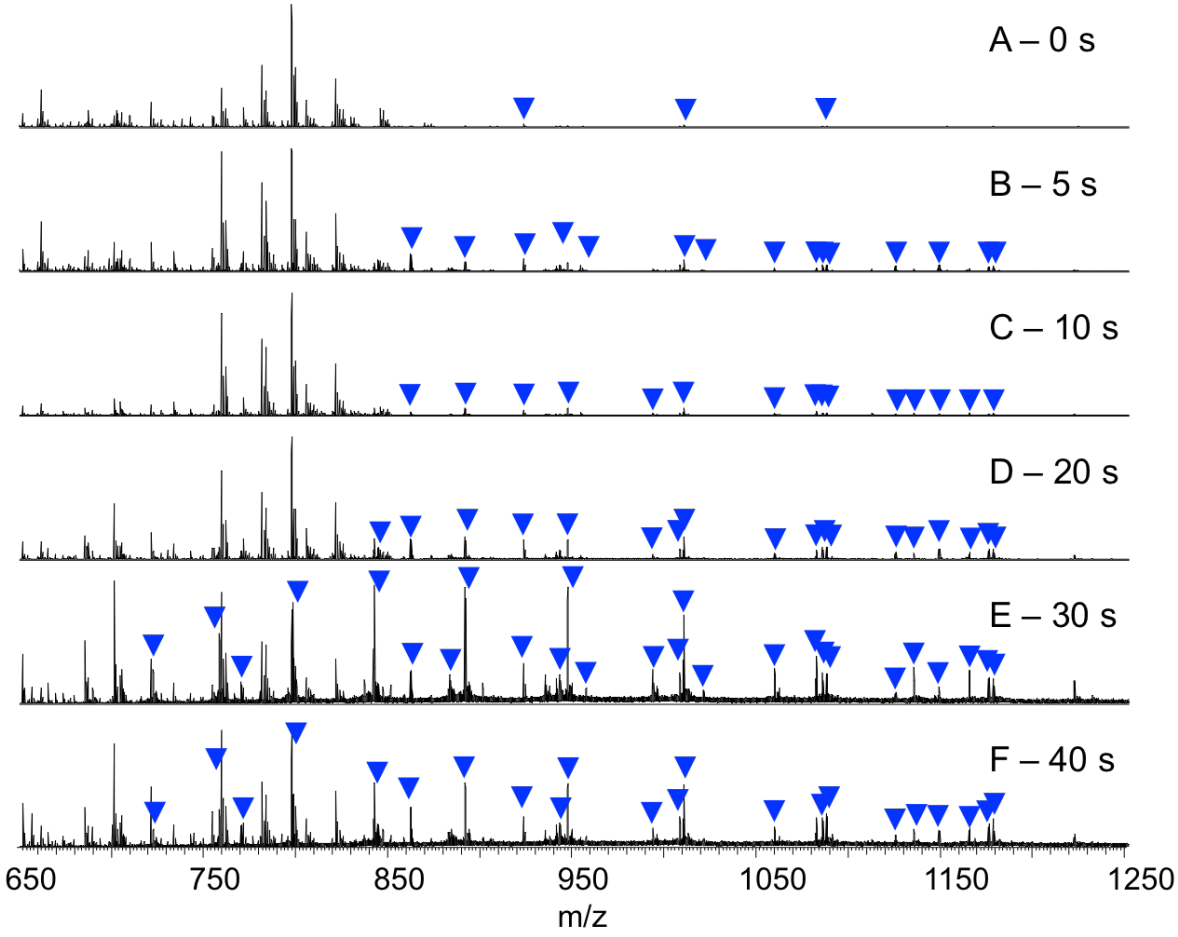

Figure 27: Enlarged region of a spectrum observed using 70% methanol +0.1 % FA as the solvent in a LESA protocol of non-diseased human liver tissue with a A) 0 sec LMJ delay, B) 5 sec LMJ delay, C) 10 sec LMJ delay, D) 20 sec LMJ delay, E) 30 sec LMJ delay, F) 40 sec LMJ delay. Blue triangles represent ions detected with multiple charges.

3.2.2. LMJ volume and height.

The height and dispensing volume are important parameters as they affect how far the droplet will spread. This will determine the spatial resolution of the

technique. There have been a wide range of droplet volumes reported from 0.5 µL [81] up to 7 µL [83]. Two volume sizes have been used in this experiment 0.3 µL and 0.5 µL, to assess these properties with respect to achievable spatial resolution (Figure 28). It was observed that at the higher dispensing height the LMJ was very difficult to maintain and during the re-aspiration the LMJ collapsed, leaving part of the solvent on the tissue. In these instances proteins were not detected, and the spectrum only revealed lipid ions. This is because proteins are less soluble in 70%$MeOH_{(aq)}$ so it takes longer for them to dissociate and as a result are predominantly at the interface between the sample and the LMJ and are not efficiently extracted if the LMJ breaks or if a large proportion of solution is left behind. This could be corrected if there is a longer delay on the tissue. Using a lower dispensing height was generally found to be more effective at complete re-aspiration of the LMJ. The highest signal intensity of 4 selected ions (Figure 28) (*m/z* 796.5257 identified as $[PC34:2+K]^+$, *m/z* 758.5699 identified as $[PC34:2+H]^+$, *m/z* 942.2346 identified as the +15 charge state of the liver fatty acid binding protein, *m/z* 124.5011 is unidentified) was observed to be when a height of 0.8 mm was used. Data shown in Figure 28.

As for the dispensing volume, higher signal intensity was observed using 0.5 µL for singly charged molecules, where as a higher intensity was observed using 0.3 µL for multiply charged molecules. High intensities of lipids are contrasted with low intensity of proteins. This may be a symptom of the extraction process rather than the height and volume.

The optimum height for single positional analysis is 0.8 mm above the surface however; the LMJ is liable to break more often than a LMJ of 0.4 mm above the surface. For imaging it is important for the sampling method to be reliable and consistent therefore a lower height should be used even thought there is a reduced sensitivity. This is because it is more important to get data from each pixel than it is to achieve the maximum sensitivity of the method. If single positional analysis is being conducted then it would be feasible to do the analysis at a higher height.

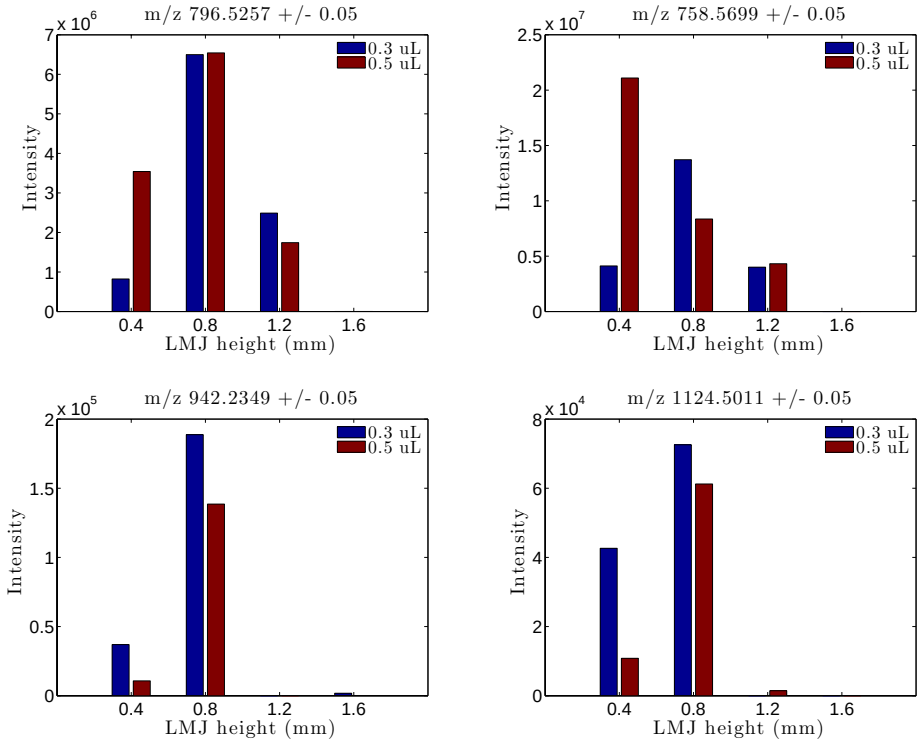

Figure 28: The intensity of four of peaks, *m/z* 796.5357 in +1 charge state, *m/z* 758.5699 in +1 charge state, *m/z* 942.2349 +16 charge state, and *m/z* 1124.5011 in +3 charge state, observed using a 0.1% formic acid in 70% methanol as the extraction solvent in a LESA protocol. Four dispension hights (0.4 mm, 0.8 mm, 1.2 mm, 1.6 mm) and two dispension volumes (0.3 µL and 0.5 µL) were used.

3.2.3. Dilutions

Only a proportion of the total volume in the LESA pipette tip is dispensed. Changing the residual volume in the pipette that does not alter the volume associated with the LMJ but will affect the dilution of the sample. Larger volumes resulted in a longer spray time, a total volume of 1 μL resulted in an average spray time of 4 min 7 sec, (over 3 repeats), increasing to 8 min 52 sec for 2 μL, 15 min 34 sec for 3 μL, and, 21 min 11 sec for 4 μL. The relationship between liquid volume and ESI spray time was not found to be linear.

A long analysis time would be ideal, especially for inhomogeneous samples where it is necessary to obtain the maximum amount of information from a single location. However, with larger volumes, a dilution effect was observed between the initial spray and the later spray. Different molecular species were observed at different time points. The length of time the droplet was spraying was determined by the background noise, which is more intense when spraying. In larger droplet volumes, 2, 3 and 4 μL the intensity of the peaks of interest reduces to the point that they are no-longer observed (Figure 29). These results indicate an inhomogeneous mixture of analytes within the solvent plug when using large residual volumes. Including a pause between extraction and analysis to allow a homogenous solution to be formed unfortunately resulted in the entire solution being too dilute to be detectable. The optimum sampling conditions for imaging were found to be a small LMJ volume and a small residual volume. This is to produce the smallest area on the surface while

maintain the ideal conditions in which to detect analytes from the surface via a LMJ.

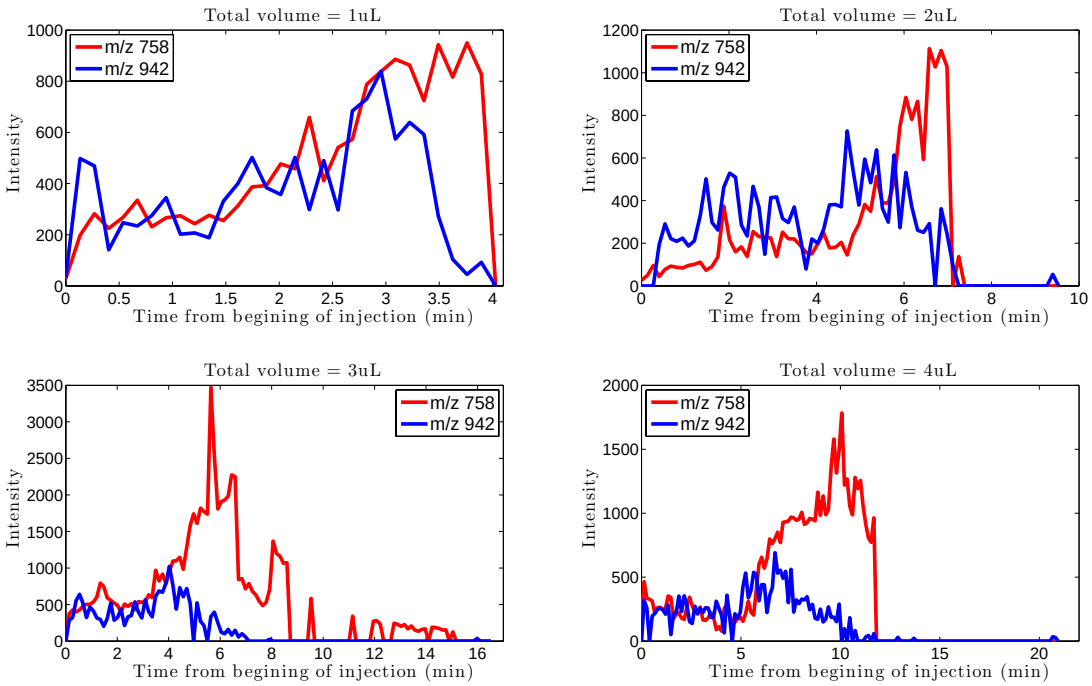

Figure 29: Signal intensity of a singly charged ion *m/z* 758.53 (red) and an ion in +16 charge state *m/z* 942.23 (blue) over the time course of the injection. Observed using 0.1 % formic acid in 70% Methanol in a LESA protocol where the total volume is 1, 2, 3, or 4 µL.

3.2.4. Acid Concentration

Modifiers are added to help the Ionisation process. Proton donors and acceptors are used to protonate and deprotonate molecules. [84] To assess how the acid affects Ionisation of lipid and protein species a 70% Methanol solution was used to observe both these species. Four acid concentrations were investigated, 0.1% formic acid, 1% formic acid, 2% formic acid and 3% formic acid.

Lipids form adducts with sodium and potassium that are extracted from the tissue. By increasing the acid concentration in the LESA solvent, formation of a protonated molecule is favoured. The protonated molecule is the least useful for characterization as it produces very few fragments therefore it is most useful to keep the protonated peak to a minimum. [209, 210] (The use of additives for lipid identification will be explored further in chapter 4).

The most intense protein peaks are detected using a solution containing 1% formic acid. It was observed during the experiment that the electrospray of solutions containing 2% and 3% formic acid were very unstable reducing the intensity of the peak (Figure 30). The detections of hemoglobin variants via LESA has been reported, in this case a solution containing 3% formic acid was used, however this was to target hemoglobin in blood spots on card. [83, 84, 197]

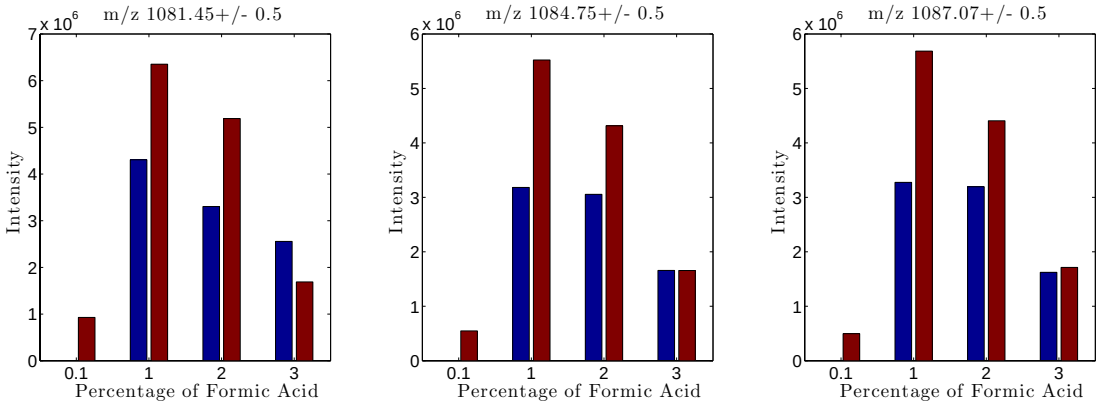

Figure 30: The intensity of three of peaks, *m/z* 1081.45 in a +13 charge state, *m/z* 1084.75 in +13 charge state, *m/z* 1087.07 in a +14 charge state, observed using 70% methanol as the extraction solvent with 4 concetrations of formic acid, in a LESA protocol. Two repeats (red and blue).

Different solvents including Chloroform/Methanol/Isopropanol 1:2:4 with ammonium acetate as a solution have been recommended for extraction and analysis of lipids. [79, 87, 193] However, each of these components have a very low surface tension (Chloroform = 26.7 dynes/cm^2 Methanol = 22.1 dynes/cm^2, Isopropanol = 23.3 dynes/cm^2 at 25 ^{o}C [211]) and when dispensed onto glass the LMJ breaks and the solution forms a thin film on the surface. Additionally methanol, chloroform and Isopropanol are volatile solvents and when dispensed will quickly evaporate.

LESA analysis using Chloroform/Methanol/Isopropanol solutions would be very difficult. To combat this the height from which is recovered is reduced to zero, so that the LESA tip is in contact with the surface. In addition the area that would be affected could be quite large, as the solvent would spread along the samples surface a relatively long way affecting the spatial distribution of lipid ions. For a reliable liquid micro junction to be formed it is necessary to have a proportion of water (surface tension of 72.7 dynes/cm^2 at 25 ^{o}C [211]) in the solvent mixture to insure that the LMJ droplet is stable and the sampling area is as restricted as possible, while still providing an organic component for optimum ESI analysis.

1.1.1 Washing

Tissue washing was found to improve analysis of proteins in tissue, reducing suppression effects caused by abundant salts and lipids, which are typically removed in the washing step. This strategy has been relatively widely deployed

by the MALDI imaging community in studies of peptide and protein distributions across a tissue surface. [44, 212-214]

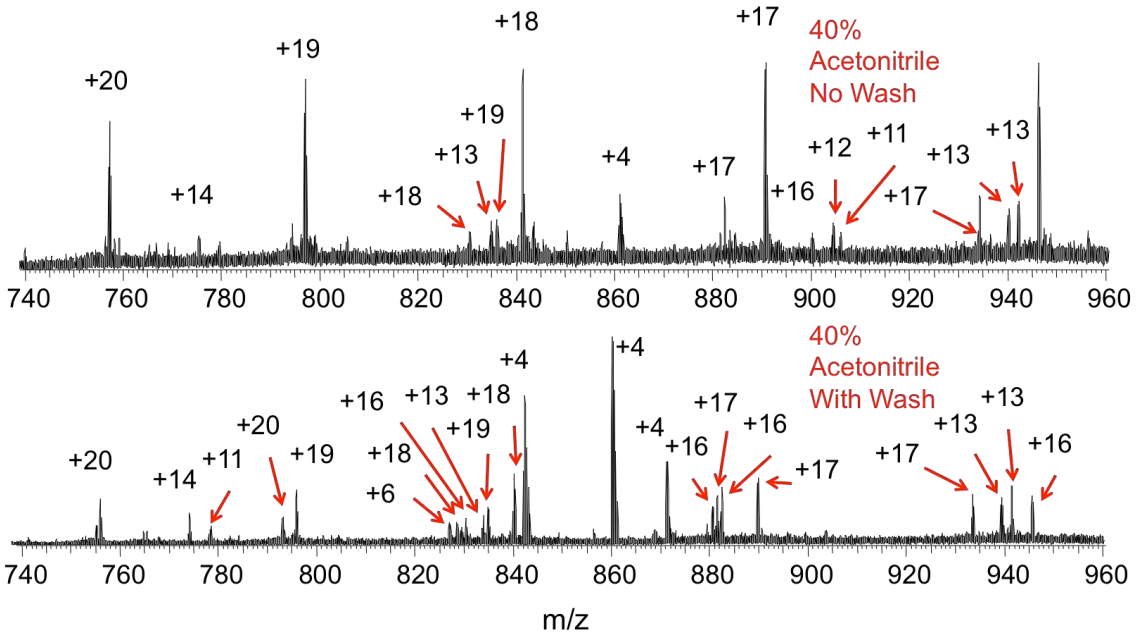

Figure 31: Top) Spectrum observed using 0.1% formic acid in 50% Acetonitrile as the solvent in a LESA protocol of non-diseased human liver tissue. Bottom) Spectrum observed using 0.1% formic acid in 50% Acetonitrile as the solvent in a LESA protocol, from the same spatial location that had previously been sampled via LESA using 0.1% formic acid in 80% Ethanol.

Liquid micro junction analysis can be viewed as a localised washing where the eluent is then analysed. A washing step using the LESA protocol was conducted using a favourable lipid extraction (80% Ethanol + 0.1% FA) followed by a favourable protein extraction (50% Acetonitrile + 1% FA). This resulted in almost double the number of proteins being observed in the second extraction, 13 proteins above 3 kDa were observed from a 50% Acetonitrile + 1% FA extraction, whereas 18 proteins (Appendix 1) were observed from a 50% Acetonitrile + 1% FA extraction using tissue washing. In both cases the largest protein observed was the beta chain of haemoglobin at 16 kDa. (Figure 31)

When targeting proteins, using the LESA as a localised washing mechanism is time consuming. In these instances it is better to wash the entire sample prior to analysis. Four sequential tissue sections were dipped into 80% ethanol for 10 seconds and then left to dry. Three were then dipped for a further 10 seconds, 2 for additional 10 seconds and then 1 section for a fourth time. Each tissue section was analysed three times using the method stated in materials and methods chapter. With one dip the signal intensity approximately doubles, and subsequent washes there is no improvement (Figure 32). A one way Anova statistical analysis on this data shows that for *m/z* 1081 and *m/z* 1084 there is a statistical difference between the groups, (95% confidence), where as for *m/z* 1087 there is no statistical difference. (Analysis in Appendix 2)

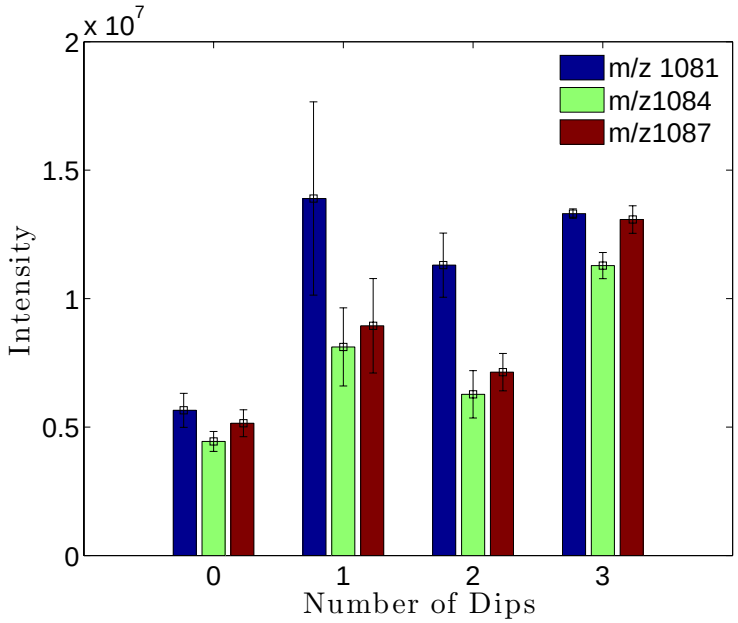

Figure 32: The intensity of three of peaks, *m/z* 1081.45 in a +13 charge state, *m/z* 1084.75 in +13 charge state, *m/z* 1087.07 in a +14 charge state, observed using 70% methanol as the extraction solvent. Tissue pretreadted with a series of washes in 80% Ethanol. Error bars are one standard deviation from three repeats.

3.2.5. Multiple sampling

In washing experiments the eluent is discarded however this solution is rich in analytes. The effect of multiple, serial extractions at the same x, y co-ordinate was evaluated using ~70% methanol. The relative abundances of selected ions detected in ten sequential extractions are presented in Figure 33. In graph B and C the change in intensity of ions in sequential extractions may be explained by the effect of repeated washing steps, depleting surface salts. Where as in graph A there is no trend in the ion intensity. This could be attributed to the ion being a protonated species and the addition of formic acid in the LESA solvent, repeatedly contributing to the salt content of the solution. The relative intensities of numerous other detected ions in ten repeated extractions are presented in Appendix 3. Similar repeat extraction experiments were conducted by Eikel *et al* in an investigation of drug detection from tissue via LESA. [80] The authors did not mention other lipids or proteins and were using a solvent system specifically optimised for the extraction of the target drug. [80] It is important to not when doing LMJ surface sampling of tissue that the sampling is not 100% efficient, and that the sample changes due to the analysis that can affect the analysis.

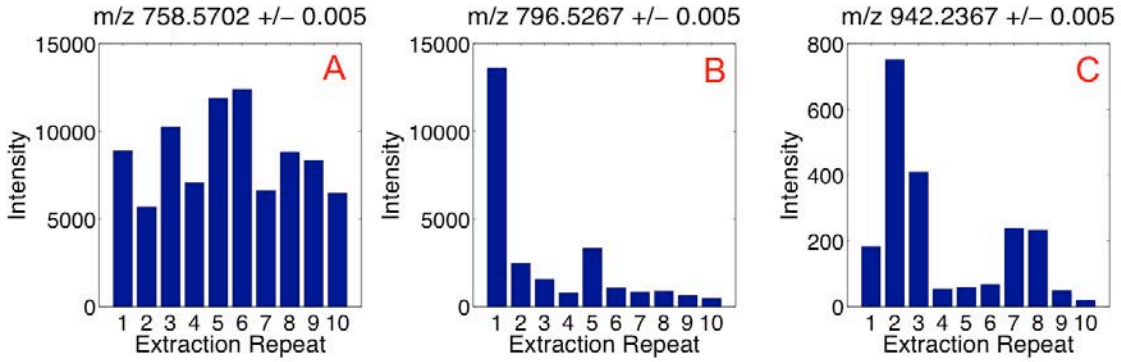

Figure 33: The intensity of three peaks (A) *m/z* 758.57 in +1 charge state, (B) *m/z* 796.53 in +1 charge state and (C) *m/z* 942.24 in +15 charge state, observed from ten sequential LESA from the same tissue location, using 0.1% formic acid in 70% methanol as the extraction solvent.

3.2.6. AGC

The automatic gain control (AGC) is a parameter that estimates the number of ions present, and adjusts the injection time into the Orbitrap for the optimum analysis and is typically set at 1,000,000 charges. The AGC relies on a pre-scan in the iontrap, which is used to hold the ions before injecting them into the Orbitrap. [215, 216] The total current in the iontrap is used to determine an approximate number of charges present, this then calculates the fill time required to inject the target value for the number of charges. This greatly improves spectral quality, as there is compensation for both concentrated and weak samples in order to achieve optimum results. However, the AGC is not suited to imaging or quantitative analysis. Imaging using the Orbitrap is typically conducted using a MALDI source where the AGC is turned off. The AGC on a MALDI Orbitrap controls the number of laser shots the reach the number of target charges. During imaging experiments the number of laser shots per position is maintained. Alternative Orbitrap imaging data sets have

been performed using a DESI source. There is conflicting advice for controlling the AGC in one instance the AGC is reported to be turned off while performing the imaging [217] however in a publication aimed at introducing DESI imaging it is suggest that the AGC should remain on, incase of instances where an ESI spray is formed instead of a DESI, so that the AGC can prevent a overload of ions, [218] many reports fail to mention how or if the AGC is controlled. [219-222]

Very few people have used LESA as an imaging platform, Eikel et al, used the LESA coupled to an Orbitrap mass analyser for imaging tissue, in this report data was not shown instead a photograph displaying sampled regions was reported instead. It was noted in the method that a short fill time was used (50ms) but the AGC target was on [82]. The only other LESA image was produced on a triple quadrupole and therefore did not use an AGC [80].

The AGC is not suitable for the use with imaging. When the AGC is off, the maximum fill time is reached for each scan. Optimisation of the maximum fill time included assessment of the signal to noise ratio and the mass accuracy had been conducted (see Appendix 4). In conclusion the signal intensity is lower that when the AGC is turned on but the s/n ratio is not affected as the noise value decreases as well. The mass accuracy is also affected by the maximum fill time (Appendix 5). The greater the disparity between the maximum fill time and the fill time assessed by the AGC the poorer the mass accuracy is. Therefore to maintain a high mass accuracy during imaging, a single position on a serial

section to the imaged section was analyzed with the AGC and the fill time was noted. This value was then used to fix the maximum fill time when the AGC was turned off.

3.2.7. Imaging

The optimum solvent system for direct analysis of lipids and proteins in tissue sections was found to comprise ~70% methanol. This solvent system was used for an automated LESA method to sample 60 locations (5 rows of 12 locations) spaced 1 mm apart in a sequential manner across a section of human liver. Limitations in the software only allow integers from 1 to 5 mm to be defined as the distance between two sampling locations.

Ion images were constructed from the mass spectrometry data using in-house software. Figure 34A shows an example mass spectrum acquired from a single pixel location, the average mass spectrum from all 60 locations is presented in Appendix 6. An inset of the H&E stained tissue and sampling locations showing the area surveyed is also shown. Selected ion images are presented in panel B from six singly charged lipid adducts.

- PC(32:1) $+H^+$ detected at *m/z* 732.5533, $+Na^+$ detected at *m/z* 754.5351, $+K^+$ detected at *m/z* 770.5093.
- PC(34:1) $+H^+$ detected at *m/z* 760.5844, $+Na^+$ detected at *m/z* 782.5678, $+K^+$ detected at *m/z* 798.5403.

- Lyso-PC(18:2) $+H^+$ detected at *m/z* 524.3549, $+Na^+$ detected at *m/z* 546.3366, $+K^+$ detected at *m/z* 562.3109.
- PC(36:4) $+H^+$ detected at *m/z* 782.5678, $+Na^+$ detected at *m/z* 804.5507, $+K^+$ detected at *m/z* 820.5250.
- SM(32:0) $+H^+$ detected at *m/z* 703.5745, $+Na^+$ detected at *m/z* 725.5557, $+K^+$ detected at *m/z* 741.5308.
- PE(40:6) $+H^+$ detected at *m/z* 764.5217, $+Na^+$ detected at *m/z* 786.5032, $+K^+$ detected at *m/z* 802.4778.

Images presented are summed spectral intensity of a window ± 0.005 Da from the specified mass. In panel C, distributions of proteins that were detected as multiply charged ions are presented. Further ion images were produced by summing intensities of 5 peaks (±0.01 *m/z*) relating to FABP1 +15 charge state (*m/z* 942.1006, 942.1676 942.2339, 942.3010 and 942.3681) and +16 charge state of the alpha chain of heamoglobin (*m/z* 946.2509, 946.3141, 946.3766, 946.4389, 946.5641). Four unidentified peaks are also presented *m/z* 845.8645 +10 charge state, *m/z* 1012.1735 +7 charge state, *m/z* 1058.8244 +15 charge state, and *m/z* 1134.3104 +14 charge state.

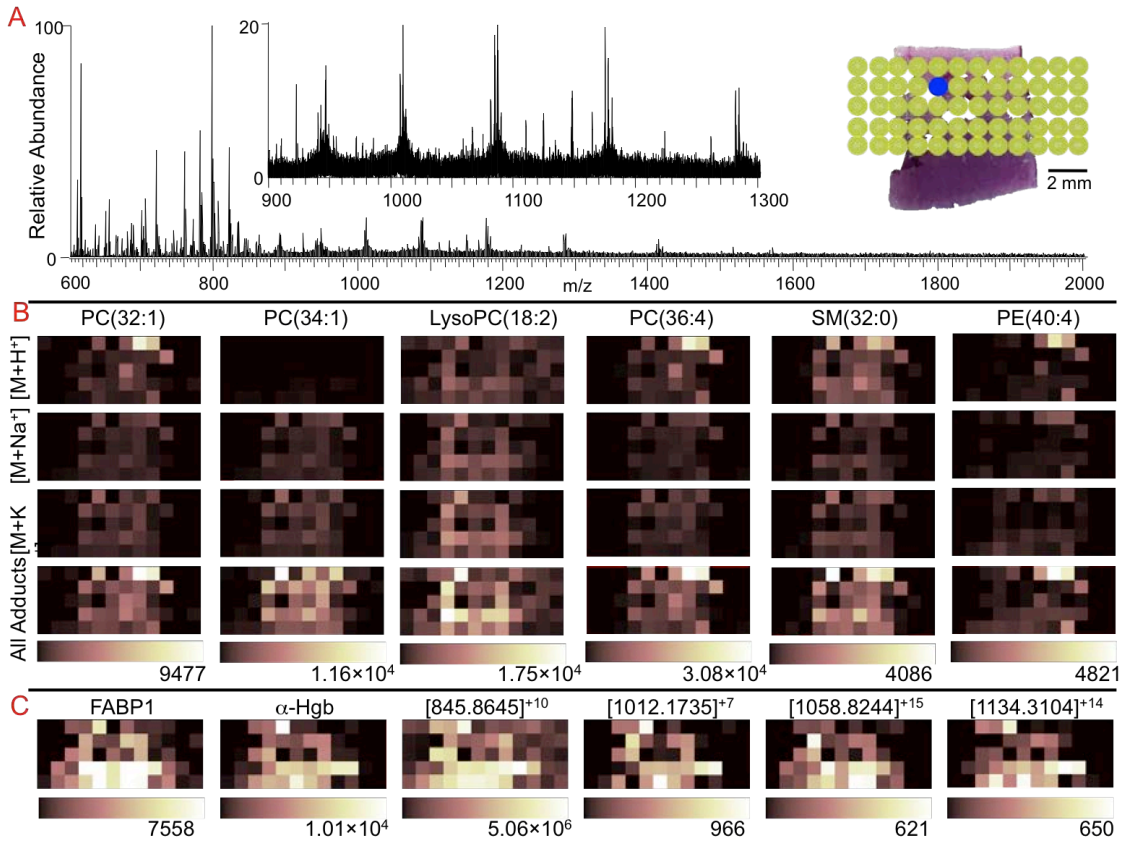

Figure 34: Panel A) Spectum produced during the imaging run, from the location indicaticated. Inset, enlargment of the protien region of the mass spectrum. Inset, Photograph of the imaged tissue section stained using H and E, overlay indecates pixle locations. Mass spectrum from blue pixel is displayed. Panel B) Distributions of six lipids as their protonated, sodiated and poassiated adducts and the sum of the three adducts. Panel C) Distribution of the sum of 5 isotopic peaks from the +15 charge state of L-FABP. Distribution of the sum of 5 isotopic peaks from the +16 charge state of α-hgb. Distribution of four unidentified peaks.

It was observed during the experiment that the droplets for each pixel overlapped the same area as the previous analysis. To determine the spot size of the LMJ the tissue was stained using hematoxylin and eosin (H and E) after the extraction process. The H and E staining process interacts with the tissue differently between where the LMJ has been and the rest of the tissue, perhaps attributed to the acidity of the LMJ solution (Figure 35). The size of the LMJ was measured for 4 volumes, 0.5 µL, 1 µL 2 µL and 3 µL. Using these measurements it is possible to predict the overlap and spacing of the LMJ when conducting an

image (Figure 36). A 0.5 µL droplet forms a LMJ with a diameter of 1.54 mm. Using a 1 mm spacing will result in a degree of oversampling. It has been shown previously that resampling the same region can change the spectra. This can improve some species and hinder others and is highly inappropriate in an imaging scenario.

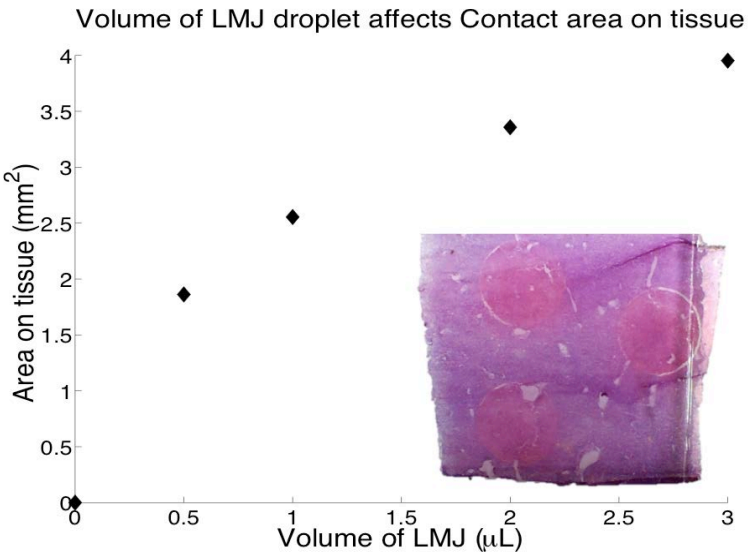

Figure 35: Graph showing the area that is affected by the LMJ during LESA analysis. Inset) Photograph of a heamotoxalin and eosin stained non-dieased human liver tissue section that has been sampled three times using LESA.

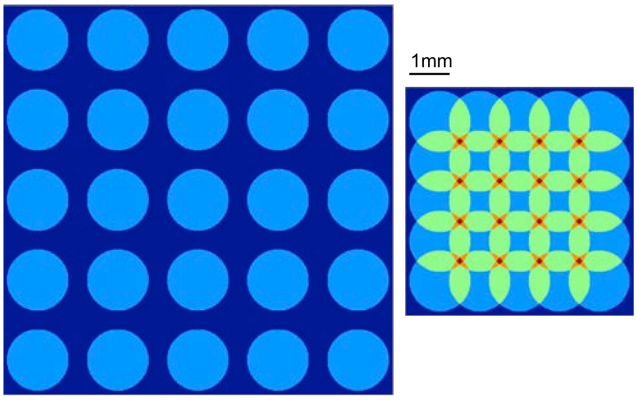

Figure 36: The theorectial coverage of imaging with a 0.5 µL LMJ with 2 mm spacing (Left) between sampling locations and 1mm sampling (right) locations. Unsampled areas are dark blue, areas sampled once are light blue, green indicates the area has been sampled twice, orange indicats the area has been sampled three times, and red indicates the area has been sampled four times.

A second imaging experiment was conducted using 2 mm spacing between each sampling location to insure that the sampling locations did not overlap. Figure 37A shows an example mass spectrum acquired from a single pixel location. Selected ion images are presented in panel B from seven singly charged lipid adducts. Lipid identities and sn1 and sn2 FA were confirmed using MS/MS techniques outlined in section 6.2.1.3.

- Lyso-PC(18:2) $+H^+$ detected at *m/z* 524.3549, $+Na^+$ detected at *m/z* 546.3366, $+K^+$ detected at *m/z* 562.3109.
- Lyso-PC(20:4) $+H^+$ detected at *m/z* 544.3428, $+Na^+$ detected at *m/z* 566.3276, $+K^+$ detected at *m/z* 582.3019.
- SM(32:0)$+H^+$ detected at *m/z* 703.5745, $+Na^+$ detected at *m/z* 725.5557, $+K^+$ detected at *m/z* 741.5308.
- PC(32:1) $+H^+$ detected at *m/z* 732.5533, $+Na^+$ detected at *m/z* 754.5351, $+K^+$ detected at *m/z* 770.5093.
- PC(34:2) $+H^+$ detected at *m/z* 758.5788, $+Na^+$ detected at *m/z* 780.5614, $+K^+$ detected at *m/z* 796.5356.
- PC(36:4) $+H^+$ detected at *m/z* 782.5678, $+Na^+$ detected at *m/z* 804.5507, $+K^+$ detected at *m/z* 820.5250.
- PC(38:4) $+H^+$ detected at *m/z* 810.6112, $+Na^+$ detected at *m/z* 786.5032, $+K^+$ detected at *m/z* 848.5686.

In panel C, distributions of proteins that were detected as multiply charged ions are presented. Further ion images were produced by summing intensities of three peaks (±0.01 *m/z*) relating to FABP1 in the +15 charge state (*m/z*, 942.1676 942.2339, 942.3010) and $FABP_{TA}$ in the +15 charge state (*m/z*, 940.2460, 940.1788, 940.3127). As well as α-hgb in the + 16 charge state (*m/z* 946.2509, 946.3141, 946.3766) and β-hgb in the + 16 charge state (*m/z* 1134.3269, 1134.2529, 1134.3979). The other map in the panel present distribution of a currently unidentified specie found at *m/z* 1148.1944 in a +3 charge state. An inset of panel C is the H&E stained tissue and sampling locations showing the area surveyed.

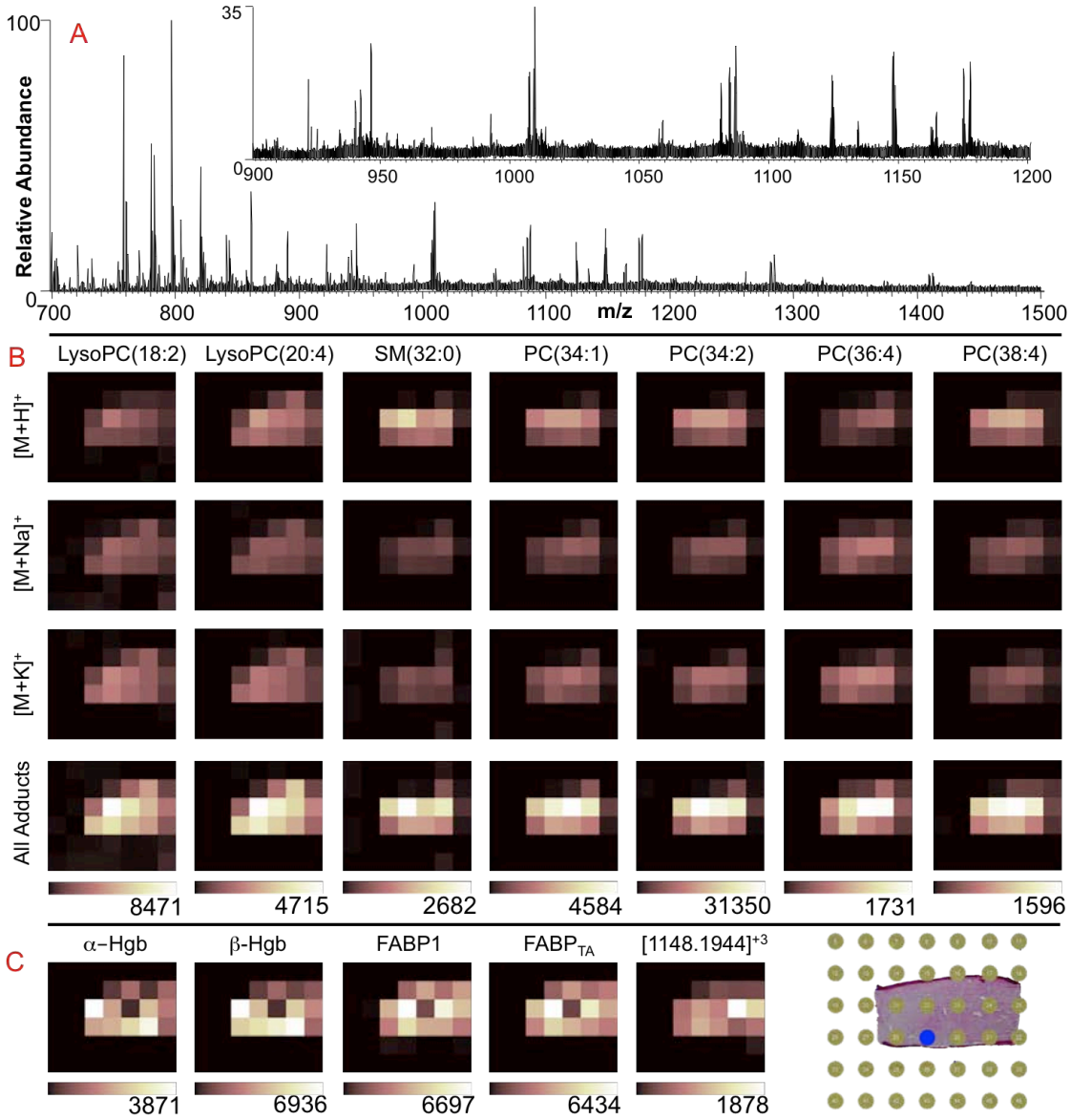

Figure 37: Panel A) Spectum produced during the imaging run, from the location indicaticated. Inset, enlargment of the protien region of the mass spectrum. Panel B) Distributions of seven lipids as their protonated, sodiated and poassiated adducts and the sum of the three adducts Panel C) The distributions of 5 protiens β-hgb (+16 charge state), α-hgb (+16 charge state), FABP1 (+15 charge state), $FABP_{TA}$ (+15 charge state) and an unidentified species in a + 3 charge at *m/z* 1148.1944. Photograph of the imaged tissue section stained using H and E, overlay indecates pixle locations. Spectrum from blue pixel is shown in panel A.

These results highlight the opportunities for profiling a diverse selection of endogenous analytes in tissue using LESA methods. The two-dimensional profiles of proteins and lipids show an inversely proportional relationship, pixels that show high lipid intensity correspond to pixels of low protein intensity. This is not ideal, as ion images produced will depend heavily on other species that are present in the solution. Therefore separation of these species for imaging is essential. Subsequent chapters in this thesis will explore the use of LESA with liquid chromatography for the analysis of proteins and the LESA coupled to ion mobility spectrometry for the analysis of lipids and proteins directly from human liver tissue.

3.3 Conclusion

Here has been demonstrated a single LESA protocol for the direct analysis of lipids and proteins. The simultaneous analysis of these molecules are challenging for most reported techniques, for example, analysis of proteins and peptides via MALDI use carefully selected, matrices and laser powers, which may not be suitable for analysis of lipids in the same section. In addition optimal analysis conditions lipids and proteins have been determined. For optimum lipid analysis, a solution of 0.1% formic acid in 80% ethanol is used, with a 10 second LMJ delay, where as for protein analysis the optimal conditions is a solution of 1% formic acid in 50% acetonitrile, with a 30 second LMJ delay. The analysis of specific lipids and proteins in human liver sections will be explored further in subsequent chapters in this thesis.

In addition, LESA methods can be used to obtain spatially resolved profiles directly from tissue. Current pixel sizes are 1.86 mm^2 this relates to an ideal pixel spacing of 1.54 mm, this sits between the 1 mm and 2 mm spacing that is allowed by the instrumentation. At 1 mm spacing there is a degree of over sampling, whereas at 2 mm spacing leaves un-sampled tissue. It would be possible to adjust the droplet size to make a more effective sampling area. A droplet of 1.6 μL would give a diameter of approximately 2 mm, preventing oversampling and reducing the amount of un-sampled tissue. To do the same for a 1 mm spaced image it would be necessary to reduce the droplet volume to approximately 0.2 μL. A recent report shows the potential for the reduction of the contact area of the liquid micro-junction by applying electro-focusing without reducing the droplet volume. [223] Alternative surface sampling probe introduced by the Van Berkel group, [94] and nano-DESI introduced by Laskin et al, [95] provide a route to improved resolutions and analysis times in LMJ sampling. At present, possibly the most significant advantage of using LESA spatial profiling is the relatively long spray times per pixel, over 4 min when compared to other imaging techniques such as MALDI and DESI which are less than 1 sec. There is the possibility to enhance the data acquisition and improve the quality of the analysis.

Chapter 4: Top-down and bottom-up identification of proteins by liquid extraction surface analysis mass spectrometry of healthy and diseased human liver tissue.

Work presented in this chapter has been published as an article in the Journal of the American Society for Mass Spectrometry [vol. 25. p.1953-1961 2014], on which I am first author. The article was written in collaboration with my supervisors, and is included in Appendix 7.

4.1 Introduction

The work presented in Chapter 3 demonstrated that LESA is suitable for the detection of proteins. In this chapter, LESA has been applied to the analysis of proteins in thin tissue sections from human liver. Specifically, the aim was to explore LESA as a means for interrogating protein biomarkers of non-alcoholic liver disease.

Identification and characterisation of liver fatty acid binding protein (FABP1) was of particular interest. The fatty acid binding protein has been shown to have a natural variant that is associated with an increased risk in the detection of fatty liver disease [181]. The variant has a single amino acid substitution at the 94th amino acid residue: Thr→Ala. Top-down and bottom-up approaches for the analysis of proteins extracted by LESA have been investigated. Top-

down methods were applied to 4 proteins to determine their identity. These four proteins were assessed in both non-diseased and NASH liver tissue from four tissue sections (two non-diseased samples, one from tumour resection margin, and one from a donor liver not suitable for transplantation). A bottom-up approach conducted on the tumour resection margin tissue section, in which intact endogenous proteins were extracted by LESA prior to automated trypsin digestion was used to investigate the scope of proteins that can be analysed and detected via LESA via an automated trypsin digestion [85, 224].

4.2 Results and discussion

4.2.1. Top-down analysis of intact proteins in human liver

Four protein ions detected using a solvent system of 50% acetonitrile (Figure 38) were subjected to CID and ETD. These ions were,

- *m/z* 775 in a +14 charge state (MW_{meas} 10836.8056 Da)
- *m/z* 940 in a +16 charge state, and *m/z* 1081 in a +15 charge state (both with a MW_{meas} of 14081.3600 Da)
- *m/z* 942 in a +16 charge state, and *m/z* 1084 in a +15 charge state (both with a MW_{meas} of 14111.4161 Da)
- *m/z* 946 in a +16 charge state (MW_{meas} of 15117.9167 Da)

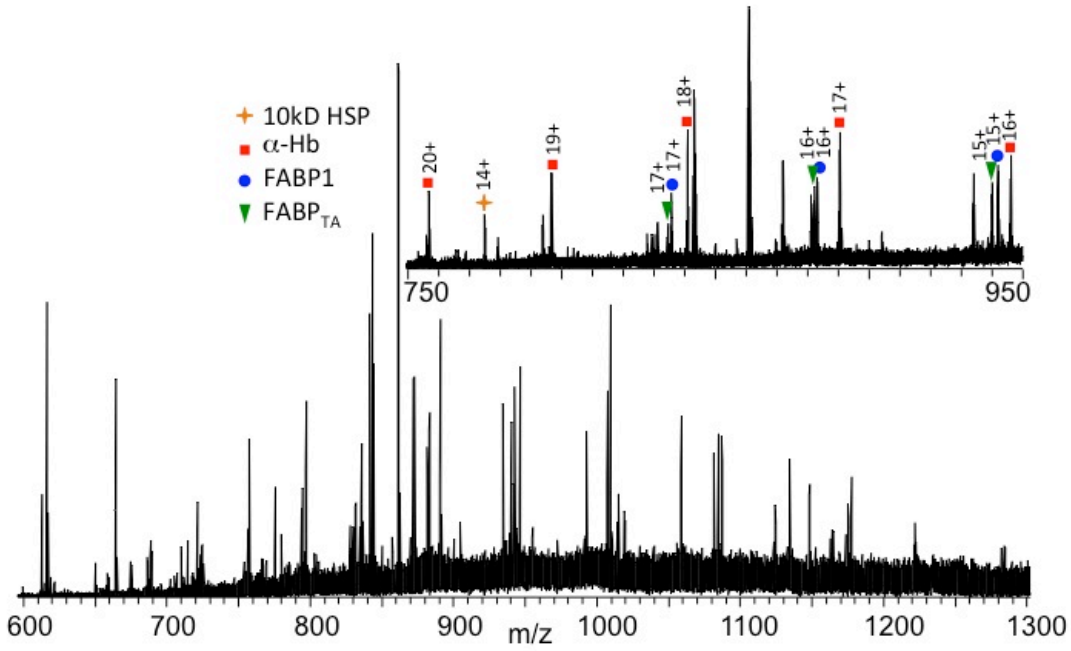

Figure 38: Spectra aquired using 50% acetonitrile + 0.1% FA as the solvent in a LESA protocol of non-dieased liver tissue section. Four protein signatures indicated are 10kDa heat shock protein (mitonchondrial), α-hemoglobin, FABP1 and FABP$_{TA}$.

Ions of *m/z* 775.42 (+14 charge state, MW$_{meas}$ 10836.8056 Da) observed in the LESA mass spectrum from non-diseased human liver tissue were selected and subjected to CID and ETD MS/MS. The CID and ETD product ions were processed using Xtract software to produce $[M+H]^+$ and were searched against the simple human database using Prosight PTM 2.0. [196]. The protein was identified as the mitochondrial 10 kDa heat shock protein (m-HSP) (MW$_{calc}$ 10836.8485 Da, Δ 3.96 ppm). All identified peaks are listed in Appendix 8 and 9. The spectra (Figure 39) were processed manually and 15 b ions and 21 y ions were identified from the CID spectrum resulting in 23% coverage. A coverage of 24% was achieved using ETD (2 a ions, 1 b ion, 17 c ions, 5 y ions and 10 z ions). Together a combined coverage of 40% was obtained (Figure 40). A peak

at this *m/z* was also observed in the LESA mass spectrum obtained from NASH tissue however its abundance was insufficient for MS/MS.

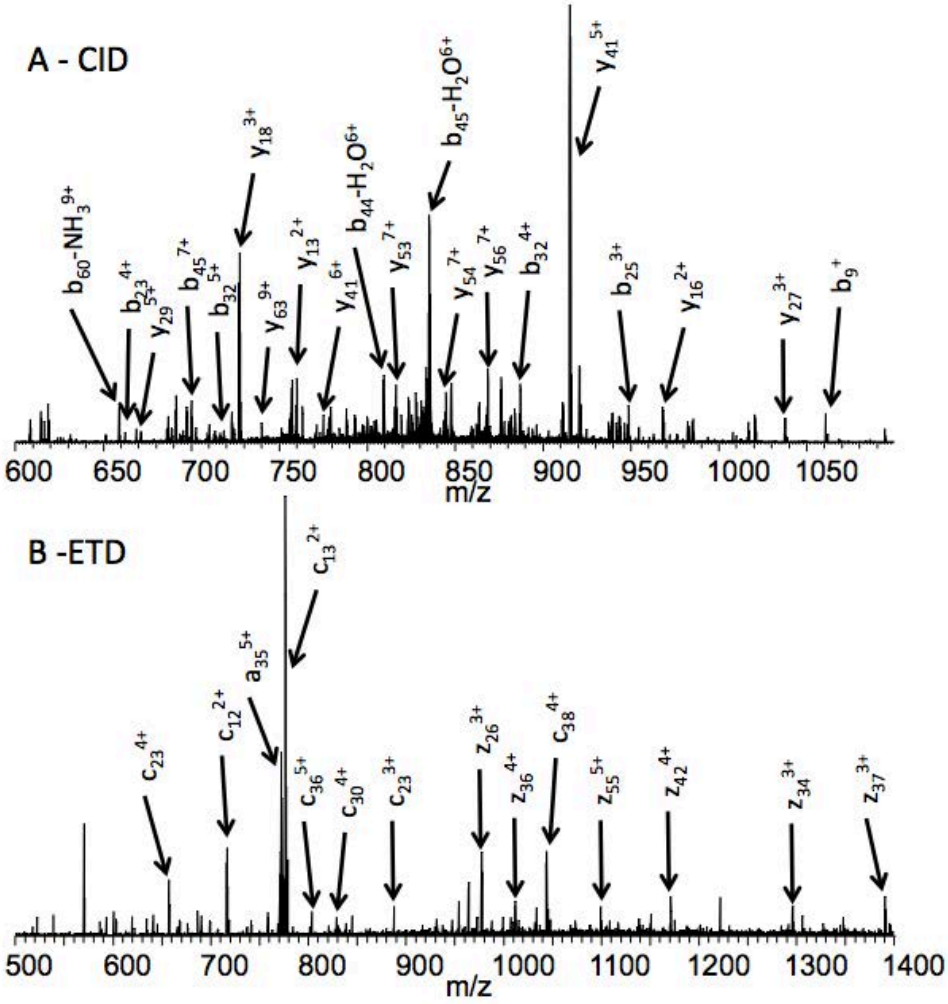

Figure 39: MS/MS spectra observed form the 10 kDa mitrocondrial heat shock protein using A) CID and B) ETD.

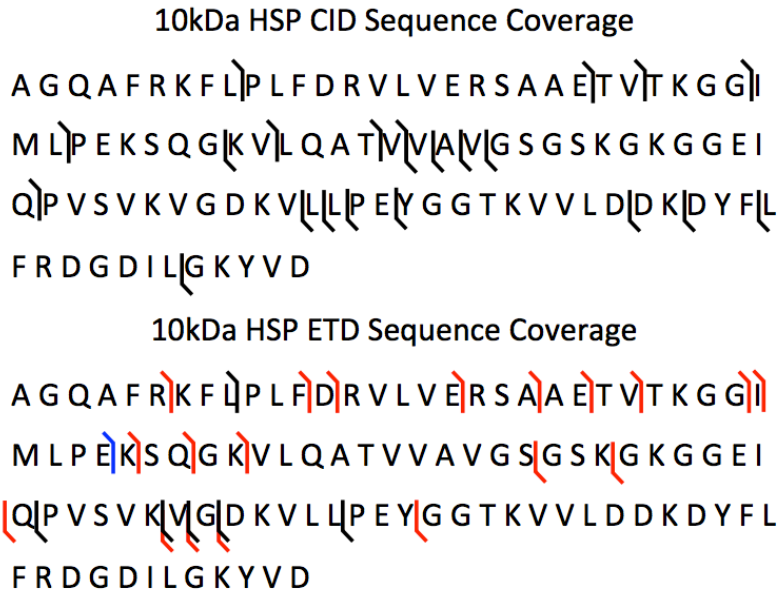

Figure 40: Protein sequence coverage of the 10 kDa mitochondrial heat shock protein determined from spectra aquired following CID (Top) and ETD (Bottom) fragmentation. b/y fragments are indicated using black markers, c/z fragments with red markers, and a fragments with blue markers.

Ions at *m/z* 946.40 (+16 charge state, 15117.9167 Da) observed in the LESA mass spectrum from non-diseased human liver tissue were selected for CID (Figure 41A). The CID product ions were processed using Xtract software to produce $[M+H]^+$ and were searched against the simple human database using Prosight PTM 2.0.

The protein was identified as alpha chain of haemoglobin (MW_{calc} 15117.8924, Δ 1.60ppm). The sequence coverage obtained using CID was 31% from 17 b ions and 52 y ions (Complete list of CID fragments is presented in Appendix 10). A peak was observed in NASH tissue at the same *m/z* and selected for ETD (Figure 41B). Again, the protein was identified as α-heamoglobin, with a coverage of 13% from 17 c ions and 6 z ions (Complete list of ETD fragments is presented in Appendix 11). Together a combined coverage of 42% was obtained.

Diagrams for the sequence coverage of the CID and ETD analysis are shown in Figure 42.

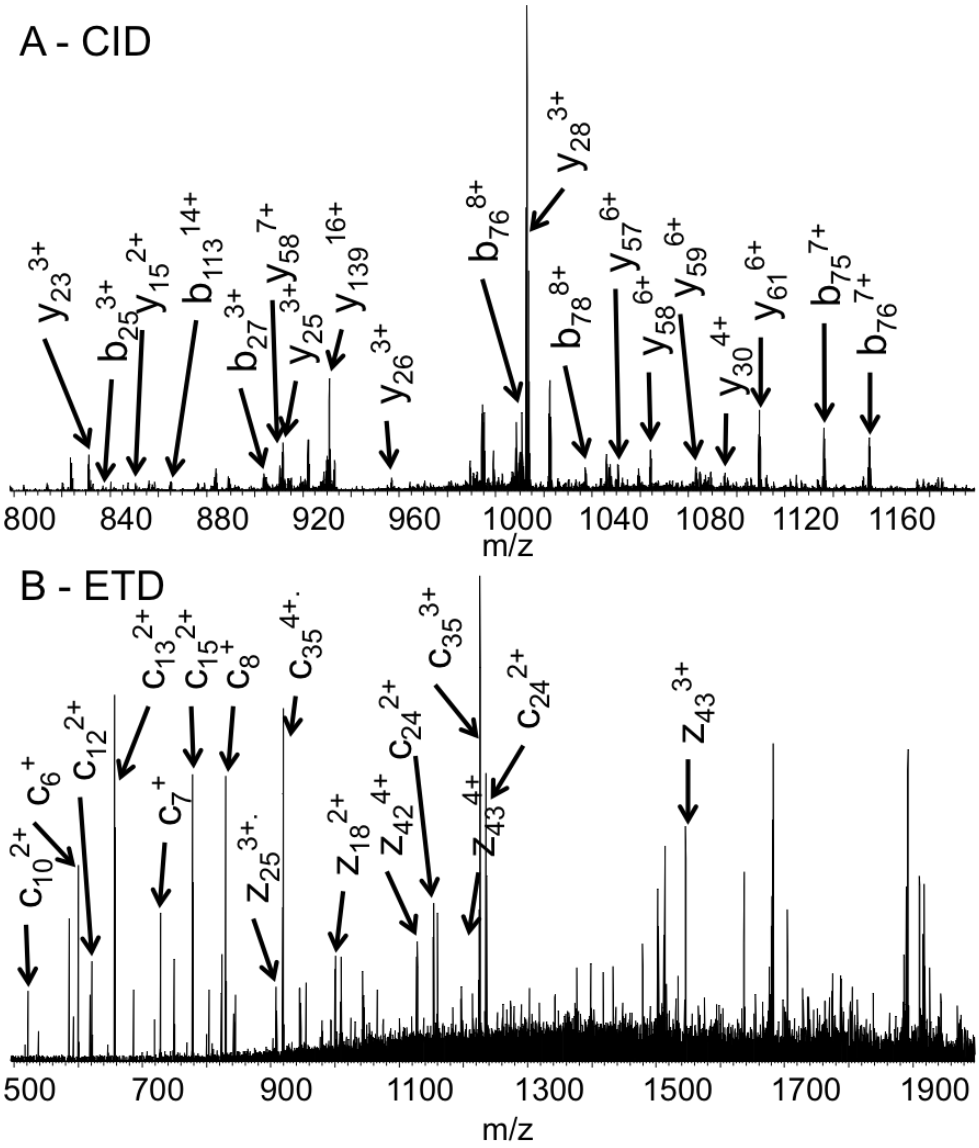

Figure 41: Enlarged regions of spectra aquired using A) CID and B) ETD of ions detected at *m/z* 946.40 identified as the alpha chain of heamoglobin

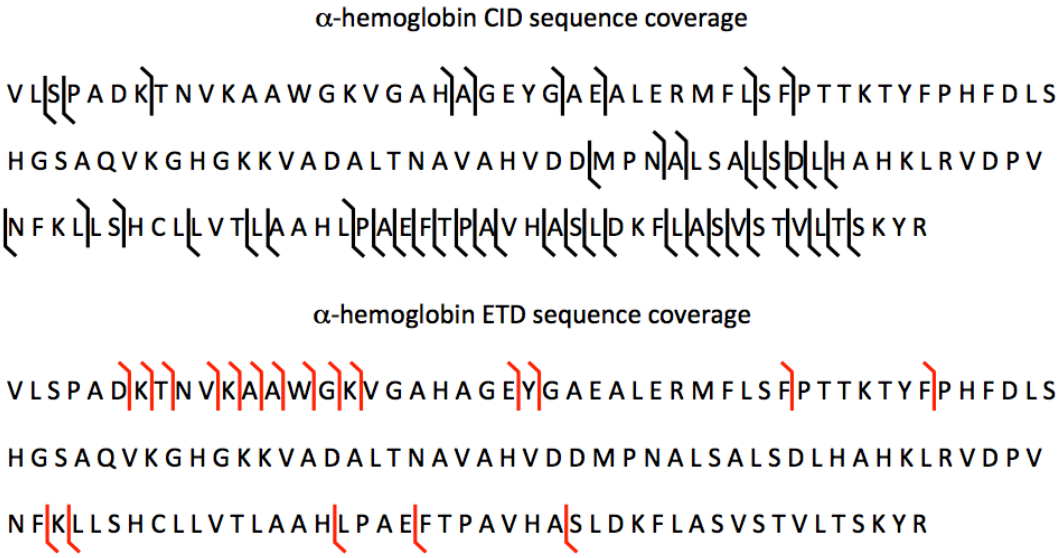

Figure 42: Amino Acid coverage of α-haemoglobin observed from CID and ETD fragmentation. b/y fragments are indicated using black markers, c/z fragments are red.

A protein of mass 14111.4161 Da was detected in a series of charge states from +10 to +16. This protein was observed in both non-diseased and NASH tissue sections. The +15 charge state (*m/z* 942.23) ions were selected from non-diseased tissue for ETD fragmentation. The +13 charge state (*m/z* 1087.04) ions from NASH tissue were selected for CID analysis. Different *m/z* values were targeted in the MS/MS experiments because for CID the most intense peak provided good separation from neighbouring peaks for optimum isolation. For ETD, a higher charge state was selected for optimum fragmentation. The CID and ETD product ions were processed using Xtract software to produce $[M+H]^+$ and were searched against the simple human database using Prosight PTM 2.0 (Complete list of fragments identified is presented in Appendix 12 and 13). The protein was identified as the liver-fatty acid binding protein (FABP1) (MW_{calc} 14111.3892, Δ 1.9 ppm). (Figure 43A and Figure 44A) The protein was observed

with the initiator methionine removed and an acetylation of the N-terminal amino acid. Manual analysis of the CID data identified 7 a ions, 48 b ions and 60 y ions resulting in a coverage of 47%. For ETD, 6 a ions, 44 c ions, 11 y ions and 26 z ions were identified resulting in a coverage of 38%. The combined coverage was 63%.

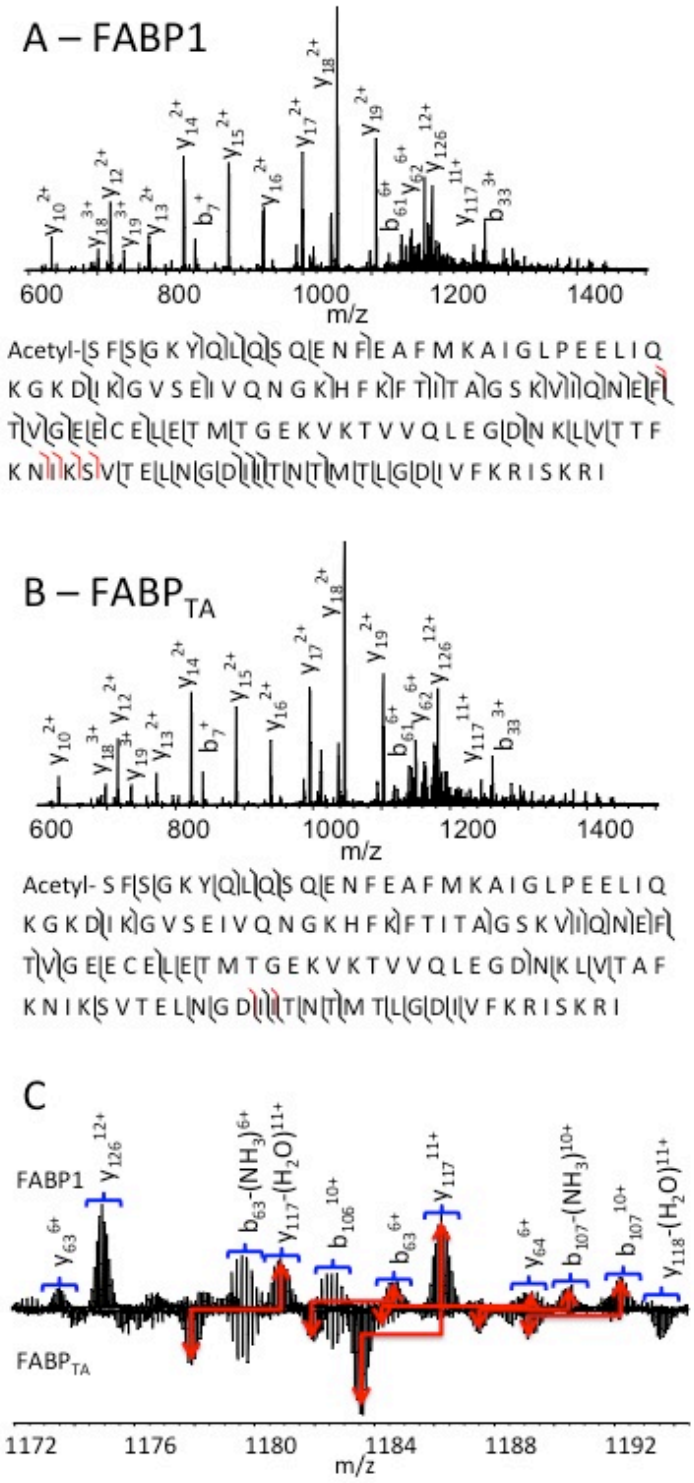

Figure 43: A) Enlarged region of the spectra observed from CID of ions found at *m/z* 942.24, and sequence coverage of the protien identified as FABP1. B) Enlarged region of the spectra observed from CID of ions found at *m/z* 940.29, and sequence coverage of the protien identified as FABP$_{TA}$. C) Illustration of the mass shift of fragments between the two proteins.

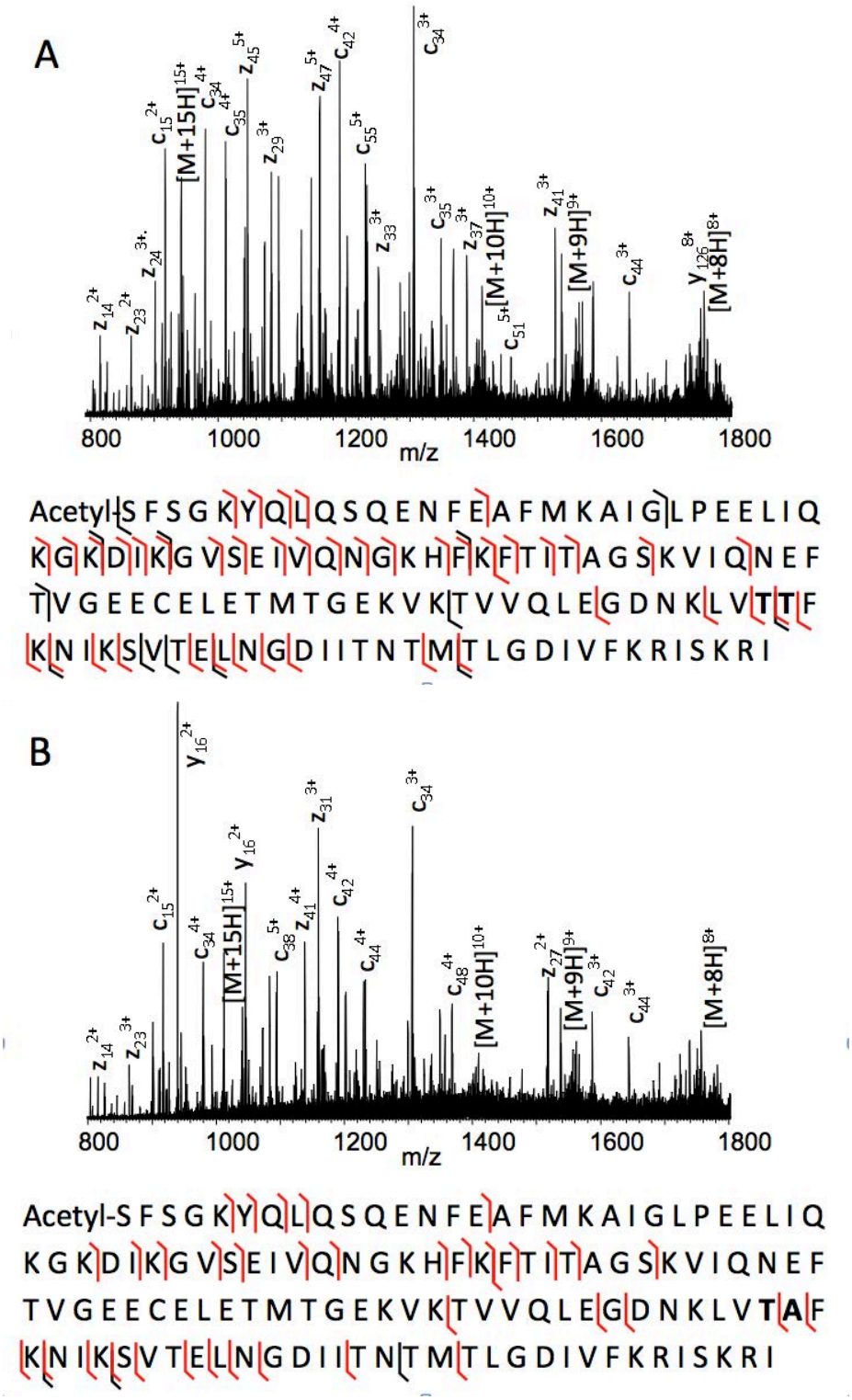

Figure 44: Enlarged region of the spectra observed from ETD of ions found at *m/z* 1087.04, and sequence coverage of the protien identified as FABP1. B) Enlarged region of the spectra observed from ETD of ions found at *m/z* 1084.04, and sequence coverage of the protien identified as $FABP_{TA}$.

The final protein that was identified by top-down mass spectrometry was the variant FABP1. This protein had a measured molecular weight of 14081.3600 Da and was detected in a series of charge states from +10 to +16. Peaks corresponding to this protein were observed in both non-diseased and NASH tissue sections. The +15 charge state (*m/z* 940.29) ions were selected from non-diseased tissue for ETD fragmentation. The +13 charge state (*m/z* 1084.04) ions from NASH tissue were selected for CID analysis. The different charge states were selected for the same reasons discussed above. The CID and ETD product ions were processed using Xtract software to produce $[M+H]^+$ and were searched against the simple human database using Prosight PTM 2.0. The protein was identified as the liver-fatty acid binding protein with the same N-terminal post translational modification, with a single acid substitution of the 94^{th} amino acid of Thr→Ala (MW_{calc} 14081.3687, Δ 0.6 ppm) (Figure 43B and Figure 44B) Manual analysis of the CID spectrum identified 2 a ions, 32 b ions and 46 y ions resulting in a coverage of 37%. For ETD 30 c ions, 3 y ions and 20 z ions were identified resulting in a coverage of 29%. (Complete list of fragments identified is presented in Appendix 14 and 15). The combined coverage was 52%. FABP1 and $FABP_{TA}$ were observed in both the non-diseased and NASH tissue sections. The study was expanded to include a further non-diseased and NASH tissue section from alternative donors. Figure 45 shows expanded *m/z* regions containing the +15 charge states of the FABP1 and $FAPB_{TA}$ and the +16 charge state of a-haemoglobin. It is clear to see that ions from the three molecules are not always detected. The FABP1 is observed in

both the non-diseased sections but only one of the NASH sections, whereas the $FABP_{TA}$ is observed in both the NASH sections but only one of the non-diseased sections. It has been demonstrated recently that $FABP_{TA}$ is linked to an increased risk of developing NASH. [181] It should be noted that the detection of the $FABP_{TA}$ in the non-diseased is not a direct indicator of NASH as there are other risk factors associated with the disease, such as diet, diabetes, ethnicity and gender. [225]

The non-diseased sections are also characterised by reduced signals for a-globin. This is due to the treatment of the tissue prior to freezing and sampling. One of the sections (Figure 45A) was from a liver rejected for transplantation due to a lesion on the exterior of the liver, the procedure to help preserve the liver and prevent organ rejection involved the liver being perfused with phosphate buffer to remove the donors blood. The other section is tumour resection margin; this means that a tumour was surgically removed with some of the surrounding tissue, and non-diseased regions were removed. During the surgical procedure it is likely that local haemolysis reduced the blood supply to the excised tissue.

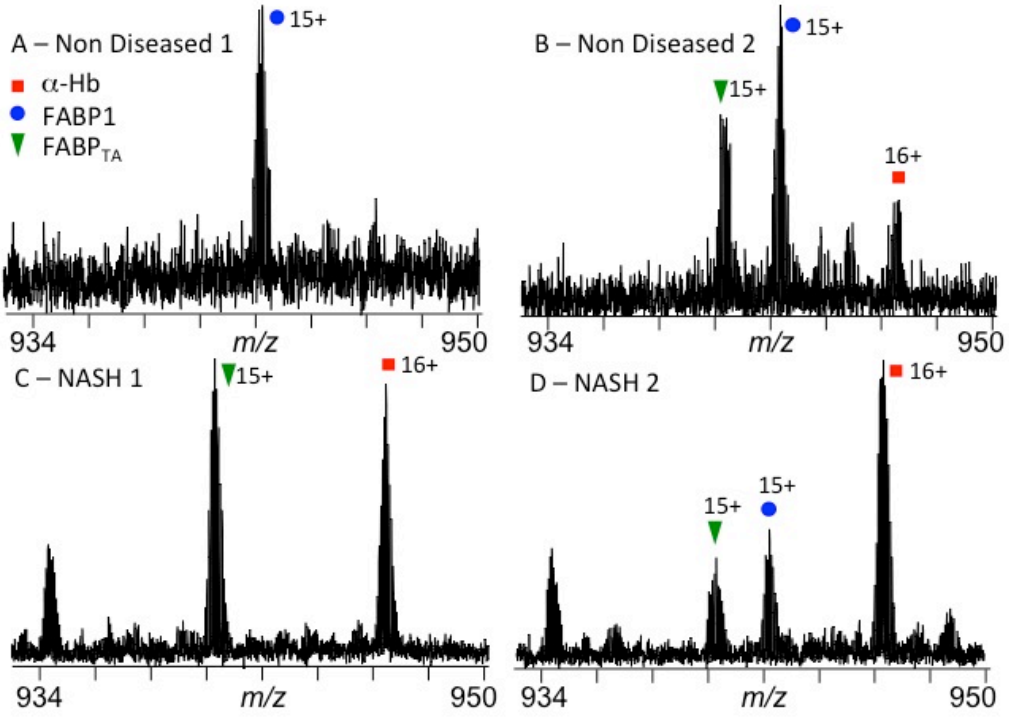

Figure 45: Enlarged regions of spectra aquired using a LESA protocol from four liver sections from different patients showing the relative abundance of three know proteins.

4.2.2. Automated extraction, digestion and LC-MS/MS analysis

Top down analysis has been used to identify four proteins extracted from human liver tissue. It is hypothesised that more proteins are extracted during LESA than are detected using direct infusion electrospray. To investigate this, bottom-up analysis was conducted. Bottom-up analysis has been shown to detect numerous proteins. For example, bottom-up analysis of dried blood spots using LESA identified over 100 proteins, [85] Here non-diseased human liver tissue was sampled using LESA with three different extraction solutions (50 mM $NH_4HCO_{3(aq)}$, 50% $MeOH_{(aq)}$, 70% $MeOH_{(aq)}$). The extracted intact proteins were subjected to an automatic digestion protocol described by Martin et al. [85] The digest was then analysed in duplicate via LC-MS/MS. In total 549

non-redundant proteins were identified, 464 from the 50mM $NH_4HCO_{3\ (aq)}$ extraction, 214 from the 50% MeOH extraction and 116 from the 70% MeOH extraction (Figure 46)

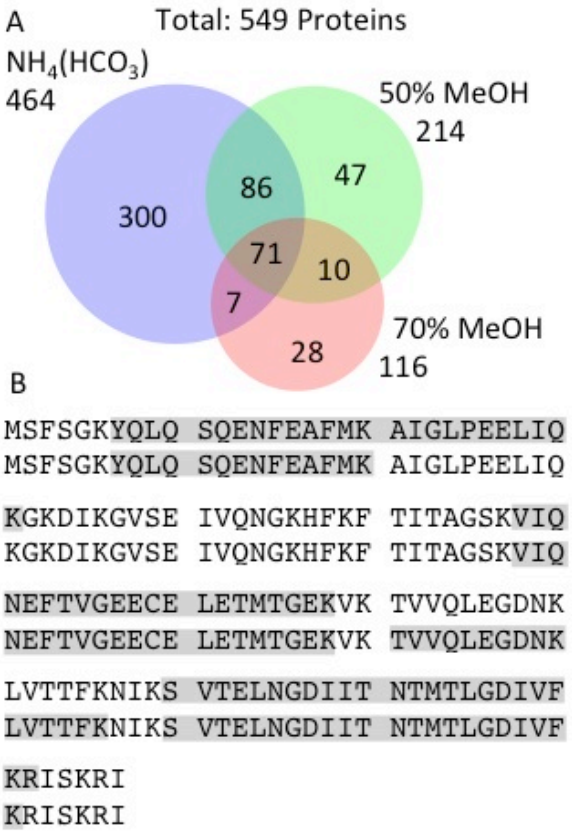

Figure 46: A) Venn diagram of the number of proteins identified using 3 extraction conditions. B) Amino ace sequence of FABP1 with highlighted regions of peptides identified from the two technical repeats of the aqueous extraction.

As expected, a substantially greater number of proteins were observed than detected by top-down methods (Typically 10-20 proteins (Appendix 16) proteins for direct infusion depending on extraction conditions and can increase to 34 protiens (Appendix 20) when using FAIMS (See chapter 5). There are two main reasons behind this. First the digestion process breaks down large proteins that were not detected into smaller peptides that are easier to detect.

The second is the chromatography that was used to separate the peptides, reducing the number of peptides entering the mass spectrometer at any time point during the analysis. This reduces ion suppression and increases the number of species detected. The MS/MS acquisition and data processing is mostly automated and provides an easy method to identify large numbers of proteins.

The ammonium bicarbonate extraction identified the greatest number of proteins. This is expected, because proteins are most soluble in water-based solutions. Work presented in earlier chapters of this thesis have shown that reducing the organic content of the extraction solvent increases the number of proteins detected, until a point where there is ineffective ionisation. It is interesting although not completely unexpected that there are proteins that are only detected in organic containing solutions. Proteins consist of polar and non-polar regions based on their function therefore it is likely that some proteins have larger non-polar region enhancing their extraction efficiency in organic-containing solvents. It may be that these proteins have a function in low aqueous regions of the cell, e.g., the lipid membrane. Not all proteins known to be present in liver were identified. With further optimization it may be possible to identify more proteins using the ammonium bicarbonate solution.

Three known biomarkers of liver disease were identified using all extraction conditions. These proteins were identified by at least one unique peptide in the current database. Gamma-glutamyltransferase (MW 77,329 Da) [202] was

identified with a maximum coverage of 32.90% from the ammonium bicarbonate extraction. Aspartate amino transferase was identified in two forms, the mitochondrial (MW 47,518 Da), and the cytoplasmic (MW 46,248 Da), both of which are associated with liver disease [176]. The homology between these two proteins is 68% (as calculated by BLAST http://blast.ncbi.nlm.nih.gov/Blast.cgi). The mitochondrial aspartate amino transferase was identified with maximum sequence coverage of 48.37% from ammonium bicarbonate extraction. The cytoplasmic aspartate amino transferase sequence coverage was 52.52% identified from the 50% methanol extraction. The fatty acid binding protein was also identified (FABP1) (MW 14208 Da) [181] and was observed in all extractions and in both repeats with a coverage of 53-57%. (Figure 47B and Appendix 17). The variant ($FABP_{TA}$) was not initially identified as it was not in the database. After manually entering the amino acid sequence for $FABP_{TA}$, the variant was identified in only one of the ammonium bicarbonate repeats.

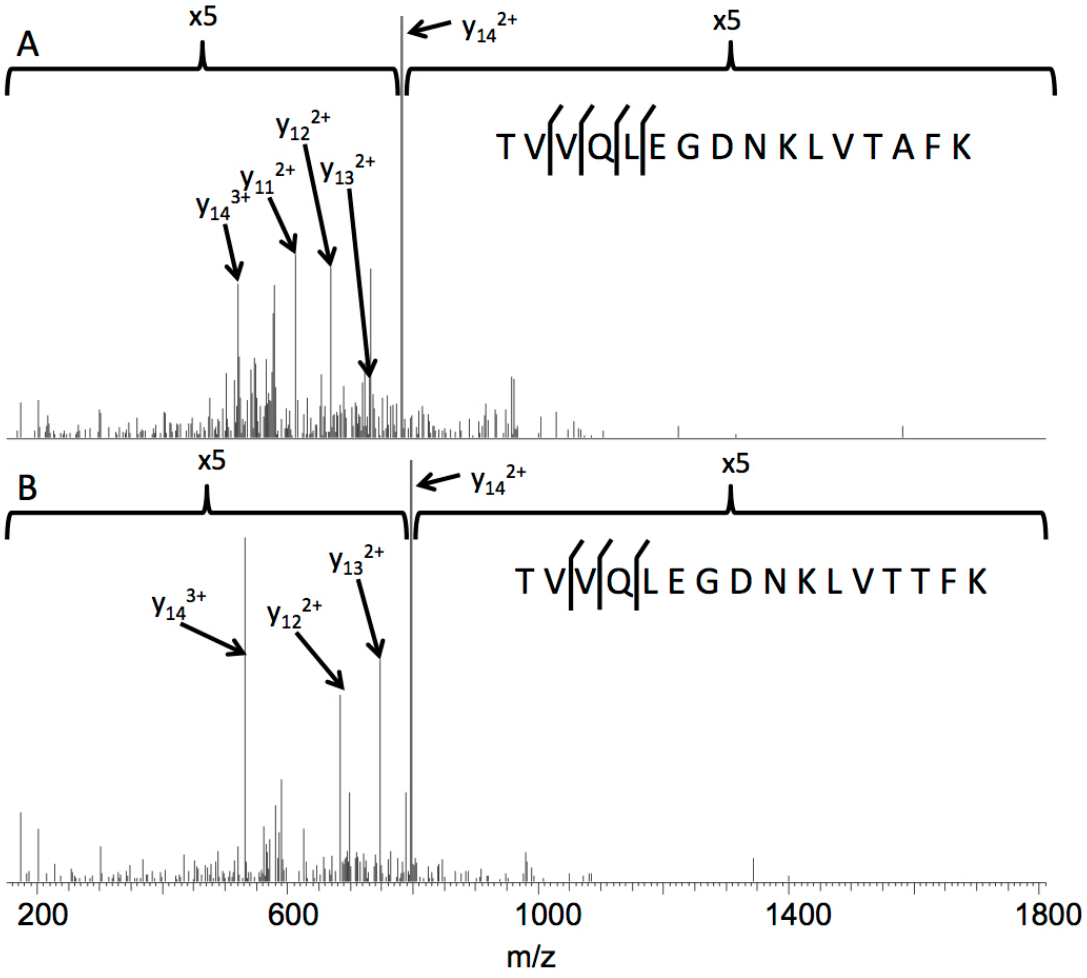

Figure 47: Spectra aquried during bottom-up analysis of non dieased human liver tissue. CID spectra of FABP peptide that distinguishes between $FABP_{TA}$ (A) and FABP1 (B).

It is possible that $FABP_{TA}$ is present in more than one extraction however these proteins only differ by one amino acid. The majority of peptides that are identified could be from either protein (FABP1 or $FABP_{TA}$). If the peptide containing the site of substitution is identified then the protein is considered to be detected. Due to the automatic acquisition it is possible that the peptide could be detected but not selected for fragmentation. Cross validation using accurate mass and retention time (collected from the one occurrence when it was identified) confirmed that the peptide relating to $FABP_{TA}$ was not detected

in the other replicates. The fragmentation of this significant peptide required to differentiate between the two peptides is poor, indicating that the bottom-up method of identification may be unreliable. It may be possible to improve the detection of this peptide by adding the peptide to an inclusion list to insure that if it is detected it is fragmented. Improving the fragmenting may be possible if the timing is optimised. Every peptide is eluted from the LC over a range of retention times. Typically fragmentation occurs when the peptide is first detected and meets minimum intensity limits, however conducting the fragmentation when the peptide is at its maximum would produce a better spectrum and more fragments may be detected.

4.2.3. Automated on-tissue digestion with LC-MS/MS

To try and improve the detection and identification of the differentiating peptide for FABP1 and $FABP_{TA,}$ as well as to increase the number of proteins detected, an on-tissue digestion protocol was developed. For optimum digestion, the trypsin needs to be held at 37 ^{o}C for 1 hour. [226] This requirement leads to the obvious problem of reagent evaporation: however it is possible to reduce the rate of dispensing so that it approximately matches the rate of evaporation and thereby maintaining a stable liquid micro-junction for extended periods of time. Using the conditions outlined in (section 2.7.3) liquid micro-junctions were maintained for 30 min while the tissue was heated to 35 ^{o}C. Tissue section was positioned on a glass slide mounted on a 96-well microtiter plate. The plate holder was then set to the maximum temperature

setting of 55 ^{o}C, this subsequently heated the glass to a temperature of 35 ^{o}C. This was measured by a thermometer placed on the glass slide. 35 ^{o}C is not the optimum temperature for trypsin digestion, which is 37 ^{o}C, but was sufficiently close for successful digestion. When this procedure is conducted twice, near ideal digestion conditions are met. Three extractions were conducted: 282 proteins were identified from the first extraction, 298 from the second and 127 from the third.

Literature also reports the use of multiple extractions to collect the digested peptides from a tissue surface using LESA in this case the trypsin was deposited by an inject printer and the digestion was conducted in an humid incubation chamber to prevent the droplet of trypsin from evaporating. LESA was then used to extract the peptides from the surface. [201] One, 5 and 10 extractions were pooled and although the methods are different the results show that for optimum protein extraction multiple extractions are required however there is a point at which no more proteins can be extracted. Here it was determined to be the 3rd extraction, which is within the same range as literature reports.

A total of 374 proteins were identified using this method. The FABP was one of the proteins identified with coverage of 35%, 53% and 25% for 1st 2nd and 3rd extractions respectively. The sequence coverage obtained are similar or less than those obtained following the digestion protocol described in Section 4.2.2. Combining all the extractions did not improve the coverage. Unfortunately the

important peptide to determining the variant was not identified, and upon manual inspection it was determined that these peptides were not detected.

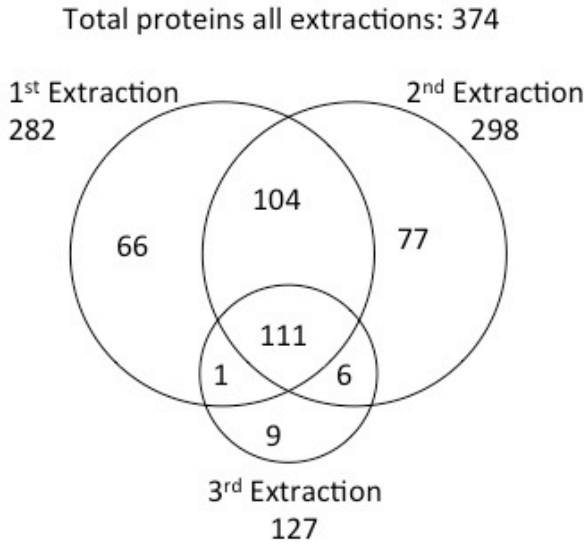

Figure 48: Venn diagram of proteins identified using on-tissue digestion

It was anticipated that a greater number of proteins would have been identified: The LESA process would only extracted the soluble proteins whereas, the on-tissue trypsin would have been exposed to all the proteins on the surface increasing the number of proteins that could be digested. This in tern should produce soluble peptides. On tissue digestions have previously used humidity chambers to control the digestion process. There are a number of possibilities that could prevent the effective digestion of proteins on tissue.

- The trypsin solution is stored in a microtitre plate. For the tissue to be heated to 35 ^{o}C ,the LESA plate holder is heated to 50 ^{o}C. The trypsin at the bottom of the well is exposed to higher than optimum temperatures for an extended period of time. That will increase the rate of denaturisation of the enzyme.

- The liver is protein rich. It is possible that the concentration of trypsin may be too low to fully digest the proteins from the region of tissue.

4.3 Conclusion

Top-down and bottom-methods have been successfully implemented to identify proteins using LESA from thin tissue sections. Top-down is capable of differentiating between the FABP1 and the $FABP_{TA}$ that differs by only one amino acid. Amino acid substitutions and post-translational modifications appear as mass shifts in a number of fragments allowing the substitution/PTM to be located. The restriction of top down analysis is that only a limited number of proteins are detected and the accompanying database search algorithms requires improvement. Bottom-up analysis has identified 549 proteins including several biomarkers for liver disease. FABP1 is also detected however due to the nature of bottom-up the peptide that distinguishes $FABP_{TA}$ from FABP1 is not always detected in a sample that is known to contain both. Furthermore poor fragmentation of this peptide means that accurately pinpointing the modification is more difficult.

Top-down and bottom up are very different approaches to identifying proteins. Top-down coverage is defined as the percentage of cleavages between each amino acid, whereas bottom-up coverage is the percentage of peptides that have been identified even if the peptide has only a few fragments. This makes direct comparison of the efficiency of these two techniques difficult however the quality of information can still be compared. In the case of FABP1 and

$FABP_{TA}$, top-down is a more effective method for identifying these proteins due to the ease at which they can be recognised and the substitution confirmed. Nevertheless, not every protein can be identified using top-down mass spectrometry and it may be necessary to implement bottom-up identification in order to observe the protein.

Chapter 5: Liquid extraction surface analysis mass spectrometry coupled with ultra-high field asymmetric ion mobility spectrometry for the analysis of intact proteins from mouse tissue

Work presented in this chapter has been published as an article in Analytical Chemistry [vol. 87, p.6794-6800 2015], on which I am first author. The article was written in collaboration with my supervisors. (Appendix 18)

5.1 Introduction

Methodology for the analysis of biological systems by mass spectrometry uses separation techniques, such as liquid chromatography and ion mobility. Often these techniques increase the time taken for analysis. Exceptions are the TWIMS, which will be discussed in chapter 6 of this thesis, and the recently developed ultra-high field asymmetric ion mobility spectrometry. [161, 162]

Recent developments in surface sampling have included the development of liquid extraction surface analysis (LESA). This method is an automated solid-liquid extraction of analytes from a surface with electrospray solvent. [227] Chapter 3 demonstrated the ability of LESA mass spectrometry to detect lipids and proteins directly from human liver tissue at specific locations and the use of optimised solvent systems to target specific analyte groups. Protein analysis by LESA mass spectrometry was explored in Chapter 4: a comparison of top-down and bottom-up methods for protein identification was conducted. The results

showed that there were a vast number of proteins that are not detected but are successfully extracted using LESA.

The work in this Chapter seeks to extend the range of species that can be detected and identified in a single injection. To achieve this objective, FAIMS (high field asymmetric waveform ion mobility spectrometry) has been coupled to LESA extraction to conduct a real time separation of lipids and proteins.

The ultraFAIMS device replaces the inlet cone of the Orbitrap mass spectrometer, (Figure 49) and enables separation of ions in real time. A chip is supported in the middle of the inlet cone, an alternating field is applied to the chip inducing a separation of the ions due to the differing mobilities of ions in high and low electric fields. The ultraFAIMS device can be operated in three modes: static analysis in which the compensation field and dispersion field are kept constant; 1-D FAIMS analysis in which the dispersion field is kept constant and the compensation field is varied; and 2-D FAIMS analysis in which both the dispersion field and the compensation field are varied. In this work, the ultraFAIMS device was operated in static mode and in 2D mode.

The work presented in this chapter is the first reported instance of the coupling of the ultraFAIMS with the LESA. This is also the first report of lipid and intact proteins being detected through the ultraFAIMS from a biological sample.

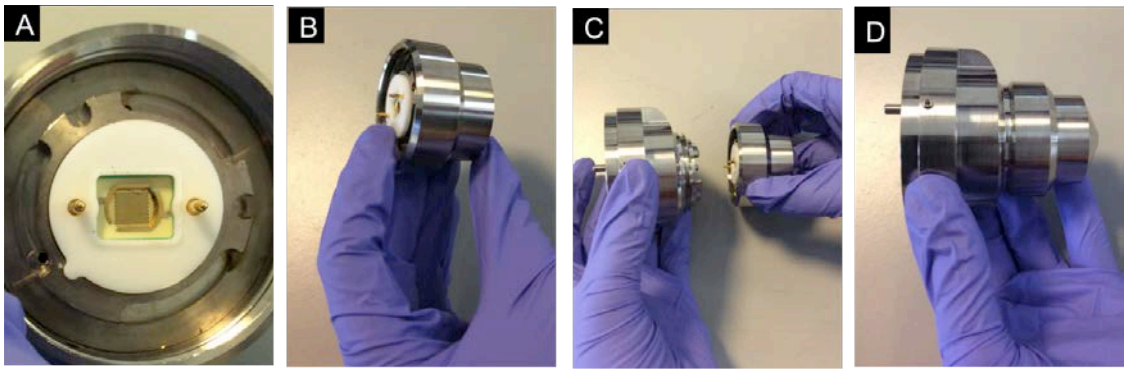

Figure 49: A) Photograph of the ultraFAIMS chip in the holder. B) Photograph of half of the ultraFAIMS cone, with the chip and electrodes visible C) Photograph of both halves of the ultraFAIMS cone not connected D) Photograph of the whole ultraFAIMS cone ready to be connected to the ESI inlet.

5.2 Results and discussion

The ultraFAIMS chip was mounted in an ESI inlet cone designed to couple with the Orbitrap mass spectrometer. The chip is held in the path of the ions and the ions traverse the chip through the shortest dimension. Due to the length of the cone and the need to attach electronics to the chip, the LESA is mounted 4.2 cm further away from the instrument (Figure 50) than in the standard set-up. LESA was conducted on thin tissue sections of mouse brain and liver, which were thaw mounted onto glass slides. The electrosprayed sample passes through the ultraFAIMS chip.

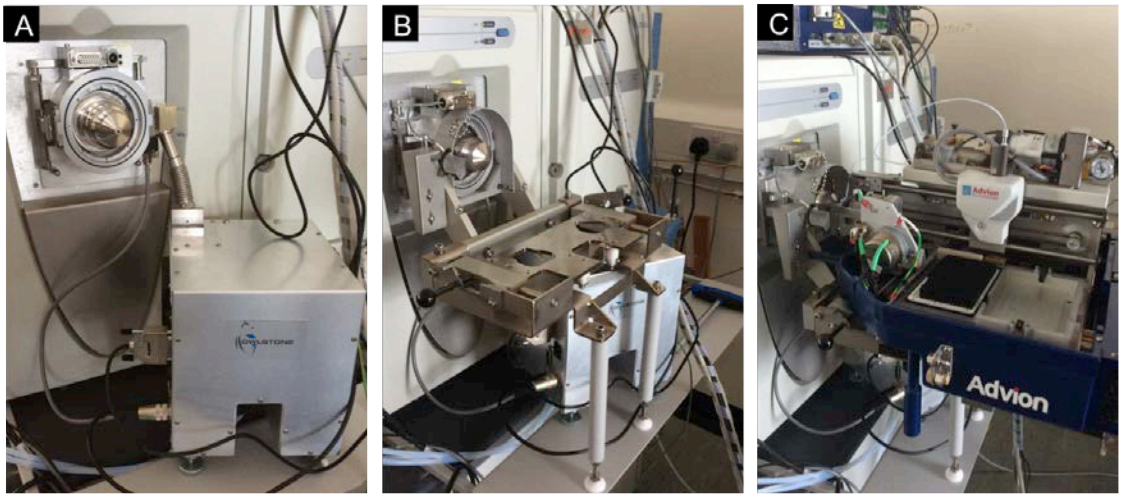

Figure 50: A) Photograph of the ultraFAIMS and electronics attached to an Orbitrap Velos ESI inlet B) The same as panel A with the addition of the Triversa mount C) A photograph of the set up of the Triversa with the ultraFAIMS

5.3 Spectral Quality

5.3.1. Two dimensional FAIMS analyses

5.3.1.1 Mouse Liver

Thin tissue sections of mouse liver were thaw mounted onto glass slides and placed into the Triversa Nanomate platform. The tissue was sampled by LESA and a 2-D FAIMS analysis was performed. The 2D FAIMS analyses were conducted 3-5 minutes after sampling and initiation of electrospray in order to enable the electrospray current to stabilise. 2D FAIMS analyses consist of eight discrete dispersion fields (DF): 130 Td to 270 Td in 20 Td steps. At each DF, the compensation field (CF) was swept between -1 Td and 4 Td shown. Each mass spectrum comprises a single scan, ensuring the data was collected at the fastest possible rate.

Using the ultraFAIMS there is a reduction in signal intensity, by about an order of magnitude. However, the spectra are comparable between these two conditions this is to be expected, as there is a longer path length for the ions to travel prior to entering the vacuum of the mass spectrometer. The LESA bracket is extended by 4 cm to allow for the longer inlet cone, no other features are changed, a picture is shown in Appendix 19.

The total ion chromatogram obtained following LESA 2D FAIMS analysis of mouse liver is shown in Figure 51. The results show that there is a general decease in the maximum intensity of the total ion chromatogram (TIC) at higher DF values. There is also a greater range of CF values in which ions are transmitted, indicating greater FAIMS separation of ions at higher DF values. At a DF of 130 Td, ions are detected between CF values of -1 Td and 2.2 Td, whereas at 270 Td ions are detected at all CF values.

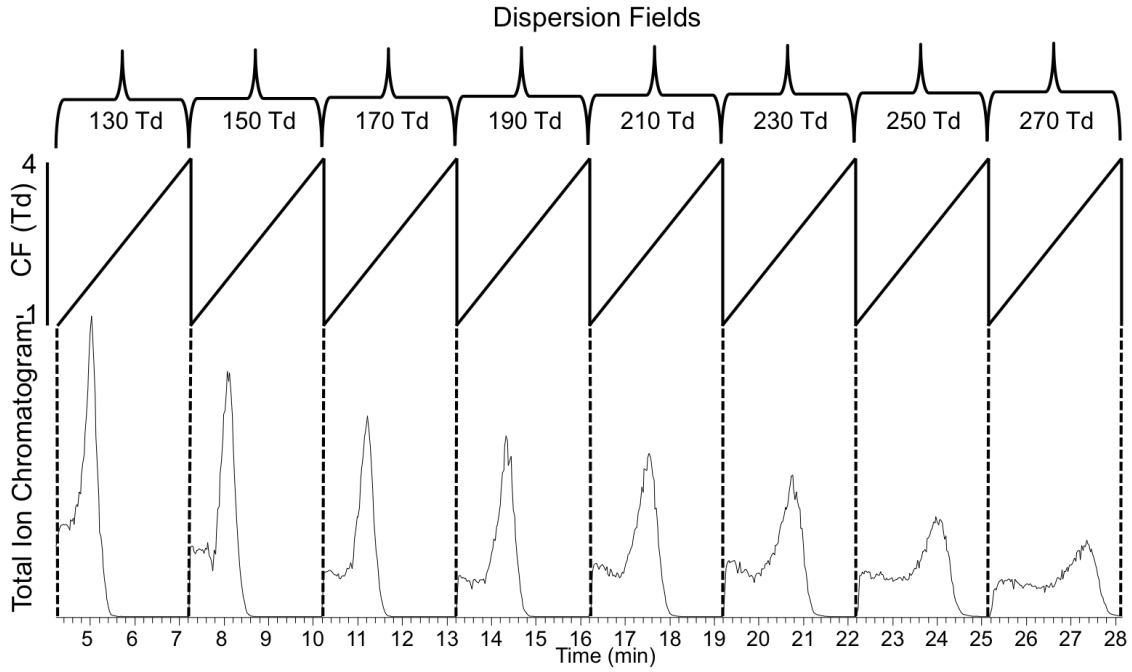

Figure 51: The total ion chromatorgtam of a 2D sweep, aquired using an extraction solvent of 70% methanol + 0.1% formic acid in a LESA protocol of mouse liver tissue.

At each DF step there are two features observed in the TIC. Figure 52D shows TIC obtained for DF step 270 Td) and the corresponding mass spectra at various CFs. The ions transmitted at CF of -0.48 Td are observed in the first feature of the TIC (Figure 52A). These ions contribute to the background noise of a typical LESA mass spectrum of tissue in the absence of FAIMS. The possible identities of these ions are large unresolved proteins however they cannot be characterised. Shvartsburg et al. showed that larger proteins (> 30 kDa) are transmitted through the ultraFAIMS at lower CF values as a result of dipole alignment [228]. The second peak in the TIC (Figure 52B) corresponds to well-resolved smaller proteins of <16,000Da (Appendix 20). The ions that elute at the

end of the CF sweep are singly charged ions made up of predominately lipid species. (Figure 52C)

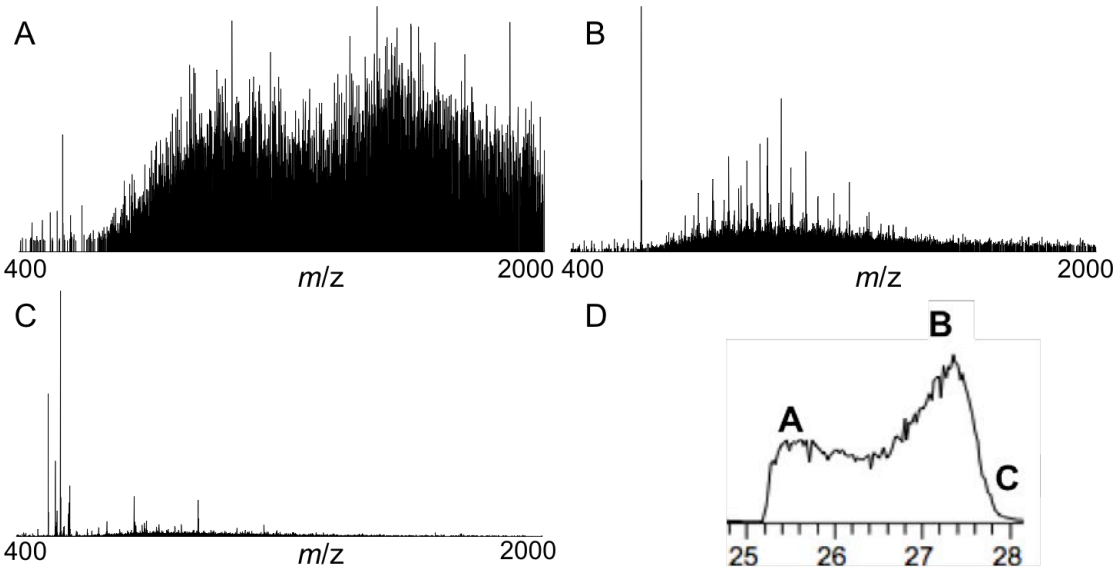

Figure 52: Representative spectra from 3 different CF values during a sweep at DF of 270 Td. A) Spectra observed from location A in the TIC shown in panel D. B) Spectra observed from location B in the TIC shown in panel D. C) Sepctra observed from location C in the TIC in panel D. D) TIC observed from a DF of 270 with CF values from -1 to 4 Td, with markers of the location of the spectra presented in panels A-C.

The order in which ions are observed, that is, signals that have not been characterised, lower MW proteins, small molecules, in a single CF sweep is the same. At a DF of 130 Td the transmission of these species overlap with each other whereas at a DF of 270 Td the separation is greater however the intensity of the ions is reduced.

FAIMS conditions for the transmission of lipids and proteins differ. For lipids, the optimum conditions were DF of 130 Td and a CF of 0.87 Td (Figure 53A). The optimum conditions for transmission of proteins were DF of 270 Td and a CF of 2.62 Td (Figure 53B). The mass spectrum obtained using the ultraFAIMS

is more informative than the spectrum obtained in the absence of FAIMS field. A comparable single scan spectrum (Figure 53C) shows very few peaks and none that are associated with proteins. Combining scans to create an average spectrum is common practice. Co-adding 37 microscans (~1min of data acquisition) (Figure 53 D) improves the spectral quality when the ultraFAIMS is not applied however it is still insufficient to match the quality with the ultraFAIMS field applied.

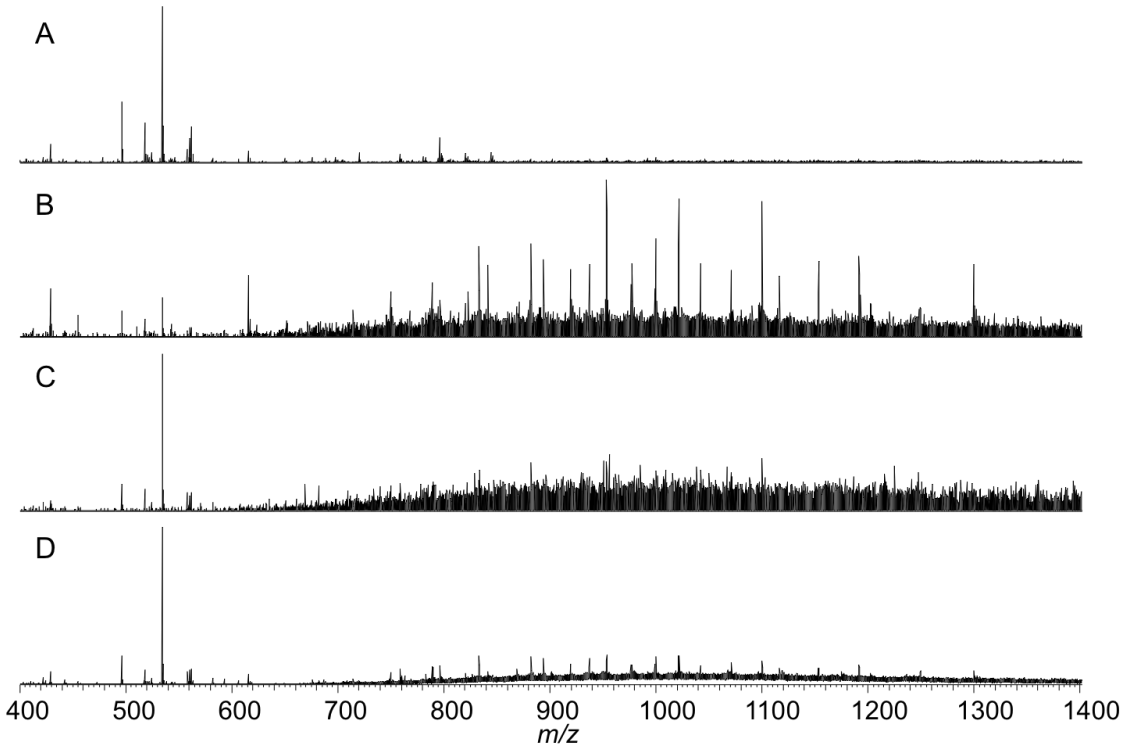

Figure 53: A) Optimum single scan spectrum using the ultraFAIMS showing Lipids and single charged molecules. B) Optimum single scan spectrum using the ultraFAIMS showing proteins C) Equivalent single scan spectrum without the ultraFAIMS D) spectrum without the ultraFAIMS produced from co-adding 37 microscan spectra (1min on analysis)

The signal to noise ratio of a particular peak can be calculated using the noise value that is allocated to each peak by the Xcalibur software algorithm and the absolute signal intensity for each peak. Table 5-1 compares the signal intensity,

the noise value and the calculated signal to noise value for six peaks. Three of the peaks correspond to the most abundant protein ions (*m/z* 1099.9689, *m/z* 1021.4731, *m/z* 883.1610) and the remaining three are lipid peaks (*m/z* 796.5205, *m/z* 720.4169, *m/z* 496.3398). To minimise any variations arising from sampling differences, the values given in Table 5-1 are taken from the same extraction.

Table 5-1: Signal to noise ratio of peaks with and without the ultraFAIMS field

m/z	**Not applying the ultraFAIMS field**			**Applying ultraFAIMS field**		
	Signal	**Noise**	**Ratio (s/n)**	**Signal**	**Noise**	**Ratio (s/n)**
1099.9689	3096.8	315.4	9.8	1164.5#	34.99#	33.3
1021.4731	3740.1	296.5	12.6	1420.3#	33.5#	42.4
883.1610	2505.9	218.8	11.5	1116.8#	28.7#	38.9
796.5205	2399.3	191.9	2.5	1195.4*	22.0*	54.3
720.4169	337.2	138.0	2.4	476.2*	21.1*	22.5
496.3398	3818.9	60.3	63.3	2844.5*	18.98*	149.7

#Using a DF of 270 Td and a CF of 2.62 Td (Optimum protein analysis), *Using a DF of 130 and a CF of 0.87 (Optimum lipid analysis).

As previously mentioned, generally absolute signal intensity is reduced in the presence of the FAIMS device. This observation is the result of both the physical presence of the FAIMS grid (ions collide with the chip and are neutralised) and ion diffusion between the electrodes. There is one exception in the present case: the peak at *m/z* 720.4169 has higher absolute signal intensity when the ultraFAIMS field applied. This observation may be the results of the

competitive nature of the detection and the use of automatic gain control in the Xcalibur software. By removing competing ions, a larger proportion of the total ions detected are those with *m/z* 720.4169. There is an overall reduction of absolute signal by about half, however, significantly, there is a more than 3 fold reduction in the noise in all examples, and in most cases there is over 7 fold reduction in noise. This leads to an increase in the signal to noise ratio of up to 22 fold. The signal to noise of the protein signal typically shows over a 3-fold improvement. The UltraFAIMS can be used to separate haemoglobin related ions from small peptides. At a DF of 270 Td and a CF of 2.6 small peptides were transmitted and were observed at a higher intensity than haemoglobin ions, which are typically the dominant species in mouse liver.

5.3.1.2 Mouse Brain

Mouse liver and brain were both analysed via ultraFAIMS. The data acquisition for mouse brain was more difficult. This could be because brain tissue has a particularly high concentration of salts that are used to transmit signals along neurones. For signalling along a neuron an ion gradient is formed using potassium, sodium and chlorine. The creation of electrical potential imbalance and the neutralisation of this create a pulse that travels the length of the neuron. These salts are typically contained within the cell or the myelin sheath surrounding the cell, during section the salts are exposed on the surface. [229] Furthermore the myelin sheath is an extension of the phospholipid membrane increasing the amount of lipids in brain tissue. [187, 230] High concentrations of

lipids and salts prevent proteins from being observed in the spectrum, and causes what visually appeared to be effective extraction using the LESA, the electrospray current temporally drops resulting in gaps in the 2D FAIMS spectrum (Figure 54).

For brain tissue it was necessary to wash the tissue using an 80% ethanol LESA extraction prior to analysis with 40% acetonitrile and allow sufficient time between washing and sampling for the tissue to dry. The trends observed in the mouse brain were similar to that observed in the mouse liver. In a separate experiment conducted using the same conditions, a repeat of the CF sweep at DF 270 Td was conducted in order to acquire a more complete sweep when the spray was more reliable. The single scan data from this sweep is shown in Figure 55. As with the mouse liver analysis there are two features in the FAIMS spectrum, the first feature at a CF of -0.6 Td comprising of non-characterised signals. The second feature at CF of 1.5 Td comprising smaller proteins however these are not clearly observed above the noise. Clear proteins signatures are observed at a CF of 2.6 Td. Lipids are not observed in this experiment due to the washing system and the solvent system used for extraction (50% Acetonitrile)

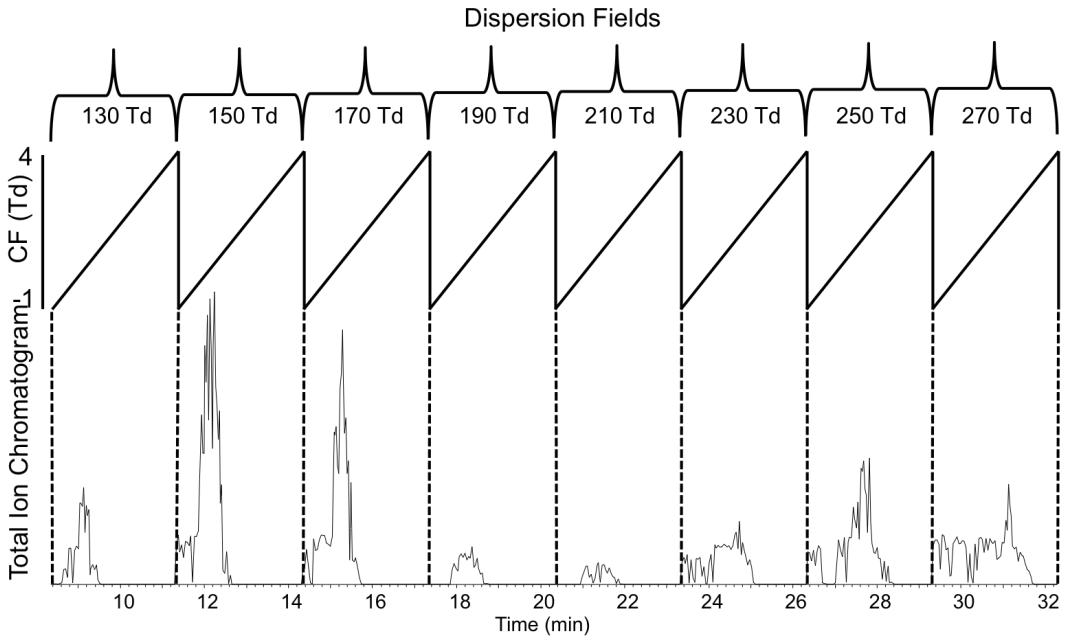

Figure 54: The total ion chromatorgtam of a 2D sweep aquired using an extraction solvent of 50% acetonitrile + 1% formic acid in a LESA protocol of mouse brian tissue.

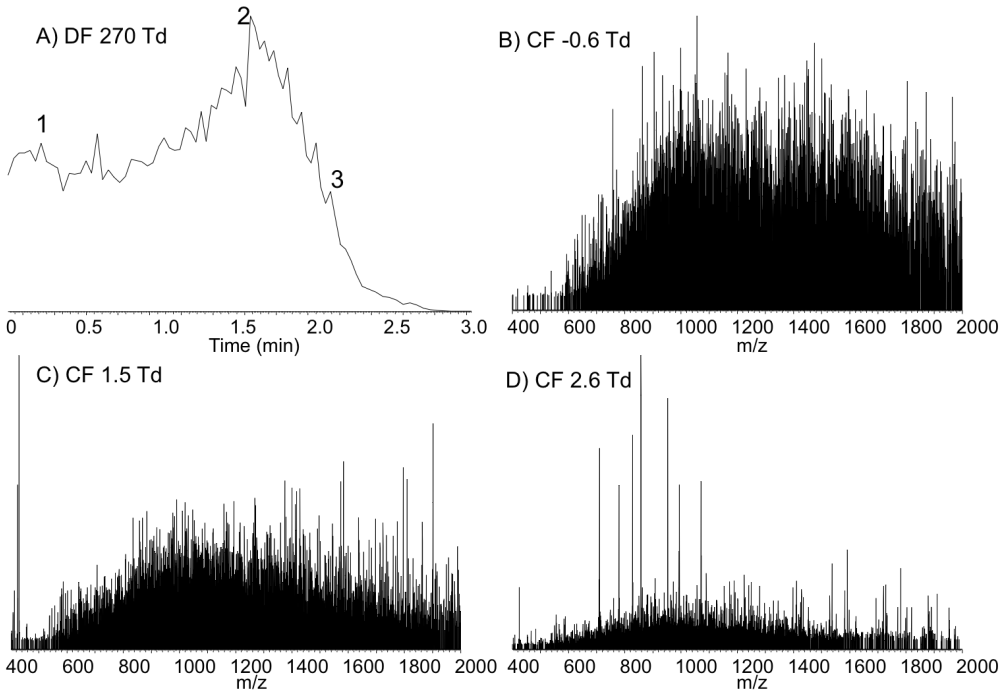

Figure 55: A) Single CF from -1 to 4 Td sweep at a DF 270 Td from mouse brian. B) Single scan with a CF of -0.6 from location marked 1 from panel A, C) Single scan with a CF of 1.5 from location marked 2 from panel A. D) Single scan with a CF of 2.6 from location marked 3 from panel A.

5.3.2. Static analysis

Static analysis using the ultraFAIMS involves maintaining a single DF and CF for the duration of the experiment. Thin tissue sections of mouse brain were sampled by LESA and subjected to a 2D FAIMS analysis as described above. The 2D FAIMS analysis enabled the optimum conditions for transmission of protein ions to be determined. A subsequent static FAIMS analysis was performed at a DF of 270 Td and a CF of 2.6 Td, allowing scans acquired under the same conditions to be co-added. (Figure 56)

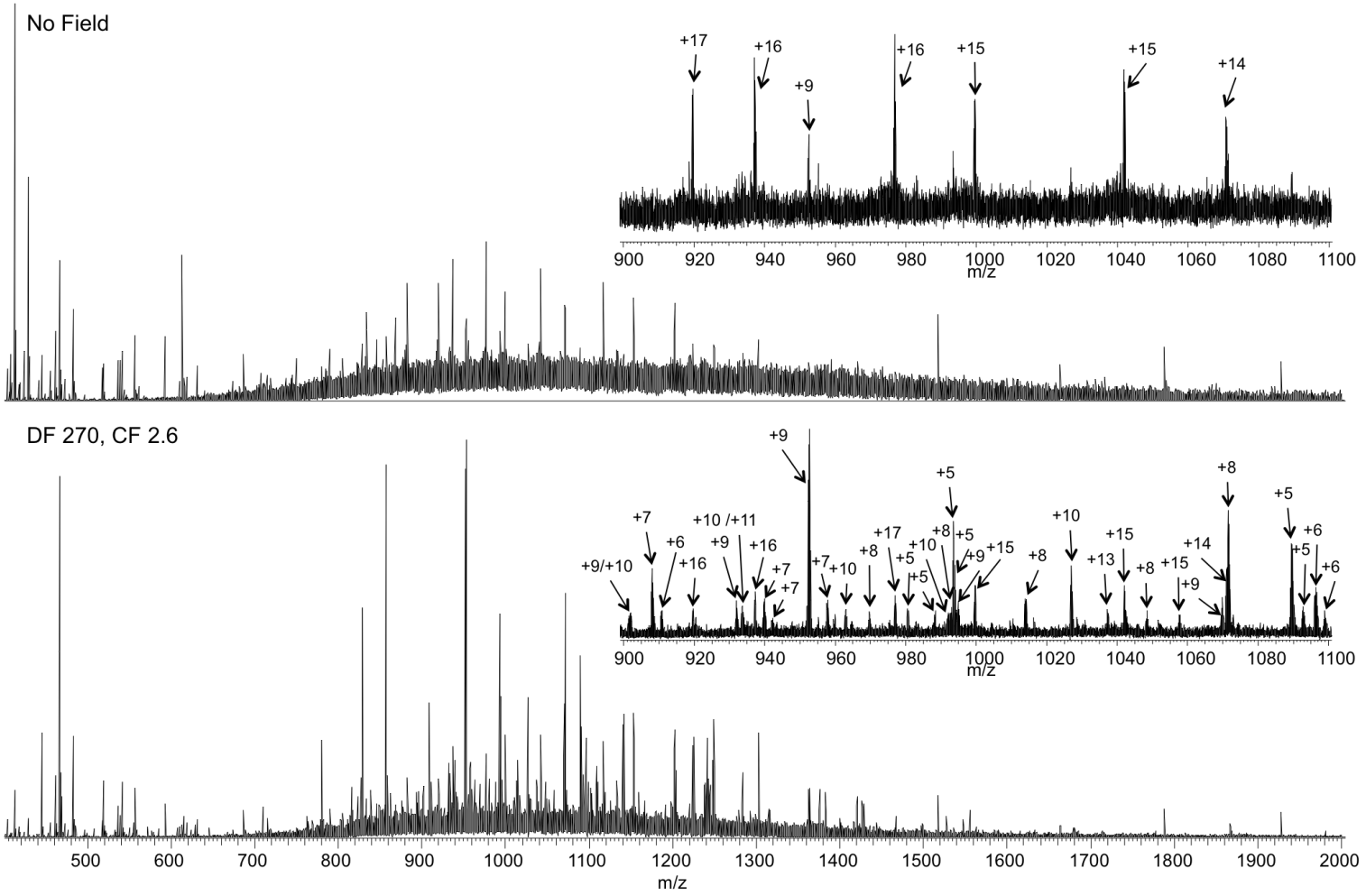

Figure 56: Spectra acquired for 1 min using 50% acetonitrile +1% FA as the solvent in a LESA protocol of mouse brain tissue. Analysis was conducted through the ultraFAIMS devices without a field applied (top) and with a field applied at a DF of 260 Td and a CF of 2.5 Td. (bottom)

The mass spectra shown in Figure 56 are the result of one min of data acquisition. The comparison mass spectrum (Figure 56 top) was recorded in absence of the ultraFAIMS field. In the absence of the ultraFAIMS field peaks corresponding to the charge state envelopes of three proteins were observed, whereas in the presence of FAIMS field, peaks corresponding to the charge state envelopes of 39 proteins were observed (Appendix 21). The monoisotopic masses of the proteins were between 4895 Da and 15839 Da. Monoisotopic masses were calculated using the Xtract function in Xcalibur software (Thermo, M mass mode and a minimum s/n 3). The majority of the additional proteins detected were small proteins below 10,000 Da. The brain is particularly rich in peptides and small proteins because they are used in signalling and regulation. [231] Many peptides are also able to cross the blood brain barrier and being able to detect these molecules is particularly usefully for progressing understanding of brain function [232, 233]. Larger proteins were also observed: two of these were identified as the alpha and beta subunits of haemoglobin. These also make up two of the three proteins observed in the absence of the ultraFAIMS field. Work presented earlier in this thesis showed that high concentrations of haemoglobin could inhibit the detection of less abundant proteins (Chapter 3).

Static FAIMS analysis can also be used for fragmentation, where longer analysis times aid in optimum detection, see below.

5.4 Fragmentation of ions detected using the ultraFAIMS

Proteins ions transmitted via the ultraFAIMS were subjected to top-down mass spectrometry. Two unknown peaks were isolated and fragmented from mouse tissue, one observed in mouse liver, *m/z* 1021.47 (14+ charge state, MW_{meas} 14279.4328) and one observed from mouse brain *m/z* 952.63 (9+ charge state, MW_{meas} 8560.6457). Both were subjected to ETD, CID and HCD MS/MS.

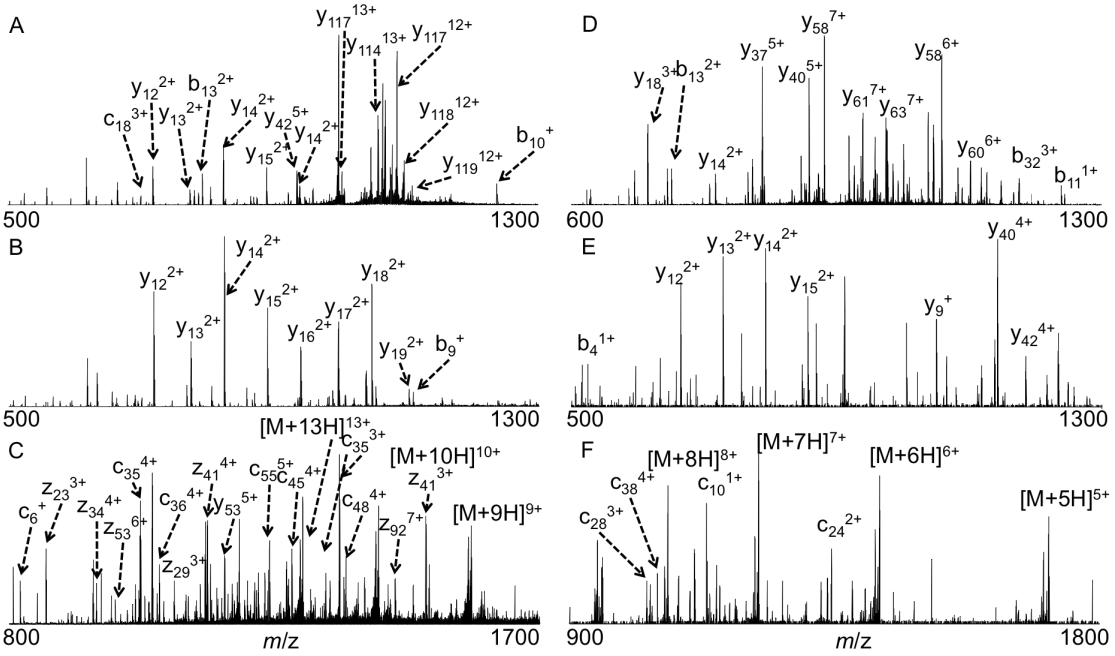

Figure 57: Spectra aquired using 70% methanol + 0.1% FA as the solvent in a LESA protocol of mouse liver with a DF of 130 Td and a CF of 0.3 Td. CID (A), HCD (B) and ETD (C) fragmentation of *m/z* 1021.47 identified as liver fatty acid binding protein. Spectra aquired using 50% acetonitrile +1% FA as the solvent in a LESA protocol of mouse brain with a DF of 270 Td and CF of 2.6 Td. CID (D), HCD (E) and ETD (F) fragmentation of *m/z* 952 identified as ubiquitin.

Work presented earlier in this thesis on human liver showed that the abundant proteins detected using LESA mass spectrometry were fatty acid binding protein and haemoglobin proteins. Mouse liver fatty acid binding protein is 127

amino acids long with a monisotopic mass of 14237.4705 Da, a mass shift of -42 Da from the measured monoisotopic mass for *m/z* 1021.47 (MWmeas 14279.4328). A known PTM of this protein according to UniProt is acetylation of the initiator methionine. With this PTM, the theoretical monoisotopic mass for mouse L-FABP is 14279.5011, which has an error of Δ -4.78 ppm. Manual analysis of the CID MS/MS data lead to the identification of 46 product ions (Appendix 22), which correspond to 30 amino acid cleavages and gave a sequence coverage of 24%, HCD fragmentation gave a coverage of 13% from 17 fragments and ETD gave a sequence coverage of 18% from 23 fragments. Combining the information these three techniques there were 52 fragments resulting in sequence coverage of 41%.

Figure 58: Coverage of the mouse liver fatty acid binding protein using CID, HCD and ETD with the ultraFAIMS at a DF of 130 Td and CF of 0.3 Td and without the ultraFAIMS. b/y ions are indicated in blue and c/z ions are indicated in red.

For comparison, the same MS/MS analyses were conducted without the ultraFAIMS. The precursor peak in the full scan had a higher signal intensity however the signal to noise ratio was lower (s/n without the ultraFAIMS was 6.78 as opposed to s/n of 14.34 using the ultraFAIMS). There was an increase in intensity when the isolation window was applied without any fragmentation. The ions were subjected to the same fragmentation conditions. The results showed that there was a decrease in the number of product ions detected from all three fragmentation methods (Appendix 23). CID fragmentation gave the

largest coverage of 15 % from 19 fragments, and HCD resulted in 10 product ions yielding 8 % coverage. The ETD mass spectrum was the poorest, with only 9 fragments being identified resulting in 7 % coverage. Combining the fragment identifications resulted in 31 fragments, which produces sequence coverage of 24 %.

Many more proteins were observed following LESA FAIMS mass spectrometry. The peak at *m/z* 952 is the most abundant protein signature under the conditions of the static analysis and has a s/n of 95.3. Without the ultraFAIMS the s/n of this peak is reduced to 8.9 and is only just detected The direct tissue analysis of mouse brain using liquid microjunctions has been conducted and published by Schey et al. [199]. In that work they used liquid chromatography coupled to mass spectrometry analysis to analyse the eluent from the liquid micro-junction. Several proteins were identified, one of which was ubiquitin. Ubiquitin has a calculated mass of 8560.6240 Da, which agrees with the measured mass (MWmeas 8560.6457) with an error of 2.53 ppm. Three fragmentation techniques were conducted on the ions: CID, HCD and ETD (Appendix 24). CID fragmentation yielded 12 b ions and 22 y ions giving a coverage of 37%. HCD fragmentation produced 15 fragments (2 b ions and 13 y ions) and sequence coverage 20%. ETD produced the smallest number of fragments, 10 fragments (7 c ions, 1 y ion and 2 z ions), giving a sequence coverage of 13%. The combined coverage from all fragmentation methods was 42%.

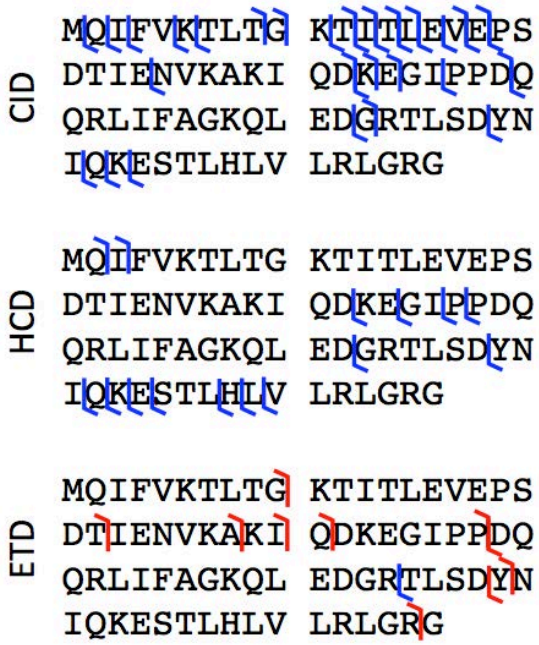

Figure 59: Coverage of mouse brain Ubiquitin using CID, HCD and ETD with the ultraFAIMS device at a DF of 270 Td and a CF of 2.6 Td. b/y ions are indicated in blue and c/z ions are indicated in red

5.4.1. Visualisation of ultraFAIMS data

There is no commercial software to process ultraFAIMS data. Two methods of visualising the data were developed in MATLAB. The first method visualises the distribution of a single peak (*m/z* or mass) over all DF and CF values recorded and is referred to here as a single ion transmission map. The second visualises the distribution of all peaks (all *m/z*) detected at a single DF across the CF sweep and is referred to here as a total ion transmission map.

5.4.1.1 Single ion transmission maps.

To produce single ion transmission maps several steps of processing were required. Lipids and proteins were treated separately. Lipids are observed as

salt adducts and are identified using their *m/z* whereas proteins are observed in multiple charge states and so were de-convoluted and their molecular weight was considered. Deconvolution of the protein peaks was performed by use of the Xtract function in the Xcalibur software (Thermo). The Xtract function was applied to every mass spectrum in the FAIMS analysis. The end product is a series of files relating to each scan (mass spectrum) in the 2D sweep. These files are converted to .mzml files using Proteowizard's msconvert program [206]. The .mzml files are then converted to .imzml files using .imzml converter [208] . The .imzml files were opened using mzAnalysis, an in-house program developed using MATLAB that enables mass spectrometry data to be displayed as images. For lipids, where the Xtract process is not required, the RAW file was directly converted to a single .mzml file and this file converted to an .imzml file. Using mzAnalysis a single *m/z* or MW value is isolated and the array is exported out of mzAnalysis into the MATLAB workspace. The array is a linear representation of the 2D sweep. To visualise the data, pixels representing a single DF sweep were isolated and stacked on top of each other (Figure 60 top). The challenge associated with this is that there are a different number of scans in each DF sweep, and the CF value that corresponds to a single scan is different in each DF sweep.

5.4.1.1.1 Aligning scan number to CF value and CF values between sweeps

The number of scans in each DF sweep is different. This is because automatic gain control (AGC) was used to obtain optimum quality mass spectra. AGC

adjusts the fill time based on the number of ions present and as a result each scan takes a different length of time. In addition to this, the CF sweep is continuous and is not connected to the scans of the Orbitrap Velos. (The ultraFAIMS software and the mass spectrometry acquisition software are not integrated). Together these factors mean that during a scan the CF is changing and the CF at the start of each mass spectrometry scan is not evenly spaced. To calculate the CF at the start of the scan (CF_s) it is necessary to calculate the rate at which the CF is changing. This can be calculated using Equation 19, where t_n is the length of time for a single sweep, and CF_0 and CF_n are the start and end CF values, t_x is the time point at which the CF is being calculated.

Equation 19

$$CF_s = \frac{CF_n - CF_0}{t_n} \times t_x + CF_0$$

It is important to note that this would result in the calculated CF increasing indefinitely, when in actual fact it cycles between CF_0 and CF_n. Therefore if the value of CF_s exceeds CF_n then it is known that another sweep has started. Each time this occurs the value of the numerator in Equation 19 (CF_n-CF_0) is taken away from CF_s one or multiple times to ensure that CF_s is always between CF_0 and CF_n, and hence calculating the CF value for the start of each scan. The MATLAB code for this calculation is supplied in Appendix 25.

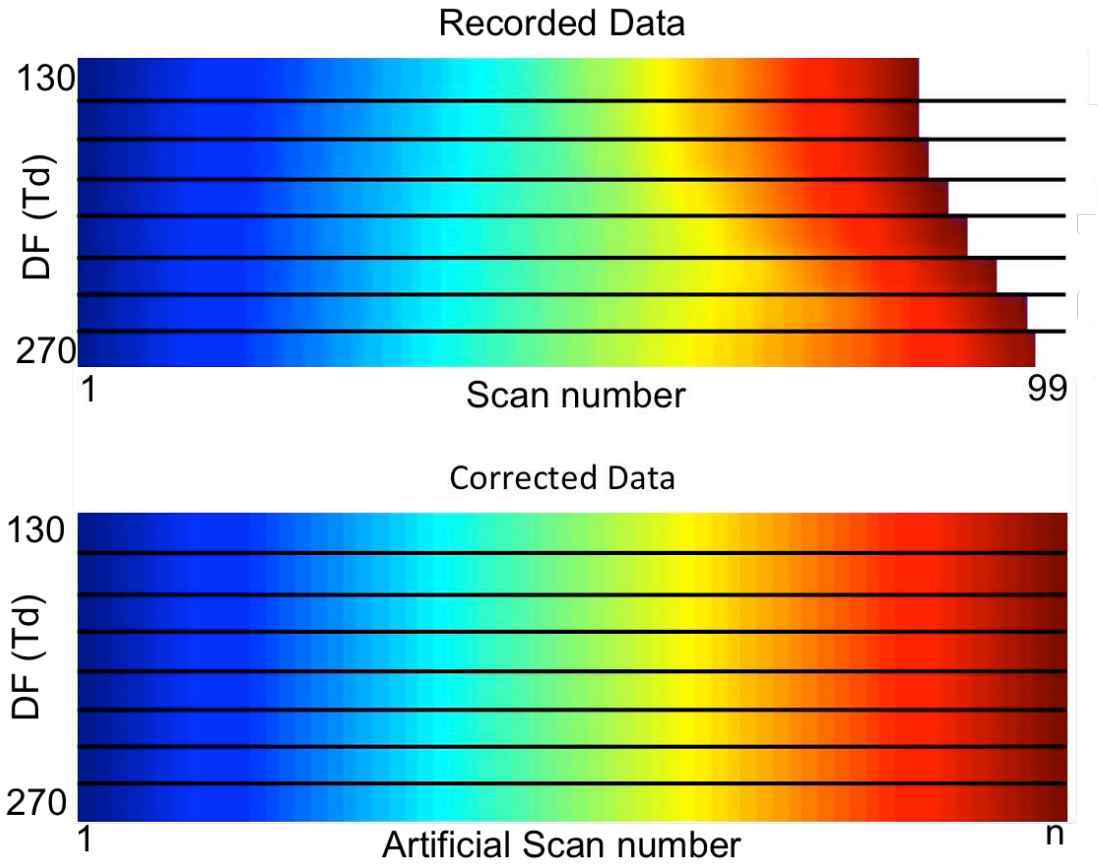

Figure 60: Top) Visual representation of the CV at each scan, where dark blue is CV= -1 Td and dark red is CV = 4 Td Bottom) The same sweeps after the MATLAB transformation has been applied.

To align the scans there are several considerations:

- The first mass spectrometry scan in each CF sweep does not correspond to a consistent CF value.
- The last mass spectrometry scan in each CF sweep will include data from the start of the subsequent CF sweep.
- The first mass spectrometry scan of the experiment aligns exactly with the first scan of FAIMS analysis.

The first two points are due to the dis-connected nature of the delivery of the ultraFAIMS field and the data recording process of the Orbitrap. The third point must be assumed true for the calculations to work. However it is unlikely to be true. The CF sweep will have started at some point during the first scan of the data set

To align the data a template of artificial scans were created with even spacing. These scans ranged from the highest starting CF to the lowest finishing CF that was calculated. This means that scans that included both the end of one sweep and the start of the next were excluded and ensured that only scans where there is an equivalent scan in each sweep were included. The spacing between each scan is defined as 1.2 second, which corresponds to the shortest scan acquisition. To populate the template with recorded data, the signal intensity at a specific CF value was approximated by interpolating between the two nearest recorded time points (one above and one below) and assuming a linear relationship. The scan number of the template directly corresponds to a CF value and each column of pixels spanning each DF refers to the same CF value. This transformation is applied to all single ion transmission maps.

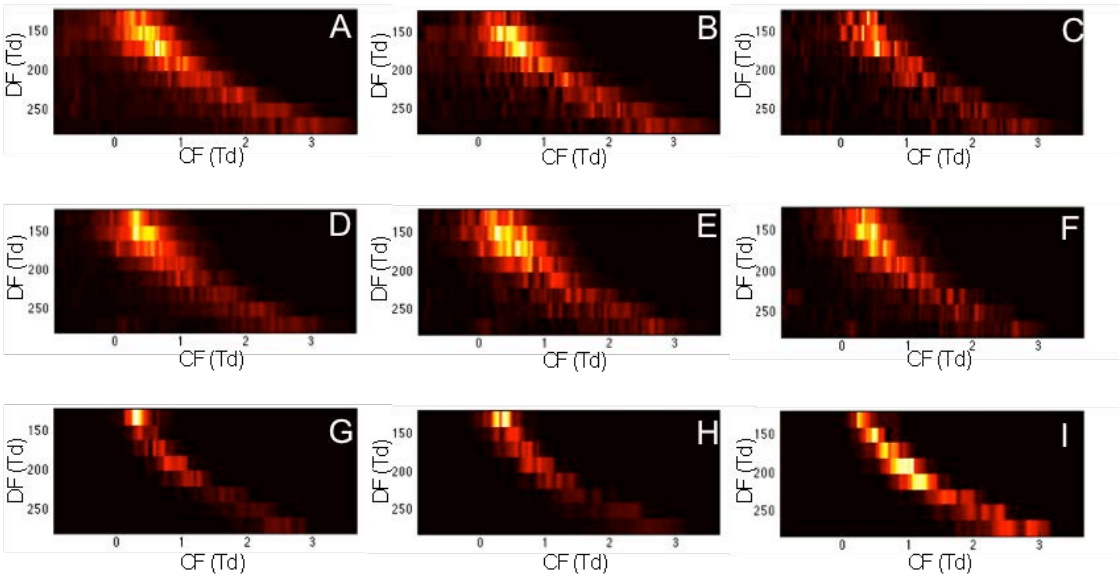

Figure 61: 2D sweeps of selected ion from mouse liver displayed as single ion transmission (SIT) maps. A) *m/z* 758.57 +/- 0.01 identified as PC(34:2)+H^+ B) *m/z* 760.58 +/- 0.01 identified as PC(34:1)+H^+. C) *m/z* 806.57 +/- 0. identified as PC(38:6)+H^+. D) *m/z* 796.52 +/- 0.01 identified as PC(34:2)+K^+. E) *m/z* 798.54 +/- 0.01 from identified as PC(34:1)+K^+. F) *m/z* 844.52 +/- 0.01 identified as PC(38:6)+K^+ G) Protein of monoisotopic 15607 Da. H) Protein of monoisotopic 15971 Da. I) Protein of monoisotopic 14278 Da identified as the Liver fatty acid binding protein

The single ion transition maps of 9 species are displayed in Figure 61. There are three types of species presented, protonated lipids (panels a-c), potassiated lipids (panel d-f) and proteins (panels g-i). All maps show a drift to higher CF values at higher DF. These results are consistent with published results, where a reserpine standard has been analysed, and shows that there is a reduction in intensity, a widening of the peak width and a shift to higher CFs at increasing increments of DF [162].

There is a similarity between the single ion transmission maps for the protonated and potassiated lipid species. There are subtle differences in the CF values in which the two adducts are transmitted. The potassium adducts

favours slightly lower CF values than the protonated species. Despite this, there is a large overlap of the CF values in which these species are transmitted and it would not be possible to isolate a specific adduct type. It would be possible to reduce the relative intensity of a specific salt adduct.

The protein maps show significant difference to those of the lipids. The proteins in panel G and panel H have been identified as the alpha and beta subunits of haemoglobin. These proteins display similar FAIMS transmission characteristics. The protein in panel I was identified as the liver fatty acid binding protein and display a very different ion transmission pattern.

5.4.1.2 Total ion transmission maps

An alternative approach for viewing the data is to display the total ion transmission, i.e., the entire mass range across a single CF sweep. This approach will produce a single total ion transmission map for each DF condition. To achieve this, the *m/z* ratio needs to be maintained, therefore the data sets are converted to an .imzml file using in-house software SpectralAnalysis. This software allows the entire dataset to be exported to MATLAB workspace. Here the data needs to be binned because each individual mass spectrum is not the same number of data points in length. Data was binned by summing the contents of the bin, to produce a single value This is because the *m/z* values for each spectrum is calculated at the end of each scan causing small variations in the mass recorded as well as variations in the number of *m/z* data points that

make up a single peak. This is especially true when the sample is continuously changing, as it is with 2D sweep data, where only specific windows of DF and CF values transmit specific ions. Assembly of a matrix that encompasses every possible calculated *m/z* is unsuitable due the memory requirements and therefore the data was binned. Figure 62 shows 6 total ion transmission maps obtained following LESA FAIMS analysis of mouse liver in which the bin sizes are *m/z* = 0.1, 0.3, 0.5, 0.75, 1 and 2. If the bin size is too small, shifts in peak *m/z* result in a patchy ion distribution over the CV range; however, if the bin size is too large, neighbouring peaks will merge into one. The optimum bin width is *m/z* 0.5.

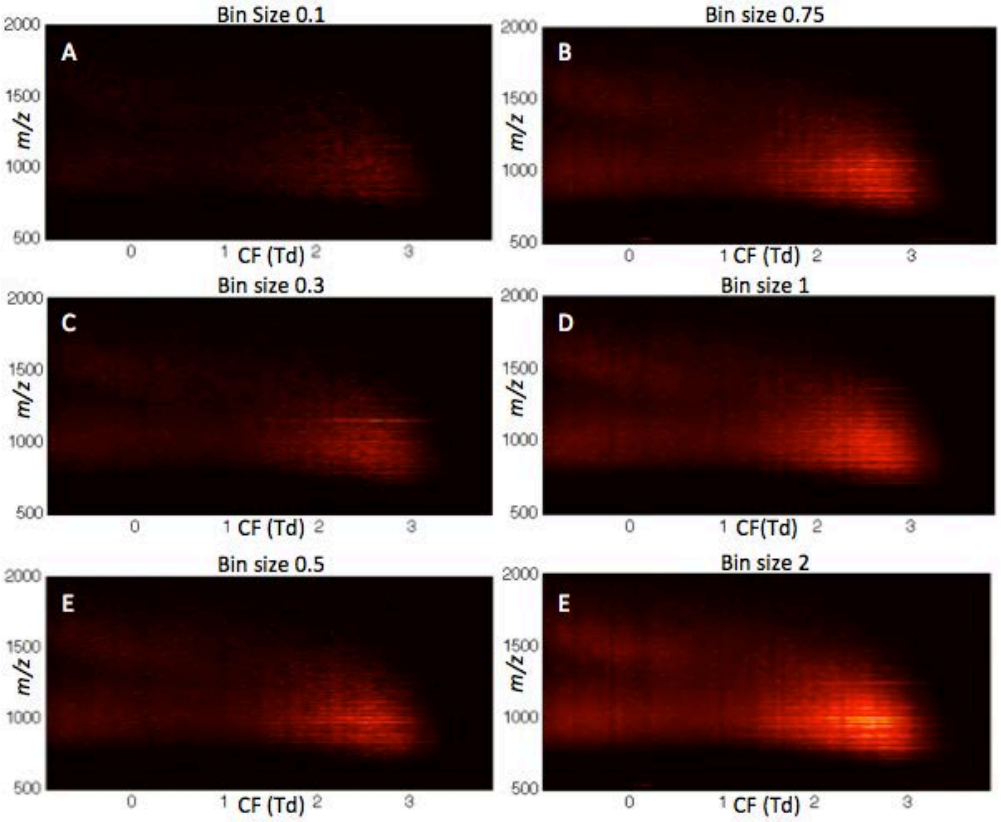

Figure 62: The total ion transmission map of the ultraFAIMS sweep at DF 270 Td, from data aquired using 70% methanol +0.1% FA as the solvent for a LESA protocol of mouse liver procesed using different bin sizes.

Figure 63A shows the complete series, it is clear to see the dominant species in the spectrum. The protein distribution is the predominant feature. Similar features are observed as previously seen: ions are transmitted at a higher CF at increasing DFs and there is a wider distribution of ions at higher DFs. By displaying the data like this the separation between signal and noise becomes clear. A disadvantage of viewing the data in this manner is the dynamic range of the ion abundance. When displayed as a linear colour scale, the lower intensity peaks may be of too low an abundance to visualise. Under these

sampling conditions, it is the lipid species that are lower in abundance. To enhance visualisation of these species it is possible to normalise the data. The normalisation approach used here was to normalise within each bin. This approach enhances each bin revealing lower abundance peaks. These normalised maps need to be read carefully, as the intensities of adjacent bins are no longer comparable, however the advantage of these normalised maps is that it is clear to see the FAIMS separation of the different species.

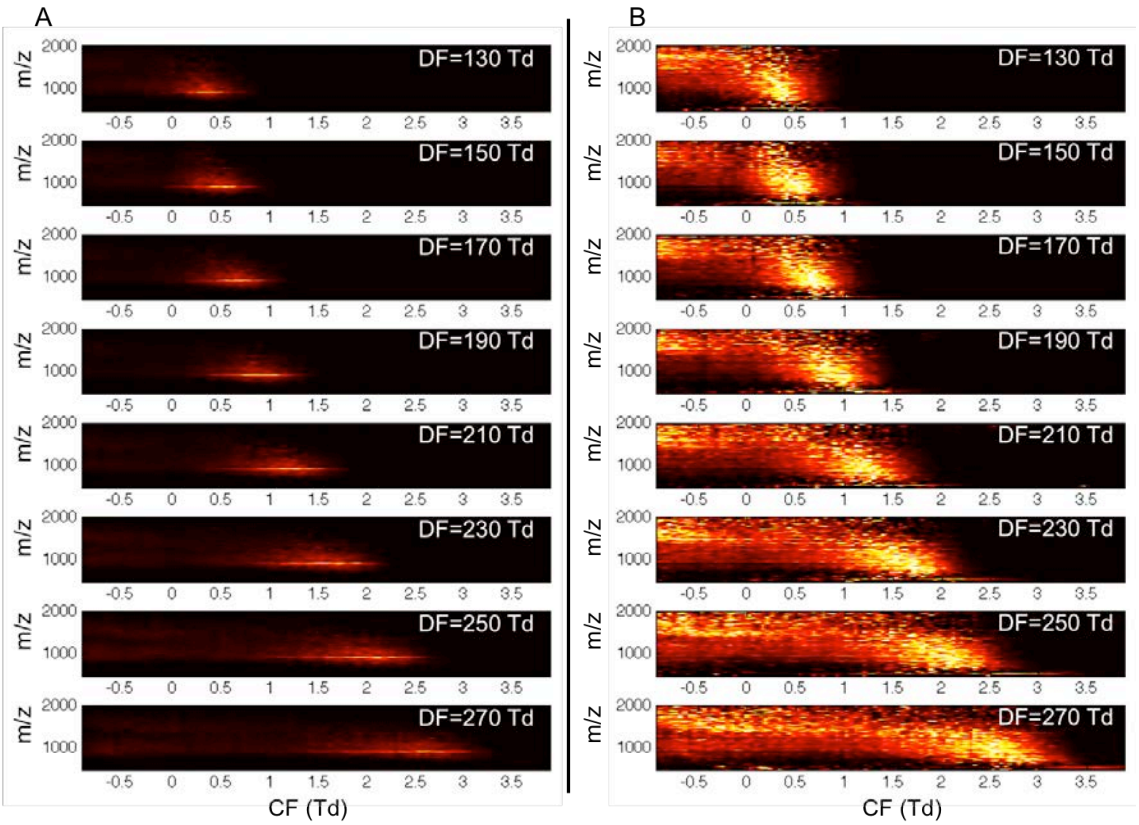

Figure 63: Total ion transmission maps of the 2D sweep of mouse liver, A) un-normalised B) normalised.

5.5 Conclusion

The work presented in this chapter is the first reported instance of the ultraFAIMS being coupled to LESA sampling. Direct tissue analysis has been successfully conducted using the ultraFAIMS as a real time separation technique. Lipids and proteins can be separated from each other and from the large amount of background that is produced when analysing complex samples. The advantage of LESA is that there is little sample preparation; however, this is accompanied by production of an incredibly complex mixture in which many type of ions are present. Current methods for complexity reduction in biological samples increase the sample preparation time, some by a little such as tissue washing [44], others considerably, such as liquid chromatography, [85, 199]. The ultraFAIMS acts as a gas-phase separation technique.

It has been shown that the reduction in the noise and the corresponding increased signal to noise ratio has increased the number of proteins detected. Fragmentation of these proteins revels an increased number of fragments being identified in those proteins. MS/MS of proteins detected using the ultraFAIMS revealed greater sequence coverage than when fragmented without the ultraFAIMS

A MATLAB program was created to visualise the ultraFAIMS data. Two types of maps were produced: single ion transmission maps in which a single ion or molecule at all the CF and DF values can be visualised; and total ion

transmission maps in which all ions across a single CF sweep are visualised. These maps show the differences in ion behaviour through the ultraFAIMS and reveal optimum conditions for analysis of lipids and proteins.

Chapter 6: Identification of lipids from tissue using LESA-ESI and MALDI coupled to traveling wave ion mobility mass spectrometry.

6.1 Introduction

Lipids are small molecules that are insoluble in water. Lipids are an important component of biological systems, they form the basis of the cell membranes, and they are important signaling molecules. One such lipid class is phosphatidylcholine (PC) lipids. These lipids have a glycerol backbone with a phosphocholine head group on carbon one, with carbon two and three supporting hydrocarbon chains. Due to the nature of PC lipids it is common to have isobaric species, this is where two sets of two hydrocarbon chains have the same number of carbons and hydrogens, however the chain lengths, and number of double bonds in the chains are different. For example, PC(34:2) has two fatty acid chains with a total number of 34 carbons and 2 double bonds. This could comprise of a 16:0 (Hexadecanoic acid) and an 18:2 (Octadecadienoic acid) chain, an alternative would be a 16:1 (Hexadecenoic acid) and an 18:1 (Octadecenoic acid) chain. It is important to differentiate between these two lipids as structure and function are closely related.

In the previous chapter suitable solvents for analysis were determined to be 80% Ethanol+0.1% FA, a highly organic solution. Fragmentation of lipids

produces characteristic fragments. The neutral loss of choline produces a fragment 59 Da below the precursor ion. This is helpful to identify the class of the lipid. Identification of the side chains also involves monitoring the neutral loss fatty acids. Monitoring the intensity of the neutral loss of the fatty acid and the head group enables the location of the fatty acid to be determined. The more abundant fragment will result from the neutral loss of the fatty acid in the sn1 position.[209, 234, 235]

Here analysis of lipids has been conducted using collision induced dissociation (CID) and high-energy collision induced dissociation (HCD). CID and HCD are very similar fragmentation techniques, both these techniques cause dissociation by bombarding the ions with neutral molecules. The difference is that HCD ions are trapped and held within an electrical field higher than that of CID. This causes ions to have an excited state, and increasing the probability of fragmentation. On an LTQ Orbitrap ETD, CID is performed in the ion trap where as HCD is performed in the HCD collision cell. As a result of this CID has a lower mass limit of 1/3 of the m/z of the ion being fragmented, where as HCD does not have this limitation (see section 1.5 of the introduction for further information). The implication of this is that any fatty acid backbone fragments that may be produced would not be observed using CID and only HCD when using the LTQ Orbitrap ETD. However in the Synapt G2-S fragmentation occurs in the trap or transfer cells and so the full mass range can be observed.

In chapter 3 analysis of lipids and proteins from human liver tissue was investigated and it was found that they could be targeted using solvent optimisation. In this chapter, methods for the identification of lipids via HCD and CID extracted from human liver tissue via LESA are presented.

LESA is an excellent tool for in-situ lipid identification as there are long spray times enable multiple fragmentation events to occur increasing the number of lipids that can be identified from a single location. Coupled to the TWIMS, LESA provided opportunities to distinguish between lipid and protein in their drift time and arguably more significant the separation of isobaric lipids. Spatially directed approach that the LESA can provide does not produce a good enough resolution to view the intricate disease specific tissue scaring that is observed in NASH. To view this detail from the tissue a MALDI source was implemented. MS/MS imaging of a precursor ion produced images of the two precursor ions, further more when coupled with the TWIMS isobaric species that displayed separate spatial locations were revealed.

6.2 Results and Discussion

LESA of formal lithium fixed tissue has been reported as a powerful strategy for the *in-situ* lipid identification. [45]cd Formaldehyde causes cross-linking of proteins [236] and so analysis of proteins in the same experiment is not possible.

Fixed tissue has the advantage of binding the proteins, which prevents their extraction and ionisation and means that they are not detected. [45] In this work the lithium is introduced to the system by dissolving lithium chlorides in the extraction solvent, and by using 80% ethanol + 0.1% formic acid (optimised in chapter 3). Even with this optimised solvent extraction there are very small contributions of proteins. It was observed that by including lithium in the solvent system it has removed any remaining trace of proteins from the spectrum. The advantage of this is that it is possible to utilise the advantages that lithium adducts can give without the need to fix the tissue.

6.2.1. Adduct formation

CID fragmentation of lipids is well documented and widely reported to differ depending on the adduct type of the precursor ion [45, 209]. Typical ions associated with the neutral losses in CID experiments are illustrated for the commonly detected PC(34:2), listed in the Table 6-1 and Table 6-2 and serve as a guide for the fragmentation described in this chapter.

Table 6-1: Product ions arising from neutral losses of the lipid PC(16:0/18:2)

	Neutral Loss of fatty acid				Neutral Loss of fatty acid and head group			
Fatty Acid	**[M+H]+**	**[M+Na]+**	**[M+K]+**	**[M+Li]+**	**[M+H]+**	**[M+Na]+**	**[M+K]+**	**[M+Li]+**
16:0	502.3292	524.3111	540.2851	508.3374	443.2557	465.2376	481.2116	449.2639
18:2	478.3292	500.3111	516.2851	484.3374	419.2557	441.2376	457.2116	425.2639

All values are *m/z*

Table 6-2: Head group product ions arising from neutral of losses the lipid PC(16:0/18:2)

	[M+H]+	**[M+Na]+**	**[M+K]+**	**[M+Li]+**
Neutral loss of choline	698.4875 (86.0964)*	721.4773	737.4513	705.5036
Neutral loss of PC Head group	575.5028 (184.0733)	597.4853	613.4593	581.5116
PC Head group without Choline	124.9998	146.9812	162.9552	131.0075

All values are *m/z*. values in brackets indicate the values the head group fragments would be detected at. * Is a rearrangement of ethyl choline in the head group, choline by its self is not detected.

The different adducts of lipids was first investigated for shotgun lipidomic approaches, to improve the fragmentation and the subsequent identification of the lipid. The salt is incorporated into LC-MS systems between the column and the ESI source. A splitter and a second pump is used to combine a solution containing the salt adducts and the LC eluent. This then resulted in salt adducts being formed during ionisation. Sodium adducts have been used to quantify lipids from biological extracts. [237] The first use of lithium was reported in 1998 to enhance the fragmentation of lipid species and to improve the identification of the fatty acids at sn1 and sn2 positions on phospholipids. [238]. Here salt adducts have been applied for the direct infusion of lipids sampled by LMJ using LESA.

6.2.1.1 CID of protonated lipid molecules

Protonated lipid molecules are reported to give few product ions. The protonated PC(18:2/16:0) molecule detected at *m/z* 758.5681 was subjected to CID and HCD fragmentation.

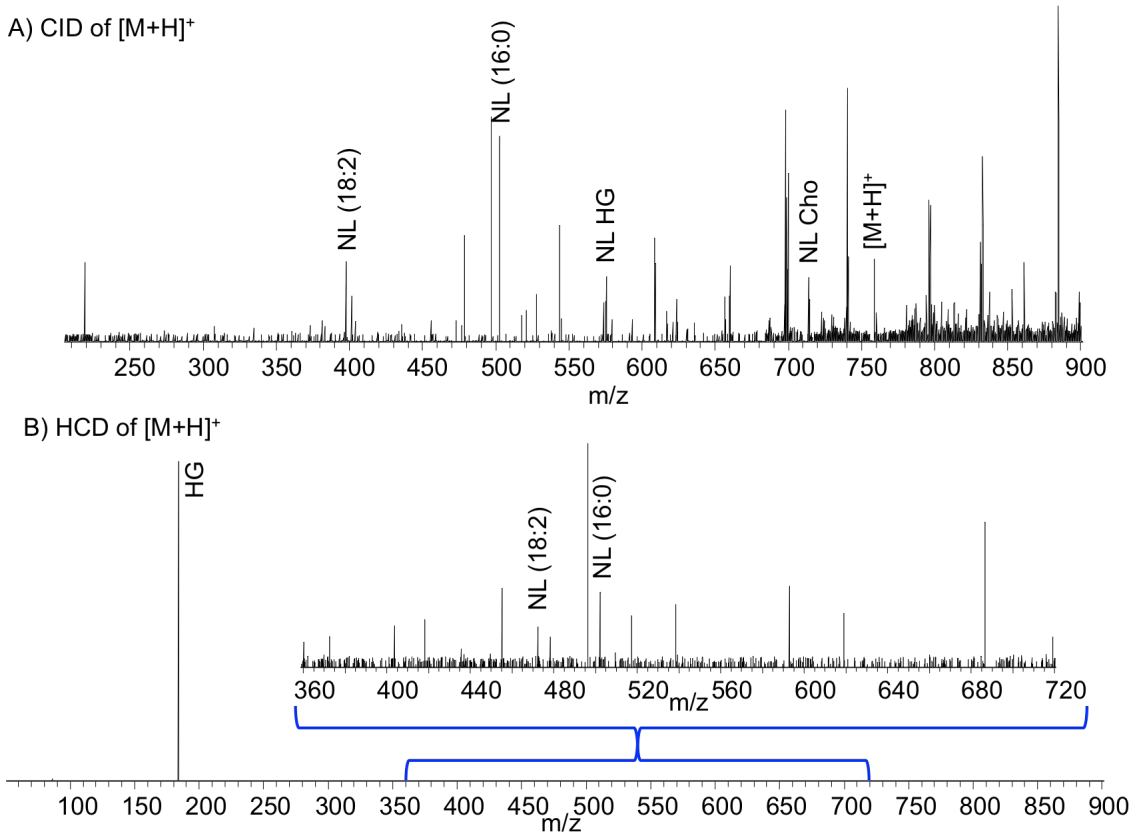

Figure 64: A) CID and B) HCD spectrum of $[PC34:2+H]^+$ detected at m/z 758.5681. Acquired using LESA sampling with 70% $Methanol_{(aq)}$ + 0.1% FA.

The mass spectrum acquired from CID of *m/z* 758.5681 (Figure 64A) displays informative peaks however all of the peaks are extremely low abundance and surrounded by equally abundant non-informative peaks. From the fragments detected it is possible to identify peaks relating to the neutral loss of the fatty acids (MW_{meas} 502.3290 neutral loss of 16:0 Δppm -0.40, MW_{meas} 478.3290

neutral loss of 18:2 Δppm -0.42) as well as a peak relating to the neutral loss of the head group (MW_{meas} 575.5032 neutral loss of HG Δppm 0.70,). However none of these peaks are the most abundant and would be very difficult to identify the lipid without prior knowledge. The HCD scans provides similar information (Figure 64B), however there is an abundant resembling the protonated head group at MW_{meas} 184.0734 (Δppm 0.54). Very small peaks were observed in the spectrum approximately 1000 times less abundant than the main peak. Two of these peaks relate to the neutral loss of the fatty acids (MW_{meas} 502.3292 neutral loss of 16:0 Δppm 0.00, MW_{meas} 478.3289 neutral loss of 18:2 Δppm -0.63). The protonated adduct does contain suitable information to identify a lipid however it would be difficulty to interpret unknown lipid due the low intensity in the MS/MS spectra. It should also be noted that PC(18:2/16:0) is the most abundant lipid observed from non-diseased human liver and fragmentation ions are barely detected, product ions from less abundant lipids may not be detected at all. The product ions identified are more informative than those reported in literature. The most dominant fragment ion for a PC lipid is found at *m/z* 184.5 corresponding to the head group fragment, other fragments identified are all of very low abundance, all of which were head group related. [239] Here fragments relating to the some neutral loss of the fatty acids chains were also identified.

1.1.1.1 CID of sodium lipid adducts

Sodium is present in tissue and may be introduced as a contaminant in the water of the solvent system. The sodium adduct is observed in low abundance and has been reported to be beneficial for fragmentation [235, 240]. The sodium adduct of PC(18:2/16:0), is detected at *m/z* 780.5500, and was subjected to CID and HCD fragmentation.

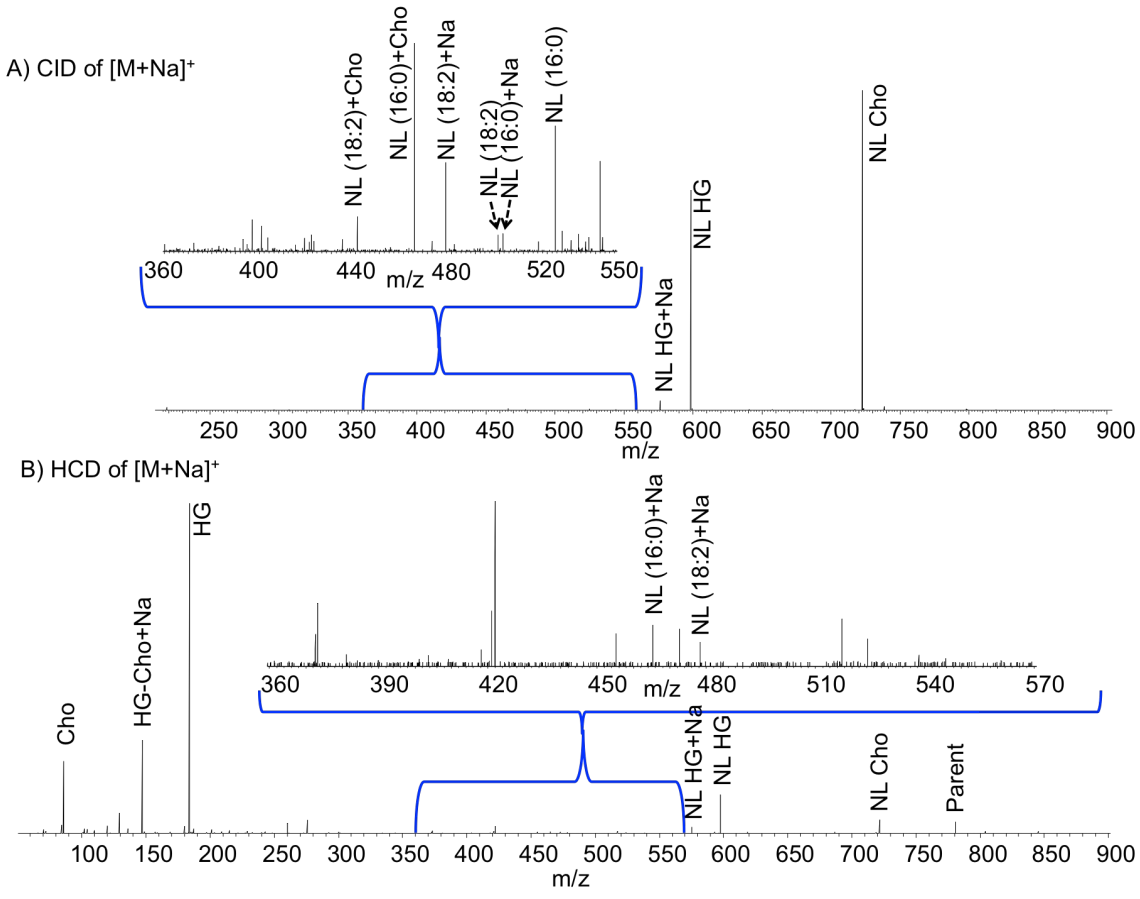

Figure 65: A) CID and B) HCD spectrum of $[PC34:2+Na]^+$ detected at *m/z* 780.5500. Acquired using LESA sampling of non-dieased human liver tissue with 70% $Methanol_{(aq)}$ + 0.1% FA

The CID spectra and HCD spectra (Figure 65) show product ions relating to the neutral loss of the head group, and the side chains (Table 6-3 and Table 6-4). The

detection of fragments relating to the neutral loss fatty acid and the head group, (found at *m/z* 465.2369 and *m/z* 441.2369) enable the assignments of the fatty acids to the sn_1 and sn_2 positions on the glycerol. The neutral loss of fatty acid 16:0+choline is more intense than the neutral loss of the fatty acid 18:1+choline therefore the fatty acid 16:0 is in the sn_1 position. Using the nomenclature $sn_3(sn_2/sn_1)$, PC(34:2) can be identified as PC(18:2/16:0). The product ions detected have enabled identification of the lipid, however, the intensity of these peaks are very low and there are many other peaks observed that could confuse identification.

Table 6-3: Fragments identified from CID spectrum using sodium adduct of PC(34:2)

Mass (*m/z*)	**Identity**	**Δppm**
721.4766	Neutral loss of choline	-0.97
597.4845	Neutral loss of head group	-1.34
575.5029	Neutral loss of head group with sodium	0.17
524.3104	Neutral loss of fatty acid 16:0	-1.33
502.3289	Neutral loss of fatty acid 16:0 with sodium	-0.60
500.3103	Neutral loss of fatty acid 18:2	-1.60
478.3285	Neutral loss of fatty acid 18:2 with sodium	-1.46
465.2369	Neutral loss of fatty acid 16:0 with head group	-1.50
441.2369	Neutral loss of fatty acid 18:2 with head group	-1.59

In the HCD spectra additional peaks are observed at the lower *m/z* values. It should be noted that the sodium adduct is the least abundant adduct that is observed, and is it still possible to detected all of these product ions.

Table 6-4: Fragments identified from HCD spectrum using sodium adduct of PC(34:2)

Mass (*m/z*)	**Identity**	**Δppm**
184.0734	Head group	0.54
146.9818	Head group with sodium without choline	4.08
86.0965	Choline	1.16

6.2.1.2 CID of Potassium adducts

Potassium adducts are observed as the most intense peaks in a typical spectrum from non-diseased human liver. The potassium adduct of PC(18:2/16:0) is observed at *m/z* 796.5239. The neutral loss of the head group is the most intense peak, in the CID spectrum (Figure 66A), and there are very small peaks that relate to the side chains (Table 6-5).

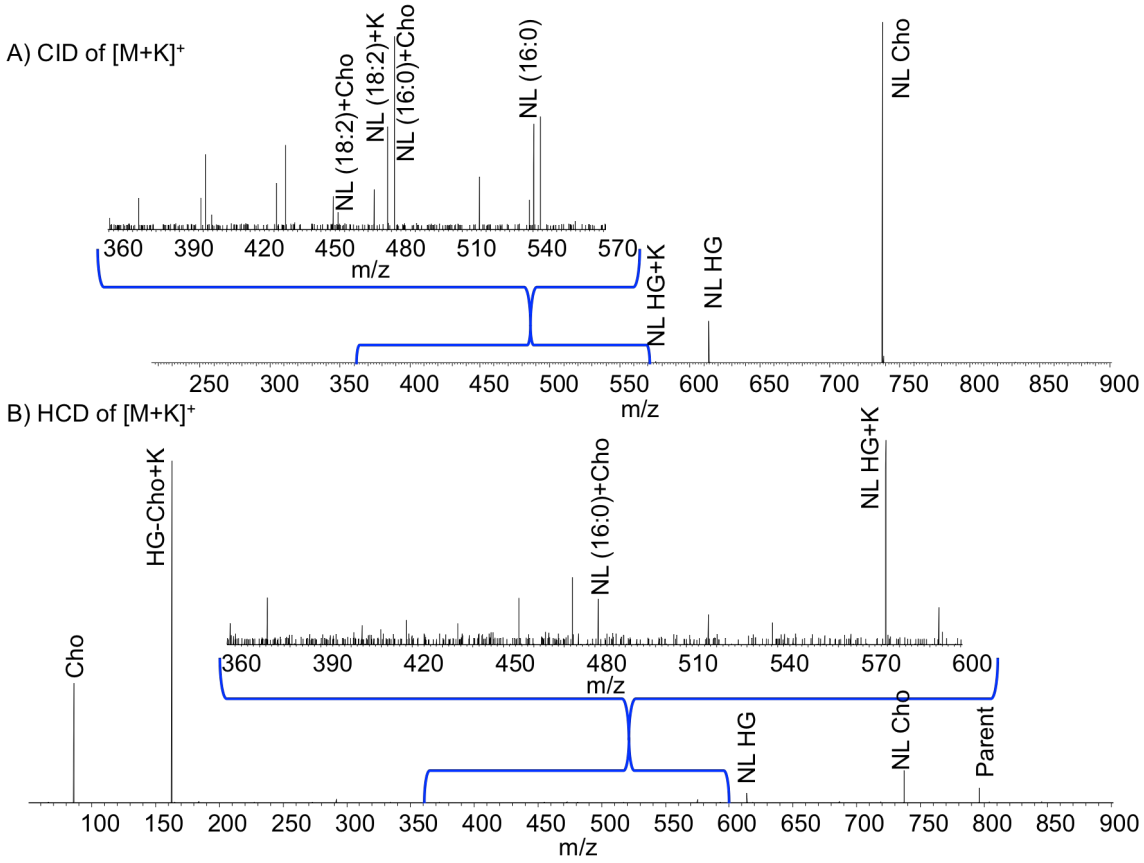

Figure 66: A) CID and B) HCD spectrum of $[PC34:2+K]^+$ detected at m/z 796.5239. Acquired using LESA sampling of non-dieased human liver tissue with 70% $Methanol_{(aq)}$ + 0.1% FA

Table 6-5: Fragments identified from CID spectrum using potassium adduct of PC(34:2)

Mass (*m/z*)	**Identity**	**Δppm**
737.4510	Neutral loss of choline	-0.41
613.4592	Neutral loss of head group	-0.16
575.5034	Neutral loss of head group with potassium	1.04
540.2850	Neutral loss of fatty acid 16:0	-0.19
478.3290	Neutral loss of fatty acid 16:0 with potassium	-0.42
481.2114	Neutral loss of fatty acid 16:0 with head group	-0.42
457.2116	Neutral loss of fatty acid 18:2 with head group	0.00

In the HCD spectrum (Figure 66B) very few informative peaks were observed. Head group related peaks and one side chain related fragments were observed.

The only additional peaks observed in the HCD spectra were potassium adduct of the head group without choline and the choline fragment. (Table 6-6)

Table 6-6: Fragments identified from HCD spectrum using potassium adduct of PC(34:2)

Mass (*m/z*)	**Identity**	**Δppm**
162.9558	Head group with potassium without choline	3.68
86.0965	Choline	1.16

6.2.1.3 Lithium

Lithium has been shown to give increased lipid fragmentation and enables the two fatty acids to be assigned to sn1 and sn2 positions. [45, 210, 234, 240] Lithium is not native in tissue so needs to be added.

Lithium was first introduced for the analysis of lipids and carbohydrates in LC-MS systems to their improve the signal intensity and identification. For LC-MS the lithium salt is added post column, prior to ESI.

Incorporating Lithium chloride into the solvent system introduces the lithium to the system. By increasing the concentration of the lithium salt solution might be possible to force the Ionisation of the lipids to the lithium adduct (Figure 67). The inclusion of 25 mM LiCl in to the LESA solution can force the formation of the lithium adduct so that for a specific lipid more then 75% is detected as the lithium adduct. Abundant lipid species are shown in Figure 68, with and without the addition of LiCl. The spectra show that the majority of peaks observed in the spectra are a lithium adduct. Protonated molecules are still

observed, however are much less abundant than previously detected. This method of doping LESA solvents with lithium has enhanced the detection of low abundant lipids, observed between *m/z* 800-850

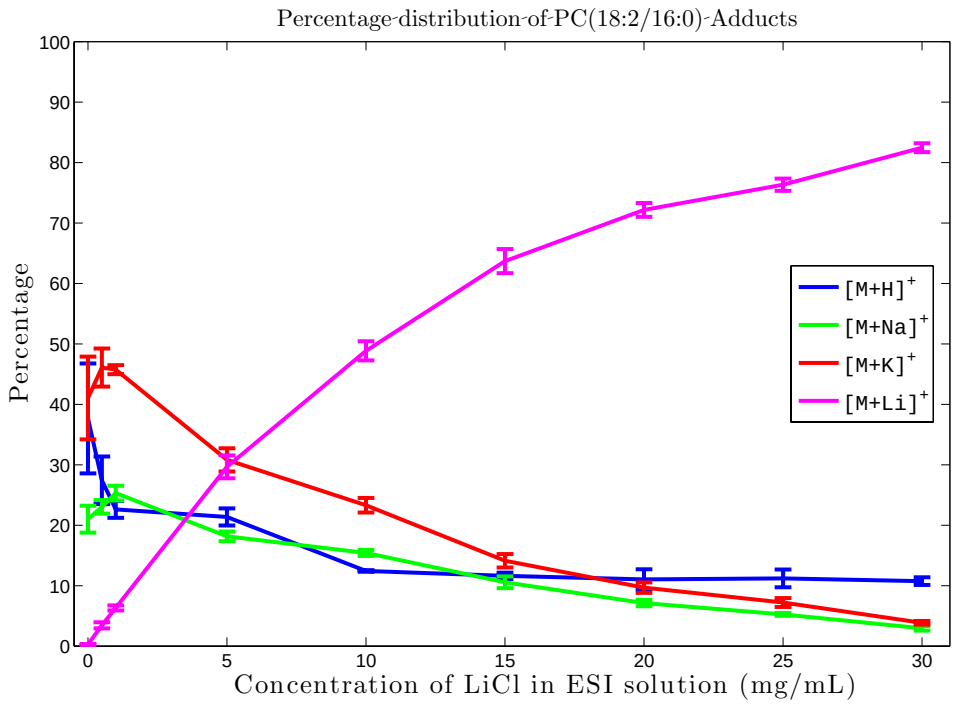

Figure 67: Percentage composition of PC(34:2) in the four adduct states observed in the spectrum. Error bars are 1 standard deviation of three repeats.

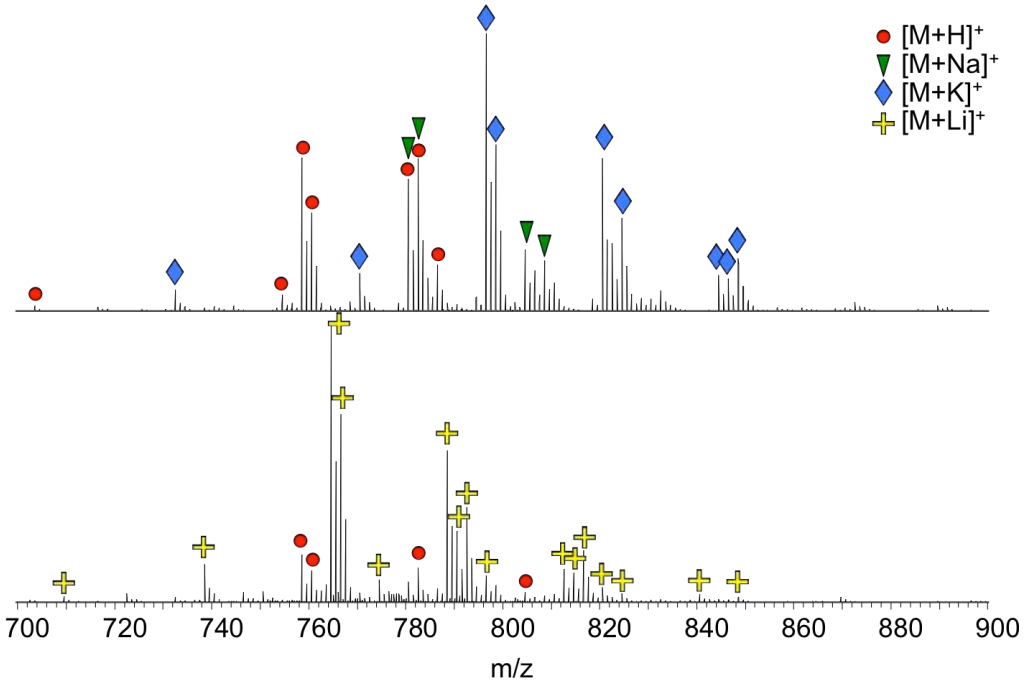

Figure 68: Enlarged region of a spectra aquired using 80% Ethanol + 0.1% formic acid (top) and 25mg/mL LiCl in 80% Ethanol+0.1% formic acid (bottom). Different adducts have been labled.

The resulting CID spectrum acquired from doping the LESA solution with 25 mM LiCl shows the lithium adduct of PC(34:2) detected at *m/z* 764.5820. Every informative peak is detected in high abundance (Figure 69 and Table 6-7). Each fragment ion is detected and they appear as the most abundant peaks observed the spectrum. Further more neutral loss of 16:0 is more abundant than 18:2 indicate that the lipid detected can also be identified as PC(18:2/16:0).

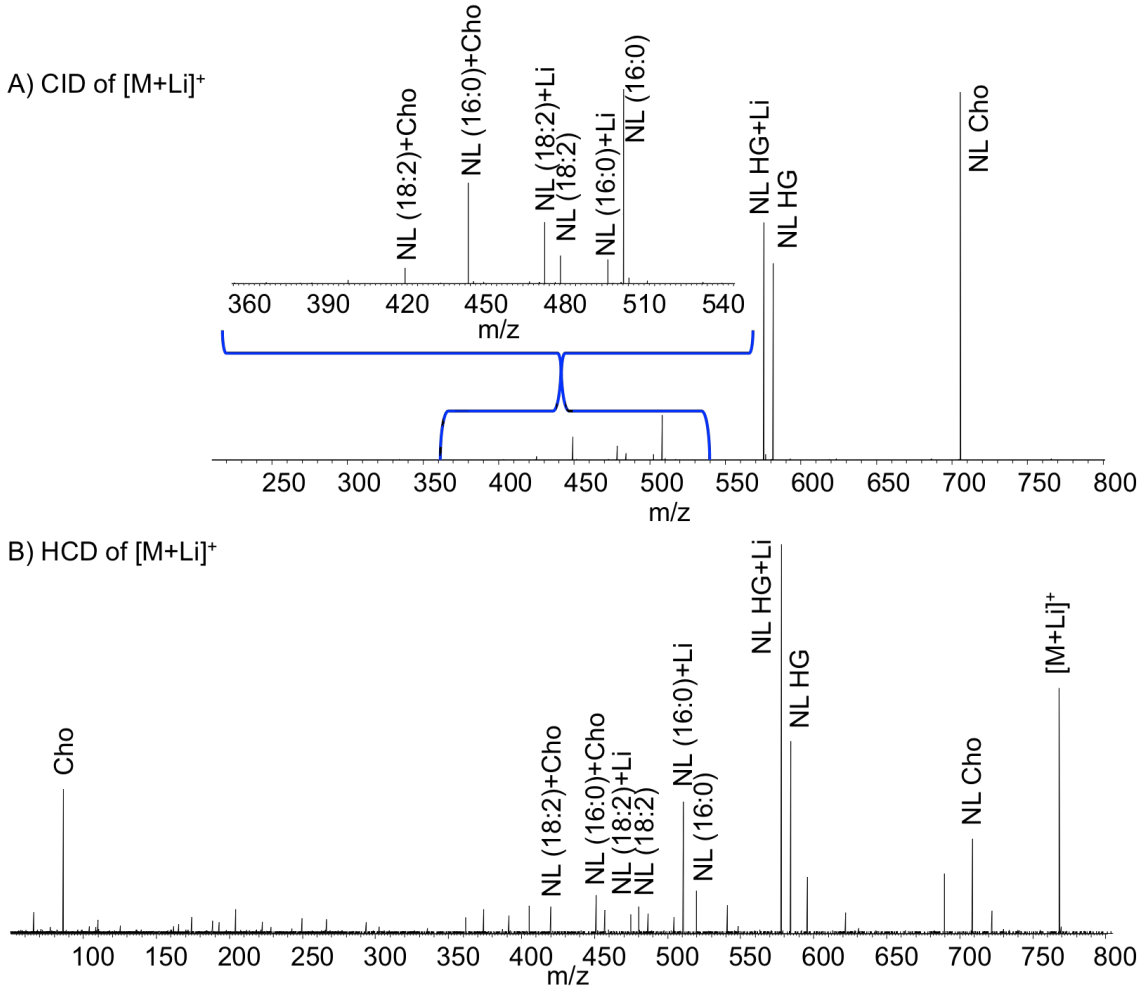

Figure 69: A) CID and B) HCD spectrum of $[PC34:2+Li]^+$ detected at *m/z* 764.5820 identified as Acquired using LESA sampling with 70% $Methanol_{(aq)}$

Table 6-7: Fragments identified from CID spectrum using lithium adduct of PC(34:2)

Mass (*m/z*)	**Identity**	**Δppm**
705.5012	Neutral loss of choline	-3.40
581.5091	Neutral loss of head group	-4.30
575.5010	Neutral loss of head group with lithium	-3.13
508.3353	Neutral loss of fatty acid 16:0	-4.13
502.3271	Neutral loss of fatty acid 16:0 with lithium	-4.18
484.3353	Neutral loss of fatty acid 18:2	-4.34
478.3271	Neutral loss of fatty acid 18:2 with lithium	-4.34
449.2619	Neutral loss of fatty acid 16:0 with head group	-4.45
425.2619	Neutral loss of fatty acid 18:2 with head group	-4.70

In the HCD spectrum the same fragments were also detected and identified in addition the lithium adducts of the neutral loss of the fatty acid fragments are easily identifiable. As with the previous analysis the choline ion is also present in the HCD spectrum (MW_{meas} 86.0962, Δppm 2.32).

6.2.1.4 HCD analysis

In previous experiments the collision energy (CE) for HCD was lower than the CE for CID. This is because less energy is required to produce comparable results. Increasing the CE for HCD was shown to further increases the fragmentation. As the CE is increased there is an increased detection of fragments below *m/z* 200. These ions were identified as fragments of the fatty acid back bone. These fragments were identified as the R^+ and RCO^+, however published reports detecting the backbone of fatty acids have detected the neutral loss of part of the fatty acid both were conducted of free fatty acid standards using either lithium or N-(4-aminomethylphenyl)pyridinium to modify the acid group on the fatty acid enhancing fragmentation. [241, 242] Detection of the fatty acid fragments from phosphatidylcholine in complex samples has been shown, using mouse plasma. The use of liquid chromatography and ion mobility were used to reduce spectral complexity prior to fragmentation. [243] Reported here is the first instance where backbone fragments have been identified directly from tissue using LESA.

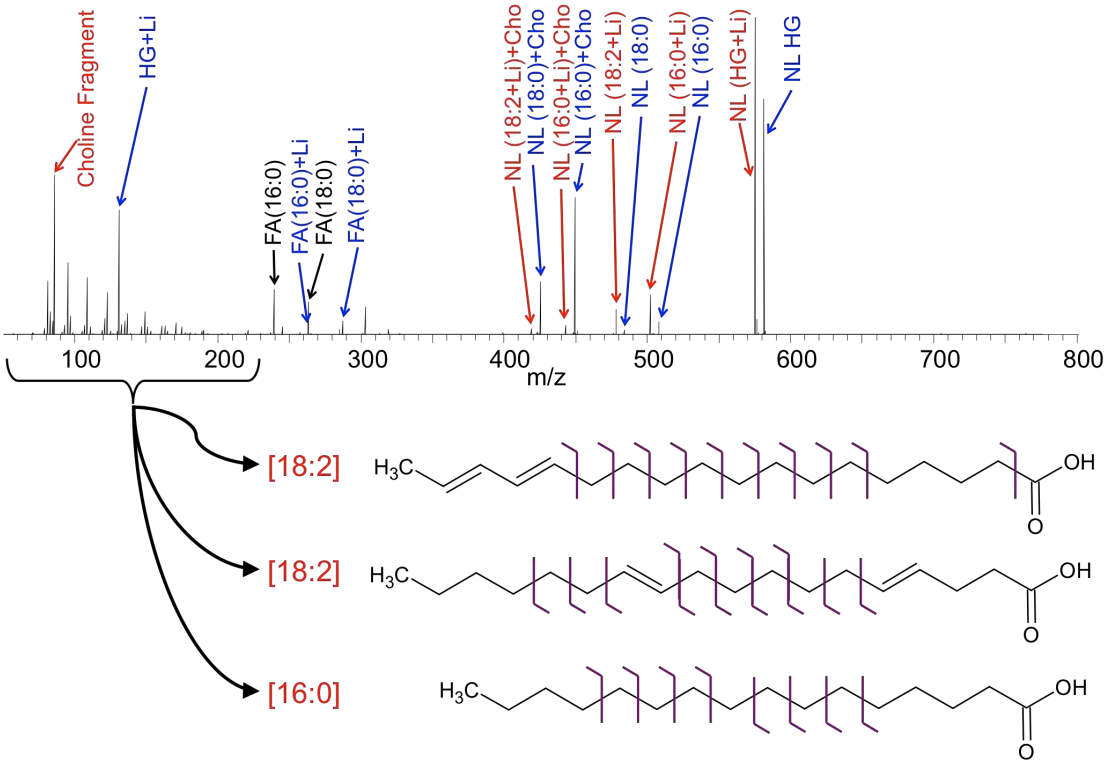

Figure 70: Fragmentation of lithium adduct of PC(18:2/16:0) produced from HCD with a collision energy of 35%. In the spectrum blue ions are lithiated red ions are protonated and black ions are RCO^+ ions.

6.2.2. Identification of multiple lipids from a single tissue location

Many of the peaks detected from human liver tissue can be assigned to a lipid. In several cases there may be two or more lipids associated with a peak. A high throughput method was developed to identify peaks from the direct infusion of LESA. Using data dependent analysis to select peaks for fragmentation, 90 lipids were identified in a single injection. Using lithium is beneficial for identifying multiple species, driving adduct formation to a specific adduct, in this case lithium, can double the intensity of some lipids. This reduces the

number of lipids that are fragmented twice in different adduct forms in addition the increase in intensity that is observed and reduce the time for analysis as the AGC target will be reached in a shorter amount of time. The addition of lithium also helps ionize diacylglycerides and triacylglycerides, which are subsequently identified. In total 90 lipids were identified from a single 15 min injection using 80% Ethanol with 25 mg/mL LiCl (Appendix 27). Literature reports of the detection of lipids using LESA have detected wax esters, cholesterol esters as well as sphingomyelins and phosphatidylcholines. The difference in the types of lipids detected can be attributed to a different solvent system used for the LESA extraction (4:2:1 chloroform/methanol/IPA) and the sample (contact lenses). [193] Another example of lipid analysis using LESA sampling, sampled from atherosclerotic plaques where 150 lipids were identified using both positive and negative mode. [79] In both these methods QqQ were used to screen for specific lipids. Here the most abundant ions have been fragmented in an untargeted manner.

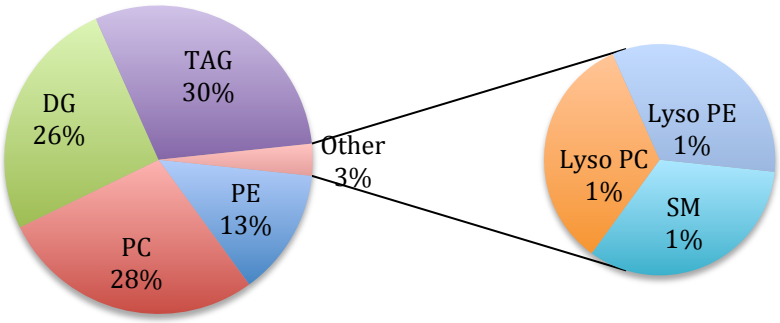

Figure 71: Pie charts of the classes of all lipids identified

6.2.3. Liquid extraction surface analysis MS/MS imaging

Using data dependant analysis, each analysis has the potential to be different if there are subtle differences in the intensity of the ions at any time point during the spray or any differences in the extraction process or the tissue samples. Therefore to use data dependant analysis for imaging would not be ideal. Using data independent analysis would be suitable. 14 specific lipids were targeted, and a full scan spectrum was also collected during a 5 min analysis time. In multiple MS/MS images can be produced using this method. Of the 14 lipids selected 13 produced MS/MS spectra with suitable for full characterisation. This is substantially more than what is achievable using other techniques such as MALDI, which may monitor one or two lipids during an image. [45, 244, 245] This is a major advantage of using LESA as an imaging technique, due to the large pixels and the long spray times that can be achieved, when compared to MALDI imaging. The disadvantage of using lithium adducts is that a residue of lithium is left on the surface which means that proteins cannot be detected in any subsequent analysis. Therefore this cannot be coupled to the repeat analysis discussed in chapter 3.

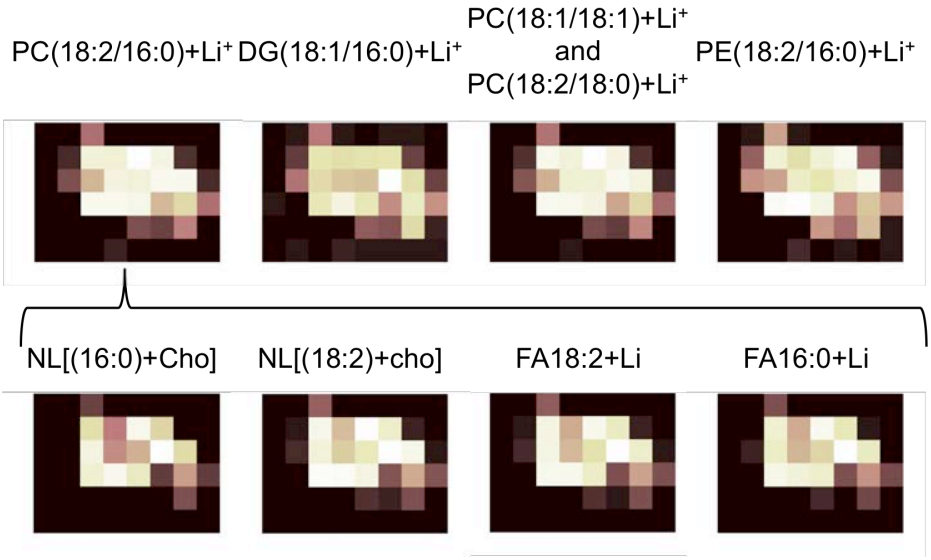

Figure 72: MS/MS images aquired using 25mg/mL LiCl in 80% ethanol +0.1% FA as the solvent is a LESA imaging protocol of non-dieased human liver tissue. Four ions from the full scan spectrum are presented in the top row. Product ions corresponding to lithium adduct of PC(18:2/16:0) are presented in the bottom row.

6.3 Traveling wave ion mobility spectrometry

Previously it has been noted that multiple lipid species have been detected and identified with the same mass to charge ratio and that it is possible to separate them based on their product ions. However this limits the number of species that can be imaged at any point in time. Chromatography techniques increase the analysis time substantially an alternative is ion mobility spectrometry. Traveling wave ion mobility spectrometry is incorporated into the mass spectrometer and separates ions in real time dependant on their average collisional cross section. [160] There are two reports coupling the LESA and the Waters Synpat G2-S, the first [82] investigated spatially targeted quantification of radioactive drug metabolites, this method used the TWIMS results in lower spectral complexity the spectrum to achieve a more sensitive quantification

approach. The second paper did not use the TWIMS, but instead used the ToF capabilities to detect native protein complexes. [246]

Here the LESA was coupled with the TWIMS for spatially resolved lipid and protein analysis.

6.3.1. Liquid extraction surface analysis coupled to traveling wave ion mobility

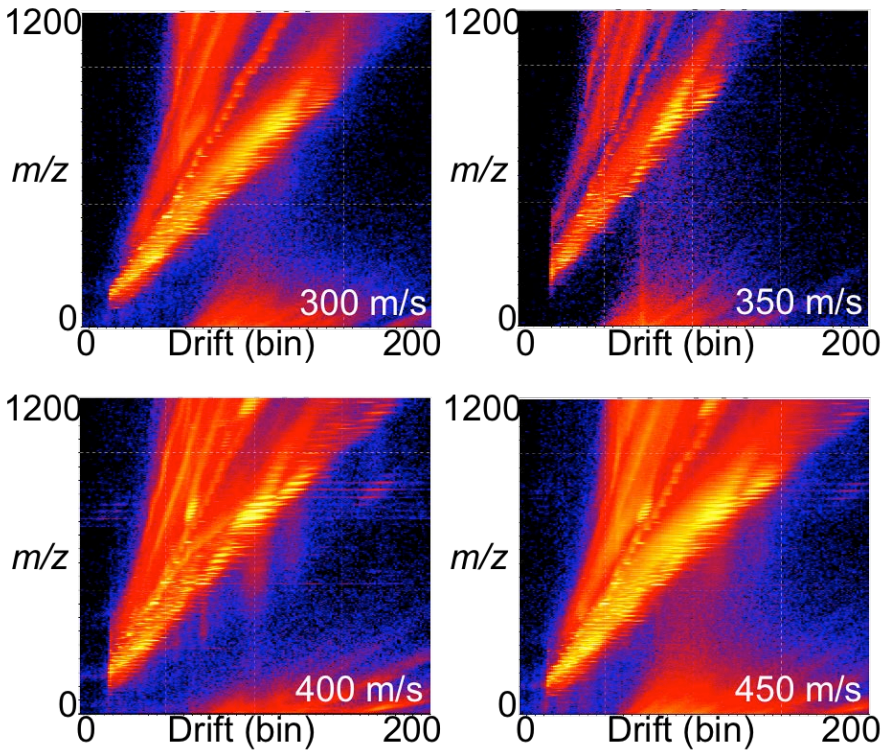

Figure 73: The ion mobility drift scopes that were aquired using 70% methanol +0.1% FA as the solvent in a LESA protocol of non-disease human liver tissue, at four wave velocities.

To tune the TWIMS for specific use the wave velocity is adjusted. In ideal situations ions are transmitted between bin 20 and 180 of the 200 bins available and there should be minimal carry over of ions. A range of wave velocities were analysed from 300 ms to 450 ms in steps of 50 ms. As the velocity is increased

there is a greater degree of separation however the range of bins that a peak is detected also increases. Having the ions spread over a number of bins decreases the overall intensity of the ions. For fragmentation intensity is just as important as separation. Figure 73 shows the drift scopes from the wave velocities, the quality of the drift scope produced using a wave velocity of 350 m/s is lower than the other drift scopes. This is probably due to the spray stability of the LESA extraction from human liver tissue, where the occasional debris can temporally reduce the spray quality for the duration of the data being recorded. The 300 m/s wave velocity there is insufficient separation and with 450 m/s wave velocity many of the peaks have merged back together. The optimum is between these two parameters. At a wave velocity of 400 m/s is the overall ideal compromise for the full scan spectrum there is multiple clear patterns within the drift scope.

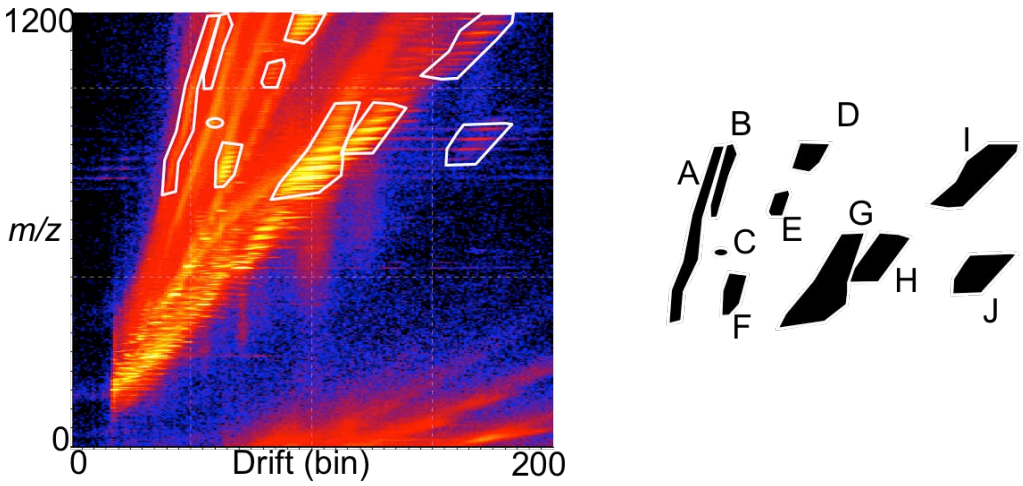

Figure 74: Drift scope using a wave velocity of 400 *m/z*. Spectra of the regions labelled A-F are presented in Figure 75

One of the advantages of using TWIMS is that after the ion mobility data has been recorded is it possible to select a region and extract a spectrum relating to that region. There are several regions of the spectrum that are the product of biological noise, these are species that do not have specific peaks and contribute to the baseline of the spectrum. This can be observed in region A and B, (Figure 74) corresponding spectra can be found in Figure 75. There are many regions that do contribute analyte signal. Ions from panel G are the ions that dominate the spectra in when no ion mobility is applied and have already been identified as lipid species. However, there are many ions that would not typically be noticeable above the baseline, specifically from regions, E, F, I, from Figure 74 (spectra in Figure 75). Regions H and J are particularly interesting, There is a large separation of these ion on the drift scope however the spectra for these regions are almost identical and are dominated by peaks with the same *m/z*. Further investigation is required to determine and what these species are.

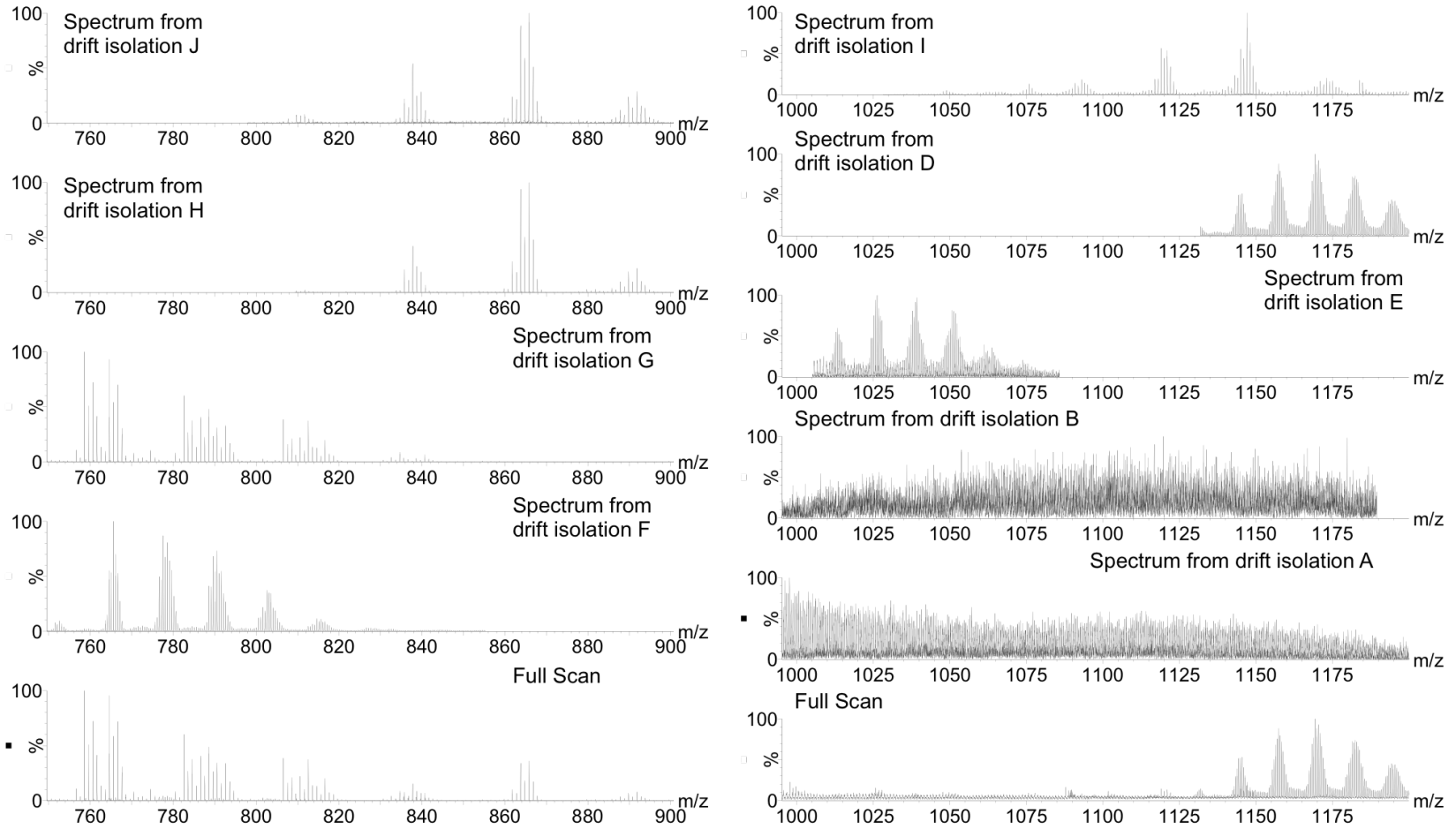

Figure 75: Spectra observed from extracting regions of the driftscope at 400 m/s velocity. A full scan spectrum of the associated region is also provided for comparison. Regions have been seperated based on their mass range, all regions that show ions from m/z 750 to 900 are in the left panal and all regions that show ions from m/z 1000 to 1800 are in the right panel. Letters refer to regions from Figure 74.

Region C on Figure 74 is the isolation of a single peak in drift scope that is part of an extended series of peaks, however it lies on a region of background noise. This drift scope peaks relates to a multiply charged species, in the +5 charge state. This isotopic distribution is completely obscured without the use of ion mobility (Figure 76).

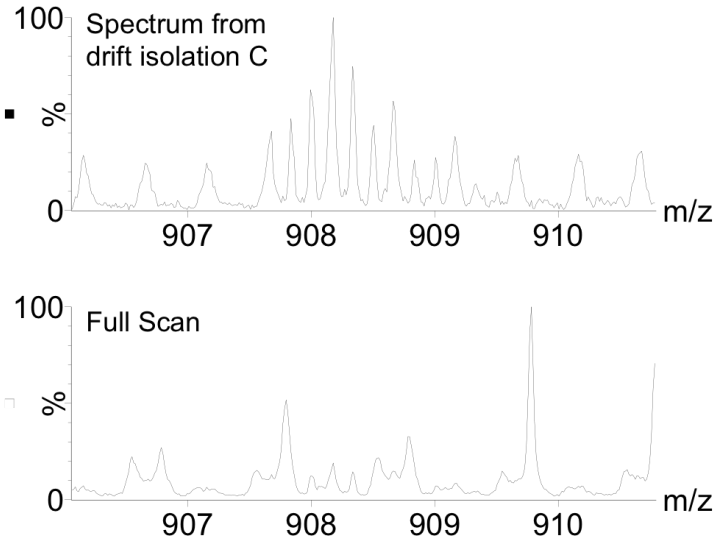

Figure 76: Extracted spectrum from location C from Figure 74 and full scan data from same *m/z* range

The ion mobility cell has an increased pressure due to the gases necessary for the collisions, hindering the progress and causing the separation of ions. A side affect of this the collisions is the possibility of an ion being neutralised, or being redirected out of the ion beam, resulting in a reduction in the number of ions reach the ToF. For MS/MS the isolation of a single mass occurs prior to the ion mobility therefore the only necessary separation occurs for the mass that is being isolated. A wave velocity of 350 m/s was selected because of the more

intense ion isolation that can be produced. For *m/z* 764.5 at this wave velocity the isolation is effective (Figure 77) in the Synapt G2-S there are two locations for fragmentation, before (trapping cell) and after (transfer cell) the ion mobility cell. Fragmentation in the trapping cell prior to ion mobility cell results in the fragments being separated by drift. This would be used to separate intact isobaric species that the mobility cell cannot separate. The mobility of product ions may be used to distinguish between them. Fragmentations in the transfer cell, after ion mobility, results in all the fragments being detected from the same drift bin. This is used to identify ions that occur from the same intact mass. The potential for this method is that that all ions passing through the ion mobility are fragmented, and the fragments are related to the intact ion based on their drift.

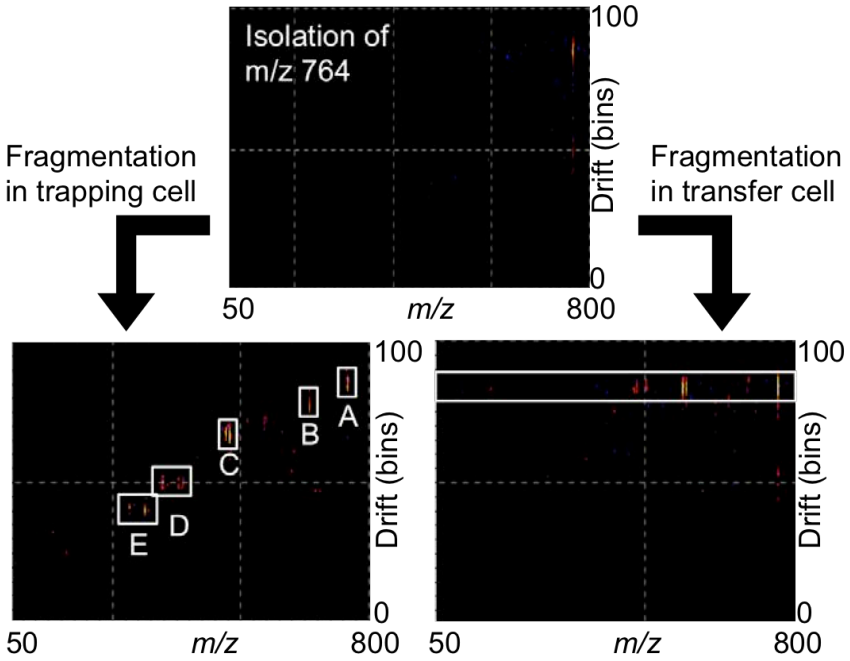

Figure 77: Isolation of *m/z* 764.5 in drift space and the fragmentation of this ion in the trapping cell, prior to ion mobility, and tranfer cell after the ion mobility

Analysis of *m/z* 792.6135 using the Orbitrap mass analyser has shown that a peak at this mass refers to 3 lipids, PC(18:1/18:1)+Li^+, PC(18:0/18:2)+Li^+ and PC(16:0/20:2)+Li^+ (Appendix 26). Using TWIMS in the isolation of *m/z* 792.6135 using a wave velocity of 350 m/s two peaks were present. Fragmentation in the transfer cell enabled the fragments to remain associated with the mobility of the intact ion. Extraction of the fragmentation spectra shows that the main peak with a maximum in bin 126, shows the product ions from the three lipids that were known about. The smaller peaks with a maximum in bin 83, shows the fragmentation of 4 lipids. Three are known and one is new to the investigation, PC(20:0/16:2)+Li^+. Product ions for this lipid are minor peaks in the fragmentation spectrum. Furthermore the smaller drift peak, is a result of smaller ions that relate to a more compact structure whereas the ions from the later drift bins relate to a larger structure. As these two peaks are separate, both structures are stable. This difference may occur due to the placement of the lithium ion during the ionisation.

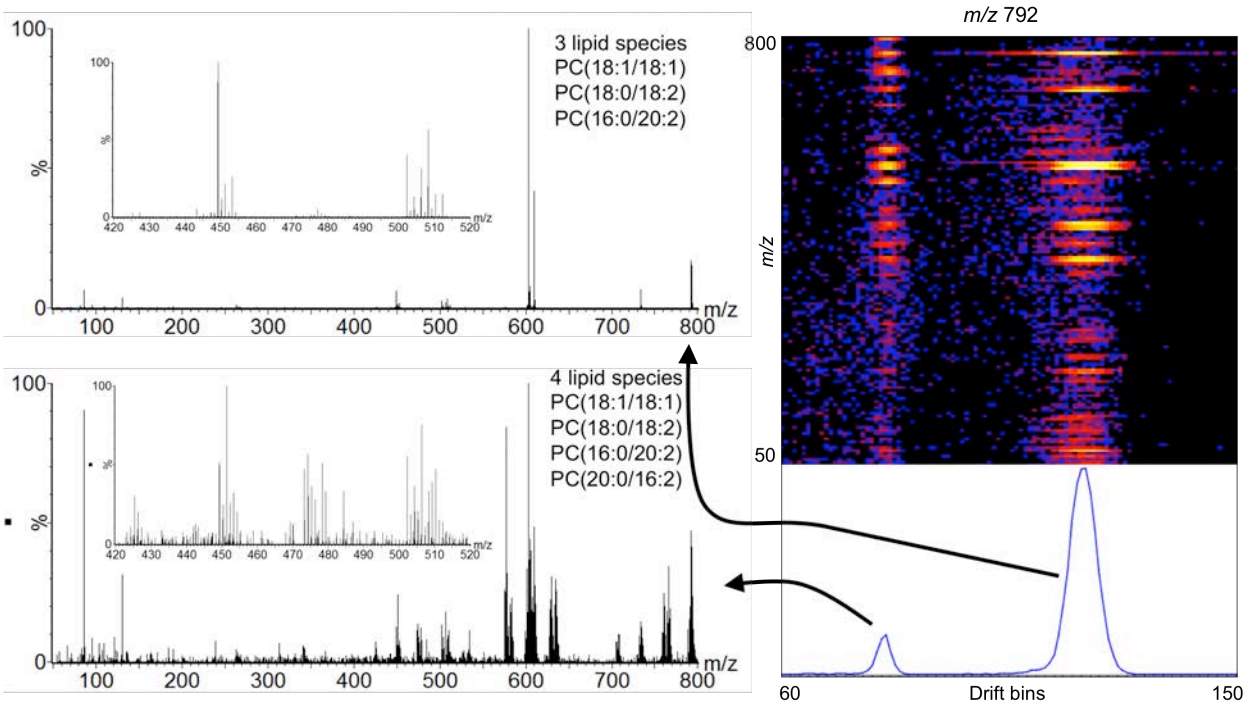

Figure 78: Separation of ions observed *m/z* 792.6135 using traveling wave ion mobility spectrometry and the MS/MS spectra from both the drift peaks detected.

LESA provides a sustainable level of quality in each analysis. Here it has been shown that TWIMS separation reduces spectral complexity enabling more species to be detected. This technique coupled to imaging could be an extremely powerful technique. The simultaneous analysis of lipids and protein that could then be separated during data processing would enable studies into both these species on the same tissue section. In addition coupled to the MS/MS capabilities identification of these species would also be possible. However LESA has a low spatial resolution. A higher spatial resolution can be achieved using techniques such as MALDI.

6.3.2. MALDI

MALDI has been used extensively for imaging lipids [52, 210, 247-249]. Using the Synapt G2-S there are two potential methods for separating isobaric species. The use of MS/MS imaging can separate isobaric species by isolating unique product ions. The alternative is the use of ion mobility, this would rely on the two species having a different integration with an electrical field. In chapter 5 the ultraFAIMS separation occurs due to the folding and unfolding of proteins in a variable electrical field. Here the traveling wave ion mobility separates ions based on collisional cross-section.

6.3.2.1 MS/MS Imaging

There are a wide number of reports using MS/MS imaging [31, 45, 250-252]. A recent report developed a method for introducing lithium in the fixation procedure [45]. The publication reported an MS/MS image of mouse brain tissue, the peak fragmented was the most abundant lipid in the spectrum and was not found to have any isobaric species. Here the same techniques were used to produce an MS/MS of diseased human liver tissue. In this case the method was targeted at low abundant species, which was known to contain multiple isobaric species. The laser energy was optimised so that the spectra contained both the intact ion and the informative peaks (Figure 79).

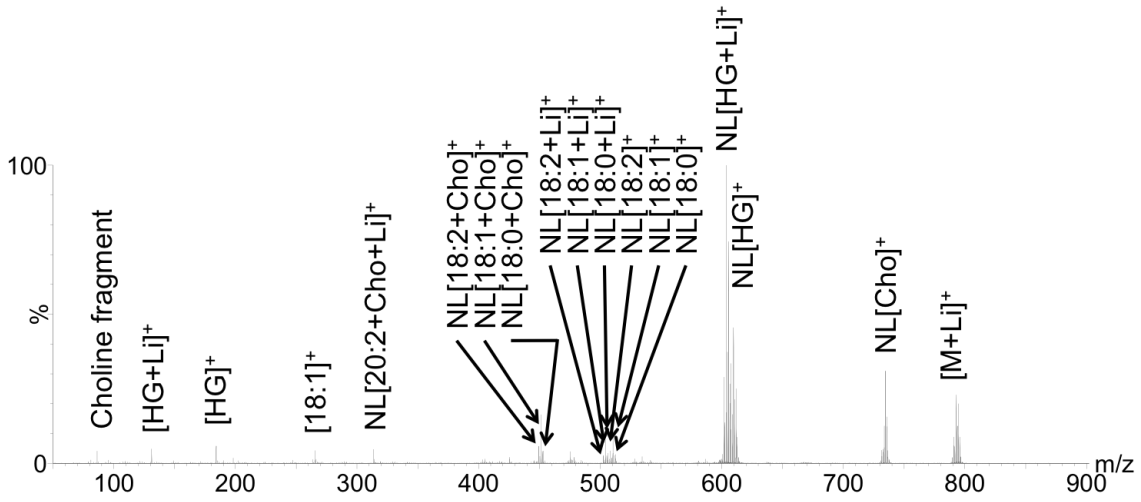

Figure 79: Optimised single scan MS/MS spectra aquired using CHCA as a matrix in a MALDI protocol from NASH liver tissue,

There is a difference between spot mode analysis and imaging analysis. In spot mode analysis, the laser rasters in a specific pattern at a specified rate and spectra are acquired over a period of time. In imaging mode the laser rests in one location and collects the spectra from a specified number of laser shots. As a result, a single scan spectrum during set up can be different to a single scan spectrum during imaging. A single scan spectrum from the imaging data shows a greater degree of fragmentation and with a greater number of the fatty acid acyl chains being detected rather than the neutral loss of these chains.

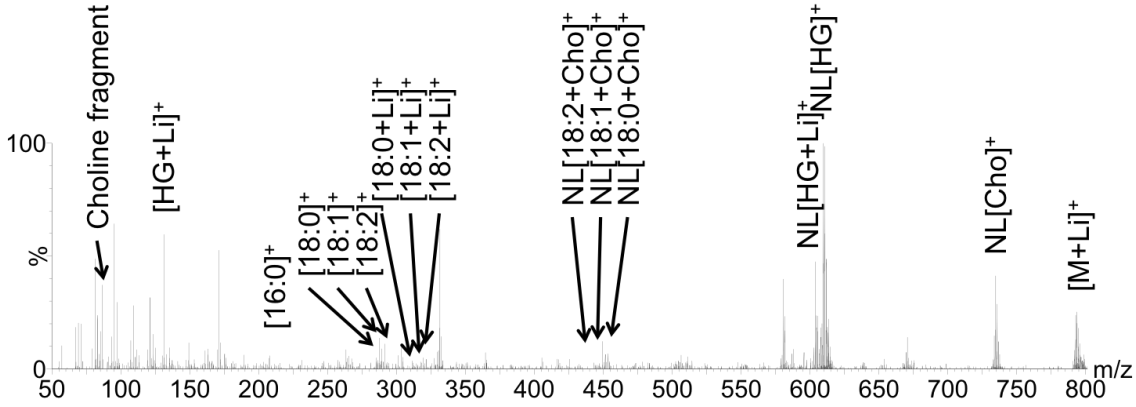

Figure 80: Single pixal spectrum aquired using CHCA as the matrix in a MALDI MS/MS imaging protocol of NASH liver tissue.

PC(18:1/18:1) and PC(18:0/18:2) are the two most abundantly detected lipids at *m/z* 792. The image showing the neutral loss of the head group this is indicative of all the PC lipids. The neutral loss of fatty acid 18:0 is a fragment from the lipid PC(18:1/18:1). Whereas PC(18:0/18:2) has been detected from the neutral loss of the fatty acid chains 18:2 and 18:0.

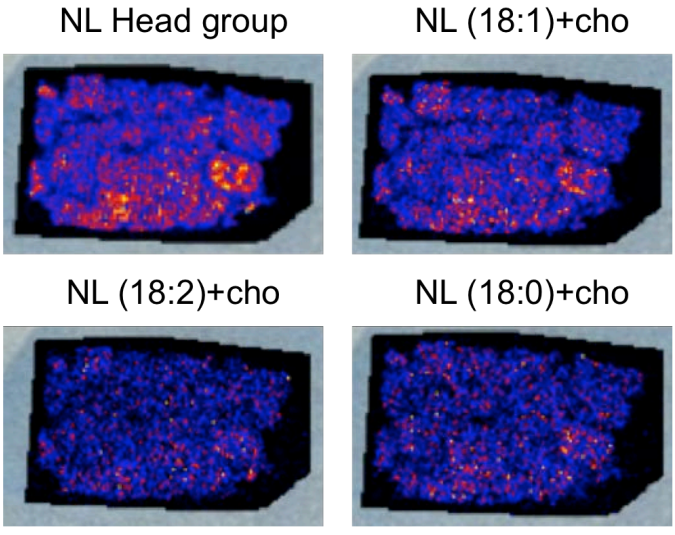

Figure 81: MALDI MS/MS image of 4 product ions of PC(36:2)+Li, from lithium fixed tissue. NL Head group is presecent from all isobaric lipids, NL(18:1)+cho, is only detected from PC(18:1.18:1) and NL (18:2)+Cho and NL(18:0)+cho are two complementary side chains from the lipid PC(18:2/18:0).

6.3.2.2 TWIMS Optimization

The second imaging option with the Synapt G2-S is imaging with the ion mobility. Initially the TWIMS was optimised using a constant wave velocity, (Figure 82) At higher velocity there is optimal separation between the low molecular weight species. However at these velocities larger ions travel through the mobility cell very slowly, this can be seen as ions are carried over into subsequent analysis and appear to have a short mobility time.

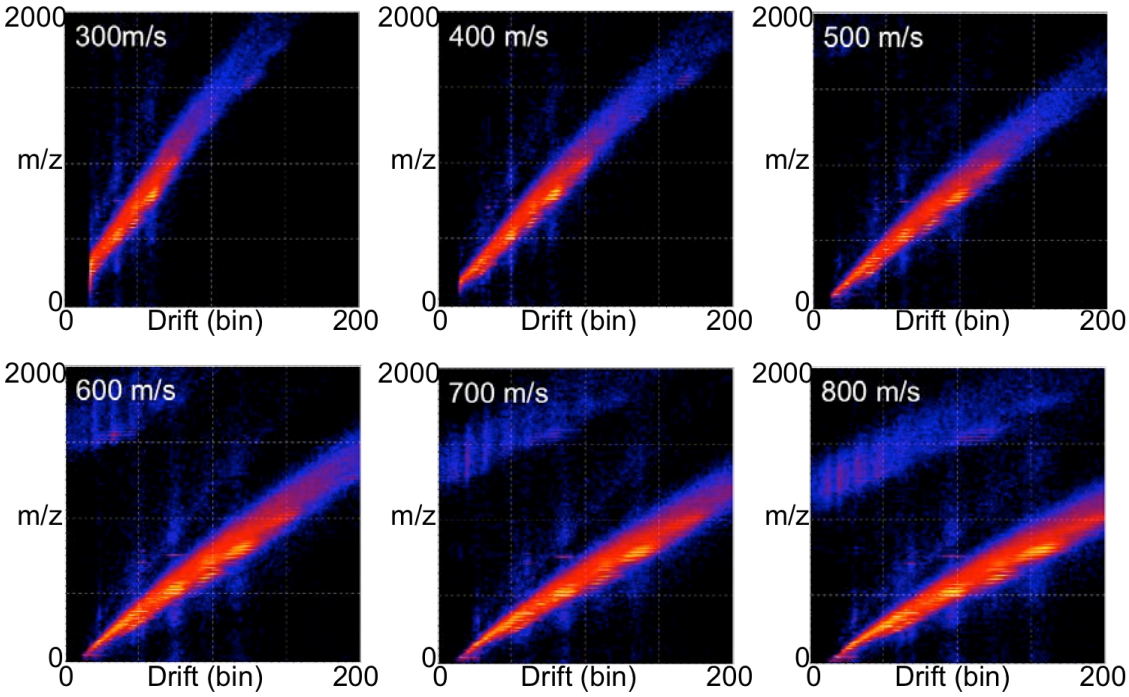

Figure 82: Drift scope of non-diseased human liver samples using 6 wave velosity. Aquired using MALDI surface sampling.

Using variable velocity profile, the wave velocity can be changed during the course of the analysis. The velocity changes along a linear gradient between the start and end velocity. This enables a greater separation of low mass ions, as well as insuring larger ions are completely through the ion mobility prior to

succeeding analysis. The shallowest gradient that can be achieved, that efficiently separates ions without leaving carry over is a gradient from 900 m/s to 300 m/s (Figure 83).

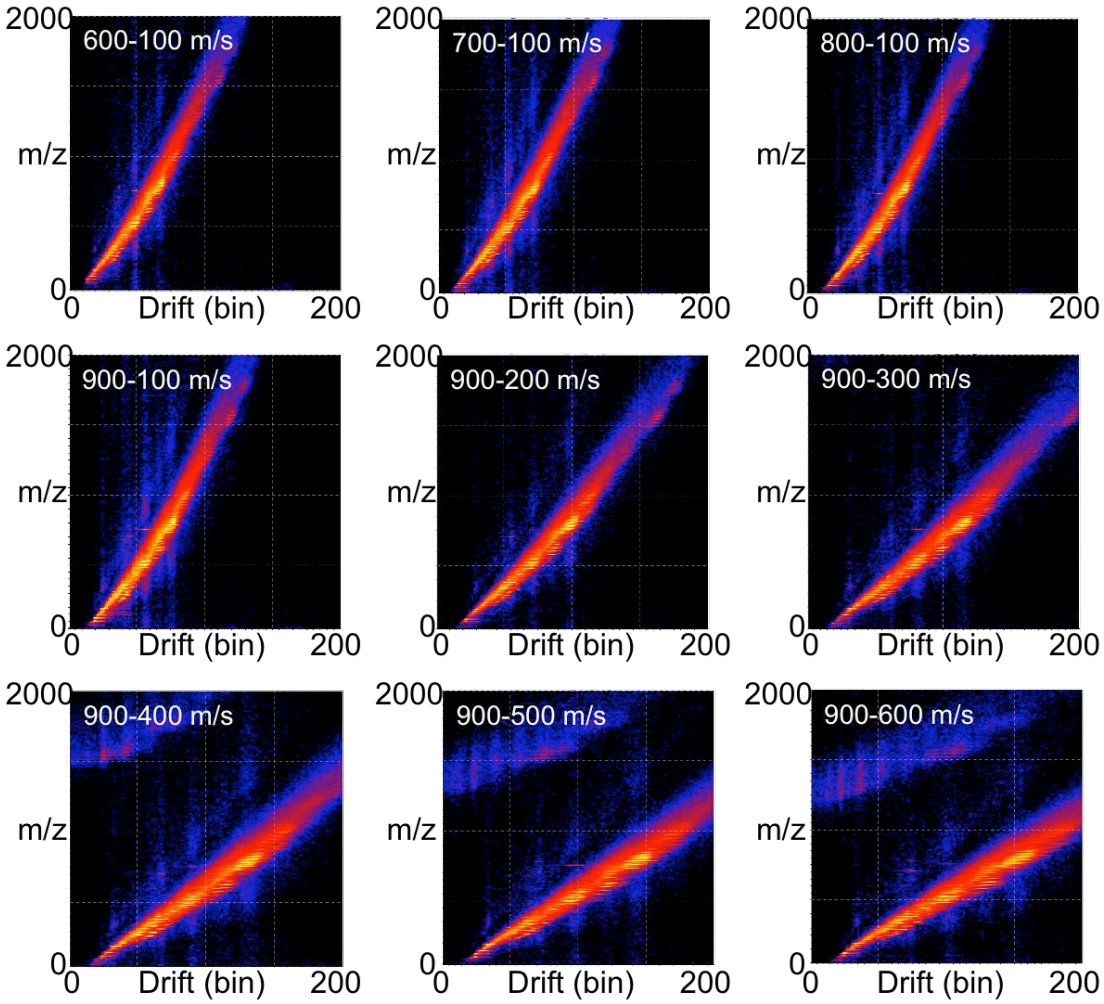

Figure 83: Drift scope of non-diseased human liver samples using variable wave velosity. Aquired using MALDI surface sampling.

6.3.2.2.1 MALDI TWIMS imaging

Combining mass spectrometry and ion mobility for imaging tissue is a newly expanding area, Within the last couple of years numerous publication have combined these two techniques. [253-258] A number of publications show that this technique has a lot of promise. Here six tissue sections were analysed using the optimised ion mobility settings, four non-diseased sections from different donors, and two NASH sections also from separate donors. The advantage of imaging using ion mobility is that it is possible to separate overlapping matrix peaks from tissue specific peaks. There are also cases where two tissue specific peaks are separated, this may be due to different species being detected or it may be due to different conformations of the same ion. There is a particularly interesting instance of two tissue specific peaks at *m/z* 699.42, where one of these peaks is only observed in NASH tissue, the differing spatial locations of these species indicate that the species have different biological functions. Under imaging conditions that would not have used the TWIMS the image would have been interpreted as an ion that is present in both non-diseased and diseased and in some areas of diseased tissue the ion is more intense, this would this would not make the ion particularly interesting. However if an ion is only expressed in diseased tissue this has significant implication into identification and understanding the disease state. Previously the only method to determine if a distribution is due to a single or multiple ions is to conduct

MS/MS imaging. MS/MS imaging is a targeted approach where as the TWIMS is able to analyse multiple ion and can be used as an exploratory technique.

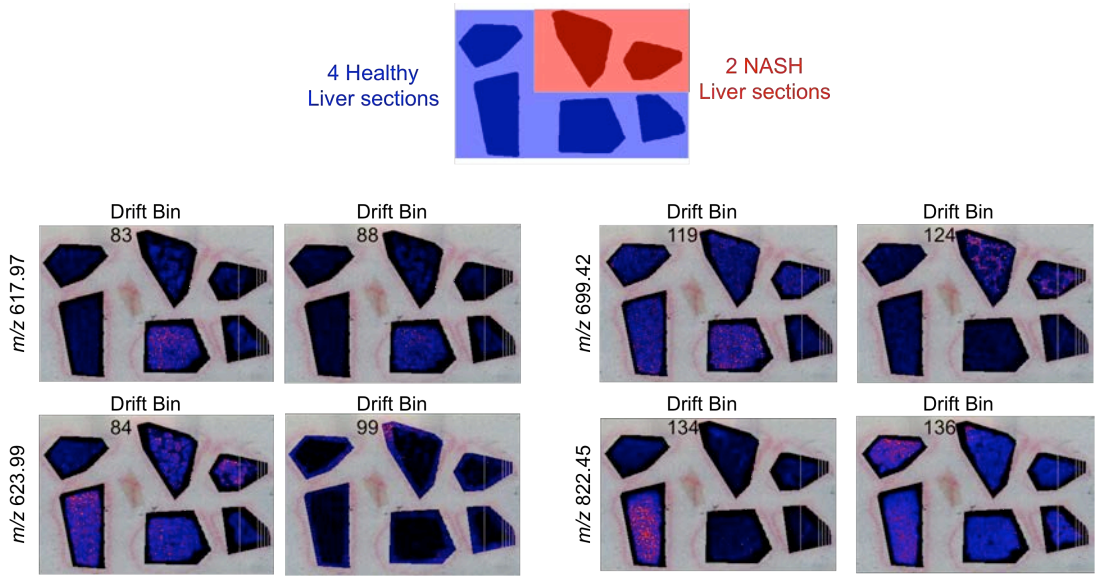

Figure 84: MALDI-TWIMS images aquired using CHCA of 4 non-dieased tissue sections and 2 NASH sections.

Biological samples are extremely complex. The advantages of using ion mobility are evident, real time separation of ions. However there are a number of disadvantages. The TWIMS cell reduces the intensity of the intact ion by approximately 100 fold. This means that conducting TWIMS-MS/MS imaging on my not be possible, as the precursor ion would be too low in abundance for the fragments to be detected. Furthermore due to size of the data sets that are collected and the limited methods for viewing the data, to date only Waters software is capable of visualising ion mobility data from the Synapt G2-S. Vendor specific data reduction tools mean that processing and accessing all of the data is difficult.

6.4 Conclusion

Here it has been shown that HCD coupled to LESA analysis are a powerful combination for the *in situ* identification of lipids. Over 90 lipids were identified from a single location on human liver tissue, spanning several different classes of lipids. Further more the coupling of TWIMS to LESA has shown to be an excellent tool to separate isobaric species with different collisional cross-sections. And can separate different classes of molecules simplifying the spectra revealing more than would have been previously observed, this can all be done post analysis. This means that all the data can be collected initially and the software and data processing can be used to reveal species that would have otherwise gone undetected.

The spatial localisation of LESA sampling has lead to MS/MS imaging of over 14 lipids from a single location. When compared to MALDI analysis form a single location only one lipid can be imaged. The advantage of MALDI MS/MS imaging is that the spatial localisation is a lot smaller enabling distinctive features of the tissue to be observed.

TWIMS analysis on the LESA and the MALDI are distinctly different. LESA is able to detect lipids and proteins using the same extraction solvents where as only lipids were detected using the MALDI source. Further more using the MALDI matrix and matrix cluster contribute significantly to the spectrum, using the TWIMS it is possible to separate using drift matrix related peaks and

tissue related peaks. Imaging using the TWIMS was conducted using the MALDI source. Experimentally a LESA-TWIMS imaging was produced however, the data produced as so large that the software used to view the drift scope could not open the data set. In contrast MALDI-TWIMS images can be processed using specialist software the uses peak picking algorithms to reduce the data size, for imagines to be produced.

The imaging using the MALDI –TWIMS produced imagines of isobaric species that were separated in drift and spatial distributions. This is particularly important form imaging as it is another step towards revealing the true distribution of a species. Three cases were identified, first the separation of a matrix related ion and an analyte ion, the separation of patient specific ion from an analyte common to all patients and possibly the most important the separation between analytes common to all patients and a disease specific analyte. This could only have been done using the MALDI- TWIMS coupling as using LESA the spatial resolution would have been too poor, and without the TWIMS these ion would have been detected using the same mass.

Chapter 7: Conclusions and further work

7.1 Conclusions

This thesis has focus on the capability of the LESA system for the direct sampling of human liver tissue and simultaneous detection of *in situ* lipids and proteins. Investigations into spatial profiling have shown the potential for using this as an explorative technique. The LESA technique benefits from having long acquisition times from a single location. The quality and quantity of data produced out performs other imaging techniques such as MALDI for single pixel data, however LESA cannot compete with spatial resolution of these techniques. The LESA has a large spatial resolution and as a consequence uses large volumes, therefor there is more to analyse resulting in the quality and quantity of data. The spatial resolution and the volume of material to be analysed are inversely proportional. Another benefit of the LESA system is that there is very little sample preparation required. This makes analysis quick and efficient when sampling directly from a surface.

The sample preparation has been used to target lipid and proteins be increased using washing techniques to target proteins, and by optimising the solvents to target and identify lipids or proteins.

Three proteins were identified using top-down methods, including 10 kDa heat shock protein, the beta chain of haemoglobin and the fatty acid binding protein. The FABP was identified from non-diseased and NASH tissue in two forms with a single amino acid variation. The presence of the $FABP_{TA}$ form has been linked to the NASH disease state, in this thesis this was also noted. Both NASH samples analysed contained $FABP_{TA}$ and both non-diseased sampled contained FABP1. Although it should be noted that these were not exclusive, in one of the non-diseased sample $FABP_{TA}$ was detected and in one of the NASH samples, FABP1 was detected. Suggesting that the FABP variant is not solely responsible for the disease.

Enhancing the analysis by digesting the sample and with coupling liquid chromatography revealed three further markers for the NASH disease state. Bottom-up analysis was also able to differentiate between $FABP_{TA}$ and FABP1 however prior to being identified using top-down methods $FABP_{TA}$ was not present in the database and therefore would not have been identified.

An alternative method for enhancing protein analysis has also been utilised. The ultra-high field asymmetric ion mobility spectrometer (ultraFAIMS) has been coupled to LESA to increase the sensitively of direct infusion of LESA by tuning the compensation field, the background noise is removed and protein or lipid signal can be enhanced. This has lead to the observation of many more proteins. This real time ion mobility techniques means that the improved

quality does not come with a time cost. Further more, there are distinctly different optimal dispersion and compensation fields for lipids and proteins, and therefore can be separated post-LESA sampling.

Lipid targeted analysis has revealed more than 80 identified lipids in a 15 min injection many were isobaric species. Using lithium salts and increasing the collision energy for HCD analysis fatty acid backbone fragments were observed this enable to further increase the number of species by being able to assign the location of the double bond. This coupled to spatial profiling 14 lipids were mapped. This is a vast increase in the number lipids that were imaged using MALDI. The spatial resolution for the MALDI image (100μm) was 20 fold smaller than LESA (2mm) however, the sensitivity of the LESA enabled the fragmentation of low abundant lipid species where as the MALDI image of the *m/z* 792, which was a relatively abundant species, occasionally did not show all the informative peaks.

Overall LESA is capable for obtaining spatially resolved data for lipids and proteins. It is an ideal surface sampling technique to be coupled with multiple separation techniques to enhancing the quality of the data.

7.2 Future work.

There are several areas in which the LESA can be developed in imaging, analysis, data processing and biomarker discovery.

The smallest resolution that is possible with the current formatting is the 1mm; this is approximately the diameter of the LESA tip. Reducing the diameter of the tip would reduce the volume of liquid that would be necessary for a LMJ, and recuse the area affected by the LMJ, reducing the resolution. This could be achieved using capillary tubing or using a fused silica tip that had a tapered end to less than 100μm. The disadvantage of using the capillary is that it would not be disposable and therefore would possibly suffer from cross-contamination between injections. Using a fused silica tip would be disposable however there would be cost implications, as these tips would be expensive and for an image of 1mm squared, at 100μm 100 tips would be necessary. Further more there is a time consideration each injection required over 30 s to conduct the LESA with the analysis time current capabilities analyse for 5 min per pixel, the time for acquiring the data for $1mm^2$ would be over 9 hours. Even reducing the time for analysis down, to 1 min per pixel, imaging using the LESA would be incredibly slow. During this time period under ambient conditions, the sample may change during the time course of the experiment. Reducing the area affected in a single liquid micro-junction would also benefit direct sampling of a single location. Enabling more accurate localised representation, of a tissue type or a collection of cells. This coupled with the long analysis time would enable in-depth interrogation from a specific location.

Some methods for improving the quality and quantity of LESA sampling have been demonstrated in this thesis. Investigations into these areas can be

developed further. Coupling the LESA to liquid chromatography would enhance the numbers of intact proteins observed. As proteins will elute over the course of a few scans, it would be possible to fragment the protein in the remaining, time. Identifying variations in amino acid sequences and post-translational modifications are an important part of investigations into disease biomarkers. Function of proteins is determined by their structure, the structure is directly related to the amino acid sequence and any post-translational modifications. Bottom-up, identifications is still very helpful, there are vast databases that include many known biomarkers. Bottom up analysis identified about 500 proteins. This is a fraction of what is contained within tissue, for full in-depth analysis strong cation exchange chromatography can be used to fractionate the sample reducing the complexity of the sample prior to LC analysis, enhancing the numbers of proteins detected. [259]

An alternative method for reducing spectral complexity is using ion mobility. Traveling wave ion mobility and ultra-high field asymmetric ion mobility spectrometry have been used to enhance spectra acquired in this thesis. There is scope for further investigations, several features of the Synapt G2-S were not utilised in this thesis, and wide-band enhancements is one of these features. This synchronises the pusher of the ToF to a specific *m/z* being transmitted at each bin of the TWIMS, this would increase the sensitivity of specific masses. This would aid a specific band of analytes of interest and would reduce the contribution of other analyse. This has the potential to counteract the reduction

of sensitivity that is observed using the TWIMS. This would be particularly useful for MS/MS analysis of low abundant ions. There are also capabilities to calculating the collisional cross section of molecules. There is also a function on the TWIMS called MS^E, this is where all ions passing through the TWIMS are fragmented in the transfer cell. Product ions that are related to each other will occur in the same bin. This would be particularly useful for explorative techniques, to identify as many analytes as possible in the same injection or location. The transmission of ions through the TWIMS is portioned to the size average collisional cross section. By calibrating the TWIMS it would be to state that one conformation is larger than another by a specific amount.

Imaging using the TWIMS has a lot of potential. MALDI MS/MS imaging was conducted without using as the intensity of these ions from a single location is relatively low, however with the wide band enhancement mentioned previously it may be possible to conduct MALDI MS/MS imaging using TWIMS separation. In addition MS^E analysis would insure the identity of a precursor ion throughout the imaging process, without having to conduct subsequent imaging runes for each individual ion. Conducting LESA spatial profiling on the Synapt is possibly however there are some technical obstacles to over come first. The synapt and the LESA technology are currently incompatible, for example the data acquisition is not triggered by the contact closure of the LESA resulting in the data being collected in one long file, alternatively the user creates and names a data file for each location during the

sampling process. In house data processing methods are able to process this type of data, however currently the processing of TWIMS data is only available using vendor specific software such as HDimaging and MassLynx. Only HDimaging can process imaging data, however the software assumes a MALDI source where there is one spectrum per location. In LESA analysis multiple spectra are acquired for a single location and the spectra for the pixel is the average. There is no software suitable for this kind of analysis at this current moment in time, which makes processing images a long task. Suitable software would enhance the user experience enabling the LESA TWIMS spatial profiling to reach it's full potential, analysing lipids and proteins, with capabilities of fragmenting and potentially identifying every peak in the image.

Ion mobility spatial profiling with the LESA would be possible using the ultraFAIMS. Conducting a series of static analysis or a single sweep at each location would be possible with the LESA where the analysis time for each location can be up to 5 min. This will enhance the spectra quality for multiple analytes, for example using extraction conditions suitable for lipids and proteins, and differentiating between them using the ultraFAIMS, enhancing the sensitivity of LESA.

Data processing is currently and will become more difficult. By using multiple separation techniques liquid chromatography and ion mobility, there is an increase in the dimensionality of the data acquired. The increased data sizes

that this produces can make processing the data more difficult. Strategies to manage this data have been developed [260-262] and will need to be continually developed as data sizes continue to expand.

There is potential for numerous instrumental developments using the LESA and coupled instrumentation, some have been mentioned. The other aspect of this thesis has been furthering the understanding of the human liver and the NASH disease state. The work included in this thesis has looked at four patient samples, to draw biologically significant conclusions it would be necessary to expand the number of patient samples. It is also unclear how $FABP_{TA}$ contributes to the disease, weather individuals with $FABP_{TA}$ in non-diseased livers at the time of biopsy go on to develop NASH later in life, and if every individual with NASH disease has the $FABP_{TA}$ variant. Further more, early research into the identification of these proteins determined the amino acid sequence from the DNA sequence [263, 264]. It is possible that this is an inherited aspect of the disease, however, errors in copying DNA in cell replication may introduce this fault later in life.

LESA has shown its self to be an extremely powerful technique, with potential to answer important biologically significant questions.

Appendix 1 – Relative molecule masses of proteins detected from tissue using 40% acetonitrile with and without a prior wash.

40% Acetonitrile	
No Wash	Ethanol Wash
MW	MW
15858.2571	15858.3208
15278.9684	15856.2641
15117.8356	15117.9084
15087.8610	14111.4080
14111.3973	14081.3555
14081.3079	10836.8616
10836.7687	10835.8622
9949.9868	9950.0196
8559.5974	8560.6326
6106.1696	7018.1799
6081.2177	6107.2729
3440.5199	6080.2142
3369.4853	5354.7798
	4961.5025
	3484.5137
	3462.4956
	3440.5231
	3369.4865

Appendix 2 – One-way Anova Statistical analysis for dipped tissue analysis.

m/z 1081

Total Sum of Squares = 3.55×10^{14} with 8 degrees of freedom
Sum of Squares within groups = 1.29×10^{14} with 3 degrees of freedom

Sum of Squares between groups = 2.25×10^{14}

F=4.65

$F_{critical}$ 95% = 4.07

m/z 1084

Total Sum of Squares = 2.54×10^{14} with 8 degrees of freedom
Sum of Squares within groups = 1.00×10^{14} with 3 degrees of freedom

Sum of Squares between groups = 1.53×10^{14}

F=4.08

$F_{critical}$ 95% = 4.07

m/z 1087

Total Sum of Squares = 2.49×10^{14} with 8 degrees of freedom
Sum of Squares within groups = 1.41×10^{14} with 3 degrees of freedom

Sum of Squares between groups = 1.08×10^{14}

F=2.03

$F_{critical}$ 95% = 4.07

Appendix 3 — Intensity of ions from repeated extractions from the same location.

Surveying a sample with a liquid micro-junction may be considered a local washing step. The effect of multiple, serial extractions at the same x, y co-ordinate was evaluated using ~70% methanol. The absolute abundances of selected ions detected in ten sequential extractions are presented. The change in intensity of ions in sequential extractions may be explained by the effect of repeated washing steps, depleting surface salts.

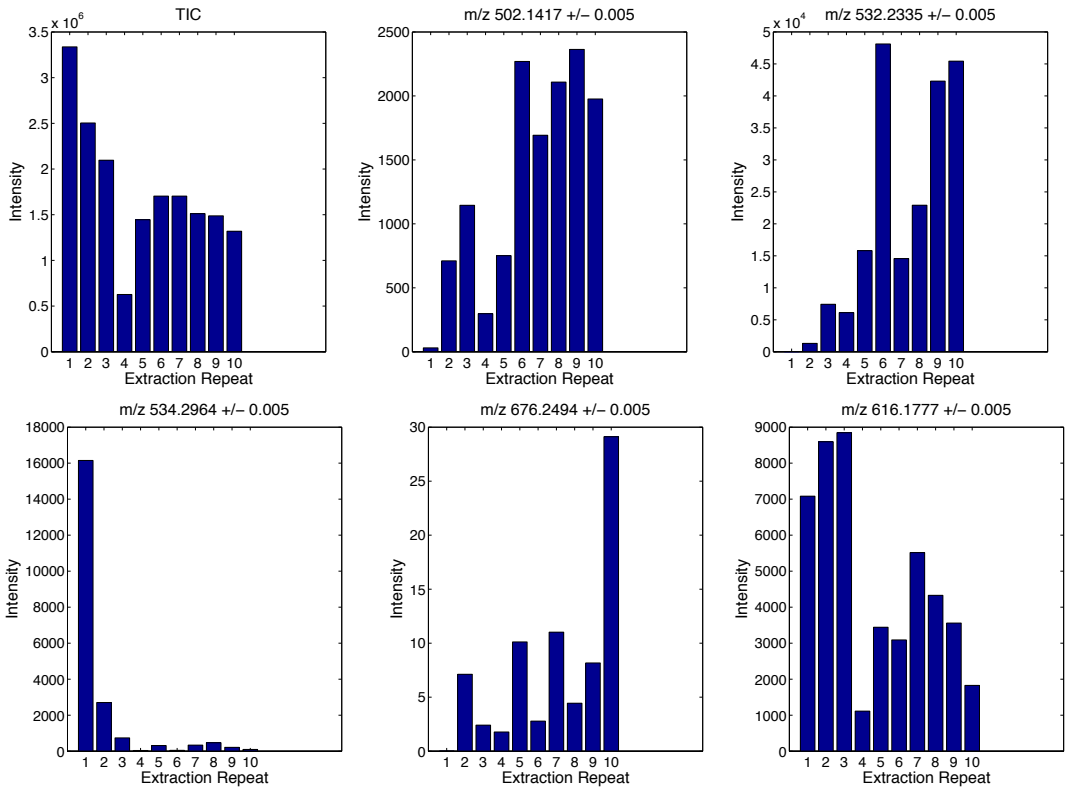

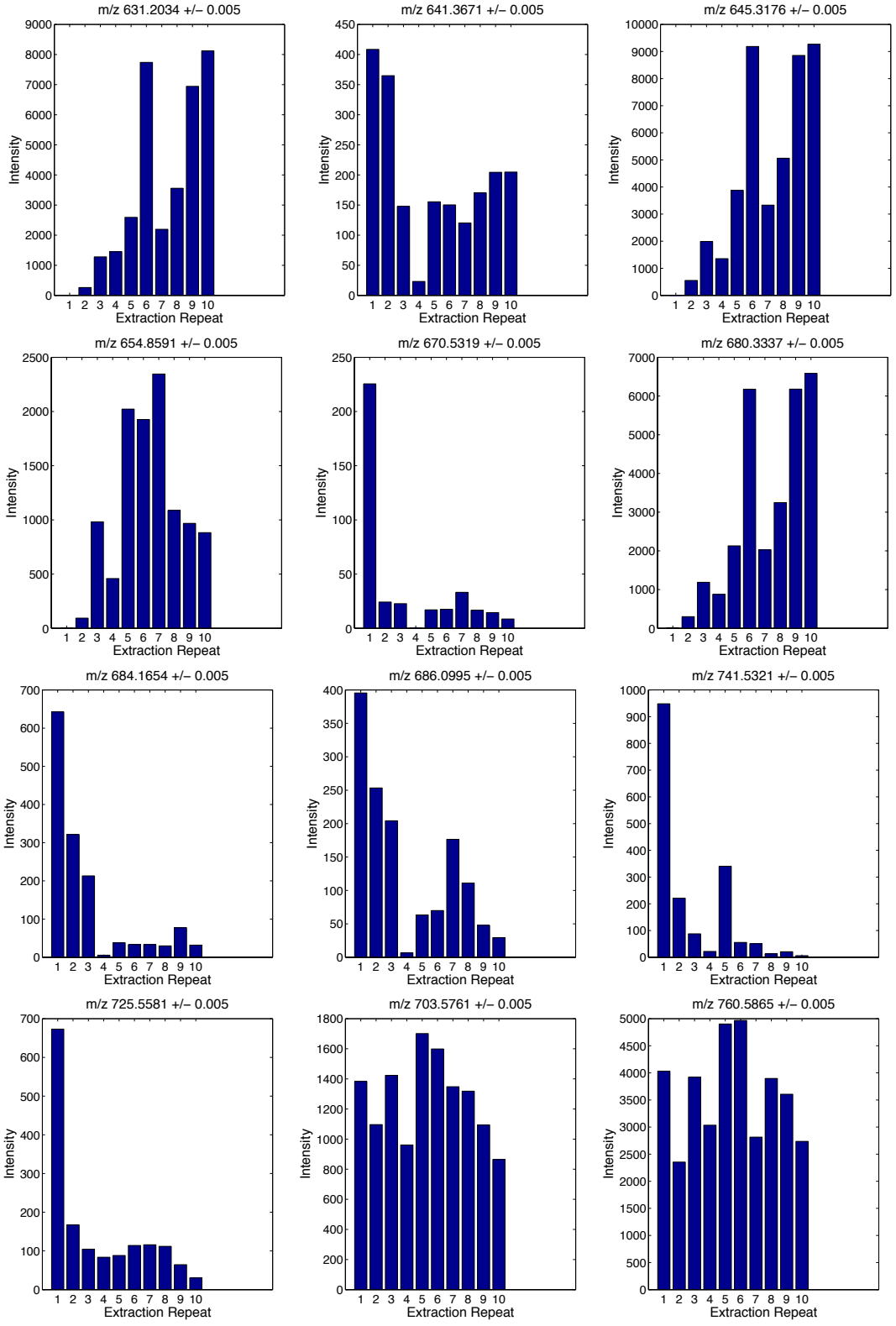
m/z 631.2034 +/– 0.005
m/z 641.3671 +/– 0.005
m/z 645.3176 +/– 0.005
m/z 654.8591 +/– 0.005
m/z 670.5319 +/– 0.005
m/z 680.3337 +/– 0.005
m/z 684.1654 +/– 0.005
m/z 686.0995 +/– 0.005
m/z 741.5321 +/– 0.005
m/z 725.5581 +/– 0.005
m/z 703.5761 +/– 0.005
m/z 760.5865 +/– 0.005
Intensity
Extraction Repeat

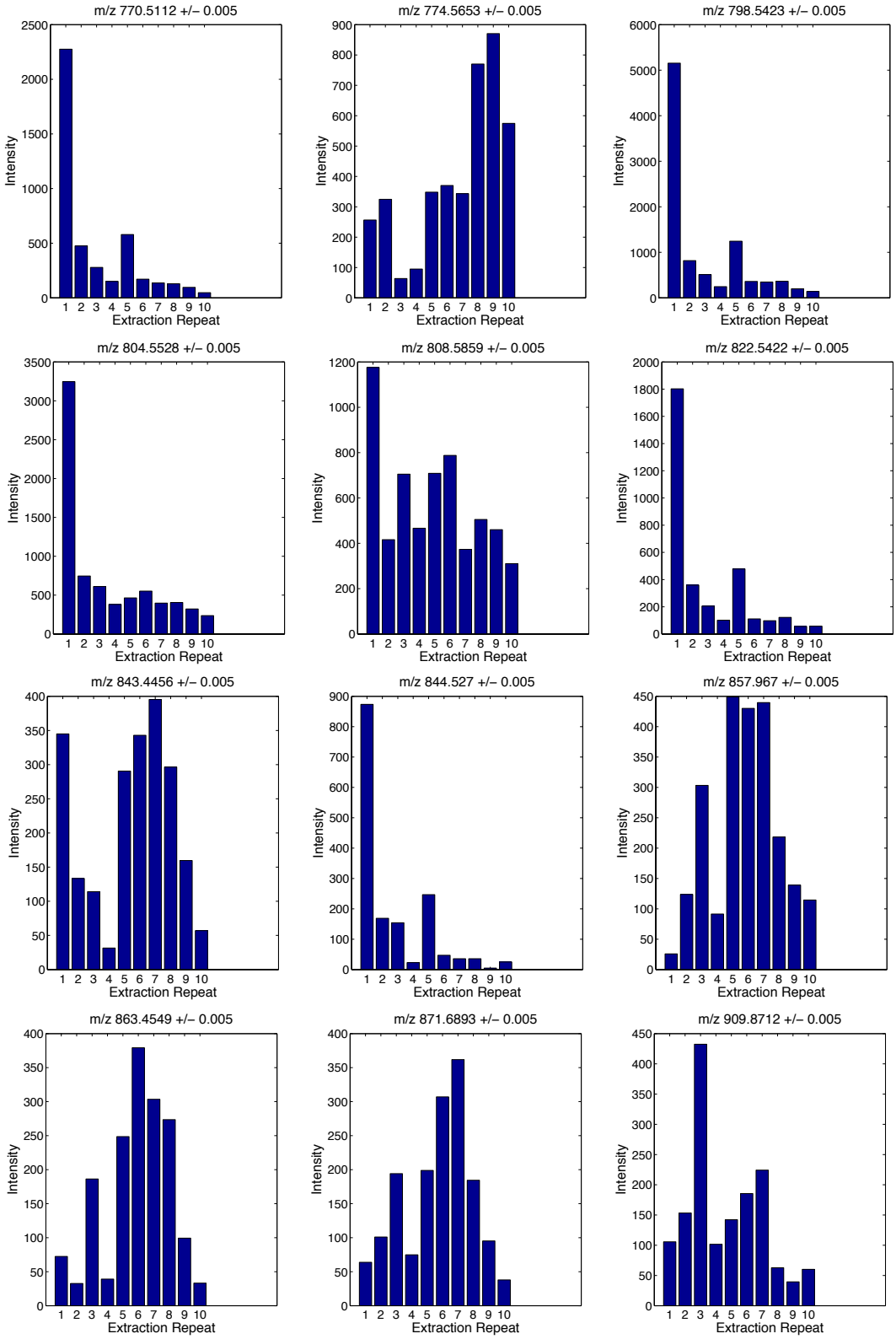
m/z 770.5112 +/– 0.005
m/z 774.5653 +/– 0.005
m/z 798.5423 +/– 0.005
m/z 804.5528 +/– 0.005
m/z 808.5859 +/– 0.005
m/z 822.5422 +/– 0.005
m/z 843.4456 +/– 0.005
m/z 844.527 +/– 0.005
m/z 857.967 +/– 0.005
m/z 863.4549 +/– 0.005
m/z 871.6893 +/– 0.005
m/z 909.8712 +/– 0.005
Intensity
Extraction Repeat

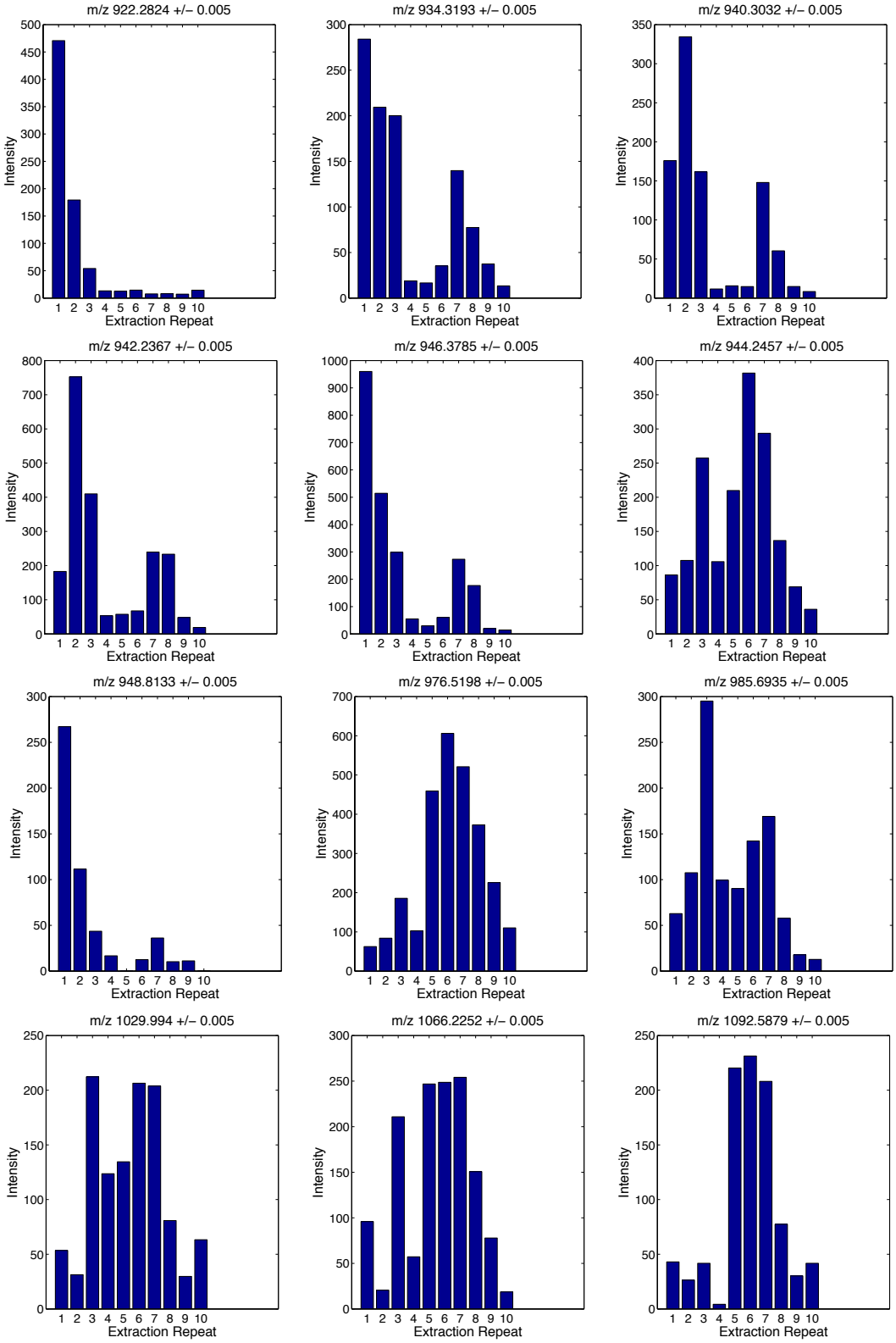
m/z 922.2824 +/– 0.005
m/z 934.3193 +/– 0.005
m/z 940.3032 +/– 0.005
m/z 942.2367 +/– 0.005
m/z 946.3785 +/– 0.005
m/z 944.2457 +/– 0.005
m/z 948.8133 +/– 0.005
m/z 976.5198 +/– 0.005
m/z 985.6935 +/– 0.005
m/z 1029.994 +/– 0.005
m/z 1066.2252 +/– 0.005
m/z 1092.5879 +/– 0.005
Intensity
Extraction Repeat

Appendix 4 – Graphs showing the effects of the automatic gain control on noise, signal and resolution.

A) The intensity of peaks detected from non-diseased human liver tissue with the AGC on and the AGC off at 5 fill times.

B) The noise associated with peaks detected in A, calculated by Xcalibur software.

C) The signal to noise ratio of peaks detected from non-diseased human liver tissue. Data Collected on an Orbitrap.

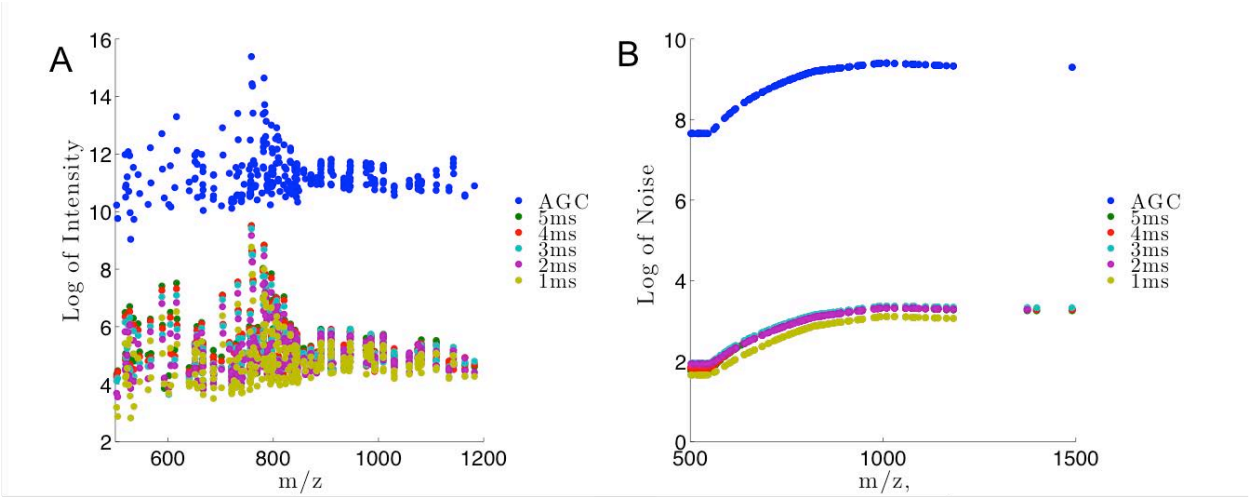
A
Log of Intensity
m/z
AGC
5ms
4ms
3ms
2ms
1ms
B
Log of Noise
m/z,
AGC
5ms
4ms
3ms
2ms
1ms

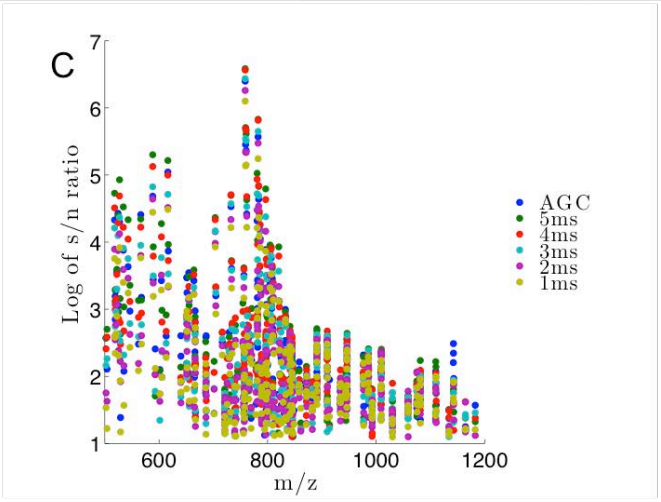
C
Log of s/n ratio
m/z
AGC
5ms
4ms
3ms
2ms
1ms

Appendix 5 — Graph showing the effects of the automatic gain control on the signal to noise ratio

The resolution of peaks detected from non-diseased human liver tissue using LESA with the AGC on and the AGC off at five different fill times, calculated using Xcalibur software. Data Collected on an Orbitrap

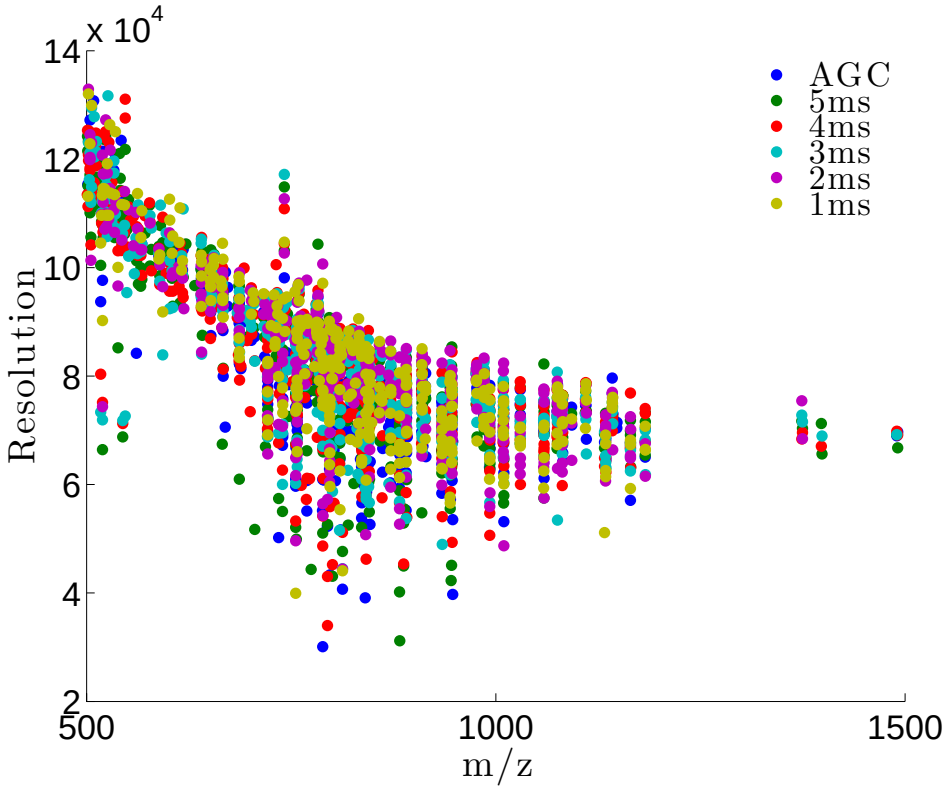

The deviation of mass accuracy of common peaks detected from non-diseased human liver tissue via LESA from the AGC on condition to the AGC off conditions. Horizontal lines are the average ppm shift.

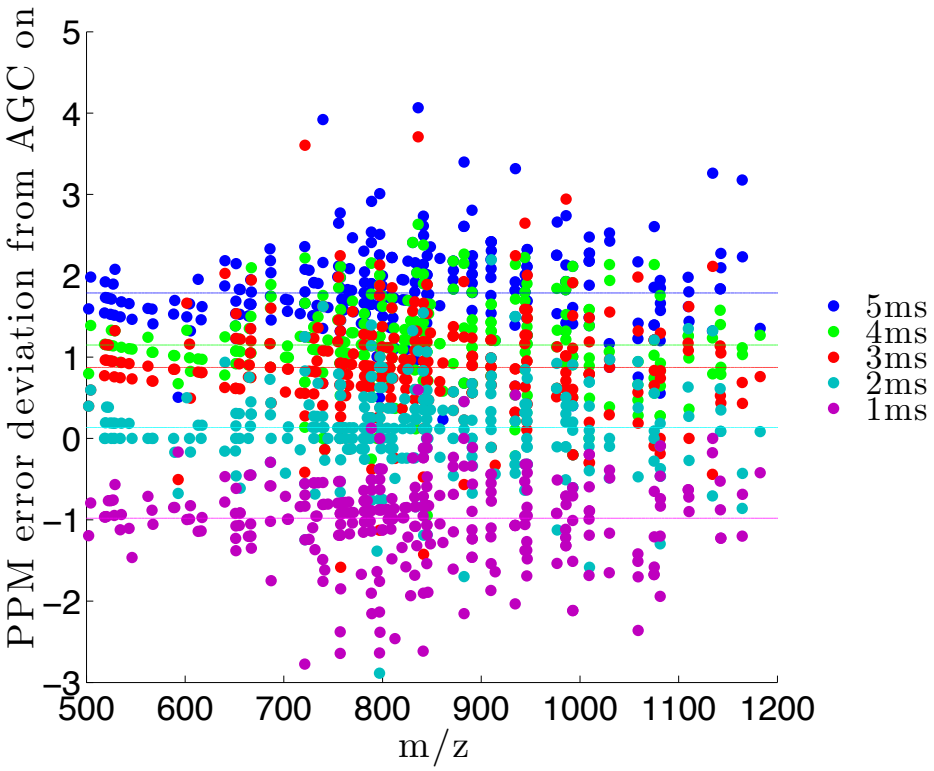

Appendix 6 — Average spectrum from 1mm spaced LESA image

Average spectrum of all pixels (60) from spatial profiling data set. including all tissue and non-tissue pixels.

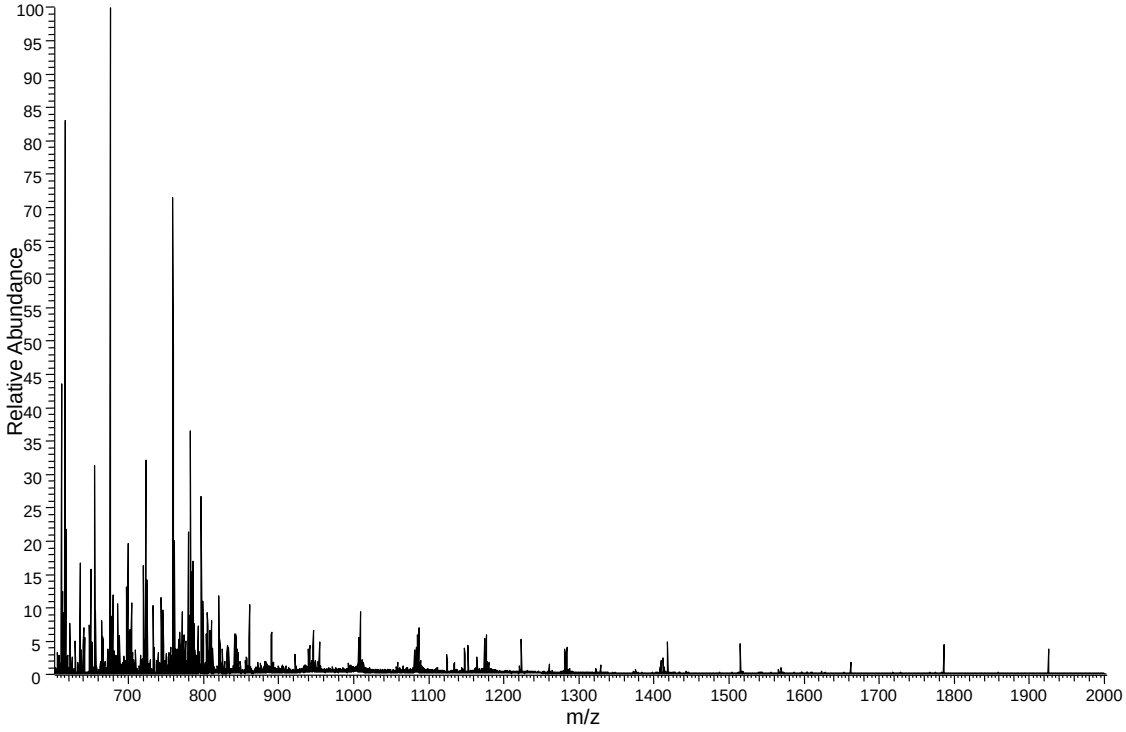

Appendix 7 – Publication: Top-Down and Bottom-Up Identification of Proteins y Liquid Extraction Surface Analysis Mass Spectrometry of Non-diseased and Diseased Human Liver tissue

J. Am. Soc. Mass Spectrom. (2014) 25:1953–1961
DOI: 10.1007/s13361-014-0967-z

RESEARCH ARTICLE

Top-Down and Bottom-Up Identification of Proteins by Liquid Extraction Surface Analysis Mass Spectrometry of Healthy and Diseased Human Liver Tissue

Joscelyn Sarsby,[1,2,3] Nicholas J. Martin,[3] Patricia F. Lalor,[4] Josephine Bunch,[1,5,6] Helen J. Cooper[3]

[1]Physical Sciences of Imaging in the Biomedical Sciences Doctoral Training Centre, University of Birmingham, Edgbaston, Birmingham, B15 2TT, UK
[2]School of Chemistry, University of Birmingham, Edgbaston, Birmingham, B15 2TT, UK
[3]School of Biosciences, University of Birmingham, Edgbaston, Birmingham, B15 2TT, UK
[4]Centre for Liver Research and NIHR BRU, School of Immunity and Infection, University of Birmingham, Edgbaston, Birmingham, B15 2TT, UK
[5]School of Pharmacy, Boots Science Building, University Park, University of Nottingham, Nottingham, NG7 2RD, UK
[6]*Present Address:* National Physical Laboratory, Hampton Road, Teddington, Middlesex TW11 0LW, UK

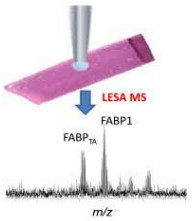

Abstract. Liquid extraction surface analysis mass spectrometry (LESA MS) has the potential to become a useful tool in the spatially-resolved profiling of proteins in substrates. Here, the approach has been applied to the analysis of thin tissue sections from human liver. The aim was to determine whether LESA MS was a suitable approach for the detection of protein biomarkers of nonalcoholic liver disease (nonalcoholic steatohepatitis, NASH), with a view to the eventual development of LESA MS for imaging NASH pathology. Two approaches were considered. In the first, endogenous proteins were extracted from liver tissue sections by LESA, subjected to automated trypsin digestion, and the resulting peptide mixture was analyzed by liquid chromatography tandem mass spectrometry (LC-MS/MS) (bottom-up approach). In the second (top-down approach), endogenous proteins were extracted by LESA, and analyzed intact. Selected protein ions were subjected to collision-induced dissociation (CID) and/or electron transfer dissociation (ETD) mass spectrometry. The bottom-up approach resulted in the identification of over 500 proteins; however identification of key protein biomarkers, liver fatty acid binding protein (FABP1), and its variant (Thr→Ala, position 94), was unreliable and irreproducible. Top-down LESA MS analysis of healthy and diseased liver tissue revealed peaks corresponding to multiple (~15–25) proteins. MS/MS of four of these proteins identified them as FABP1, its variant, α-hemoglobin, and 10 kDa heat shock protein. The reliable identification of FABP1 and its variant by top-down LESA MS suggests that the approach may be suitable for imaging NASH pathology in sections from liver biopsies.
Key words: LESA, Liquid microjunction, Ambient, Bottom-up, Top-down, Proteomics

Received: 28 March 2014/Revised: 10 July 2014/Accepted: 15 July 2014/Published online: 3 September 2014

Introduction

Nonalcoholic steatohepatitis (NASH) is an inflammatory condition of the liver that mimics the damage caused by alcohol without the consumption of large quantities of alcohol. The disease is characterized by the presence of steatosis and fibrosis that can lead to cirrhosis. The lobular destruction and cell loss characteristic of cirrhosis compromise liver function and ultimately lead to liver failure [1]. Causes of the disease remain to be fully characterized but both genetic predisposition and lifestyle choices are important [2]. In common with other liver diseases, serum biomarkers such as elevated amino transferases and a glutamyltransferase are found in patients with NASH, but to date no disease-specific profile of biomarkers

Electronic supplementary material The online version of this article (doi:10.1007/s13361-014-0967-z) contains supplementary material, which is available to authorized users.

Correspondence to: Josephine Bunch; *e-mail:* josephine.bunch@npl.co.uk, Helen Cooper; *e-mail:* h.j.cooper@bham.ac.uk

has been reported. However, changes in the liver fatty acid binding protein [1, 3–5] show promise. Liver fatty acid binding protein (FABP1 or L-FABP) is a regulator of hepatic lipid metabolism. Recent work by Peng et al. [6] has shown that two single nucleotide polymorphisms in the *FABP1* gene are associated with increased risk of developing non-alcoholic fatty liver disease. The first results in substitution of threonine for alanine at position 94 in FABP1, whereas the second is intronic. Increased risk of disease is linked to the two single nucleotide polymorphisms both individually and cumulatively; however, the mechanisms by which these polymorphisms contribute to the disease process are unknown. Recent work by Huang et al. [7] suggests that the Thr→Ala substitution alters the structure of FABP1 and the conformational changes that accompany binding of long chain fatty acids.

In the present work, we seek to determine whether liquid extraction surface analysis mass spectrometry (LESA MS) of thin tissue sections from human liver could be applied to the study of NASH. Specifically, the aim was to determine whether the approach could be applied for the analysis of protein biomarkers of the disease, with particular emphasis on FABP1 and its Thr→Ala variant. Both bottom-up and top-down approaches have been considered. In the former, endogenous proteins were extracted from the tissue and subjected to automated tryspin digestion [8] before the resulting peptides were analyzed by LC-MS/MS, and in the latter, endogenous proteins were extracted and analyzed intact [9].

LESA, also known as liquid microjunction surface sampling, has the potential to become a useful tool in mass spectrometry imaging of proteins. The technique involves deposition of a solvent droplet from a pipette tip onto a surface [10–12]. The solvent droplet maintains contact with both the surface and the pipette tip for a defined time period (a few seconds) before being re-aspirated. The resulting sample can either be directly electrosprayed or subjected to further manipulation before mass spectrometry analysis. In the present work, automated LESA was performed.

LESA mass spectrometry of intact proteins was first demonstrated by Van Berkel and coworkers [13]. They used a continuous flow liquid microjunction system coupled with an ion trap mass spectrometer to analyze lysozyme protein standard (14.3 kDa) spotted onto a glass surface. Earlier work from our laboratory demonstrated that LESA MS was suitable for the top-down analysis of proteins from dried blood spots. The approach was applied to the screening for known hemoglobin variants [14, 15] and to the diagnosis of unknown hemoglobin variants [16] (~15 kDa) in neonatal samples. A continuous flow version of the LESA technology has been applied to the analysis of hemoglobin in dried blood spots from sheep [13]. More recently, manual LESA was applied to sampling of intact proteins from thin tissue sections of bovine lens, and murine brain and kidney [9].

In order for LESA to be coupled with bottom-up proteomics, a proteolytic digestion step needs to be introduced into the workflow. Two approaches exist; in the first, intact proteins are extracted by LESA prior to digestion [8], and in the second, in-situ digestion is performed prior to liquid microjunction extraction [17, 18]. The first approach was applied to the analysis of dried blood spots, identifying over 100 proteins, and made use of the Advion TriVersa NanoMate (Advion Biosciences, Ithaca, NY, USA) for both the liquid microjunction extraction and the automated digestion procedure. A key challenge for the latter approach is preventing evaporation of the trypsin solution. In-situ digestion was demonstrated for protein arrays (cytochrome *c*, myglobin, and bovine serum albumin) printed on a biomaterial substrate commonly used for cell culture [19]. Quanico et al. [17] applied the in-situ digestion approach, via repeated deposition of trypsin solution, to the analysis of thin tissue sections from frozen rat brain. The approach was subsequently applied to formalin-fixed and paraffin-embedded tissue sections from fallopian tube cancer biopsies [18].

Here, we apply LESA coupled with high resolution MS and MS/MS to survey proteins in sections of human liver. A bottom-up proteomics approach in which intact endogenous proteins are extracted by LESA prior to automated trypsin analysis is compared with a top-down approach in which the proteins are extracted and directly introduced into the mass spectrometer. The bottom-up approach identified more proteins than the top-down approach. Nevertheless, bottom-up identification of FABP1 and its variant is irreproducible, whereas the top-down approach reliably identified this potential biomarker of nonalcoholic liver disease. The results suggest that top-down LESA MS may be a suitable approach for imaging NASH pathology in sections from liver biopsies.

Methods

Sample Preparation

The work was approved by the NHS Walsall Local Research Ethics Committee (98/CA5192). All patient liver tissue was collected at The Queen Elizabeth Hospital in Birmingham with written informed patient consent. Healthy liver tissue was collected from donor material surplus to transplantation requirements or from resection margin specimens. Diseased liver specimens were collected upon transplantation surgery. All samples were rapidly processed and snap-frozen in liquid nitrogen prior to storage at –80°C.

Sections of normal human liver tissue of area approximately 1.5 cm^2 were obtained at a thickness of 10 µm using a CM1810 cryostat (Leica Microsystems, Wetzlar, Germany) and thaw mounted onto glass slides.

Bottom-Up LESA Mass Spectrometry of Human Liver Tissue Sections

Intact proteins were extracted from healthy human tissue via automated LESA. Samples were mounted onto a 96-well microtiter plate (Thermo Scientific, Loughbrough, UK) and placed in the TriVersa NanoMate nanoelectrospray device. Three of the sample wells contained extraction solvents: one contained 50 mM ammonium bicarbonate, one contained 50% methanol, and one contained 70% methanol. A fourth well

contained 0.1 μg/μL trypsin (Trypsin Gold; Promega, Southampton, UK) in 50 mM acetic acid. Surface sampling of the thin tissue section and trypsin digestion was performed using the advanced user interface (AUI) feature of the ChipSoft Manager software, which controls the Triversa Nanomate. Following LESA extraction and digestion, each sample was analyzed in duplicate by LC-MS/MS.

Liquid Extraction Surface Analysis Two μL of extraction solvent was aspirated from the solvent well. The robotic arm relocated to a position above the tissue section and descended to a height of approximately 0.6 mm above the surface. One μL of the solution was dispensed onto the tissue section to form a liquid microjunction. The liquid microjunction was maintained between the probe tip and the surface for 1 s; then 1.3 μL were reaspirated into the pipette tip. The dispense-reaspiration cycle was repeated three times before finally dispensing into a clean well in the microtiter plate. The experiment was conducted using three extraction solutions: (1) 50% methanol, (2) 70% methanol, and (3) 50 mM NH_4HCO_3. After extraction, the 50% and 70% methanol solutions were left for 30 min until dry to remove the organic content, and the sample was resuspended in 10 μL 50 mM NH_4HCO_3, using one mix cycle (repeat dispense/reaspiration) to promote resuspension. For each of the samples, 4.5 μL of trypsin solution was aspirated from the tryspin-containing well and dispensed into the sample well. The solutions were mixed by a single mix cycle (repeat dispense/reaspiration). The samples were incubated at 37°C for 1 h by using the temperature control unit of the TriVersa NanoMate. At 30 min and 1 h into the incubation, 7 μL of 50 mM NH_4HCO_3 was aspirated from the solvent well and added to the sample well in order to account for evaporation. The final volume was approximately 10 μL.

LC MS/MS The microtiter plate was transferred to the HPLC autosampler (Ultimate 3000; Dionex Thermo Fisher Scientific, Loughborough, UK), which is coupled to an Orbitrap Velos ETD mass spectrometer (Thermo Fisher Scientific, Bremen, Germany) via the TriVersa NanoMate. The proteolytic digests were each analyzed in duplicate by LC-MS/MS. Five μL aliquots were injected onto a Pepmap 100, C_{18} 100 μm trap (Thermo Fisher Scientific). The trap was treated with a 5 min wash cycle with 0.1% formic acid prior to injection onto the analytical column (Pepmap 100 reversed phase C18 75 μm, 3 μm, 100 Å; Thermo Fisher Scientific). Peptides were separated using a 30 min 3.2% to 44% ACN (J. T. Baker, Deventer, The Netherlands) gradient at a flow rate of 0.35 μL/min.

Samples eluted into the mass spectrometer via the Triversa Nanomate chip-based nanoelectrospray device. Ionization voltage was 1.4 kV, gas pressure was 0.3 psi, and capillary temperature was 250°C. Mass spectrometry analysis was performed via a 'top 7' method in which a survey scan was followed by MS/MS of the seven most abundant precursor ions. Survey scans were acquired in the Orbitrap with a *m/z* range 380–1800, an automatic gain control (AGC) target of 1×10^6 charges, a maximum fill time of 1 s, and a resolution of 60,000 at *m/z* 400. CID was performed in the linear ion trap (AGC target: 30,000 charges) with helium gas and a normalized collision energy of 35%. The width of the precursor isolation window was 2 Th and only multiply charged precursor ions were subjected to CID. The mass exclusion window was *m/z* ±0.05 and the exclusion list was set to 500. Dynamic exclusion was applied for 60 s.

MS/MS data were searched against the SwissProt human database (downloaded November 2012), composed of 20,203 sequences, supplemented with the FABP1 variant, using the Mascot and Sequest algorithms in Proteome Discoverer 1.4. Two sets of parameters were applied. In one set, the parameters were: precursor ion mass accuracy 10 ppm, fragment mass tolerance 0.8 Da, methionine oxidation was allowed as a dynamic modification, up to two missed cleavages in the digestion. In the second set, three missed cleavages were allowed, with all other parameters the same as before. Data were filtered to a false discovery rate of 1% by including only high confidence peptides. The protein grouping algorithm was applied, which grouped all non-unique peptides to the highest scoring protein.

Top-Down LESA Mass Spectrometry of Human Liver Tissue Sections

Sections of human liver thaw-mounted onto glass slides were washed in a solution of 80% ethanol. The slides were mounted onto the Advion LESA universal plate adapter and an image of the tissue section was acquired using an Epson Perfection V300 photo scanner. The LESA Points software (Advion) was used to select the precise location of the tissue section to be sampled. The universal plate adapter was placed into the TriVersa NanoMate. Extraction/electrospray solution comprising 40% acetonitrile + 1% formic acid was placed in the solvent well.

Liquid Extraction Surface Analysis Two μL of 40% acetonitrile + 1% formic acid was aspirated from the solvent well. The robotic arm relocated to a position above the tissue section and descended to a height of approximately 1 mm above the surface. One μL of the solution was dispensed onto the tissue section to form a liquid microjunction. The liquid microjunction was maintained between the probe tip and the surface for 10 s. Then, 1.3 μL was reaspirated into the pipette tip. The dispense/reaspirate cycle was repeated three times. The sample was introduced into the mass spectrometer via the TriVersa NanoMate, at a flow rate of ~150 nL/min, with gas pressure 1.3 psi, a tip voltage of 1.7 kV, and a capillary temperature of 250°C. All spectra were collected in the Orbitrap at a resolution of 100,000 at *m/z* 400. Full scan mass spectra (*m/z* 500–2000) were collected for 3 min. AGC target

was 1×10^6 charges with a maximum injection time of 2 s. CID was performed in the ion trap at a normalized collision energy of 30% and the fragments detected in the Orbitrap (*m/z* 300–2000). The isolation width was 3 Th. AGC target was 1×10^6 charges with a maximum injection time of 2 s. Each CID MS/MS scan comprised of 20 co-added microscans. Data were recorded for 10 min (~10 scans). ETD was performed in the ion trap and the fragments detected in the Orbitrap. The isolation width was 3 Th. AGC target was 1×10^6 charges with a maximum injection time of 1 s. ETD activation time was 20 ms. Each ETD scan comprised of 20 co-added microscans. Data were recorded for 6 min (~9 scans).

All mass spectra were deconvoluted using Xcalibur's Xtract function, in order to obtain monoisotopic masses. Mass spectra were processed with a signal to noise ratio threshold of three. The processed fragment ion list was submitted to Prosight PTM 2.0 (https://prosightptm2.northwestern.edu) using the simple human database, allowing all modifications, and peak accuracy of 10 ppm. Identity was confirmed by manual analysis using Protein Prospector (http://prospector.ucsf.edu/prospector/mshome.htm).

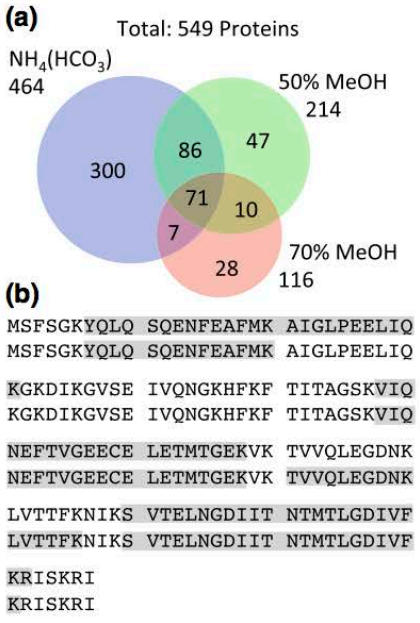

Figure 1. (**a**) Total number of proteins identified from healthy human liver tissue using a bottom-up approach following LESA extraction using solvents comprising 50 mM $NH_4(HCO_3)$, 70% methanol, and 50% methanol. (**b**) Sequence coverage obtained for FABP1 following 50 mM $NH_4(HCO_3)$ extraction, automated tryptic digestion, and LC MS/MS from two technical replicates

Results and Discussion

Bottom-Up LESA Mass Spectrometry of Human Liver Tissue Sections

Intact proteins were extracted from healthy human liver tissue via automated direct surface sampling by LESA and subjected to automated trypsin digestion using the method described by Martin et al. [8]. In that work, Martin et al. found that 1 h was the optimum digestion time. Three extraction solvents were considered: 70% (v/v) methanol, 50% (v/v) methanol, and 50 mM ammonium bicarbonate. The three extraction solvents were applied for LESA of three serial sections from a tumor resection margin. For each extraction solvent composition, two technical replicates were performed. Two searches of the data against the protein database were performed in order to determine the effect of the short digestion time. In the first, two missed trypsin cleavages were allowed, and in the second, three missed cleavages were allowed. When two missed cleavages were allowed, a total of 475 non-redundant proteins were detected: 428 proteins were detected following the ammonium bicarbonate extraction; 200 were detected following the 50% methanol extraction, and 99 were detected following the 70% methanol extraction. When three missed cleavages were allowed, 549 non-redundant proteins were detected: 464 proteins were detected following the ammonium bicarbonate extraction; 214 were detected following the 50% methanol extraction, and 116 were detected following the 70% methanol extraction. See Figure 1a. Proteins identified are detailed in Supplementary File 1. Single peptide protein identifications are presented in Supplementary File 2. Increasing the organic solvent content of the extraction solution resulted in fewer identifications, and this is perhaps not surprising. This observation has relevance to the top-down analysis and is discussed further below.

The bottom-up protocol used here was originally developed for the analysis of dried blood spots [8]. The number of proteins identified from the liver tissue is over 4-fold greater than were detected in dried blood spots, despite using a much smaller volume for the liquid microjunction (1 µL versus 6 µL). This observation is perhaps expected given that the liver is a center for metabolism within the body and has an abundance of proteins and enzymes [20]. Blood is a small component of liver tissue and abundant proteins such as alpha and beta hemoglobin chains were also detected. It is possible that the numbers of identified proteins could be increased, either by pooling extracted samples or by performing on-tissue digestion [17]. The latter cannot be achieved, at least in our hands, using the TriVersa NanoMate because of the problem of evaporation of the trypsin solution.

Three known liver disease markers were identified in each of the three extractions: the liver fatty acid binding protein (FABP1) (MW 15.1 kDa) [6], gamma-glutamyltransferase (MW 77.3 kDa) [18], and aspartate amino transferase [3]. There are two forms of aspartate amino transferase, one found in the mitochondria (MW 47.5 kDa) and the other found in the cytoplasm (MW 46.2 kDa). The homology between the two sequences is 68% (as calculated by BLAST http://blast.ncbi.nlm.nih.gov/Blast.cgi). Both proteins were

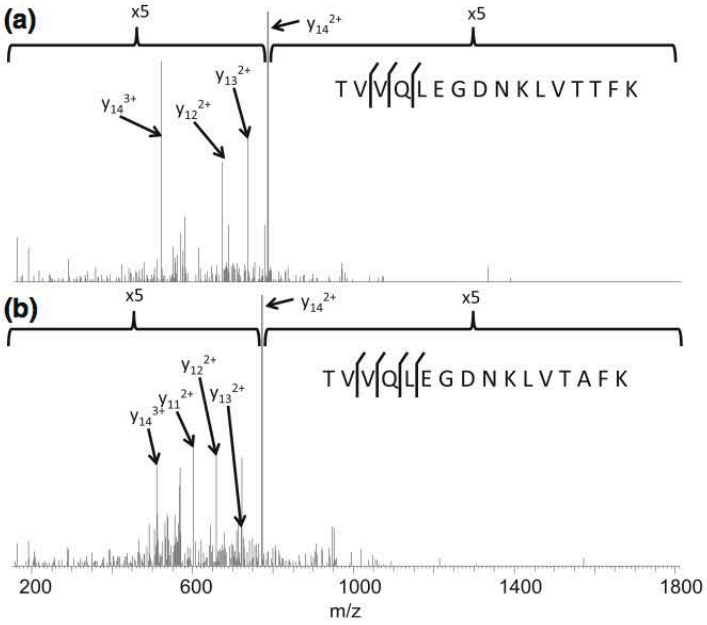

Figure 2. CID mass spectra of +3 ions of tryptic peptides [TVVQLEGDNKLVTTFK] and [TVVQLEGDNKLVTAFK] from FABP1 and $FABP1_{TA}$ identified following LESA extraction with 50 mM $NH_4(HCO_3)$ extraction followed by trypsin digestion and LC-MS/MS

identified by unique peptides in the current dataset. Proteins gamma-glutamyltransferase and the mitochondrial aspartate amino transferase were detected with greatest sequence coverages (32.90% and 48.37% respectively) following the ammonium bicarbonate extraction. The greatest sequence coverage (52.52%) for cytoplasmic aspartate amino transferase was observed following extraction with 50% methanol.

FABP1 was detected in each of the six experiments with sequence coverage ranging between 53% and 57% (see Supplementary Figure 1). Figure 1b shows the sequence coverages

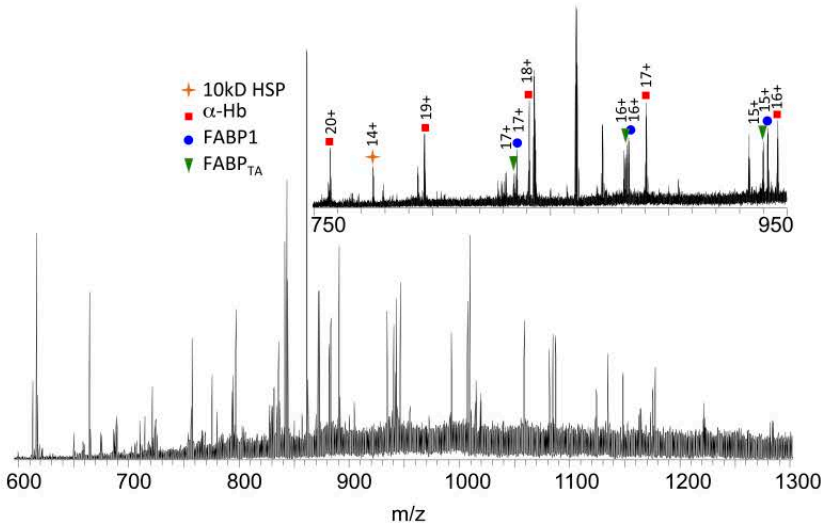

Figure 3. Full scan mass spectrum obtained following LESA MS analysis of healthy human liver tissue. Inset: enlarged region (*m/z* 750–950). Labeled peaks are: FABP1 (blue circle), $FABP1_{TA}$ (green triangle), α-hemoglobin (red square), and 10 kDa heat shock protein (yellow star). Proteins were identified using CID and/or ETD

obtained for the two replicates obtained following extraction with ammonium bicarbonate solution. As described above, FABP1 and its variant implicated in NASH differ by a single amino acid residue (i.e., Thr→Ala at position 94). The tryptic peptide containing residue 94, that is [91-96], was not observed in any of the analyses. (It is possible that an SRM approach may identify the relevant peptide more reproducibly; however, the Orbitrap instrument used in this work is not suited to such an approach). One of the analyses following extraction with ammonium bicarbonate resulted in the identification of the missed-cleavage tryptic peptide [81-96] (m/z_{meas} 1791.9931, m/z_{calc} 1791.9851, Δ 4.9 ppm) from FABP1. The CID mass spectrum obtained from the $[M+3H]^{3+}$ peptide ions is shown in Figure 2a. The fragmentation sequence coverage for the peptide is poor with no cleavage around the potential substitution site. Clearly, as the variant is the result of a single amino acid substitution and the sequences of FAPB1 and its variant are virtually identical, with the exception of peptide [81-96], the peptides assigned to FABP1 in the database search could also have originated from the variant. The human SwissProt database against which the database was searched was supplemented with the FABP1 variant (hereafter referred to as $FABP1_{TA}$). The peptide [90-96] from $FABP1_{TA}$ was not identified in any of the analyses; however, the missed-cleavage peptide [81-96] was identified in one of the ammonium bicarbonate extraction replicates (m/z_{meas} 1761.9831, m/z_{calc} 1761.9745, Δ 4.5 ppm). The CID spectrum is shown in Figure 2b. Again, fragmentation sequence coverage is poor and no fragmentation was observed adjacent to the site of substitution. It should be noted that top-down analysis of this tissue sample (see below) revealed the presence of the variant.

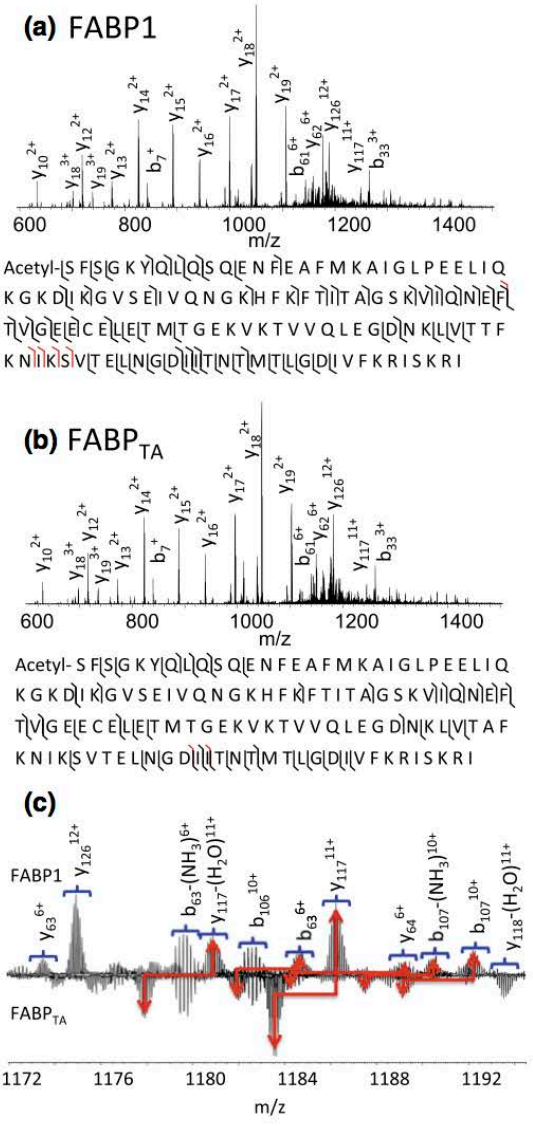

Figure 4. CID mass spectra obtained from +15 ions of (**a**) FABP1 and (**b**) $FABP_{TA}$ following LESA of human liver sections. Insets: observed sequence coverage: b/y ions are shown in black and a ions in red. (**c**) Enlarged region showing *m/z* 1172–1193

Untargeted Identification of Intact Proteins in Human Liver

Four samples were investigated by top-down LESA mass spectrometry: two NASH samples and two healthy (non-diseased) samples. The non-diseased samples were from (1) a tumor resection margin, and (2) a donor liver not suitable for transplantation.

Liver sections were thaw-mounted onto glass slides and dipped into 80% (v/v) ethanol prior to LESA analysis. This washing step removes lipids and improves protein signal in the mass spectra. The sections were subjected to LESA using extraction solvent comprising 40% (v/v) acetonitrile + 1% formic acid, and the resulting samples introduced directly, via electrospray ionization, into the mass spectrometer. Deconvolution of the resulting mass spectra using the Xtract program suggested that the spectra comprised peaks corresponding to up to 16 proteins in healthy tissue and up to 25 proteins in NASH tissue, with molecular weights ranging between 3000 and 20,000 Da. The results from the bottom-up analyses described above suggest that a greater number of proteins are extracted using ammonium bicarbonate solution; however, the top-down workflow requires that the extraction solution must also be suitable for electrospray ionization. If the extraction and electrospray steps were decoupled, it may be possible to increase the number of top-down identifications.

Figure 3 shows the mass spectrum obtained from a healthy liver sample. Four abundant protein ions were selected for tandem mass spectrometry. Note that the nature of the proteins was not known a priori. Ions at *m/z* 946.38 (+16 charge state)

were selected for collision induced dissociation MS/MS. The data were searched against the simple human database in Prosight PTM 2.0, and the protein was identified as the alpha chain of hemoglobin (MW_{meas} 15117.9167, MW_{calc} 15117.8924, Δ 1.6 ppm). Fragments identified are detailed in Supplementary Table 1. The protein sequence coverage following CID was 31%. Ions of the same *m/z* (*m/z* 946.38) observed in the analysis of NASH tissue were selected and subjected to electron transfer dissociation MS/MS. Again, the protein was identified as α-hemoglobin. The ETD protein sequence coverage was 13% and the fragments observed are detailed in Supplementary Table 2. The combined sequence coverage from the two analyses was 42%.

Ions at *m/z* 775.42 (+14 charge state) observed in the mass spectrum from healthy tissue were selected and subjected to both CID MS/MS and ETD MS/MS and the data searched against the simple human database in Prosight PTM 2.0. (A peak at this *m/z* was also observed in NASH tissue however its abundance was insufficient for MS/MS). The protein was identified as mitochondrial 10 kDa heat shock protein (MW_{meas} 10836.8056, MW_{calc} 10836.8485, Δ 3.96 ppm). The protein sequence coverage was 25% (CID) and 21% (ETD), giving an overall coverage of 39%. Details of the fragments observed are given in Supplementary Tables 3 and 4.

The ions at *m/z* 1084.80 and 1087.04 (both +15 charge state) were each selected for CID MS/MS. The two species were identified as FABP1 (MW_{meas} 14111.4161, MW_{calc} 14111.3892, Δ 1.9 ppm) and the variant $FABP1_{TA}$ (MW_{meas} 14081.3600, MW_{calc} 14081.3687, Δ 0.6 ppm). Both proteins were detected with the initiator methionine removed and acetylation of the N-terminus. Therefore, the 92nd and 93rd amino acids in each chain are TT and TA, respectively. The CID sequence coverage obtained was 47% for FABP1 and 33% for the variant $FABP1_{TA}$. Fragments observed are detailed in Supplementary Tables 5 and 6. The site of substitution can be confirmed. The CID MS/MS spectra from both FABP1 and $FABP1_{TA}$ are shown in Figure 4.

Ions of *m/z* 942.23 and 940.29 (+16 charge state) (corresponding to FABP1 (MW_{meas} 14111.3943, MW_{calc} 14111.3892, Δ 2.4 ppm) and $FABP1_{TA}$ (MW_{meas} 14081.2845, MW_{calc} 14081.3687, Δ 6.0 ppm) from a NASH sample were subjected to ETD MS/MS. The sequence coverages obtained were 38% and 29%, see Supplementary Tables 7 and 8. The ETD MS/MS spectra of FABP1 and $FABP1_{TA}$ from NASH tissue are shown in Figure 5.

Figure 6 shows expanded *m/z* regions containing the +16 charge state of FABP1 and $FABP1_{TA}$ of the mass spectra obtained for the four samples analyzed. Figure 6a and b show the mass spectra from healthy (non-diseased) tissue. In one sample, only FABP1 is observed, whereas in the other both FABP1 and the variant are observed. Figure 6c and d show the mass spectra from NASH tissue. Similarly, one sample contains the variant alone, whereas the other reveals the presence of both FABP1 and $FABP1_{TA}$. As described above, it has been demonstrated recently that individuals with $FABP_{TA}$ have an

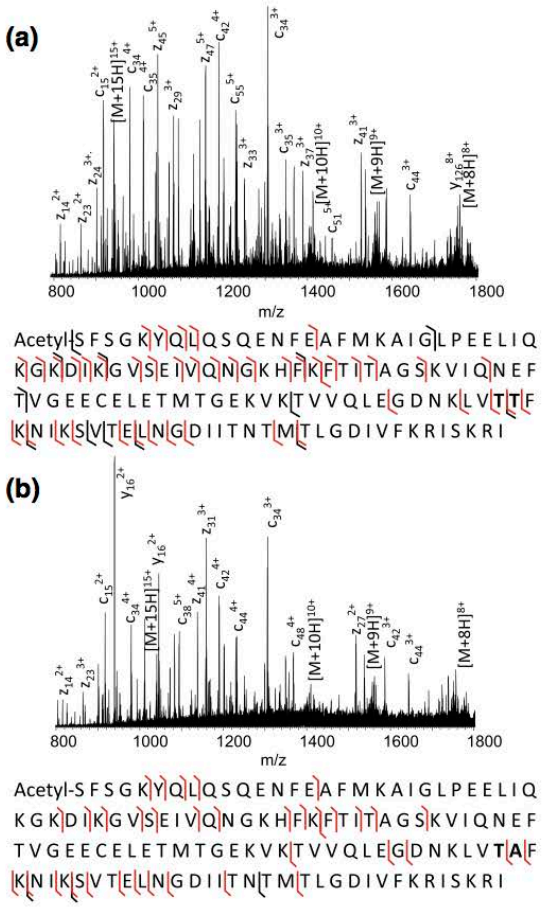

Figure 5. ETD mass spectra obtained from +16 ions of (**a**) FABP1 and (**b**) $FABP_{TA}$ following LESA of NASH human liver sections. Insets: observed sequence coverage: c/z ions are shown in red, a/y ions in black

increased risk of developing NASH [6]. In addition, it was shown that another polymorphism compounds that risk. The observation of the variant in non-diseased tissue could be explained by the risk associated with $FABP_{TA}$ being attenuated by other factors. It is worth noting, however, that the sample containing both FAPB1 and the variant was from a tumor resection margin, whereas the sample containing FAPB1 alone was from a liver rejected for transplant because of the presence of a small lesion. The non-diseased samples are also characterized by reduced signals for α-hemoglobin. In the case of the liver rejected for transplant (Figure 6a), the organ was perfused with buffer (i.e., blood was removed) following removal from the donor. In the case of the tumor resection margin (Figure 6b), it is likely that the surgical procedure resulted in local hemolysis and reduced blood supply.

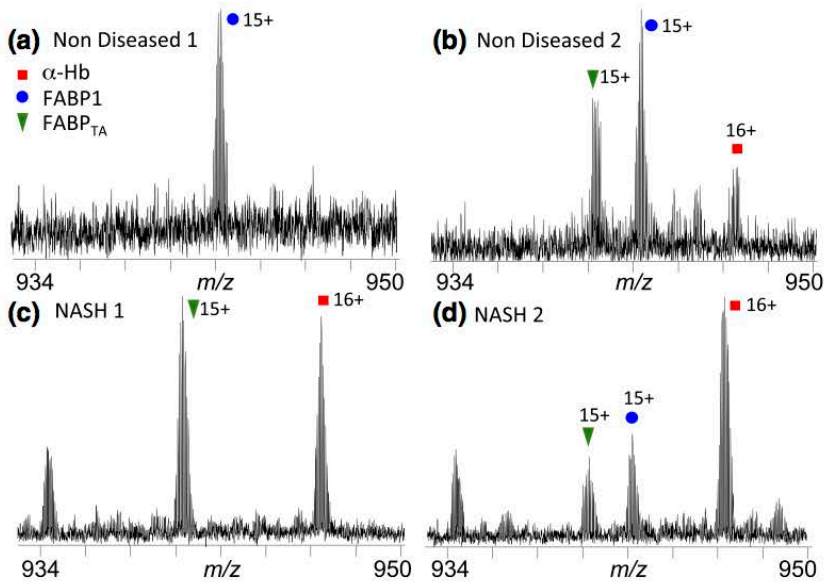

Figure 6. Expanded *m/z* regions from the full scan mass spectra obtained following LESA MS analysis of two healthy human liver sections (**a**) and (**b**), and two NASH human liver sections (**c**) and (**d**). Labeled peaks are FABP1 (+16 charge state) (blue circle), FABP1$_{TA}$ (+16 charge state) (green triangle), and α-Hb (+16 charge state) (red square)

Conclusion

We have shown that LESA mass spectrometry is a suitable tool for the investigation of proteins in healthy and diseased human liver tissue. Bottom-up analysis results in identification of far greater numbers of proteins than does top-down analysis. It may be possible to increase the number of top-down identifications by introducing a liquid chromatography step or by decoupling the extraction step from the electrospray ionization step thereby enabling the use of different solvent systems in each case.

Given that the protein FABP1 and its variant FABP$_{TA}$ are implicated in nonalcoholic liver disease, it is particularly important to be able to distinguish between the two forms. The bottom-up approach, although confidently identifying the FABP1 protein in all cases, does not reliably and reproducibly detect the peptide containing the site of amino acid substitution. The results suggest that the bottom-up approach is not suitable for the spatially resolved profiling of NASH tissue sections. (It should be noted, however, that the timescale of the trypsin proteolysis step best-suited for efficient, integrated LESA-based analysis is 1 h. An overnight digestion may yield better sequence coverage, as might alternative proteases). Conversely, the top-down approach easily distinguishes FABP1 and FABP$_{TA}$. Peaks corresponding to the two species are clearly discerned in the mass spectra and are, in fact, some of the most abundant. MS/MS of the intact proteins (either CID or ETD) allows the nature of the proteins to be confirmed, including the site of substitution. Further work will focus on validation of the approach on larger numbers of samples, together with development of LESA-based top-down mass spectrometry for spatially-resolved profiling of NASH tissue.

Acknowledgments

H.J.C. is an EPSRC Established Career Fellow (EP/L023490/1). J.S. received funding from the EPSRC via the PSIBS doctoral training center (EP/F50053X/1). N.J.M. received an EPSRC CASE studentship in collaboration with Advion. The Advion TriVersa NanoMate and Thermo Fisher Orbitrap Velos mass spectrometers used in this research were funded thought Birmingham Science City Translational Medicine, Experimental Medicine Network of Excellence Project with support from Advantage West Midlands. The authors acknowledge Dr. Rebecca L. Edwards and Dr. Andrew J. Creese for technical discussions.

Open Access

References

1. Obika, M., Noguchi, H.: Diagnosis and evaluation of nonalcoholic fatty liver disease. Exp. Diabetes Res. **2012**, 1–12 (2012)
2. Das, K., Kar, P.: Nonalcoholic steatohepatitis. J. Assoc. Physicians India **53**, 195–199 (2005)
3. Pratt, D.S., Kaplan, M.M.: Evaluation of abnormal liver-enzyme results in asymptomatic patients. N. Engl. J. Med. **342**, 1266–1271 (2000)

4. Furuhashi, M., Hotamisligil, G.S.: Fatty acid-binding proteins: role in metabolic diseases and potential as drug targets. Nat. Rev. Drug Discov. **7**, 489–503 (2008)
5. Chen, A., Tang, Y., Davis, V., Hsu, F.F., Kennedy, S.M., Song, H., Turk, J., Brunt, E.M., Newberry, E.P., Davidson, N.O.: Liver fatty acid binding protein (L-Fabp) modulates murine stellate cell activation and diet-induced nonalcoholic fatty liver disease. Hepatology **57**, 2202–2212 (2013)
6. Peng, X.E., Wu, Y.L., Lu, Q.Q., Hu, Z.J., Lin, X.: Two genetic variants in FABP1 and susceptibility to nonalcohol fatty liver disease in a Chinese population. Gene **500**, 54–58 (2012)
7. Huang, H., McIntosh, A.L., Martin, G.G., Landrock, K.K., Landrock, D., Gupta, S., Atshaves, B.P., Kier, A.B.., Schroeder, F.: Structural and functional interaction of fatty acids with human liver fatty acid-binding protein (L-FABP) T94A variant. FEBS J. **281**, 2266–2283 (2014)
8. Martin, N.J., Bunch, J., Cooper, H.J.: Dried blood spot proteomics: surface extraction of endogenous proteins coupled with automated sample preparation and mass spectrometry analysis. J. Am. Soc. Mass Spectrom. **24**, 1242–1249 (2013)
9. Schey, K.L., Anderson, D.M., Rose, K.L.: Spatially-directed protein identification from tissue sections by top-down LC-MS/MS with electron transfer dissociation. Anal. Chem. **85**, 6767–6774 (2013)
10. Kertesz, V., Van Berkel, G.J.: Fully automated liquid extraction-based surface sampling and ionization using a chip-based robotic nanoelectrospray platform. J. Mass Spectrom. **45**, 252–260 (2009)
11. Marshall, P., Toteu-Djomte, V., Bareille, P., Perry, H., Brown, G., Baumert, M., Biggadike, K.: Correlation of skin blanching and percutaneous absorption for glucocorticoid receptor agonists by matrix-assisted laser desorption ionization mass spectrometry imaging and liquid extraction surface analysis with nanoelectrospray ionization mass spectrometry. Anal. Chem. **82**, 7787–7794 (2010)
12. Blatherwick, E.Q., Van Berkel, G.J., Pickup, K., Johansson, M.K., Beaudoin, M.E., Cole, R.O., Day, J.M., Iverson, S., Wilson, I.D., Scrivens, J.H., Weston, D.J.: Utility of spatially-resolved atmospheric pressure surface sampling and ionization techniques as alternatives to mass spectrometric imaging (MSI) in drug metabolism. Xenobiotica **41**, 720–734 (2011)
13. Van Berkel, G.J., Kertesz, V.: Continuous-flow liquid microjunction surface sampling probe connected on-line with high-performance liquid chromatography/mass spectrometry for spatially resolved analysis of small molecules and proteins. Rapid Commun. Mass Spectrom. **27**, 1329–1334 (2013)
14. Edwards, R.L., Creese, A.J., Baumert, M., Griffiths, P., Bunch, J., Cooper, H.J.: Hemoglobin variant analysis via direct surface sampling of dried blood spots coupled with high-resolution mass spectrometry. Anal. Chem. **83**, 2265–2270 (2011)
15. Edwards, R.L., Griffiths, P., Bunch, J., Cooper, H.J.: Compound heterozygostes and beta-thalassemia: top-down mass spectrometry for detection of hemoglobinopathies. Proteomics **14**, 1232–1238 (2014)
16. Edwards, R.L., Griffiths, P., Bunch, J., Cooper, H.J.: Top-down proteomics and direct surface sampling of neonatal dried blood spots: diagnosis of unknown hemoglobin variants. J. Am. Soc. Mass Spectrom. **23**, 1–10 (2012)
17. Quanico, J., Franck, J., Dauly, C., Strupat, K., Dupuy, J., Day, R., Salzet, M., Fournier, I., Wisztorski, M.: Development of liquid microjunction extraction strategy for improving protein identification from tissue sections. J. Proteom. **79**, 200–218 (2013)
18. Wisztorski, M., Fatou, B., Franck, J., Desmons, A., Farre, I., Leblanc, E., Fournier, I., Salzet, M.: Microproteomics by liquid extraction surface analysis: application to FFPE tissue to study the fimbria region of tubo-ovarian cancer. Proteomics Clin. Appl. **7**, 234–240 (2013)
19. Rao, W., Celiz, A.D., Scurr, D.J., Alexander, M.R., Barrett, D.A.: Ambient DESI- and LESA-MS analysis of proteins adsorbed to a biomaterial surface using in-situ surface tryptic digestion. J. Am. Soc. Mass Spectrom. **24**, 1927–1936 (2013)
20. Barle, H., Nyberg, B., Essen, P., Andersson, K., McNurlan, M.A., Wernerman, J., Garlick, P.J.: The synthesis rates of total liver protein and plasma albumin determined simultaneously in vivo in humans. Hepatology **25**, 154–158 (1997)

Appendix 8 – MW of proteins detected using 70% Methanol, 50% Methanol and 50% Acetonitrile

70% Methanol	50% Methanol	50% Acetonitrile
3195.67	3195.67	3369.49
3369.5	3326.72	3440.52
3440.53	3369.5	3484.51
3484.52	3440.53	3585.87
3901.06	3484.52	3938.8
8446.62	4745.45	4006.07
9950.04	8446.61	4961.5
14081.43	8560.65	5005.52
14111.4	9950.04	6080.21
15960.75	14065.39	6107.29
	14081.41	7569.94
	14100.49	8560.67
	14111.44	10836.86
	14120.39	14067.44
	14122.4	14081.38
	14133.39	14111.45
	14149.41	15118.07
	14186.27	15835.87
		15858.37

Appendix 9 — Fragments observed following CID of +14 ions with m/z 775.42 from non-diseased liver tissue (identified as 10kDa heat shock protein (mitochondrial)).

Measured (*m/z*)	Theoretical (*m/z*)	Δppm	Assignment
581.2924	581.2930	1.03	y_5^{1+}
659.1627	659.1622	-0.76	$b_{60}\text{-}NH_3^{9+}$
661.8642	661.8644	0.30	b_{23}^{4+}
668.3382	668.3384	0.30	y_{29}^{5+}
679.0526	679.0540	2.06	b_{60}^{9+}
685.8093	685.8081	-1.75	$b_{44}\text{-}NH_3^{7+}$
699.8188	699.8201	1.86	$b_{45}\text{-}H_2O^{7+}$
702.3912	702.3931	2.71	b_{45}^{7+}
709.7940	709.7950	1.41	b_{32}^{5+}
727.0272	727.0284	1.65	y_{18}^{3+}
739.7415	739.7377	-5.14	y_{63}^{9+}
755.8973	755.8986	1.72	y_{13}^{2+}
762.9104	762.9107	0.39	y_{41}^{6+}
799.7760	799.7775	1.88	$b_{44}\text{-}H_2O^{6+}$
809.1444	809.1454	1.24	y_{53}^{7+}
816.2874	816.2889	1.84	$b_{45}\text{-}H_2O^{6+}$
819.2888	819.2907	2.32	b_{45}^{6+}
823.2969	823.2980	1.34	y_{54}^{7+}
832.0836	832.0790	-5.53	$y_{63}\text{-}NH_3^{8+}$
833.4447	833.4462	1.80	y_{55}^{7+}
835.1697	835.1711	1.68	y_{29}^{6+}
844.6394	844.6398	0.47	$b_{47}\text{-}H_2O^{6+}$
847.5953	847.5988	4.13	y_{56}^{7+}
863.4402	863.4421	2.20	y_{30}^{4+}
876.0657	876.0671	1.60	y_{39}^{5+}
880.4868	880.4882	1.59	b_{40}^{5+}
886.9909	886.9920	1.24	b_{32}^{4+}
910.9621	910.9645	2.63	y_{14}^{2+}
915.2896	915.2913	1.86	y_{41}^{5+}
948.8537	948.8555	1.90	b_{25}^{3+}
968.4762	968.4780	1.86	y_{16}^{2+}
1037.8581	1037.8606	2.41	y_{27}^{3+}
1061.5872	1061.5891	1.79	b_9^{1+}
1094.8294	1094.8321	2.47	y_{39}^{4+}
1113.2240	1113.2258	1.62	y_{29}^{3+}
1188.6136	1188.6151	1.26	y_{31}^{3+}

Appendix 10 — Fragments observed following ETD of +14 ions with m/z 775.42 from non-diseased liver tissue (identified as 10kDa heat shock protein (mitochondrial)).

Measured (*m/z*)	Theoretical (*m/z*)	Δppm	Assignment
666.1198	666.1210	1.80	c_{23}^{4+}
668.0371	668.0386	2.25	c_{36}^{6+}
690.3671	690.3682	1.59	c_{6}^{1+}
690.5825	690.5835	1.45	c_{31}^{5+}
698.8852	698.8852	0.00	c_{38}^{6+}
716.1491	716.1501	1.40	c_{25}^{4+}
716.4074	716.4090	2.23	c_{18}^{3+}
718.4129	718.4141	1.67	c_{12}^{2+}
736.7445	736.7458	1.76	c_{40}^{6+}
741.4122	741.4120	-0.27	c_{26}^{4+}
758.4180	758.4194	1.85	y_{34}^{5+}
771.629	771.6288	-0.26	a_{35}^{5+}
775.9272	775.9275	0.39	c_{13}^{2+}
801.4445	801.4448	0.37	c_{36}^{5+}
821.1307	821.1324	2.07	c_{21}^{3+}
830.2134	830.2175	4.94	c_{30}^{4+}
838.4611	838.4608	-0.36	c_{38}^{5+}
887.8237	887.8256	2.14	c_{23}^{3+}
915.2896	915.2913	1.86	y_{41}^{5+}
964.2852	964.2842	-1.04	$a_{35}\text{-}NH_3^{4+}$
973.2548	973.2561	1.34	z_{34}^{4+}
978.1647	978.1666	1.94	z_{26}^{3+}
1012.2776	1012.2785	0.89	z_{36}^{4+}
1016.2817	1016.2832	1.48	y_{36}^{4+}
1044.0497	1044.0503	0.57	$y_{37}\text{-}NH_3^{4+}$
1047.8200	1047.8242	4.01	c_{38}^{4+}
1061.5872	1061.5891	1.79	b_{9}^{1+}
1100.3869	1100.3862	-0.64	z_{51}^{5+}
1113.2240	1113.2258	1.62	y_{29}^{3+}
1171.8651	1171.8723	6.14	z_{42}^{4+}
1297.3378	1297.3390	0.92	z_{34}^{3+}
1307.1917	1307.1938	1.61	z_{48}^{4+}
1349.3694	1349.3690	-0.30	z_{36}^{3+}
1392.0636	1392.0630	-0.43	z_{37}^{3+}
1562.1624	1562.1607	-1.09	z_{42}^{3+}

Appendix 11 — Fragments observed following CID of +16 ions with m/z 946.40 from non-diseased liver tissue (identified as α=haemoglobin).

Measured (*m/z*)	Theoretical (*m/z*)	Δppm	Assignment
527.7966	527.7982	3.03	y_9^{2+}
553.3101	553.3093	-1.45	y_4^{1+}
620.8496	620.8484	-1.93	y_{11}^{2+}
623.3494	623.3483	-1.76	y_{23}^{4+}
654.3581	654.3570	-1.68	y_5^{1+}
656.3680	656.3670	-1.52	y_{12}^{2+}
672.3766	672.3772	0.89	y_{18}^{3+}
677.7105	677.7093	-1.77	b_{20}^{3+}
693.3874	693.3930	8.08	$b_7\text{-}H_2O^{1+}$
696.0576	696.0563	-1.87	y_{19}^{3+}
701.3896	701.3884	-1.71	b_{21}^{3+}
712.9102	712.9090	-1.68	y_{13}^{2+}
741.7438	741.7426	-1.62	y_{20}^{3+}
755.1591	755.1578	-1.72	$y_{28}\text{-}H_2O^{4+}$
759.6616	759.6605	-1.45	y_{28}^{4+}
767.4425	767.4410	-1.95	y_6^{1+}
774.7673	774.7654	-2.45	y_{21}^{3+}
786.4440	786.4432	-1.02	y_{14}^{2+}
787.9330	787.9315	-1.90	y_{29}^{4+}
824.7938	824.7918	-2.42	$y_{23}\text{-}H_2O^{3+}$
830.7966	830.7953	-1.56	y_{23}^{3+}
836.7724	836.7713	-1.31	b_{25}^{3+}
850.4922	850.4907	-1.76	y_{15}^{2+}
864.1694	864.1696	0.23	b_{113}^{14+}
864.4794	864.4779	-1.74	y_{24}^{3+}
866.5108	866.5094	-1.62	y_7^{1+}
903.4657	903.4645	-1.33	b_{27}^{3+}
905.7042	905.7067	2.76	b_{100}^{13+}
910.2216	910.2201	-1.65	$b_{34}\text{-}H_2O^{4+}$
911.2490	911.2477	-1.43	y_{34}^{4+}
911.9266	911.9312	5.04	y_{58}^{7+}
913.5023	913.5007	-1.75	y_{25}^{3+}
927.2371	927.2386	1.62	y_{138}^{16+}
929.6957	929.6940	-1.83	b_{79}^{9+}
931.6800	931.6774	-2.79	$y_{139}\text{-}H_2O^{16+}$
931.6800	931.6764	-3.86	$y_{139}\text{-}NH_3^{16+}$

932.6817	932.6781	-3.86	y_{139}^{16+}
936.0169	936.0148	-2.24	y_{35}^{4+}
938.2323	938.2342	2.03	y_{60}^{7+}
956.5168	956.5149	-1.99	y_{26}^{3+}
980.1953	980.1939	-1.43	y_{27}^{3+}
993.8845	993.8832	-1.31	b_{75}^{8+}
1010.3902	1010.3882	-1.98	b_{76}^{8+}
1012.5463	1012.5449	-1.38	y_{28}^{3+}
1018.5608	1018.5591	-1.67	y_{38}^{4+}
1021.9672	1021.9661	-1.08	y_{47}^{5+}
1036.7795	1036.7752	-4.15	b_{78}^{8+}
1043.5821	1043.5808	-1.25	y_{19}^{2+}
1045.7826	1045.7798	-2.68	b_{79}^{8+}
1049.4150	1049.4132	-1.72	y_{57}^{6+}
1050.2403	1050.2396	-0.67	y_{29}^{3+}
1054.5902	1054.5891	-1.04	y_{9}^{1+}
1058.8553	1058.8546	-0.66	y_{68}^{7+}
1063.7533	1063.7516	-1.60	y_{58}^{6+}
1082.7680	1082.7659	-1.94	y_{59}^{6+}
1094.6065	1094.6053	-1.10	y_{60}^{6+}
1095.9266	1095.9259	-0.64	y_{30}^{4+}
1108.9402	1108.9441	3.52	y_{61}^{6+}
1112.1114	1112.1104	-0.90	y_{20}^{2+}
1135.8672	1135.8654	-1.58	b_{75}^{7+}
1154.4374	1154.4426	4.50	b_{76}^{7+}
1213.2925	1213.2982	4.70	b_{102}^{9+}
1245.6904	1245.6894	-0.80	y_{23}^{2+}
1268.3189	1268.3173	-1.26	b_{36}^{3+}
1277.7085	1277.7058	-2.11	y_{47}^{4+}
1296.2147	1296.2132	-1.16	y_{24}^{2+}
1311.7273	1311.7267	-0.46	y_{12}^{1+}
1369.7483	1369.7474	-0.66	y_{25}^{2+}
1518.3146	1518.3137	-0.59	y_{28}^{2+}

Appendix 12 – Fragments observed following ETD of +16 ions with m/z 946.40 from NASH liver tissue (identified as α=haemoglobin).

Measured (*m/z*)	Calculated (*m/z*)	Δppm	Assignment
521.7976	521.7982	-1.15	c_{10}^{2+}
585.8450	585.8457	-1.19	c_{11}^{2+}
600.3344	600.3352	-1.33	c_{6}^{1+}
621.3635	621.3642	-1.13	c_{12}^{2+}
656.8821	656.8828	-1.07	c_{13}^{2+}
728.4296	728.4301	-0.69	c_{7}^{1+}
749.9214	749.9225	-1.47	c_{14}^{2+}
778.4325	778.4332	-0.90	c_{15}^{2+}
823.4394	823.4397	-0.36	c_{24}^{3+}
829.4771	829.4778	-0.84	c_{8}^{1+}
842.4797	842.4807	-1.19	c_{16}^{2+}
908.4953	908.4971	-1.98	$z_{25}^{3+\cdot}$
918.9791	918.9793	-0.22	$c_{35}^{4+\cdot}$
1000.0522	1000.0529	-0.70	z_{18}^{2+}
1042.5890	1042.5891	-0.10	c_{10}^{1+}
1044.8998	1044.9000	-0.19	z_{29}^{3+}
1127.1196	1127.1212	-1.42	$z_{42}^{4+\cdot}$
1128.8341	1128.8350	-0.80	c_{42}^{4+}
1153.1239	1153.1242	-0.26	c_{23}^{2+}
1159.1432	1159.1449	-1.47	$z_{43}^{4+\cdot}$
1224.6322	1224.6341	-1.55	$c_{35}^{3+\cdot}$
1234.6555	1234.6559	-0.32	c_{24}^{2+}
1545.1897	1545.1908	-0.71	$z_{43}^{3+\cdot}$

Appendix 13 — Fragments observed following CID of +15 ions with m/z 1087.04 from non-diseased liver tissue (identified as FABP1).

Measured (*m/z*)	Theoretical (*m/z*)	Δppm	Assignment
620.6970	620.7011	-6.61	y_{16}-H_2O^{3+}
630.4153	630.4192	-6.19	y_{10}^{2+}
664.7148	664.7189	-6.17	y_{17}^{3+}
687.9283	687.9326	-6.25	y_{11}^{2+}
692.3941	692.3980	-5.63	y_{18}-H_2O^{3+}
698.3972	698.4015	-6.16	y_{18}^{3+}
712.3259	712.3301	-5.90	b_6^{1+}
716.4390	716.4434	-6.14	y_{12}^{2+}
730.0882	730.0927	-6.16	y_{19}-H_2O^{3+}
736.0916	736.0962	-6.25	y_{19}^{3+}
772.9807	772.9854	-6.08	y_{13}^{2+}
823.5043	823.5096	-6.44	y_{14}^{2+}
831.1353	831.1403	-6.02	y_{22}^{3+}
840.3837	840.3886	-5.83	b_7^{1+}
843.8865	843.8916	-6.04	b_{14}^{2+}
869.1495	869.1547	-5.98	y_{23}^{3+}
880.0189	880.0242	-6.02	y_{15}-H_2O^{2+}
885.0999	885.1049	-5.65	y_{39}^{5+}
889.0242	889.0295	-5.96	y_{15}^{2+}
906.8436	906.8493	-6.29	y_{24}^{3+}
919.7096	919.7146	-5.44	y_{41}^{5+}
930.5424	930.5480	-6.02	y_{16}-H_2O^{2+}
935.4568	935.4621	-5.67	b_8-H_2O^{1+}
939.5477	939.5533	-5.96	y_{16}^{2+}
983.5407	983.5461	-5.49	y_{26}^{3+}
985.2162	985.2200	-3.82	y_{53}^{6+}
987.5637	987.5695	-5.87	y_{17}-H_2O^{2+}
992.8021	992.8067	-4.63	y_{35}^{4+}
996.5689	996.5748	-5.92	y_{17}^{2+}
1007.2662	1007.2725	-6.25	b_{35}^{4+}
1010.8091	1010.8126	-3.46	b_{63}-NH_3^{7+}
1017.3183	1017.3238	-5.41	y_{36}^{4+}
1023.7342	1023.7347	-0.49	y_{55}^{6+}
1033.9520	1033.9573	-5.13	y_{93}^{10+}
1038.0872	1038.0933	-5.88	y_{18}-H_2O^{2+}
1042.5673	1042.5733	-5.79	y_{56}-H_2O^{6+}

1045.4028	1045.4085	-5.42	y_{56}^{6+}
1045.5881	1045.5948	-6.41	y_{37}^{4+}
1047.0925	1047.0986	-5.83	y_{18}^{2+}
1060.0547	1060.0603	-5.25	b_{57}^{6+}
1063.5144	1063.5207	-5.92	$b_{9}\text{-}H_2O^{1+}$
1064.2476	1064.2558	-7.67	y_{57}^{6+}
1090.7665	1090.7709	-4.03	b_{48}^{6+}
1094.6290	1094.6354	-5.85	$y_{19}\text{-}H_2O^{2+}$
1100.2465	1100.2511	-4.15	b_{59}^{6+}
1100.5572	1100.5636	-5.82	b_{39}^{4+}
1103.6342	1103.6406	-5.80	y_{19}^{2+}
1116.5825	1116.5871	-4.15	$b_{60}\text{-}NH_3^{6+}$
1119.2524	1119.2582	-5.15	b_{60}^{6+}
1121.0315	1121.0355	-3.59	$b_{111}\text{-}NH_3^{11+}$
1122.5780	1122.5834	-4.83	b_{111}^{11+}
1124.4329	1124.4382	-4.68	y_{60}^{6+}
1128.5775	1128.5846	-6.29	b_{40}^{4+}
1131.5600	1131.5663	-5.60	b_{106}^{9+}
1137.9231	1137.9276	-3.93	$b_{61}\text{-}NH_3^{6+}$
1140.5886	1140.5941	-4.82	b_{50}^{5+}
1140.7582	1140.7653	-6.19	b_{61}^{6+}
1145.6049	1145.6096	-4.10	$y_{123}\text{-}H_2O^{12+}$
1146.1067	1146.1119	-4.57	y_{61}^{6+}
1146.9393	1146.9438	-3.95	y_{123}^{12+}
1152.6089	1152.6137	-4.19	$y_{62}\text{-}H_2O^{6+}$
1154.1892	1154.1965	-6.35	y_{124}^{12+}
1155.4439	1155.4489	-4.30	y_{62}^{6+}
1157.7714	1157.7731	-1.44	a_{62}^{6+}
1160.1757	1160.1827	-6.03	y_{20}^{2+}
1163.2052	1163.2109	-4.90	b_{51}^{5+}
1165.4368	1165.4433	-5.61	b_{62}^{6+}
1166.3439	1166.3497	-5.00	y_{115}^{11+}
1172.1232	1172.1269	-3.19	y_{63}^{6+}
1174.5311	1174.5383	-6.10	y_{126}^{12+}
1179.2763	1179.2802	-3.28	$b_{63}\text{-}NH_3^{6+}$
1180.4031	1180.4104	-6.18	b_{106}^{10+}
1182.1116	1182.1180	-5.39	b_{63}^{6+}
1184.3505	1184.3570	-5.53	$y_{117}\text{-}H_2O^{11+}$
1185.7123	1185.7216	-7.86	y_{117}^{11+}
1188.9624	1188.9682	-4.91	y_{64}^{6+}
1191.4998	1191.5063	-5.44	a_{96}^{9+}
1191.6113	1191.6188	-6.29	b_{107}^{10+}

1195.6208	1195.6249	-3.43	b_{64}^{6+}
1197.6344	1197.6360	-1.37	y_{118}^{11+}
1198.0222	1198.0297	-6.26	b_{53}^{5+}
1201.5233	1201.5246	-1.08	$b_{108}\text{-}NH_3^{10+}$
1203.9539	1203.9601	-5.12	a_{97}^{9+}
1208.2932	1208.2996	-5.32	b_{65}^{6+}
1212.6122	1212.6190	-5.61	b_{87}^{8+}
1213.6416	1213.6463	-3.87	y_{65}^{6+}
1216.4073	1216.4121	-3.93	$a_{98}\text{-}NH_3^{9+}$
1217.6884	1217.6962	-6.41	y_{21}^{2+}
1225.8583	1225.8602	-1.51	$a_{99}\text{-}NH_3^{9+}$
1232.9330	1232.9384	-4.38	$b_{111}\text{-}NH_3^{10+}$
1234.8348	1234.8410	-5.02	b_{111}^{10+}
1246.1991	1246.2069	-6.26	y_{22}^{2+}
1251.3071	1251.3138	-5.38	b_{67}^{3+}
1252.0500	1252.0576	-6.07	b_{56}^{5+}
1254.2829	1254.2887	-4.62	y_{56}^{5+}
1260.3986	1260.4062	-6.03	b_{45}^{4+}
1262.2935	1262.3012	-6.10	b_{33}^{3+}
1271.8636	1271.8712	-5.98	b_{57}^{5+}
1289.8163	1289.8225	-4.78	b_{69}^{6+}
1294.4824	1294.4881	-4.40	b_{58}^{5+}
1303.2203	1303.2283	-6.14	y_{23}^{2+}
1320.0918	1320.0998	-6.06	b_{59}^{5+}
1340.1905	1340.1927	-1.64	a_{96}^{8+}
1343.1000	1343.1084	-6.25	b_{60}^{5+}
1354.4481	1354.4542	-4.50	a_{97}^{8+}
1359.7623	1359.7704	-5.96	y_{24}^{2+}
1368.7094	1368.7169	-5.48	b_{61}^{5+}
1382.9269	1382.9351	-5.93	$y_{62}\text{-}H_2O^{5+}$
1386.3293	1386.3372	-5.70	y_{62}^{5+}
1398.1219	1398.1306	-6.22	b_{62}^{5+}
1414.7300	1414.7348	-3.39	$b_{63}\text{-}NH_3^{5+}$
1418.3321	1418.3401	-5.64	b_{63}^{5+}
1434.5449	1434.5485	-2.51	$b_{64}\text{-}NH_3^{5+}$
1438.1508	1438.1538	-2.09	b_{64}^{5+}

Appendix 14 — Fragments observed following ETD of +16 ions with m/z 942.24 from NASH liver tissue (identified as FABP1).

Measured (*m/z*)	Calculated (*m/z*)	Δppm	Assignment
566.2926	566.2933	-1.24	c_5^{1+}
729.3557	729.3566	-1.23	c_6^{1+}
806.7926	806.7936	-1.24	z_{21}^{3+}
815.4995	815.4999	-0.49	z_{14}^{2+}
823.5086	823.5092	-0.73	y_{14}^{2+}
825.8002	825.8008	-0.73	z_{22}^{3+}
857.4146	857.4152	-0.70	c_7^{1+}
863.8144	863.8151	-0.81	z_{23}^{3+}
881.0195	881.0201	-0.68	z_{15}^{2+}
901.2601	901.2611	-1.11	z_{32}^{4+}
901.8437	901.8457	-2.22	$z_{24}^{3+\cdot}$
911.9820	911.9814	0.66	c_{48}^{6+}
916.3101	916.3108	-0.76	z_{41}^{5+}
916.9255	916.9261	-0.65	c_{15}^{2+}
922.4772	922.4776	-0.43	c_{32}^{4+}
926.4851	926.4881	-3.24	c_{41}^{5+}
936.6598	936.6593	0.57	c_{49}^{6+}
938.0276	938.0282	-0.64	z_{33}^{6+}
944.5235	944.5240	-0.53	z_{25}^{3+}
949.8633	949.8635	-0.21	y_{25}^{3+}
951.4841	951.4844	-0.32	c_{33}^{4+}
952.0999	952.0999	0.00	c_{52}^{5+}
963.2893	963.2901	-0.83	z_{34}^{4+}
967.2933	967.2948	-1.55	y_{34}^{4+}
970.4984	970.4993	-0.93	c_8^{1+}
974.9085	974.9085	0.00	c_{43}^{4+}
979.5049	979.5054	-0.51	c_{34}^{4+}
988.5514	988.5520	-0.61	z_{35}^{4+}
1000.5260	1000.5238	2.20	a_{35}^{4+}
1011.5287	1011.5291	-0.40	c_{35}^{4+}
1016.5686	1016.5689	-0.30	y_{27}^{3+}
1025.0371	1025.0378	-0.65	c_{55}^{6+}
1039.1435	1039.1435	0.00	c_{46}^{5+}
1040.2395	1040.2400	-0.48	z_{28}^{3+}
1041.5887	1041.5901	-1.34	z_{37}^{4+}
1045.5789	1045.5796	-0.67	y_{28}^{3+}

1050.5510	1050.5516	-0.57	c_{37}^{4+}
1053.3880	1053.3885	-0.47	y_{47}^{5+}
1068.5582	1068.5572	0.94	c_{47}^{5+}
1072.3084	1072.3096	-1.12	c_{38}^{4+}
1082.9377	1082.9383	-0.55	z_{29}^{3+}
1094.1748	1094.1762	-1.28	c_{48}^{5+}
1123.7902	1123.7899	0.27	c_{49}^{5+}
1132.8388	1132.8393	-0.44	c_{40}^{4+}
1145.1362	1145.1367	-0.44	z_{41}^{4+}
1158.6471	1158.6473	-0.17	z_{31}^{3+}
1159.6084	1159.6084	0.00	c_{41}^{4+}
1164.3221	1164.3202	1.60	y_{31}^{3+}
1166.6154	1166.6162	-0.69	c_{51}^{5+}
1167.9287	1167.9289	-0.17	c_{30}^{3+}
1187.2701	1187.2694	0.56	c_{31}^{3+}
1189.6223	1189.6230	-0.59	c_{42}^{4+}
1201.6800	1201.6816	-1.33	$z_{32}^{3+\cdot}$
1214.9638	1214.9606	2.61	a_{32}^{3+}
1218.1333	1218.1318	1.23	$c_{41}^{4+\cdot}$
1229.8444	1229.8439	0.41	c_{55}^{5+}
1229.9686	1229.9677	0.70	c_{32}^{2+}
1232.3884	1232.3891	-0.57	c_{44}^{4+}
1250.7035	1250.7018	1.33	z_{33}^{3+}
1254.1108	1254.1072	2.87	a_{22}^{2+}
1284.3857	1284.3870	-1.01	$z_{34}^{3+\cdot}$
1298.9276	1298.9276	0.00	c_{46}^{4+}
1305.6717	1305.6714	0.23	c_{34}^{3+}
1316.7358	1316.7338	1.52	y_{47}^{4+}
1323.7074	1323.7051	1.74	c_{59}^{5+}
1324.9443	1324.9393	3.77	a_{47}^{4+}
1333.6969	1333.6959	0.72	a_{35}^{3+}
1335.6949	1335.6947	0.15	c_{47}^{4+}
1348.3696	1348.3697	-0.07	c_{35}^{3+}
1352.2643	1352.2649	-0.44	$z_{24}^{2+\cdot}$
1367.4701	1367.4684	1.24	c_{48}^{4+}
1388.7870	1388.7870	0.00	z_{37}^{3+}
1404.7368	1404.7355	0.93	c_{49}^{4+}
1408.0442	1408.0444	-0.14	y_{126}^{10+}
1412.5408	1412.5411	-0.21	a_{63}^{5+}
1416.7877	1416.7864	0.92	z_{25}^{2+}
1429.7476	1429.7437	2.70	c_{38}^{3+}
1442.6015	1442.5994	1.46	$z_{78}^{6+\cdot}$

1458.2708	1458.2685	1.58	c_{51}^{4+}
1526.8494	1526.8491	0.20	$z_{41}^{3+\cdot}$
1537.0566	1537.0530	2.34	c_{55}^{4+}
1558.8639	1558.8605	2.18	z_{28}^{2+}
1564.4942	1564.4930	0.75	y_{126}^{9+}
1586.1657	1586.1616	2.56	c_{42}^{4+}
1624.1791	1624.1759	1.95	c_{43}^{3+}
1643.1858	1643.1830	1.70	c_{44}^{3+}
1760.1848	1760.1787	3.47	y_{126}^{8+}

Appendix 15 — Fragments observed following CID of +15 ions with m/z 1084.08 from non-diseased liver tissue (identified as $FABP_{TA}$).

Measured (*m/z*)	Theoretical (*m/z*)	Δppm	Assignment
477.2368	477.2400	-6.71	b_8^{2+}
573.8734	573.8771	-6.45	y_9^{2+}
584.7817	584.7853	-6.16	b_{10}^{2+}
620.6969	620.7011	-6.77	$y_{16}\text{-}H_2O^{3+}$
630.4150	630.4192	-6.66	y_{10}^{2+}
687.9281	687.9326	-6.54	y_{11}^{2+}
692.3934	692.3980	-6.64	$y_{18}\text{-}H_2O^{3+}$
698.3968	698.4015	-6.73	y_{18}^{3+}
712.3254	712.3301	-6.60	b_6^{1+}
716.4387	716.4434	-6.56	y_{12}^{2+}
730.0879	730.0927	-6.57	y_{19}^{3+}
736.0911	736.0962	-6.93	y_{19}^{3+}
772.9803	772.9854	-6.60	y_{13}^{2+}
773.7861	773.7909	-6.20	y_{20}^{3+}
823.5039	823.5092	-6.44	y_{14}^{2+}
831.1341	831.1403	-7.46	y_{22}^{2+}
840.3834	840.3886	-6.19	b_7^{1+}
869.1488	869.1547	-6.79	y_{23}^{3+}
879.0963	879.1028	-7.39	y_{38}^{5+}
889.0237	889.0295	-6.52	y_{15}^{2+}
930.5419	930.5480	-6.56	$y_{16}\text{-}H_2O^{2+}$
939.5471	939.5533	-6.60	y_{16}^{2+}
953.4668	953.4727	-6.19	y_8^{1+}
985.2983	985.3040	-5.79	y_{35}^{4+}
987.5631	987.5695	-6.48	$y_{17}\text{-}H_2O^{2+}$
996.5684	996.5748	-6.42	y_{17}^{2+}
1007.2651	1007.2725	-7.35	b_{35}^{4+}
1009.8155	1009.8211	-5.55	y_{36}^{4+}
1010.9526	1010.9555	-2.83	$b_{63}\text{-}NH_3^{7+}$
1018.8932	1018.8996	-6.25	y_{55}^{6+}
1038.0865	1038.0933	-6.55	$y_{18}\text{-}H_2O^{2+}$
1040.4000	1040.4067	-6.41	y_{56}^{6+}
1045.5732	1045.5796	-6.12	y_{28}^{3+}
1047.0918	1047.0986	-6.49	y_{18}^{2+}
1059.2478	1059.2541	-5.92	y_{57}^{6+}
1091.1647	1091.1709	-5.68	b_{48}^{5+}

1094.6284	1094.6354	-6.39	y_{19}-H_2O^{2+}
1103.6335	1103.6406	-6.43	y_{19}^{2+}
1118.3942	1118.3982	-3.61	b_{111}-NH_3^{11+}
1119.4195	1119.4248	-4.76	b_{60}^{6+}
1119.5984	1119.6030	-4.14	y_{60}^{6+}
1119.9413	1119.9461	-4.32	b_{111}^{11+}
1140.7582	1140.7653	-6.19	b_{61}^{6+}
1143.1029	1143.1088	-5.16	y_{123}-H_2O^{12+}
1144.5203	1144.5263	-5.21	y_{123}^{12+}
1150.2724	1150.2804	-6.95	y_{62}^{6+}
1151.7724	1151.7790	-5.70	y_{124}^{12+}
1160.1750	1160.1827	-6.64	y_{20}^{2+}
1163.6046	1163.6072	-2.23	a_{105}^{5+}
1165.6043	1165.6100	-4.89	b_{62}^{6+}
1166.9515	1166.9585	-5.97	y_{63}^{6+}
1177.4013	1177.4093	-6.79	b_{106}^{10+}
1179.1082	1179.1135	-4.49	b_{63}-NH_3^{6+}
1181.5303	1181.5379	-6.46	y_{117}-H_2O^{11+}
1182.1109	1182.1180	-5.98	b_{63}^{6+}
1183.1681	1183.1752	-6.03	y_{117}^{11+}
1183.9601	1183.9664	-5.35	y_{64}^{6+}
1186.2120	1186.2183	-5.31	a_{107}^{10+}
1187.1088	1187.1151	-5.31	b_{107}-NH_3^{10+}
1188.9096	1188.9177	-6.81	b_{107}^{10+}
1193.2638	1193.2704	-5.57	y_{118}-H_2O^{11+}
1194.9012	1194.9078	-5.56	y_{118}^{11+}
1195.7870	1195.7916	-3.82	b_{64}^{6+}
1197.6204	1197.6279	-6.26	b_{53}^{5+}
1212.6108	1212.6190	-6.76	b_{87}^{8+}
1231.8308	1231.8400	-7.47	b_{111}^{10+}
1260.3979	1260.4062	-6.59	b_{45}^{4+}
1262.2927	1262.3012	-6.73	b_{33}^{3+}
1279.7738	1279.7830	-7.19	y_{115}^{10+}
1289.9810	1289.9891	-6.30	b_{69}^{6+}
1294.6811	1294.6881	-5.41	b_{58}^{5+}
1303.2194	1303.2283	-6.83	y_{23}^{2+}
1308.3406	1308.3429	-1.79	b_{106}^{9+}
1320.2931	1320.2998	-5.07	b_{59}^{5+}
1368.7149	1368.7169	-1.46	b_{61}^{5+}
1380.3269	1380.3351	-5.94	y_{62}^{5+}
1398.3225	1398.3306	-5.79	b_{62}^{5+}
1414.9289	1414.9348	-4.17	b_{63}-NH_3^{5+}

1418.5317	1418.5401	-5.92	b_{63}^{5+}
1438.3462	1438.3538	-5.28	b_{64}^{5+}

Appendix 16 — Fragments observed following ETD of +16 ions with m/z 940.24 from NASH liver tissue (identified as $FABP_{TA}$).

Measured (*m/z*)	Calculated (*m/z*)	Δppm	Assignment
566.2923	566.2933	-1.77	c_5^{1+}
729.3552	729.3566	-1.92	c_6^{1+}
815.4987	815.4999	-1.47	z_{14}^{2+}
826.1347	826.1367	-2.42	$z_{22}^{3+\cdot}$
857.4141	857.4152	-1.28	c_7^{1+}
863.8139	863.8151	-1.39	z_{23}^{3+}
869.2355	869.2373	-2.07	z_{31}^{4+}
901.2595	901.2611	-1.78	z^{324+}
901.8432	901.8457	-2.77	$z_{24}^{3+\cdot}$
910.3072	910.3087	-1.65	z_{41}^{5+}
912.1470	912.1481	-1.17	c_{48}^{6+}
916.9252	916.9261	-0.98	c_{15}^{2+}
922.7268	922.7276	-0.87	c_{32}^{4+}
939.5525	939.5533	-0.85	y_{16}^{2+}
944.5225	944.5240	-1.59	z_{25}^{3+}
952.0989	952.0999	-1.05	c_{52}^{5+}
956.0359	956.0394	-3.66	$z_{34}^{4+\cdot}$
970.4984	970.4993	-0.93	c_8^{1+}
979.5044	979.5054	-1.02	c_{34}^{4+}
1011.5285	1011.5291	-0.59	c_{35}^{4+}
1025.0362	1025.0378	-1.53	c_{55}^{6+}
1039.3439	1039.3435	0.38	c_{46}^{5+}
1040.2394	1040.2400	-0.58	z_{28}^{3+}
1044.3813	1044.3842	-2.78	$z_{47}^{5+\cdot}$
1045.5785	1045.5796	-1.05	y_{28}^{3+}
1050.5537	1050.5516	2.00	c_{37}^{4+}
1068.5621	1068.5572	4.59	c_{47}^{5+}
1072.3072	1072.3096	-2.24	c_{38}^{4+}
1082.9376	1082.9383	-0.65	z_{29}^{3+}
1094.3759	1094.3762	-0.27	c_{48}^{5+}
1123.6280	1123.6306	-2.31	$z_{40}^{4+\cdot}$
1123.7895	1123.7899	-0.36	c_{49}^{5+}
1135.9464	1135.9447	1.50	c_{47}^{4+}
1137.6325	1137.6340	-1.32	z_{41}^{4+}
1158.6464	1158.6473	-0.78	z_{31}^{3+}
1164.3209	1164.3202	0.57	y_{31}^{3+}

1166.6172	1166.6162	0.86	c_{51}^{5+}
1189.6225	1189.6230	-0.42	c_{42}^{4+}
1201.6801	1201.6816	-1.25	$z_{32}^{3+\cdot}$
1218.1369	1218.1318	4.19	$c_{41}^{4+\cdot}$
1229.8437	1229.8439	-0.16	c_{55}^{5+}
1229.9682	1229.9677	0.38	c_{32}^{2+}
1232.6393	1232.6391	0.16	c_{44}^{4+}
1250.7030	1250.7018	0.93	z_{33}^{3+}
1274.3844	1274.3834	0.78	$z_{34}^{3+\cdot}$
1305.6709	1305.6714	-0.38	c_{34}^{3+}
1348.3695	1348.3697	-0.15	c_{35}^{3+}
1367.7199	1367.7184	1.10	c_{48}^{4+}
1516.8444	1516.8443	0.07	$z_{27}^{3+\cdot}$
1537.0569	1537.0530	2.54	c_{55}^{4+}
1586.1619	1586.1616	0.19	c_{42}^{3+}
1643.1868	1643.1830	2.31	c_{44}^{3+}
1725.3199	1725.3158	2.38	$z_{78}^{5+\cdot}$
1737.9724	1737.9674	2.88	z_{31}^{2+}

Appendix 17 — Bottom-up coverage of FABP in All extractions and replicates.

Ammonium bicarbonate extraction, replicate1 Coverage 54.33%

MSFSGKYQLQ SQENFEAFMK AIGLPEELIQ KGKDIKGVSE IVQNGKHFKF
TITAGSKVIQ NEFTVGEECE LETMTGEKVK TVVQLEGDNK LVTTFKNIKS
VTELNGDIIT NTMTLGDIVF KRISKRI

Ammonium bicarbonate extraction, replicate 2 Coverage 57.48%

MSFSGKYQLQ SQENFEAFMK AIGLPEELIQ KGKDIKGVSE IVQNGKHFKF
TITAGSKVIQ NEFTVGEECE LETMTGEKVK TVVQLEGDNK LVTTFKNIKS
VTELNGDIIT NTMTLGDIVF KRISKRI

50% Methanol extraction, replicate 1 Coverage 54.33%

MSFSGKYQLQ SQENFEAFMK AIGLPEELIQ KGKDIKGVSE IVQNGKHFKF
TITAGSKVIQ NEFTVGEECE LETMTGEKVK TVVQLEGDNK LVTTFKNIKS
VTELNGDIIT NTMTLGDIVF KRISKRI

50% Methanol extraction, replicate 2 Coverage 53.54%

MSFSGKYQLQ SQENFEAFMK AIGLPEELIQ KGKDIKGVSE IVQNGKHFKF
TITAGSKVIQ NEFTVGEECE LETMTGEKVK TVVQLEGDNK LVTTFKNIKS
VTELNGDIIT NTMTLGDIVF KRISKRI

70% Methanol extraction, replicate 1 Coverage 53.54%

MSFSGKYQLQ SQENFEAFMK AIGLPEELIQ KGKDIKGVSE IVQNGKHFKF
TITAGSKVIQ NEFTVGEECE LETMTGEKVK TVVQLEGDNK LVTTFKNIKS
VTELNGDIIT NTMTLGDIVF KRISKRI

70% Methanol extraction, replicate 2 Coverage 54.33%

MSFSGKYQLQ SQENFEAFMK AIGLPEELIQ KGKDIKGVSE IVQNGKHFKF
TITAGSKVIQ NEFTVGEECE LETMTGEKVK TVVQLEGDNK LVTTFKNIKS
VTELNGDIIT NTMTLGDIVF KRISKRI

Appendix 18 – Publication: Liquid Extraction Surface Analysis Mass Spectrometry Coupled with Field Asymmetric Waveform Ion Mobility Spectrometry for Analysis of Intact Proteins from Biological Substrates.

analytical chemistry

Article

pubs.acs.org/ac

Liquid Extraction Surface Analysis Mass Spectrometry Coupled with Field Asymmetric Waveform Ion Mobility Spectrometry for Analysis of Intact Proteins from Biological Substrates

Joscelyn Sarsby,[†] Rian L. Griffiths,[†] Alan M. Race,[‡] Josephine Bunch,[‡,§] Elizabeth C. Randall,[†] Andrew J. Creese,[†] and Helen J. Cooper*[,†]

[†]School of Biosciences, University of Birmingham, Edgbaston, Birmingham B15 2TT, United Kingdom

[‡]National Physical Laboratory, Hampton Road, Teddington, Middlesex TW11 0LW, United Kingdom

[§]School of Pharmacy, University of Nottingham, University Park, Nottingham NG7 2RD, United Kingdom

Supporting Information

ABSTRACT: Previously we have shown that liquid extraction surface analysis (LESA) mass spectrometry is suitable for the analysis of intact proteins from a range of biological substrates. Here we show that LESA mass spectrometry may be coupled with high field asymmetric waveform ion mobility spectrometry (FAIMS) for top-down protein analysis directly from thin tissue sections (mouse liver, mouse brain) and from bacterial colonies (*Escherichia coli*) growing on agar. Incorporation of FAIMS results in significant improvements in signal-to-noise and reduced analysis time. Abundant protein signals are observed in single scan mass spectra. In addition, FAIMS enables gas-phase separation of molecular classes, for example, lipids and proteins, enabling improved analysis of both sets of species from a single LESA extraction.

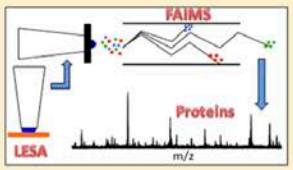

Liquid extraction surface analysis (LESA)[1] mass spectrometry is emerging as a powerful tool for in situ analysis of intact proteins. In LESA, a robotic pipet dispenses a droplet (a few μL) of solvent onto the surface under investigation. The droplet is held in contact between the pipet and the surface for a few seconds, that is, a liquid microjunction is maintained, and soluble analytes are extracted. The sample droplet is reaspirated and introduced into the mass spectrometer via electrospray ionization. Edwards et al. demonstrated that the approach, which is also known as liquid microjunction sampling, could be applied to the analysis of hemoglobin variants from neonatal dried blood spots.[2−4] Schey et al. demonstrated manual LESA of intact proteins from thin tissue sections of mouse brain and kidney, and bovine ocular lens.[5] Sarsby et al. applied LESA mass spectrometry for the analysis of intact protein biomarkers of nonalcoholic liver disease.[6] More recently, we have shown that a variation of LESA, which we termed "contact" LESA allows top-down analysis of proteins from living bacterial colonies[7] and intact protein complexes.[8]

Challenges for top-down protein analysis by LESA mass spectrometry include those faced in any top-down electrospray analysis—the requirement for high resolution mass spectrometry, the presence of multiple charge states (for both precursor and fragment ions), the large number of fragmentation channels available. These challenges are compounded in LESA mass spectrometry by the potential complexity of the sample, particularly for biological substrates. Multiple proteins and proteoforms may be present over a wide dynamic range. In addition, the presence of other molecular classes, for example, lipids, may cause interference as a result of ion suppression. To date, LESA MS of proteins tends to involve collection and coadding of multiple scans in order to obtain sufficient S/N for peak detection. This feature could present a barrier to the adoption of LESA MS for imaging of intact proteins. A potential solution to the issue of sample complexity is the coupling of liquid-phase separation methods; however, this brings a significant time cost. A typical HPLC MS analysis takes ~1 h,[5] clearly incompatible with fast acquisition of a LESA image even of relatively few pixels. In contrast, the gas-phase separation afforded by ion mobility spectrometry, which separates ions on the basis of shape and charge, can be achieved on the order of milliseconds.

High-field asymmetric waveform ion mobility spectrometry (FAIMS), also known as differential ion mobility spectrometry, offers several advantages for the analysis of peptides and proteins, including reduced chemical noise, improved S/N,[9−12] and separation of peptide isomers.[13−16] FAIMS separates gas-phase ions at atmospheric pressure on the basis of differences in the ion mobilities in high and low electric fields.[17,18] Ions are passed between two parallel electrodes by a carrier gas. An asymmetric waveform is applied to the electrodes to provide alternating high and low electric fields perpendicular to the direction of the ions' trajectory through the device. The high electric field is designated the dispersion field (DF). As a result of the differences in mobilities in high and low electric fields, the ions will deviate from their original trajectory toward one of

Received: March 12, 2015
Accepted: June 11, 2015
Published: June 11, 2015

DOI: 10.1021/acs.analchem.5b01151
Anal. Chem. 2015, 87, 6794−6800

the electrodes. If uncorrected, they will collide with the electrode. Superposition of a compensation field (CF) prevents this occurrence. By tuning the compensation field, it is possible to selectively transmit ions of a particular differential mobility.

FAIMS devices have previously been coupled to ambient ionization techniques for the analysis of small molecules. Fernandez and co-workers coupled desorption electrospray (DESI) with FAIMS for the analysis of counterfeit pharmaceuticals.[19] More recently, they demonstrated DESI FAIMS mass spectrometry for the imaging of phosphatidylcholines (m/z 700−900) in rat brain tissue.[20] Manicke and Belford coupled paperspray ionization with FAIMS for the separation of isomeric drug compounds.[21] Porta and co-workers have shown that LESA coupled with FAIMS is suitable for the analysis of drugs of abuse and their metabolites.[22] In that work, a prototype FAIMS device was coupled with a triple quadrupole linear ion trap mass spectrometer.

Here, we demonstrate the benefits of FAIMS for intact and top-down protein analysis by LESA mass spectrometry. We have coupled LESA with a miniaturized chip-based FAIMS device[23] and a high resolution orbitrap mass spectrometer. LESA FAIMS analyses were performed on thin tissue sections from mouse liver and mouse brain and on *E. coli* colonies growing on agar (Note, the analysis of bacteria made use of the "contact" LESA approach described in ref 7). The results show significant improvements in protein peak S/N, enabling detection of proteins in single scan mass spectra (i.e., in under 2 s, compared with several minutes required in the absence of FAIMS). Moreover, it is possible to separate molecular classes such that different species may be analyzed from a single LESA extraction. That is, FAIMS addresses the inherent challenge of sample complexity in LESA MS of biological substrates.

EXPERIMENTAL SECTION

Materials. *Thin Tissue Sections.* Liver and brain from wild-type mice (extraneous tissue from culled animals) were the gift of Prof. Steve Watson (University of Birmingham). Organs were frozen on dry ice prior to storage at −80 °C. Sections of murine liver tissue and brain tissue of area ∼1.5 cm^2 were obtained at a thickness of 10 μm using a CM1810 Cryostat (Leica Microsystmes, Wetzlar, Germany) and thaw mounted onto glass slides.

E. coli Colonies. A strain of *Escherichia coli* K-12 was inoculated onto solid LBA medium (LB 20 g L-1 Agar 20 g L-1) in 6 cm diameter Petri dishes. Samples were incubated at 37 °C for ∼12 h and subsequently stored in the dark at 4 °C until analysis (∼43 days).

Solvents. The following solvents were used: acetonitrile (J. T. Baker, The Netherlands), methanol (J. T. Baker, The Netherlands), ethanol (Fisher Scientific, Loughborough, U.K.), HPLC grade water (J. T. Baker, The Netherlands), and formic acid (Sigma-Aldrich Company Ltd., Dorset, U.K.).

Peptide and Protein Standards (for direct infusion electrospray). A solution comprising AAAAAAnYK (2 μM; nY = nitrotyrosine; AltaBioscience, Birmingham, U.K.) and angiotensin I (2 μM), substance P (2 μM), bovine ubiquitin (5 μM), and hemoglobin S (5 μM) (all Sigma-Aldrich, Dorset, U.K.) was prepared in 69.5:29.5:1 methanol/water/formic acid.

Liquid Extraction Surface Analysis. Thin tissue section samples were loaded onto a universal LESA adapter plate and placed in the TriVersa Nanomate chip-based electrospray device (Advion, Ithaca, NY) coupled to the Thermo Fisher Scientific Orbitrap Velos or Elite (Thermo Fisher Scientific, Bremen, Germany). Bacteria samples were placed directly in the Triversa Nanomate (see ref 7 for details).

Thin Tissue Sections. The solvent system used for LESA extraction/electrospray was 69.5:29.5:1 methanol/water/formic acid (mouse liver) or 39.5:59.5:1 acetonitrile/water/formic acid (mouse brain). Brain sections were prewashed by LESA sampling with 80:20 ethanol/water. Wash solutions were dispensed to waste. A total of 6 μL were aspirated from the solvent well. The robotic arm relocated to a position above the tissue and descended to a height 0.2 mm above the surface of the sample. A total of 3 μL of the solution was dispensed onto the sample surface to form a liquid microjunction. The liquid microjunction was maintained for 10 s; then 3.5 μL were reaspirated into the pipet tip.

E. coli. The solvent system used for LESA extraction/electrospray was 39.5:59.5:1 acetonitrile/water/formic acid. Three μL were aspirated from the solvent well. The robotic arm relocated to a position above the bacterial colony and descended until in contact with the surface of the bacterial colony. A total of 2 μL of the solution was dispensed onto the sample surface to form a liquid microjunction. The liquid microjunction was maintained with the surface for 3 s; then 2.5 μL were reaspirated into the pipet tip.

Samples were introduced into the mass spectrometer via the TriVersa NanoMate, with gas pressure 0.3 psi, a tip voltage of 1.75 kV (or 1.55 kV for direct infusion electrospray), and a capillary temperature of 250 °C.

UltraFAIMS. The Triversa Nanomate was coupled to a miniaturized ultra-FAIMS device (Owlstone, Cambridge, U.K.), which was coupled to an Orbitrap Velos or Orbitrap Elite mass spectrometer (Thermo Fisher Scientific, Bremen Germany), see Supporting Information, Figure 1. FAIMS separation was carried out in positive ion mode using a microchip device (Owlstone).[24] The FAIMS device was operated either in 2D mode or in static mode.

2-D FAIMS Analyses. FAIMS separation was carried out at eight discrete dispersion fields (DFs) between 130 and 270 Td with a step size of 20 Td. At each DF, the compensation field was varied between −1 to +4 Td (step size 2.5 mTd) over a time period of 180 s.

Static FAIMS Analyses. Optimal DF and CF conditions for the transmission of ions of interest were selected from the 2D FAIMS analyses. Data shown were recorded as follows: Mouse Liver: DF = 130 Td, CF = 0.30 Td. Mouse brain: DF = 270 Td, CF = 2.60 Td. *E. coli*: DF = 210 Td, CF = 1.65 Td.

Mass Spectrometry. The majority of mass spectrometry experiments were performed on a Thermo Fisher Orbitrap Velos. Results shown for the 2D FAIMS analysis of mouse brain sections were recorded on a Thermo Fisher Orbitrap Elite.

Mass spectra were collected in full scan mode (m/z 400−2000 (mouse samples); m/z 500−2000 (*E. coli* samples)) at a resolving power of 100000 at m/z 400 (Orbitrap Velos) or 120000 (Orbitrap Elite) at m/z 200. The AGC target was 1×10^6 charges with a maximum injection time of 1000 ms. Each scan was composed of 1 microscan.

Tandem Mass Spectrometry. CID: CID was carried out in the linear ion trap at normalized collision energy of 30%, and fragment ions were detected in the orbitrap at a resolving power of 100000 at m/z 400. AGC target was 1×10^6 (mouse tissue samples) or 1×10^5 (*E. coli* samples) with maximum injection time of 1 s. HCD: HCD experiments (NCE 30%)

DOI: 10.1021/acs.analchem.5b01151
Anal. Chem. 2015, 87, 6794−6800

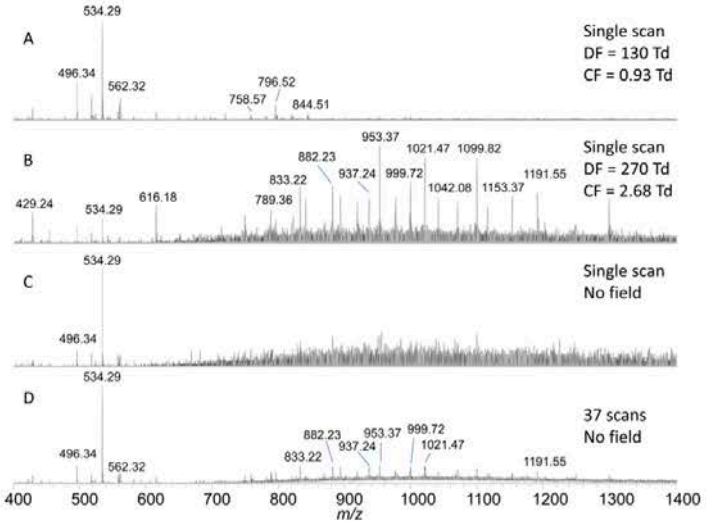

Figure 1. LESA 2D-FAIMS mass spectrometry of mouse liver. (A) Single scan mass spectrum at DF = 130 Td, CF = 0.93 Td; (B) Single scan mass spectrum at DF = 270 Td, CF = 2.68 Td; (C) Single scan mass spectrum recorded in the absence of FAIMS field; (D) Mass spectrum recorded in the absence of FAIMS field comprising 37 coadded scans (~1 min data).

were recorded at a resolving power of 100000 at m/z 400. AGC target was 1×10^6 (mouse tissue samples) or 1×10^5 (*E. coli* samples) with maximum injection time of 1 s. ETD: ETD was performed with fluoranthene ions. AGC target for precursor ions was 1×10^6 with maximum injection time 1 s. AGC target for fluoranthene ions was 1×10^6 (maximum inject time 1 s). Precursor ions were activated for 30 ms. For all fragmentation methods, isolation widths were 3 Th (m/z 1021.54 from liver), 7.5 Th (m/z 952.63 from brain), and 10 Th (m/z 1392.27 from *E. coli*). MS/MS spectra were comprised of five microscans. Data were recorded for 2–5 min in each case.

Data were analyzed using either Xcalibur version 2.1.0.1139 or 3.0.63 software.

DATA ANALYSIS

Visualization of FAIMS Data. Data were converted from Thermo.raw format to mzML using msconvert as part of ProteoWizard[25] and then to imzML using imzMLConverter.[26] Data in the imzML format were then loaded into MATLAB (version 2013, The MathWorks Inc., Natick, Massachusetts) using imzMLConverter and in-house software.

Total Ion Transmission Maps. A linear m/z axis was generated between m/z 500 and 2000 with a step interval of 0.5. Generation of total ion transmission maps were performed by sequentially loading in each spectrum from the 2D FAIMS analysis, summing all data points that fell between adjacent intervals on the linear m/z axis and inserting into a 2D matrix ($m \times n$, where m is number of scans in the 2D FAIMS analysis and n is number of m/z bins on the generated m/z axis). Isolation and display of a single DF value was performed by extracting the relevant scans from the full data matrix and normalizing to CF.

Single Ion Transmission Maps. Selected m/z values (with user defined tolerance) from the 2D FAIMS analysis were loaded into an array. Generation of single ion transmission maps was performed by selecting scans from each DF value, and projecting signal intensities of the selected m/z into a 2D matrix ($m \times n$, where m is the CF (normalized to scan number) and n is the DF). The 2D matrix was displayed in false color normalized to the maximum intensity of the ion.

Software for generation of total ion transmission maps and single ion transmission maps, together with a step-by-step guide, is available for download from http://www.biosciences-labs.bham.ac.uk/cooper/software.html.

Analysis of MS/MS Data. All mass spectra were deconvoluted using the Xtract function in Xcalibur in order to obtain monoisotopic masses. Mass spectra were processed with a signal-to-noise ratio threshold of three. The processed fragment ion list was submitted to Prosight PTM 2.0 (https://prosightptm2.northwestern.edu) and searched against the mouse or *E. coli* K-12 database accordingly, allowing all modifications, with a fragment tolerance of 10 ppm. Identity was confirmed by manual analysis using Protein Prospector (http://prospector.ucsf.edu/prospector/mshome.htm).

RESULTS AND DISCUSSION

The miniaturized chip-based ultraFAIMS device was coupled with the orbitrap mass spectrometer and the Triversa Nanomate, see Supporting Information, Figure 1. LESA FAIMS mass spectrometry analyses, in which both the dispersion field (DF) and the compensation field (CF) were varied (2D FAIMS analysis), were performed on thin tissue sections from mouse liver and mouse brain and on *E. coli* growing on agar. Optimal DF and CF conditions for the transmission of a particular species of interest were determined and static FAIMS analyses, at a single DF and single CF setting, were conducted. Static FAIMS analyses were coupled with tandem mass spectrometry for protein identification.

The transmission efficiency through the ultraFAIMS device is illustrated in Supporting Information, Figure 2. The figure shows single scan mass spectra of substance P and ubiquitin following direct infusion electrospray of a peptide/protein mixture (i.e., no LESA). In each case, the top mass spectrum was recorded in the absence of the FAIMS device, the middle

DOI: 10.1021/acs.analchem.5b01151
Anal. Chem. 2015, 87, 6794–6800

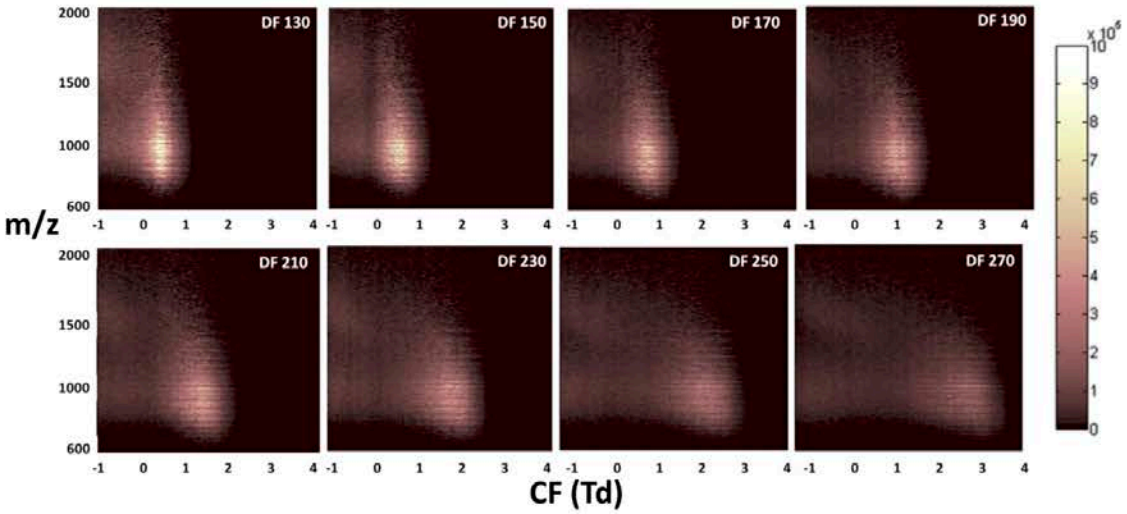

Figure 2. Total ion transmission maps obtained following LESA 2D FAIMS analyses of mouse liver.

mass spectrum was recorded with the FAIMS device coupled but with no field applied, and the bottom mass spectrum was recorded at the optimum FAIMS conditions for the ions of interest. The results show that, while there is a drop in sensitivity (~1 order of magnitude) as a result of coupling the FAIMS device, once coupled, the transmission efficiency (FAIMS field applied vs FAIMS no field) is ~80%. Moreover, with FAIMS field applied the signal-to-noise improves ~2-fold and ~14-fold for the monoisotopic peaks of substance P and ubiquitin, respectively.

2D FAIMS Analyses. Incorporation of FAIMS into the LESA workflow resulted in improved signal-to-noise for both intact protein peaks and small singly charged species. Figure 1A,B shows mass spectra obtained during a 2-D sweep of dispersion field (DF) and compensation field (CF) following LESA sampling of thin tissue sections of mouse liver. Each mass spectrum represents a single scan, that is, total MS analysis time of 1.8 s. At DF = 130 Td and CF = 0.93 Td (Figure 1A), the mass spectrum is dominated by peaks corresponding to singly charged small molecules. The abundant peaks at m/z 534.29 and 496.34 correspond to lysophosphatidylcholine (lyso-PC) 16:0 $[M + K]^+$ and $[M + H]^+$ adducts, respectively. Abundant peaks at m/z 796.52 and 758.57 correspond to phosphatidylcholine PC 34:2 $[M + K]^+$ and $[M + H]^+$ adducts, respectively. At DF = 270 Td and CF = 2.68 Td, the mass spectrum is dominated by peaks corresponding to intact protein ions, notably α- and β-globin (~15 and ~16 kDa, respectively) and fatty acid binding protein FABP1 (~15 kDa; see below). For comparison, a single scan mass spectrum in the absence of FAIMS field is shown in Figure 1C and a 1 min data summation (37 scans) in Figure 1D. After coadding 37 scans, the S/N of the peak at m/z 953 is 14. The same peak in the single FAIMS MS spectrum (Figure 1B) has S/N of 50. Similar results were obtained following LESA FAIMS analysis of mouse brain and *E. coli*, see Supporting Information, Figures 3 and 4. For the mouse brain sample, dominant peaks corresponding to an unknown protein of ~22 kDa were observed, including in the absence of the FAIMS field. Nevertheless, at certain FAIMS parameters, for example, DF = 270 Td, CF = 3.32 Td (Supporting Information, Figure 3A), 17 proteins in the molecular weight range 1−9 kDa were observed.

The results obtained from a 2D FAIMS analysis inform on the gas-phase separation achieved and the optimum FAIMS conditions (DF and CF) for transmission of a particular molecular ion. Figure 2 shows the total ion transmission maps obtained from the LESA FAIMS analysis of mouse liver. The distribution of observed m/z with compensation field at each of the dispersion fields is shown. As DF increases, greater separation with CF is observed. Three notable regions emerge. Consider the results at DF = 270 Td. In the region CF = 1.5−3.5 Td and m/z ~ 700−1500, proteins in the molecular weight range 14−23 kDa are transmitted. (The mass spectrum shown in Figure 1B corresponds to this region of the FAIMS space.) A second cluster is apparent in the region CF = −0.5−1 Td and m/z ~800−1100, and a third in the region CF = −0.5−1 Td and m/z ~1400−1900. The species in these clusters correspond to high molecular weight (unresolved) proteins, see Supporting Information, Figure 5.

The separation of lower and higher molecular weight proteins is in agreement with the work of Shvartsburg and co-workers.[27−29] Shvartsburg et al.[27] showed that whereas smaller proteins displayed type C behavior[18] (i.e., ion mobility decreases with electric field strength), proteins with molecular weight >30 kDa showed an increase in ion mobility with electric field strength (A- or B-type behavior[18]). This observation was attributed to alignment of the protein dipole for the larger proteins with the electric field during the high field portion of the FAIMS cycle (generally, dipole moment scales with protein size). As a result, the collision cross section of the protein ion in the plane orthogonal to the dipole moment, rather than the rotationally averaged collision cross section, dictates the ion mobility. Further work[28] suggested that the minimum dipole moment required for alignment in any field was ~450 D, corresponding to a protein of MW ~30 kDa. The hypothesis was validated using the ultrahigh field FAIMS devices used in the current work:[29] Ubiquitin ions (~8.6 kDa) displayed C-type behavior, that is, did not align, whereas bovine serum albumin (~66 kDa) displayed A-type behavior, that is,

DOI: 10.1021/acs.analchem.5b01151
Anal. Chem. 2015, 87, 6794−6800

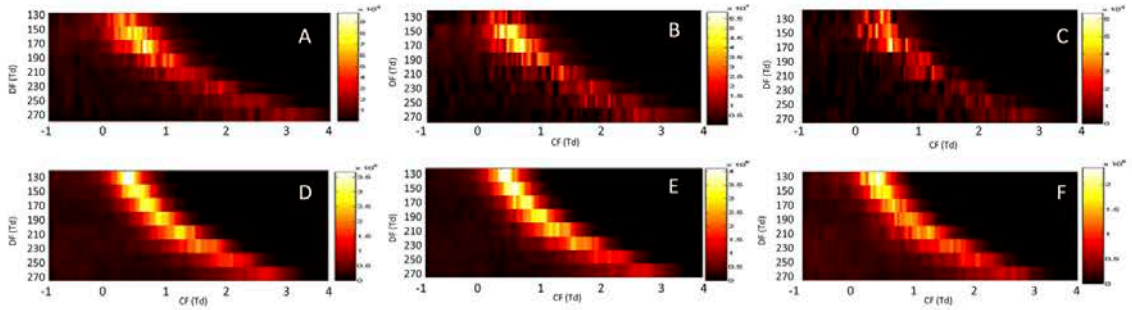

Figure 3. Ion transmission maps for specific m/z following LESA 2D FAIMS analyses of mouse liver (A) m/z 758.57 ± 0.01 (PC(34:2) + H^+); (B) m/z 760.58 ± 0.01 (PC(34:1) + H^+); (C) m/z 806.57 ± 0.01 (PC(38:6) + H^+); (D) m/z 919.7 ± 1.0 (β-globin, +17 charge state); (E) m/z 882.7 ± 1.0 (α-globin, +17 charge state); (F) m/z 894.0 ± 1.0 (fatty acid binding protein FABP1, +16 charge state).

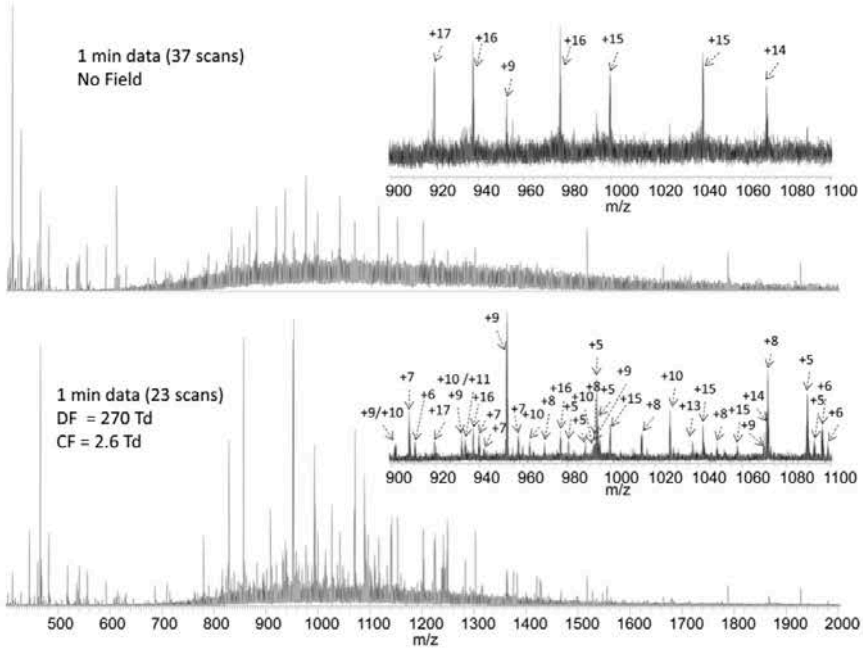

Figure 4. LESA FAIMS mass spectrometry of mouse brain: static FAIMS mode. (Top) LESA mass spectrum obtained in the absence of FAIMS field. (Bottom) LESA FAIMS mass spectrum obtained at DF = 270 Td, CF = 2.6 Td. Inset: Expanded m/z regions. Both mass spectra comprise 1 min of data.

dipoles aligned. In the experiments described here, the high field portion of the FAIMS cycle (the dispersion field) varies between ~30 kV/cm (130 Td) and ~70 kV/cm (270 Td), and dipole alignment of the higher molecular weight protein ions is expected. That is, the improved signals observed here for proteins are the result of the separation of higher molecular weight A-type protein ions and the lower molecular weight C-type protein ions.

The total ion transmission maps obtained following LESA 2D-FAIMS MS analyses of mouse brain and *E. coli* are shown in Supporting Information, Figure 6. Similar trends were observed in both cases. As discussed, this particular mouse brain sample is dominated by the presence of an unknown protein of ~22 kDa, and this feature is apparent in the total ion transmission maps. Nevertheless, higher molecular weight proteins (~30 kDa) were transmitted at lower compensation fields, whereas lower molecular weight proteins (~10 kDa) were transmitted at higher compensation fields (see Supporting Information, Figure 3). For all samples, the total ion transmission maps have a striated appearance. These striations arise from the various charge states of the proteins.

Figure 3 shows ion transmission maps for specific m/z values. Figure 3A–C shows maps obtained following analysis of mouse liver for m/z 758.57, 760.58, and 806.57 corresponding to protonated lipids phosphatidylcholine PC(34:2), PC(34:1), and PC(38:6), respectively. The results suggest that, for these species, the optimum FAIMS parameters are dispersion fields of 150–170 Td and compensation fields between 0 and 1 Td. At higher dispersion fields, the lipids are transmitted at higher compensation fields.

DOI: 10.1021/acs.analchem.5b01151
Anal. Chem. 2015, 87, 6794–6800

Figures 3D–F shows the transmission maps for three proteins from mouse liver. Transmission maps for ions of m/z 919.7, 882.7, and 894.0, corresponding to β-globin (+17 charge state), α-globin (+17 charge state), and liver fatty acid binding protein FABP1 (+16 charge state), respectively, are shown. The data show that for proteins α- and β-globin in the 17+ charge state, optimum transmission occurs at DF = 130 Td and CF ~ 0.65 Td. Similar conditions were optimal for FABP1 in the 16+ charge state.

Static FAIMS Analyses. Optimum CF and DF conditions were identified for the maximum transmission (and separation) of proteins of interest by interrogating the results of 2D FAIMS analyses. These conditions were subsequently applied for static FAIMS analyses. Figure 4 shows results obtained following LESA of a mouse brain section in the absence of FAIMS field and in a static FAIMS analysis (DF = 270 Td, CF = 2.6 Td). (Note, this sample is separate from that described above and is not dominated by the 22 kDa protein.) Both mass spectra represent 1 min of data collection (a total of 37 scans for the non-FAIMS analysis and 23 scans with FAIMS applied). Clearly, the LESA FAIMS mass spectrum is far richer in information than the spectrum obtained without FAIMS. In this example, the majority of the peaks in the non-FAIMS spectrum correspond to α-globin and β-globin in charge states +19 to +12, with an additional +9 peak at m/z 952.63, that is, three proteins were detected. It may be that in this analysis a blood vessel on the tissue surface was sampled. In contrast, the FAIMS mass spectrum reveals peaks corresponding to numerous protein species (total of 29 individual protein masses) in the range ~5 to ~37 kDa in a range of charge states, and the globins are not the most abundant species.

The use of static FAIMS conditions enables tandem mass spectrometry of the intact proteins. Supporting Information, Figure 7, shows LESA FAIMS MS/MS spectra for ions with m/z 1021.54 (+14 charge state; DF = 130 Td, CF = 0.30 Td) from mouse liver and m/z 952.63 (+9 charge state; DF = 270 Td, CF = 2.60 Td) from mouse brain. Note that static FAIMS conditions are optimized for both maximum transmission *and* separation of ions of interest from other species and, therefore, depend on the complexity of the substrate. Thus, the optimum CF and DF values differ between the liver and brain samples (and *E. coli* samples below). Collision-induced dissociation (CID), higher energy collision dissociation (HCD), and electron transfer dissociation (ETD) were performed. The data were searched against a mouse protein database using the Prosight software to obtain putative assignments. The fragment ions were subsequently manually analyzed and protein identifications confirmed. The proteins were identified as liver fatty acid binding protein (FABP1) and ubiquitin. A similar analysis was performed on a protein from the *E. coli* sample. Ions of m/z 1392.27 (+7 charge state; DF = 210 Td, CF = 1.65 Td) were selected for CID. The MS/MS spectrum and fragment ion summary are shown in Supporting Information, Figure 8. The protein was identified as acid stress chaperone HdeA. This protein has not previously been identified following LESA of *E. coli* colonies.

■ CONCLUSION

We have shown that high resolution LESA mass spectrometry may be coupled with FAIMS for the analysis of intact proteins from a range of biological substrates. The approach has been demonstrated on thin tissue sections from liver and brain and on bacterial colonies growing on agar. Improvements in S/N were observed due to the separation of higher molecular weight proteins and small singly charged species from proteins of lower molecular weight. These improvements in S/N result in shorter analysis times making FAIMS a potentially promising approach for intact protein imaging by LESA.

Various operating modes are available. It is possible to determine optimum FAIMS conditions through 2-D sweeps of dispersion field and compensation field and visualization of separation in the m/z/CF and in the DF/CF space. Optimum conditions (DF and CF) can subsequently be utilized in static FAIMS analysis which may be coupled with tandem mass spectrometry (CID, HCD, or ETD) for protein identification.

■ ASSOCIATED CONTENT

Supporting Information

Photographs of experimental setup; LESA-FAIMS mass spectra; LESA-FAIMS MS/MS spectra; total ion transmission maps from LESA-FAIMS analyses. The Supporting Information is available free of charge on the ACS Publications website at DOI: 10.1021/acs.analchem.5b01151.

■ AUTHOR INFORMATION

Corresponding Author

*E-mail: h.j.cooper@bham.ac.uk.

Notes

The authors declare no competing financial interest.

■ ACKNOWLEDGMENTS

H.J.C. is an EPSRC Established Career Fellow (EP/L023490/1). J.S. and E.C.R. received funding from the EPSRC via the PSIBS doctoral training centre (EP/F50053X/1). E.C.R.'s studentship is in collaboration with Astra Zeneca and the National Physical Laboratory. The Advion Triversa Nanomate and Thermo Fisher Orbitrap Velos mass spectrometer used in this research were funded through Birmingham Science City Translational Medicine, Experimental Medicine Network of Excellence Project, with support from Advantage West Midlands. Supplementary data supporting this research is openly available from the University of Birmingham data archive at http://findit.bham.ac.uk/.

■ REFERENCES

(1) Kertesz, V.; Van Berkel, G. J. *J. Mass Spectrom.* **2010**, *45* (3), 252–260.
(2) Edwards, R. L.; Creese, A. J.; Baumert, M.; Griffiths, P.; Bunch, J.; Cooper, H. J. *Anal. Chem.* **2011**, *83*, 2265–2270.
(3) Edwards, R. L.; Griffiths, P.; Bunch, J.; Cooper, H. J. *Proteomics* **2014**, *14* (10), 1232–1238.
(4) Edwards, R. L.; Griffiths, P.; Bunch, J.; Cooper, H. J. *J. Am. Soc. Mass Spectrom.* **2012**, *23*, 1921–1930.
(5) Schey, K. L.; Anderson, D. M.; Rose, K. L. *Anal. Chem.* **2013**, *85* (14), 6767–6774.
(6) Sarsby, J.; Martin, N. J.; Lalor, P. F.; Bunch, J.; Cooper, H. J. *J. Am. Soc. Mass Spectrom.* **2014**, *25* (11), 1953–1961.
(7) Randall, E. C.; Bunch, J.; Cooper, H. J. *Anal. Chem.* **2014**, *86* (21), 10504–10510.
(8) Martin, N. J.; Griffiths, R. L.; Edwards, R. L.; Cooper, H. J. *J. Am. Soc. Mass Spectrom.* **2015**, DOI: 10.1007/s13361-015-1152-8.
(9) Guevremont, R.; Barnett, D. A.; Purves, R. W.; Vandermey, J. *Anal. Chem.* **2000**, *72*, 4577–4584.
(10) Barnett, D. A.; Ells, B.; Guevremont, R.; Purves, R. W. *J. Am. Soc. Mass Spectrom.* **2002**, *13*, 1282–1291.
(11) Venne, K.; Bonneil, E.; Eng, K.; Thibault, P. *Anal. Chem.* **2005**, *77*, 2176–2186.

DOI: 10.1021/acs.analchem.5b01151
Anal. Chem. 2015, 87, 6794–6800

(12) Creese, A. J.; Shimwell, N. J.; Larkins, K. P. B.; Heath, J. K.; Cooper, H. J. *J. Am. Soc. Mass Spectrom.* **2013**, *24*, 431−443.
(13) Creese, A. J.; Cooper, H. J. *Anal. Chem.* **2012**, *84*, 2597−2601.
(14) Shvartsburg, A. A.; Creese, A. J.; Smith, R. D.; Cooper, H. J. *Anal. Chem.* **2010**, *82*, 8327−8334.
(15) Shvartsburg, A. A.; Creese, A. J.; Smith, R. D.; Cooper, H. J. *Anal. Chem.* **2011**, *83*, 6918−6923.
(16) Xuan, Y.; Creese, A. J.; Horner, J. A.; Cooper, H. J. *Rapid Commun. Mass Spectrom.* **2009**, *23*, 1963−1969.
(17) Guevremont, R. *J. Chromatogr. A* **2004**, *1058*, 3−19.
(18) Purves, R. W.; Guevremont, R.; Day, S.; Pipich, C. W.; Matyjaszczyk, M. *Rev. Sci. Instrum.* **1998**, *69*, 4094.
(19) Galhena, A. S.; Harris, G. A.; Kwasnik, M.; Fernandez, F. M. *Anal. Chem.* **2010**, *82* (22), 9159−9163.
(20) Bennett, R. V.; Gamage, C. M.; Galhena, A. S.; Fernandez, F. M. *Anal. Chem.* **2014**, *86*, 3756−3763.
(21) Manicke, N. E.; Belford, M. *J. Am. Soc. Mass Spectrom.* **2015**, *26*, 701−705.
(22) Porta, T.; Varesio, E.; Hopfgartner, G. *Anal. Chem.* **2013**, *85*, 11771−11779.
(23) Shvartsburg, A. A.; Tang, K.; Smith, R. D.; Holden, M.; Rush, M.; Thompson, A.; Toutoungi, D. *Anal. Chem.* **2009**, *81* (19), 8048−8053.
(24) Shvartsburg, A. A.; Smith, R. D.; Wilks, A.; Koehl, A.; Ruiz-Alonso, D.; Boyle, B. *Anal. Chem.* **2009**, *81* (15), 6489−6495.
(25) Chambers, M. C.; Maclean, B.; Burke, R.; Amodei, D.; Ruderman, D. L.; Neumann, S.; Gatto, L.; Fischer, B.; Pratt, B.; Egertson, J.; Hoff, K.; Kessner, D.; Tasman, N.; Shulman, N.; Frewen, B.; Baker, T. A.; Brusniak, M. Y.; Paulse, C.; Creasey, D.; Flashner, L.; Kani, K.; Moulding, C.; Seymour, S. L.; Nuwaysir, L. M.; Lefebvre, B.; Kuhlmann, F.; Roark, J.; Rainer, P.; Detlev, S.; Hemenway, T.; Huhmer, A.; Langridge, J.; Connolly, B.; Chadick, T.; Holly, K.; Eckels, J.; Deutsch, E. W.; Moritz, R. L.; Katz, J. E.; Agus, D. B.; Maccoss, M.; Tabb, D. L.; Mallick, P. *Nat. Biotechnol.* **2012**, *30*, 918−920.
(26) Race, A. M.; Styles, I. B.; Bunch, J. *J. Proteomics* **2012**, *75* (16), 5111−5112.
(27) Shvartsburg, A. A.; Bryskiewicz, T.; Purves, R. W.; Tang, K.; Guevremont, R.; Smith, R. D. *J. Phys. Chem. B* **2006**, *110* (43), 21966−21980.
(28) Shvartsburg, A. A.; Noskov, S. Y.; Purves, R. W.; Smith, R. D. *Proc. Natl. Acad. Sci. U.S.A.* **2009**, *106* (16), 6495−6500.
(29) Shvartsburg, A. A.; Smith, R. D. *Anal. Chem.* **2012**, *84*, 7297−7300.

DOI: 10.1021/acs.analchem.5b01151
Anal. Chem. 2015, 87, 6794−6800

Appendix 19 – Illustration of the extra brackets required for the LESA to increase the gap between the instrument and the Triversa to allow for the longer cone used for the ultraFAIMS.

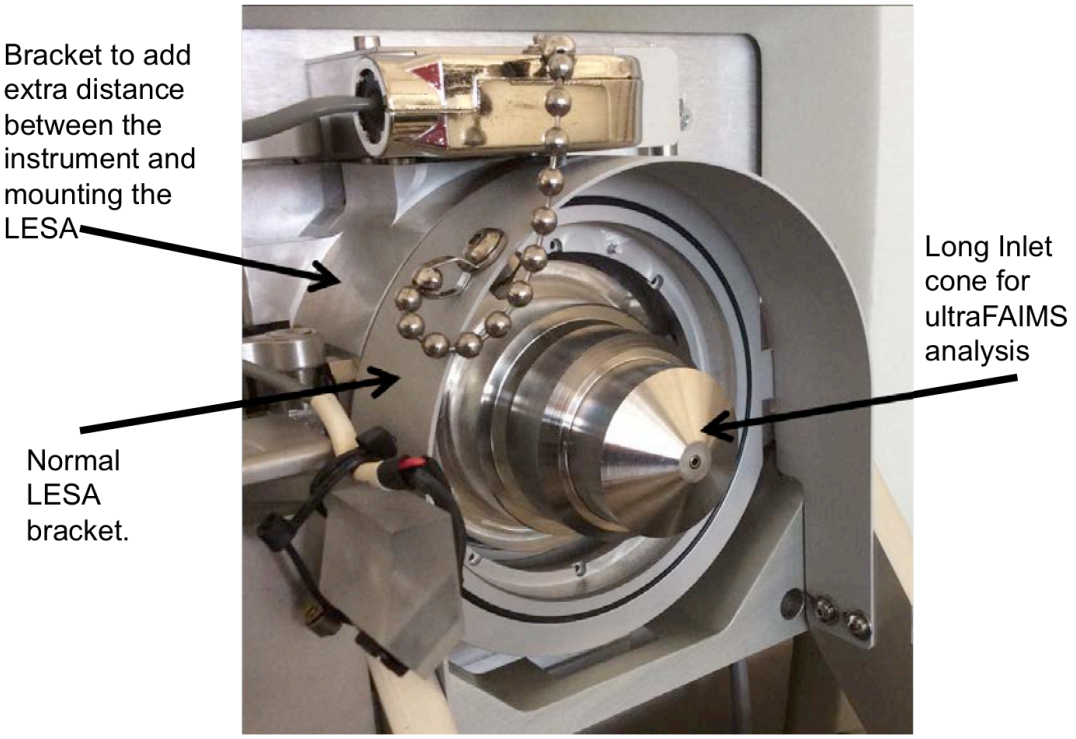

Appendix 20 — Relative molecule masses of proteins detected from mouse brain tissue using the ultra-FAIMS.

Mouse Brain	
With Ultra-FAIMS	Without Ultra-FAIMS
MW	MW
4895.6390	8559.6696
4933.5890	12365.1983
4960.5527	14955.8663
5439.8902	14971.8789
5455.9021	15549.1450
5703.1946	15562.0597
5751.0834	15590.1511
6246.3368	15607.2468
6568.4907	15841.9500
6584.5553	16780.0867
6693.6855	
7308.8543	
7350.8786	
7746.0861	
7850.1582	
7930.4376	
8099.5844	
8373.5721	
8501.6310	
8514.7185	
8542.6698	
8559.7427	
8581.7654	
8939.5860	
9320.9570	
9613.8989	
9905.2786	
9971.9289	
10254.2017	
10270.2129	
10711.2785	
12365.2972	
12428.5548	
14126.4726	
14971.8621	
14990.0092	

15564.1857
15607.4189
15839.9454

Appendix 21 – Relative molecule masses of proteins detected from mouse liver tissue using the ultra-FAIMS.

Mouse liver	
With Ultra-FAIMS	Without Ultra-FAIMS
5184.7285	5329.6470
5569.1897	14194.4401
7159.2736	14220.4481
7159.7520	14236.4717
7455.7883	14252.4361
14160.5286	14262.4559
14195.4872	14279.4967
14200.5275	14296.5258
14204.4581	14305.5173
14220.4320	14316.4938
14234.4307	14926.7514
14260.5207	14955.7170
14279.5268	14972.7901
14295.5366	15010.7615
14315.4114	15550.0201
14343.3976	15608.1105
14406.4311	15646.1398
14548.3305	18634.2003
14928.6248	18698.2250
14972.7671	23463.1848
14973.8941	
14992.7933	
15011.6677	
15589.1740	
15607.1015	
15627.1558	
15644.0586	
22348.0711	
23467.3873	

Appendix 22 – Fragments observed following MS/MS of +9 ions with m/z 1021.47.

Fragments observed following CID, HCD and ETD of +14 ions with m/z 1021.47 from mouse liver tissue using DF of 130 Td and a CF of 0.3 Td identified as liver fatty acid binding protein

CID		HCD		ETD			
Measured Mass	**Δppm**	**Measured Mass**	**Δppm**	**Measured Mass**	**Δppm**	**Calculated Mass**	**Assignment**
		288.0998	-5.21			288.1013	b_2^+
		435.1675	-5.06			435.1697	b_3^+
				724.3412	-4.83	724.3447	c_6^+
870.3777	-4.37	870.3773	-4.83			870.3815	b_7^+
		981.4088	-4.79			981.4135	b_8-NH_3^+
998.4358	-4.21	998.4352	-4.81			998.4400	b_8^+
1111.5191	-4.50	1111.5187	-4.86			1111.5241	b_9^+
		1148.7203	-5.14			1148.7262	y_9^+
1239.5769	-4.68					1239.5827	b_{10}^+
1261.8044	-4.68	1261.8040	-4.99			1261.8103	y_{10}^+
1308.5981	-4.59					1308.6041	b_{11}-H_2O^+
1326.6088	-4.45					1326.6147	b_{11}^+
1433.8523	-4.46	1433.8516	-4.95			1433.8587	y_{12}^+
1546.9360	-4.40	1546.9352	-4.91			1546.9428	y_{13}^+
1583.7088	-4.48					1583.7159	b_{13}^+
				1631.9636	-4.96	1631.9717	z_{14}^+
1647.9831	-4.49	1647.9825	-4.85			1647.9905	y_{14}^+
1779.0232	-4.33	1779.0222	-4.89			1779.0309	y_{15}^+
1844.8193	-4.28					1844.8272	b_{15}^+
		1862.0589	-4.89			1862.0680	y_{16}-H_2O^+
1880.0702	-4.47					1880.0786	y_{16}^+
		1977.0868	-4.15			1977.0950	y_{17}-NH_3^+
2077.1497	-4.33					2077.1587	y_{18}-H_2O^+
		2078.1324	-4.96			2078.1427	y_{18}-NH_3^+
2095.1601	-4.34	2095.1587	-5.01			2095.1692	y_{18}^+
		2191.2312	1.96			2191.2269	y_{19}-NH_3^+
2208.2427	-4.80	2208.2427	-4.80			2208.2533	y_{19}^+
2309.2907	-4.46	2309.2898	-4.85			2309.3010	y_{20}^+

2481.3374	-4.84	2481.3377	-4.72			2481.3494	y_{22}^{+}
				2579.3607	-5.00	2579.3736	z_{23}^{+}
2595.3813	-4.24					2595.3923	y_{23}^{+}
				2821.4870	-4.68	2821.5002	z_{25}^{+}
				3037.6203	-4.84	3037.6350	y_{27}^{+}
				3124.6516	-4.96	3124.6671	y_{28}^{+}
				3236.7255	-5.50	3236.7433	z_{29}^{+}
				3406.8324	-4.81	3406.8488	z_{31}^{+}
				3534.9258	-5.09	3534.9438	z_{32}^{+}
				3856.9201	-5.19	3856.9401	c_{33}^{+}
				4085.0296	-5.26	4085.0511	c_{35}^{+}
				4114.1948	-5.27	4114.2165	z_{37}^{+}
				4213.1229	-5.48	4213.1460	c_{36}^{+}
4372.3538	-4.41					4372.3731	y_{39}^{+}
				4528.3784	-5.39	4528.4028	z_{41}^{+}
				4797.4379	-5.42	4797.4639	c_{42}^{+}
				4934.4959	-5.27	4934.5219	c_{43}^{+}
				5120.5602	-5.04	5120.5860	c_{45}^{+}
				5826.1535	-5.77	5826.1871	y_{53}^{+}
				6209.2513	-4.91	6209.2818	c_{54}^{+}
				6362.3184	-4.68	6362.3482	$c_{55}^{+\cdot}$
6627.5538	2.11					6627.5398	a_{59}-NH_3^{+}
				6689.5524	-5.29	6689.5878	c_{59}^{+}
				6845.6525	-5.32	6845.6889	c_{60}^{+}
				7435.7881	-5.27	7435.8273	z_{67}^{+}
				8073.1933	-6.07	8073.2423	$z_{73}^{+\cdot}$
10307.4924	-6.31					10307.5574	y_{93}-H_2O^{+}
10325.5666	-0.13					10325.5679	y_{93}^{+}
11027.8384	8.34					11027.7464	b_{98}^{+}
11562.1731	-5.73					11562.2393	y_{104}^{+}
11619.1968	-5.51					11619.2608	y_{105}^{+}
12372.5394	8.45					12372.4349	a_{111}^{+}
12435.5803	-8.11					12435.6812	y_{112}^{+}
12678.7254	-4.46					12678.7820	y_{114}-H_2O^{+}
12808.7315	-6.02					12808.8086	y_{115}-NH_3^{+} +
12825.8724	2.91					12825.8351	y_{115}^{+}
12936.8025	-5.00					12936.8672	y_{116}-NH_3^{+}
12953.7884	-8.13					12953.8937	y_{116}^{+}
13023.8476	-3.96					13023.8992	y_{117}-NH_3^{+}
13040.8588	-5.13					13040.9257	y_{117}^{+}
13151.9202	-2.86					13151.9578	y_{118}-NH_3^{+}
13168.8767	-8.17					13168.9843	y_{118}^{+}

13281.9538	-8.63					13282.0684	y_{119}^{+}
13828.2412	-5.13					13828.3122	y_{124}-NH_3^{+}
13845.2728	-4.76					13845.3387	y_{124}^{+}
13974.2810	-0.99					13974.2948	b_{125}-H_2O^{+}
13974.2810	-8.27					13974.3966	y_{125}-H_2O^{+} +
13992.3216	1.16					13992.3054	b_{125}^{+}
13992.3216	-6.11					13992.4071	y_{125}^{+}
14106.3499	-7.10					14106.4501	y_{126}^{+}
				14237.4663	-1.71	14237.4906	y_{127}^{+}

Appendix 23 —Fragments observed following MS/MS of +9 ions with m/z 1021.47.

Fragments observed following CID, HCD and ETD of +14 ions with m/z 1021.47 from mouse liver tissue not using the ultraFAIMS

CID		HCD		ETD			
Measured Mass	**Δppm**	**Measured Mass**	**Δppm**	**Measured Mass**	**Δppm**	**Calculated Mass**	**Assignment**
		998.4347	-5.31			998.4400	b_8^+
1111.5194	-4.23					1111.5241	b_9^+
1239.5766	-4.92					1239.5827	b_{10}^+
		1261.8033	-5.55			1261.8103	y_{10}^+
1326.6085	-4.67					1326.6147	b_{11}^+
1433.8521	-4.60	1433.8510	-5.37			1433.8587	y_{12}^+
1546.9357	-4.59	1546.9345	-5.37			1546.9428	y_{13}^+
1583.7086	-4.61					1583.7159	b_{13}^+
				1631.9635	-5.02	1631.9717	z_{14}^+
1647.9829	-4.61	1647.9818	-5.28			1647.9905	y_{14}^+
1779.0227	-4.61	1779.0213	-5.40			1779.0309	y_{15}^+
1880.0703	-4.41	1880.0686	-5.32			1880.0786	y_{16}^+
		1977.0847	-5.21			1977.0950	y_{17}-NH_3^+
		1994.1107	-5.42			1994.1215	y_{17}^+
		2077.1468	-5.73			2077.1587	y_{18}-H_2O^+
		2078.1307	-5.77			2078.1427	y_{18}-NH_3^+
2095.1593	-4.73	2095.1577	-5.49			2095.1692	y_{18}^+
						2191.2269	y_{19}-NH_3^+
		2208.2415	-5.34			2208.2533	y_{19}^+
				3124.6482	-6.05	3124.6671	y_{28}^+
				3406.8299	-5.55	3406.8488	z_{31}^+
				4085.0231	-6.85	4085.0511	c_{35}^+
				4528.3755	-6.03	4528.4028	z_{41}^+
				4934.4932	-5.82	4934.5219	c_{43}^+
5029.5075	-0.80					5029.5115	b_{44}-NH_3^+
				5826.1543	-5.63	5826.1871	y_{53}^+
				6209.2462	-5.73	6209.2818	c_{54}^+
6627.5346	-0.78					6627.5398	a_{59}-NH_3^+
7208.7265	-4.72					7208.7605	y_{65}^+
8566.5067	1.26					8566.4959	y_{77}^+

				9753.0577	-5.72	9753.1135	c_{86}^{+}
12696.6792	-8.92					12696.7925	y_{114}^{+}
12807.7429	-6.38					12807.8246	y_{115}-H_2O^{+}
12936.8407	-2.05					12936.8672	y_{116}-NH_3^{+}
13040.8635	-4.77					13040.9257	y_{117}^{+}
13151.9246	-2.52					13151.9578	y_{118}-NH_3^{+}
13202.8466	-0.69					13202.8557	a_{119}^{+}
13741.2107	-5.06					13741.2802	y_{123}-NH_3^{+}
13760.2329	5.89					13760.1518	b_{123}-NH_3^{+}
13828.2515	-4.39					13828.3122	y_{124}-NH_3^{+}
13845.2451	-6.76					13845.3387	y_{124}^{+}
13975.2685	-0.74					13975.2788	b_{125}-NH_3^{+}
13992.4139	7.75					13992.3054	b_{125}^{+}
13992.4139	0.49					13992.4071	y_{125}^{+}
14088.4936	3.84					14088.4395	y_{126}-H_2O^{+}
14089.3338	-6.37					14089.4235	y_{126}-NH_3^{+}
				14219.3835	-6.79	14219.4800	y_{127}-H_2O^{+}

Appendix 24 —Fragments observed following MS/MS of +9 ions with m/z 952.63.

Fragments observed following CID, HCD and ETD of +9 ions with m/z 952.63 from mouse brain tissue using DF of 270 Td and a CF of 2.6 Td identified as unbiquitin.

CID		HCD		ETD			
Measured Mass	**Δppm**	**Measured Mass**	**Δppm**	**Measured Mass**	**Δppm**	**Calculated Mass**	**Assignment**
		260.1057	-2.31			260.1063	b^{2+}
		373.1895	-2.41			373.1904	b^{3+}
		753.4712	-2.39			753.4730	y_7-NH_3^+
		866.5551	-2.19			866.5570	y_8-NH_3^+
		1003.6137	-2.29			1003.6160	y_9-NH_3^+
1062.5993	-2.16					1062.6016	b_9^+
				1136.6468	-2.46	1136.6496	c_{10}^+
1247.7159	-1.68					1247.7180	b_{10}^+
		1304.7768	-2.22			1304.7797	y_{12}-NH_3^+
		1321.8033	-2.27			1321.8063	y_{12}^+
1348.7635	-1.63					1348.7657	b_{12}^+
		1433.8198	-1.74			1433.8223	y_{13}-NH_3^+
1443.8366	-1.80					1443.8392	b_{13}-H_2O^+
1450.8459	-2.07	1450.8454	-2.41			1450.8489	y_{13}^+
1461.8469	-1.98					1461.8498	b_{13}^+
1562.8944	-1.98					1562.8975	b_{14}^+
1578.9406	-2.03	1578.9403	-2.22			1578.9438	y_{14}^+
1657.9679	-1.87					1657.9710	b_{15}-H_2O^+
1675.9782	-1.97					1675.9815	b_{15}^+
1706.9992	-1.87	1706.9985	-2.28			1707.0024	y_{15}^+
1805.0209	-1.77					1805.0241	b_{16}^+
2033.1309	-2.07					2033.1351	b_{18}^+
2097.1884	-2.05	2097.1881	-2.19			2097.1927	y_{18}^+
				2081.1692	-2.31	2081.1740	z_{18}^+
				2513.3779	-2.19	2513.3834	y_{22}^+
				2692.4419	-2.15	2692.4477	c_{24}^+
2726.5013	-1.72	2726.4993	-2.46			2726.5060	y_{24}^+
				3104.6855	-1.84	3104.6912	c_{28}^+

				3345.8626	-2.27	3345.8702	c_{30}^{+}
				3473.9228	-1.73	3473.9288	c_{31}^{+}
3571.9212	-2.24					3571.9292	b_{32}^{+}
3700.0168	-1.97					3700.0241	b_{33}^{+}
				4209.2909	-1.33	4209.2965	$c_{38}^{+\cdot}$
				4210.2886	-3.73	4210.3043	c_{38}^{+}
4253.3183	-1.93	4253.3149	-2.73			4253.3265	y_{37}^{+}
4308.2960	-2.02					4308.3047	b_{39}^{+}
				4352.3261	-2.00	4352.3348	z_{38}^{+}
		4465.3956	-2.40			4465.4063	y_{39}^{+}
		4545.4271	-1.19			4545.4325	y_{40}-NH_3^{+}
4562.4495	-2.08	4562.4473	-2.56			4562.4590	y_{40}^{+}
		4732.5531	-2.41			4732.5645	y_{42}^{+}
4989.6898	-2.47	4989.6887	-2.69			4989.7021	y_{44}^{+}
5835.1125	-2.18					5835.1252	y_{52}^{+}
6015.2411	-1.93					6015.2527	b_{53}^{+}
6511.4608	-1.35					6511.4696	y_{58}-NH_3^{+}
6528.4821	-2.14					6528.4961	y_{58}^{+}
6639.5150	-1.99					6639.5282	y_{59}-H_2O^{+}
				6643.5147	-0.89	6643.5206	$c_{59}^{+\cdot}$
6657.5261	-1.89					6657.5387	y_{59}^{+}
6756.5900	-2.53					6756.6071	y_{60}^{+}
6867.6246	-2.13					6867.6392	y_{61}-H_2O^{+}
6885.6379	-1.71					6885.6497	y_{61}^{+}
6982.6837	-0.53					6982.6874	b_{62}^{+}
6998.7206	-1.89					6998.7338	y_{62}^{+}
7099.7673	-2.00					7099.7815	y_{63}^{+}
7212.8508	-2.04					7212.8655	y_{64}^{+}
7295.8890	-1.88					7295.9027	y_{65}-H_2O^{+}
7313.8963	-2.31					7313.9132	y^{65+}
7814.1953	-1.77					7814.2091	y_{70}^{+}
7942.2869	-2.15					7942.3040	y_{71}^{+}
8188.4225	-2.25					8188.4409	y_{73}^{+}
8301.5071	-2.14					8301.5249	y_{74}^{+}
				8501.5787	-3.76	8501.6107	$c_{75}^{+\cdot}$
8560.6044	-2.29			8560.6080	-1.87	8560.6240	Precursor

Appendix 25 – MATLAB Code for Interpolation of FAIMS data.

```
function  [vq]=multiInterpol(Ydata,Xdata,xq)
[R,C]=size(Ydata);
vq=zeros(R,length(xq));
   for j=1:R
       v=1;
      for k=1:length(xq)
         True=0;
         while True == 0

         if Xdata(j,v)<=xq(k) && xq(k)<Xdata(j,(v+1))
               x1=Xdata(j,v);
               x2=Xdata(j,(v+1));
               y1=Ydata(j,v);
               y2=Ydata(j,(v+1));

               m=(y2-y1)/(x2-x1);
               c=y1-m*x1;

               vq(j,k)=(m*xq(k))+c;

               True=1;

         else

            v=v+1;

         end
         end
      end
   end
end
```

Appendix 26 – Fragments observed following CID of *m/z* 792 using LESA extraction and an Orbitrap mass analyser.

Fragmentation of m/z revealed fragments specific to three different lipid species. PC(18:1/18:1)+Li^+, PC(18:0/18:2)+Li^+ and PC(16:0/20:2)+Li^+. With the possibility of a forth lipid as PC(16:1/20:1)+Li^+.

The fragments detected were.

PC(36:2)+Li^+	792.6089	792.6072	-2.14
NL Choline	733.5349	733.5334	-2.04
NL PC	609.5429	609.5415	-2.30
NL PC+Li	603.5341	603.5333	-1.33
NL (16:1)	538.3843	538.3809	-6.32
NL (16:0)	536.3687	536.3674	-2.42
NL (18:2)	512.3687	512.3676	-2.15
NL (18:1)	510.353	510.352	-1.96
NL (18:0)	508.3374	508.3364	-1.97
NL (18:2) +Li	506.3605	506.3595	-1.97
NL (18:1)+Li	504.3449	504.3438	-2.18
NL (18:0) +Li	502.3292	502.3281	-2.19
NL (20:2) +Li	478.3292	478.3284	-1.67

Appendix 27 — All Identified Lipids via MS/MS analysis on the Orbitrap Velos.

Table of all identified lipids.

Measured *(m/z)*	**Calculated** *(m/z)*	**Δppm**	**Assignment**
502.3469	502.3479	-0.20	LysoPC(16:0)+Li^+
545.4749	545.4752	-0.05	DG(12:0/18:1)+Li^+
545.4749	545.4752	-0.05	DG(14:0/16:1)+Li^+
545.4749	545.4752	-0.05	DG(14:1/16:0)+Li^+
548.3530	548.3323	3.78	LysoPC(20:5)+Li^+
571.4907	571.4908	-0.02	DG(14:0/18:2)+Li^+
571.4907	571.4908	-0.02	DG(16:1/16:1)+Li^+
573.5063	573.5065	-0.03	DG(14:0/18:1)+Li^+
573.5063	573.5065	-0.03	DG(16:0/16:1)+Li^+
575.5218	575.5221	-0.05	DG(16:0/16:0)+Li^+
597.5064	597.5070	-0.09	DG(16:0/18:3)+Li^+
597.5064	597.5070	-0.09	DG(16:1/18:2)+Li^+
599.5221	599.5221	0.00	DG(16:0/18:2)+Li^+
599.5221	599.5221	0.00	DG(16:1/18:1)+Li^+
601.5378	601.5378	0.00	DG(18:1/16:0)+Li^+
601.5378	601.5378	0.00	DG(18:1/16:0)+Li^+
603.5446	603.5534	-1.46	DG(16:0/18:0)+Li^+
623.5221	623.5221	0.00	DG(16:0/20:4)+Li^+
623.5221	623.5221	0.00	DG(16:1/20:3)+Li^+
623.5221	623.5221	0.00	DG(18:2/18:2)+Li^+
623.5221	623.5221	0.00	DG(18:3/18:1)+Li^+
625.5367	625.5378	-0.18	DG(18:2/18:1)+Li^+
625.5367	625.5378	-0.18	DG(20:3/16:0)+Li^+
627.5535	627.5534	0.02	DG(18:0/18:2)+Li^+
627.5535	627.5534	0.02	DG(18:1/18:1)+Li^+
629.5686	629.5671	0.24	DG(16:0/18:1)+Li^+
629.5686	629.5671	0.24	DG(16:1/18:0)+Li^+
644.4016	644.4262	-3.82	LysoPE(30:6)+Li^+
709.5833	709.5830	0.04	SM(16:0)+Li^+
722.5292	722.5307	-0.21	PE(18:2/16:0)+Li^+
724.5471	744.5619	-2688.13	PE(18:1/16:0)+Li^+
736.5468	736.5461	0.10	PC(14:0/18:2)+Li^+
736.5468	736.5461	0.10	PC(16:1/16:1)+Li^+

738.5613	738.5620	-0.09	PC(16:0/16:1)+Li+
738.5624	738.5619	0.07	PC(16:0/16:1)+Li+
738.5624	738.5619	0.07	PC(18:1/14:0)+Li+
740.5789	740.5776	0.18	PC(16:0/16:0)+Li+
744.5100	744.5150	-0.67	PE(20:5/16:0)+Li+
746.5295	746.5307	-0.16	PE(20:4/16:0)+Li+
748.5481	748.5463	0.24	PE(18:2/18:1)+Li+
748.5481	748.5463	0.24	PE(20:3/16:0)+Li+
750.5612	750.5620	-0.11	PE(18:1/18:1)+Li+
750.5627	750.5620	0.09	PE(18:0/18:2)+Li+
762.5627	762.5612	0.20	PC(18:2/16:1)+Li+
762.5627	762.5612	0.20	PC(18:3/16:0)+Li+
764.5768	764.5776	-0.10	PC(18:2/16:0)+Li+
766.5938	766.5933	0.07	PC(18:1/16:0)+Li+
768.6000	768.6089	-1.16	PC(18:0/16:0)+Li+
770.5311	770.5307	0.05	PE(20:5/18:1)+Li+
770.5311	770.5307	0.05	PE(22:6/16:0)+Li+
772.5478	772.5463	0.19	PE(22:4/18:1)+Li+
774.5624	774.5620	0.05	PE(20:4/18:0)+Li+
776.5786	776.5776	0.13	PE(20:3/18:0)+Li+
786.5624	786.5620	0.05	PC(20:4/16:1)+Li+
786.5624	786.5620	0.05	PC(20:5/16:0)+Li+
788.5768	788.5776	-0.10	PC(18:2/18:2)+Li+
788.5768	788.5776	-0.10	PC(20:4/16:0)+Li+
790.5944	790.5933	0.14	PC(18:2/18:1)+Li+
790.5944	790.5933	0.14	PC(20:3/16:0)+Li+
792.6077	792.6089	-0.15	PC(18:1/18:1)+Li+
792.6077	792.6089	-0.15	PC(18:2/18:0)+Li+
792.6077	792.6089	-0.15	PC(20:2/16:0)+Li+
794.6270	794.6246	0.30	PC(18:1/18:0)+Li+
809.7209	809.7205	0.05	TAG(12:0/18:1/18:1)+Li+
809.7209	809.7205	0.05	TAG(14:0/16:0/18:2)+Li+
809.7209	809.7205	0.05	TAG(14:0/16:1/18:1)+Li+
809.7209	809.7205	0.05	TAG(14:1/16:0/18:1)+Li+
809.7209	809.7205	0.05	TAG(16:0/16:1/16:1)+Li+
811.7369	811.7362	0.09	TAG(14:0/16:0/18:1)+Li+
811.7369	811.7362	0.09	TAG(16:1/16:0/16:0)+Li+
812.5765	812.5776	-0.14	PC(20:4/18:2)+Li+
812.5765	812.5776	-0.14	PC(22:6/16:0)+Li+
814.5942	814.5933	0.11	PC(20:4/18:1)+Li+
814.5942	814.5933	0.11	PC(20:5/18:0)+Li+
814.5942	814.5933	0.11	PC(22:5/16:0)+Li+

816.6083	816.6089	-0.07	PC(16:0/22:4)+Li^+
816.6083	816.6089	-0.07	PC(20:3/18:1)+Li^+
816.6083	816.6089	-0.07	PC(20:4/18:0)+Li^+
816.6083	816.6089	-0.07	PC(20:4/18:0)+Li^+
818.6273	818.6246	0.33	PC(18:2/20:1)+Li^+
818.6273	818.6246	0.33	PC(20:3/18:0)+Li^+
835.7366	835.7362	0.05	TAG(14:0/18:2/18:1)+Li^+
835.7366	835.7362	0.05	TAG(16:0/16:0/18:3)+Li^+
835.7366	835.7362	0.05	TAG(16:0/16:1/18:2)+Li^+
835.7366	835.7362	0.05	TAG(16:1/16:1/18:1)+Li^+
837.7522	837.7518	0.05	TAG(14:0/18:1/18:1)+Li^+
837.7522	837.7518	0.05	TAG(16:0/16:0/18:1)+Li^+
837.7522	837.7518	0.05	TAG(16:0/16:1/18:1)+Li^+
840.6091	840.6088	0.04	PC(22:6/18:0)+Li^+
846.5952	846.5984	-0.38	LysoPC(42:10)+Li^+
861.7524	861.7518	0.07	TAG(16:0/16:0/20:4)+Li^+
861.7524	861.7518	0.07	TAG(16:0/16:1/20:3)+Li^+
861.7524	861.7518	0.07	TAG(16:0/18:1/18:3)+Li^+
861.7524	861.7518	0.07	TAG(16:0/18:2/18:2)+Li^+
861.7524	861.7518	0.07	TAG(16:1/18:0/18:3)+Li^+
863.7675	863.7875	-2.32	TAG(18:1/18:1/16:1)+Li^+
863.7675	863.7875	-2.32	TAG(18:2/18:1/16:0)+Li^+
865.7831	865.7831	0.00	TAG(18:1/18:0/16:1)+Li^+
865.7831	865.7831	0.00	TAG(18:1/18:1/16:0)+Li^+
867.7881	867.7988	-1.23	TAG(16:0/18:0/18:1)+Li^+
891.8000	891.7988	0.13	TAG(18:0/18:1/18:2)+Li^+
891.8000	891.7988	0.13	TAG(18:1/18:1/18:1)+Li^+

References

1. Jennings, K.R., ed. *A History of European Mass Spectrometry*. 2012, IM Publications: Chichester.

2. Grayson, M.A., ed. *Measuring Mass: From Positive Rays to Proteins*. 2002, Chemical Heritage Press: Philadelphia, PA.

3. NobelPrize. *All Nobel Prizes*. [2015 Apr 30]; Available from: http://www.nobelprize.org/nobel_prizes/lists/all/.

4. Aston, F.W., *The Constitution of the Elements.* Nature, 1919. **104**(393): p. 2616.

5. Lawrence, E.O. and D. Cooksey, *On the Apparatus for the Multiple Acceleration of Light Ions to High Speeds.* Phys. Rev., 1936. **50**(12): p. 1131-1140.

6. Paul, W., H.P. Reinhard, and U. von Zahn, *THE ELECTRIC MASS FILTER AS A MASS SPECTROMETER AND ISOTOPE SEPARATOR. Z.* Physik, 1958. **152**: p. 143-82.

7. Wineland, D.J. and H.G. Dehmelt, *Principles of Stored Ion Calorimeter.* J. Appl. Phys., 1975. **46**(2): p. 919-930.

8. Fenn, J.B., et al., *Electrospray ionization for mass spectrometry of large biomolecules.* Science, 1989. **246**(4926): p. 64-71.

9. Tanaka, K., et al., *Protein and polymer analyses up to m/z 100 000 by laser ionization time? of? flight mass spectrometry.* Rapid Commun. Mass Spectrom., 1988. **2**(8): p. 151-153.

10. Nier, A.O., *A Mass Spectrometer for Isotope and Gas Analysis.* Rev Sci Instrum, 1947. **18**(6): p. 398-411.

11. Hoffmann, E.d. and V. Stroobant, *Mass spectrometry: Principles and Applications*. Third Edition ed. 2007, Chichester: John Wiley and Sons, Ltd.

12. Signor, L. and E. Boeri Erba, *Matrix-assisted laser desorption/ionization time of flight (MALDI-TOF) mass spectrometric analysis of intact proteins larger than 100 kDa.* J. Vis. Exp., 2013(79).

13. Vellaichamy, A., et al., *Size-sorting combined with improved nanocapillary liquid chromatography-mass spectrometry for identification of intact proteins up to 80 kDa.* Anal. Chem., 2010. **82**(4): p. 1234-44.

14. Laiko, V.V., S.C. Moyer, and R.J. Cotter, *Atmospheric pressure MALDI/ion trap mass spectrometry.* Anal. Chem., 2000. **72**(21): p. 5239-43.

15. Herzog, R.F.K. and F.P. Viehbock, *Ion Source for Mass Spectrography.* Phys. Rev., 1949. **76**(6): p. 855-856.

16. Karas, M., et al., *Matrix-assisted ultraviolet laser desorption of non-volatile compounds.* Int. J. Mass Spectrom. Ion Processes, 1987. **78**(0): p. 53-68.

17. Carroll, D.I., et al., *Atmospheric-Pressure Ionization Mass-Spectrometry - Corona Discharge Ion-Source for Use in Liquid Chromatograph Mass Spectrometer-Computer Analytical System.* Anal. Chem., 1975. **47**(14): p. 2369-2373.

18. Robb, D.B., T.R. Covey, and A.P. Bruins, *Atmospheric pressure photoionisation: An ionization method for liquid chromatography-mass spectrometry.* Anal. Chem., 2000. **72**(15): p. 3653-3659.

19. Whitehouse, C.M., et al., *Electrospray interface for liquid chromatographs and mass spectrometers.* Anal. Chem., 1985. **57**(3): p. 675-9.

20. Takats, Z., et al., *Mass spectrometry sampling under ambient conditions with desorption electrospray ionization.* Science, 2004. **306**(5695): p. 471-473.

21. Sachfer, K.C., et al., *In situ, real-time identification of biological tissues by ultraviolet and infrared laser desorption ionization mass spectrometry.* Anal. Chem., 2011. **83**(5): p. 1632-40.

22. Wiegelmann, M., et al., *Matching the laser wavelength to the absorption properties of matrices increases the ion yield in UV-MALDI mass spectrometry.* Anal. Bioanal. Chem., 2013. **405**(22): p. 6925-6932.

23. Cohen, S.L. and B.T. Chait, *Influence of matrix solution conditions on the MALDI-MS analysis of peptides and proteins.* Anal. Chem., 1996. **68**(1): p. 31-37.

24. Puolitaival, S.M., et al., *Solvent-free matrix dry-coating for MALDI imaging of phospholipids.* Journal of the American Society for Mass Spectrometry, 2008. **19**(6): p. 882-886.

25. Hoteling, A.J., et al., *Exploring the importance of the relative solubility of matrix and analyte in MALDI sample preparation using HPLC.* Anal. Chem., 2004. **76**(17): p. 5157-5164.

26. Armstrong, D.W., et al., *Ionic liquids as matrixes for matrix-assisted laser desorption/ionization mass spectrometry.* Anal. Chem., 2001. **73**(15): p. 3679-3686.

27. Knochenmuss, R., et al., *The matrix suppression effect and ionization mechanism in MALDI.* Rapid. Commun. Mass Spectrom., 1996. **10**: p. 871-879.

28. Cohen, L.H. and A.I. Gusev, *Small molecule analysis by MALDI mass spectrometry.* Anal. Bioanal. Chem., 2002. **373**(7): p. 571-586.

29. Fuchs, B., R. Suss, and J. Schiller, *An update of MALDI-TOF mass spectrometry in lipid research.* Prog. Lipid Res., 2011. **50**(1): p. 132.

30. Kussmann, M., et al., *Matrix-assisted laser desorption/ionization mass spectrometry sample preparation techniques designed for various peptide and protein analytes.* J. Mass Spectrom., 1997. **32**(6): p. 593-601.

31. Steven, R.T. and J. Bunch, *Repeat MALDI MS imaging of a single tissue section using multiple matrices and tissue washes.* Anal. Bioanal. Chem., 2013. **405**(14): p. 4719-28.

32. Crecelius, A.C., et al., *Three-dimensional visualization of protein expression in mouse brain structures using imaging mass spectrometry.* J. AM. Soc. Mass Spectrom., 2005. **16**(7): p. 1093-1099.

33. Hsu, N.Y., et al., *Matrix‐assisted laser desorption/ionization mass spectrometry of polysaccharides with 2′, 4′, 6′‐trihydroxyacetophenone as matrix.* Rapid Commun. Mass Spectrom., 2007. **21**(13): p. 2137-2146.

34. Zhu, Y., et al., *The Study of 2, 3, 4‐Trihydroxyacetophenone and 2, 4, 6‐Trihydroxyacetophenone as Matrices for DNA Detection in Matrix‐assisted Laser Desorption/Ionization Time‐of‐flight Mass Spectrometry.* Rapid Commun. Mass Spectrom., 1996. **10**(3): p. 383-388.

35. Stübiger, G. and O. Belgacem, *Analysis of lipids using 2, 4, 6-trihydroxyacetophenone as a matrix for MALDI mass spectrometry.* Anal. Chem., 2007. **79**(8): p. 3206-3213.

36. Sarsby, J., et al., *Mass spectrometry imaging of glucosinolates in Arabidopsis flowers and siliques.* Phytochemistry, 2012. **77**(0): p. 110-118.

37. Vermillion‐Salsbury, R.L. and D.M. Hercules, *9‐Aminoacridine as a matrix for negative mode matrix‐assisted laser desorption/ionization.* Rapid Commun. Mass Spectrom., 2002. **16**(16): p. 1575-1581.

38. Cerruti, C.D., et al., *MALDI imaging and structural analysis of rat brain lipid negative ions with 9-aminoacridine matrix.* Anal. Chem., 2012. **84**(5): p. 2164-2171.

39. Goodwin, R.J., et al., *Time-dependent evolution of tissue markers by MALDI-MS imaging.* Proteomics, 2008. **8**(18): p. 3801-8.

40. Ahmed, M.M. and K.J. Gardiner, *Preserving protein profiles in tissue samples: differing outcomes with and without heat stabilization.* J. Neurosci. Methods, 2011. **196**(1): p. 99-106.

41. Goodwin, R.J., *Sample preparation for mass spectrometry imaging: small mistakes can lead to big consequences.* J. Proteomics, 2012. **75**(16): p. 4893-911.

42. Palmer, A.D., et al., *Sucrose cryo-protection facilitates imaging of whole eye sections by MALDI mass spectrometry.* J. Mass Spectrom., 2012. **47**(2): p. 237-241.

43. Martin-Lorenzo, M., et al., *30mum spatial resolution protein MALDI MSI: In-depth comparison of five sample preparation protocols applied to human healthy and atherosclerotic arteries.* J. Proteomics, 2014. **108**: p. 465-8.

44. Seeley, E.H., et al., *Enhancement of protein sensitivity for MALDI imaging mass spectrometry after chemical treatment of tissue sections.* J. Am. Soc. Mass Spectrom., 2008. **19**(8): p. 1069-77.

45. Griffiths, R.L., et al., *Formal lithium fixation improves direct analysis of lipids in tissue by mass spectrometry.* Anal. Chem., 2013. **85**(15): p. 7146-53.

46. Kaletas, B.K., et al., *Sample preparation issues for tissue imaging by imaging MS.* Proteomics, 2009. **9**(10): p. 2622-33.

47. Bonnel, D., et al., *Ionic matrices pre-spotted matrix-assisted laser desorption/ionization plates for patient maker following in course of treatment, drug titration, and MALDI mass spectrometry imaging.* Anal Biochem, 2013. **434**(1): p. 187-98.

48. Muller, L., et al., *Lipid imaging within the normal rat kidney using silver nanoparticles by matrix-assisted laser desorption/ionization mass spectrometry.* Kidney international, 2015.

49. Puolitaival, S.M., et al., *Solvent-free matrix dry-coating for MALDI imaging of phospholipids.* J. Am. Soc. Mass. Spectrom., 2008. **19**(6): p. 882-6.

50. Gemperline, E., S. Rawson, and L. Li, *Optimization and comparison of multiple MALDI matrix application methods for small molecule mass spectrometric imaging.* Anal. Chem., 2014. **86**(20): p. 10030-5.

51. Zenobi, R. and R. Knochenmuss, *Ion formation in MALDI mass spectrometry.* Mass Spectrom. Rev., 1998. **17**(5): p. 337-366.

52. Fuchs, B., R. Suss, and J. Schiller, *An update of MALDI-TOF mass spectrometry in lipid research.* Prog. Lipid Res., 2010. **49**(4): p. 450-75.

53. Mann, M., R.C. Hendrickson, and A. Pandey, *Analysis of proteins and proteomes by mass spectrometry.* Annu. Rev. Biochem., 2001. **70**: p. 437-73.

54. Cohen, L.H. and A.I. Gusev, *Small molecule analysis by MALDI mass spectrometry.* Anal. Bioanal. Chem., 2002. **373**(7): p. 571-86.

55. Sleno, L. and D.A. Volmer, *Some fundamental and technical aspects of the quantitative analysis of pharmaceutical drugs by matrix-assisted laser desorption/ionization mass spectrometry.* Rapid. Commun. Mass Spectrom., 2005. **19**(14): p. 1928-36.

56. Gut, I.G., *DNA analysis by MALDI-TOF mass spectrometry.* Hum. Mutat., 2004. **23**(5): p. 437-41.

57. Cazares, L.H., et al., *MALDI tissue imaging: from biomarker discovery to clinical applications.* Anal. Bioanal. Chem., 2011. **401**(1): p. 17-27.

58. Fuchs, B. and J. Schiller, *MALDI-TOF MS analysis of lipids from cells, tissues and body fluids.* Subcell. Biochem., 2008. **49**: p. 541-65.

59. Sandrin, T.R., J.E. Goldstein, and S. Schumaker, *MALDI TOF MS profiling of bacteria at the strain level: a review.* Mass Spectrom. Rev., 2013. **32**(3): p. 188-217.

60. Thiery-Lavenant, G., A.I. Zavalin, and R.M. Caprioli, *Targeted multiplex imaging mass spectrometry in transmission geometry for subcellular spatial resolution.* J. Am. Soc. Mass. Spectrom., 2013. **24**(4): p. 609-14.

61. Gessel, M.M., J.L. Norris, and R.M. Caprioli, *MALDI imaging mass spectrometry: spatial molecular analysis to enable a new age of discovery.* J. Proteomics, 2014. **107**: p. 71-82.

62. Short, R.T., et al., *Charge compensation for imaging large insulating samples by using secondary ion tandem mass spectrometry.* J. Am. Soc. Mass. Spectrom., 1994. **5**(1): p. 37-43.

63. Caprioli, R.M., T.B. Farmer, and J. Gile, *Molecular imaging of biological samples: Localization of peptides and proteins using MALDI-TOF MS.* Anal. Chem., 1997. **69**(23): p. 4751-4760.

64. Jurchen, J.C., S.S. Rubakhin, and J.V. Sweedler, *MALDI-MS imaging of features smaller than the size of the laser beam.* J. Am. Soc. Mass. Spectrom., 2005. **16**(10): p. 1654-9.

65. Konermann, L., et al., *Unraveling the mechanism of electrospray ionization.* Anal. Chem., 2013. **85**(1): p. 2-9.

66. Awad, H., M.M. Khamis, and A. El-Aneed, *Mass Spectrometry, Review of the Basics: Ionization.* Appl. Spectrosc. Rev., 2015. **50**(2): p. 158-175.

67. Konijnenberg, A., A. Butterer, and F. Sobott, *Native ion mobility-mass spectrometry and related methods in structural biology.* Biochim Biophys Acta, 2013. **1834**(6): p. 1239-56.

68. Wilm, M. and M. Mann, *Analytical properties of the nanoelectrospray ion source.* Anal. Chem., 1996. **68**(1): p. 1-8.

69. Wachs, T. and J. Henion, *Electrospray Device for Coupling Microscale Separations and Other Miniaturized Devices with Electrospray Mass Spectrometry.* Anal. Chem., 2001. **73**(3): p. 632-638.

70. Van Berkel, G.J., A.D. Sanchez, and J.M.E. Quirke, *Thin-Layer Chromatography and Electrospray Mass Spectrometry Coupled Using a Surface Sampling Probe.* Anal. Chem., 2002. **74**(24): p. 6216-6223.

71. Wachs, T. and J. Henion, *A Device for Automated Direct Sampling and Quantitation from Solid-Phase Sorbent Extraction Cards by Electrospray Tandem Mass Spectrometry.* Anal. Chem., 2003. **75**(7): p. 1769-1775.

72. Asano, K.G., et al., *Self-aspirating atmospheric pressure chemical ionization source for direct sampling of analytes on surfaces and in liquid solutions.* Rapid Commun. Mass Spectrom., 2005. **19**(16): p. 2305-2312.

73. Ovchinnikova, O.S., V. Kertesz, and G.J. Van Berkel, *Combining transmission geometry laser ablation and a non-contact continuous flow surface sampling probe/electrospray emitter for mass spectrometry based chemical imaging.* Rapid Commun. Mass Spectrom., 2011. **25**(24): p. 3735-3740.

74. Ford, M.J., V. Kertesz, and G.J. Van Berkel, *Thin-layer chromatography/electrospray ionization triple-quadrupole linear ion trap mass spectrometry system: analysis of rhodamine dyes separated on reversed-phase C8 plates.* J. Mass Spectrom., 2005. **40**(7): p. 866-875.

75. Ford, M.J. and G.J. Van Berkel, *An improved thin-layer chromatography/mass spectrometry coupling using a surface sampling probe electrospray ion trap system.* Rapid Commun. Mass Spectrom., 2004. **18**(12): p. 1303-1309.

76. ElNaggar, M., C. Barbier, and G. Van Berkel, *Liquid Microjunction Surface Sampling Probe Fluid Dynamics: Computational and Experimental Analysis of*

Coaxial Intercapillary Positioning Effects on Sample Manipulation. J. Am. Soc. Mass Spectrom., 2011. **22**(7): p. 1157-1166.

77. ElNaggar, M. and G. Van Berkel, *Liquid Microjunction Surface Sampling Probe Fluid Dynamics: Characterization and Application of an Analyte Plug Formation Operational Mode.* J. Am. Soc. Mass Spectrom., 2011. **22**(10): p. 1737-1743.

78. Kertesz, V. and G.J. Van Berkel, *Fully automated liquid extraction-based surface sampling and ionization using a chip-based robotic nanoelectrospray platform.* J Mass Spectrom, 2009. **45**(3): p. 252-260.

79. Stegemann, C., et al., *Comparative Lipidomics Profiling of Human Atherosclerotic Plaques / Clinical Perspective.* Circ. Cardiovasc. Genet., 2011. **4**(3): p. 232-242.

80. Eikel, D., et al., *Liquid extraction surface analysis mass spectrometry (LESA-MS) as a novel profiling tool for drug distribution and metabolism analysis: the terfenadine example.* Rapid Commun. Mass Spectrom., 2011. **25**(23): p. 3587-3596.

81. Marshall, P., et al., *Correlation of Skin Blanching and Percutaneous Absorption for Glucocorticoid Receptor Agonists by Matrix-Assisted Laser Desorption Ionization Mass Spectrometry Imaging and Liquid Extraction Surface Analysis with Nanoelectrospray Ionization Mass Spectrometry.* Anal. Chem., 2010. **82**(18): p. 7787-7794.

82. Blatherwick, E.Q., et al., *Utility of spatially-resolved atmospheric pressure surface sampling and ionization techniques as alternatives to mass spectrometric imaging (MSI) in drug metabolism.* Xenobiotica, 2011. **41**(8): p. 720-34.

83. Edwards, R.L., et al., *Hemoglobin Variant Analysis via Direct Surface Sampling of Dried Blood Spots Coupled with High-Resolution Mass Spectrometry.* Anal. Chem., 2011. **83**(6): p. 2265-2270.

84. Edwards, R.L., et al., *Top-Down Proteomics and Direct Surface Sampling of Neonatal Dried Blood Spots: Diagnosis of Unknown Hemoglobin Variants.* J. AM. Soc. Mass Spectrom., 2012. **23**(11): p. 1-10.

85. Martin, N.J., J. Bunch, and H.J. Cooper, *Dried Blood Spot Proteomics: Surface Extraction of Endogenous Proteins Coupled with Automated Sample Preparation and Mass Spectrometry Analysis.* J. Am. Soc. Mass Spectrom., 2013. **24**(8): p. 1242-1249.

86. Randall, E.C., J. Bunch, and H.J. Cooper, *Direct analysis of intact proteins from Escherichia coli colonies by liquid extraction surface analysis mass spectrometry.* Anal. Chem., 2014. **86**(21): p. 10504-10.

87. Ellis, S.R., et al., *Direct lipid profiling of single cells from inkjet printed microarrays.* Anal. Chem., 2012. **84**(22): p. 9679-83.

88. Folch, J., M. Lees, and G.H.S. Stanley, *A Simple Method for the Isolation and Purification of Lipids from Animal Tissue.* J. Bol. Chem., 1957. **226**(1): p. 497-509.

89. Parson, W.B., et al., *Analysis of chloroquine and metabolites directly from whole-body animal tissue sections by liquid extraction surface analysis (LESA) and tandem mass spectrometry.* J Mass Spectrom, 2012. **47**(11): p. 1420-8.

90. Eikel, D. and J. Henion, *Liquid extraction surface analysis (LESA) of food surfaces employing chip-based nano-electrospray mass spectrometry.* Rapid Commun. Mass Spectrom., 2011. **25**(16): p. 2345-2354.

91. ElNaggar, M.S., et al., *Metabolic Imaging through Continuous In Situ Micro-extractions of Tissue Samples via Flowprobe Mass Spectrometry.* Curr. Metabolomics, 2014. **2**(2): p. 122-131.

92. Monge, M.E., et al., *Mass Spectrometry: Recent Advances in Direct Open Air Surface Sampling/Ionization.* Chem. Rev., 2013.

93. Harris, G.A., A.S. Galhena, and F.M. Fernandez, *Ambient Sampling/Ionization Mass Spectrometry: Applications and Current Trends.* Anal. Chem., 2011. **83**(12): p. 4508-4538.

94. Van Berkel, G.J. and V. Kertesz, *Application of a Liquid Extraction Based Sealing Surface Sampling Probe for Mass Spectrometric Analysis of Dried Blood Spots and Mouse Whole-Body Thin Tissue Sections.* Anal. Chem., 2009. **81**(21): p. 9146-9152.

95. Roach, P.J., J. Laskin, and A. Laskin, *Nanospray desorption electrospray ionization: an ambient method for liquid-extraction surface sampling in mass spectrometry.* Analyst, 2010. **135**(9).

96. Ratcliffe, L.V., et al., *Surface analysis under ambient conditions using plasma-assisted desorption/ionization mass spectrometry.* Anal. Chem., 2007. **79**(16): p. 6094-101.

97. Zhang, J., et al., *Thin layer chromatography/plasma assisted multiwavelength laser desorption ionization mass spectrometry for facile separation and selective identification of low molecular weight compounds.* Anal. Chem., 2012. **84**(3): p. 1496-503.

98. Harper, J.D., et al., *Low-temperature plasma probe for ambient desorption ionization.* Anal. Chem., 2008. **80**(23): p. 9097-104.

99. Dixon, R.B., J.S. Sampson, and D.C. Muddiman, *Generation of multiply charged peptides and proteins by radio frequency acoustic desorption and ionization for mass spectrometric detection.* J. Am. Soc. Mass. Spectrom., 2009. **20**(4): p. 597-600.

100. Peng, W.P., et al., *Laser-induced acoustic desorption mass spectrometry of single bioparticles.* Angew. Chem. Int. Ed. Engl., 2006. **45**(9): p. 1423-6.

101. Chen, H., Z. Ouyang, and R.G. Cooks, *Thermal production and reactions of organic ions at atmospheric pressure.* Angew. Chem. Int. Ed. Engl., 2006. **45**(22): p. 3656-60.

102. Basile, F., et al., *Atmospheric pressure-thermal desorption (AP-TD)/electrospray ionization-mass spectrometry for the rapid analysis of Bacillus spores.* Analyst, 2010. **135**(4): p. 797-803.

103. Rezenom, Y.H., J. Dong, and K.K. Murray, *Infrared laser-assisted desorption electrospray ionization mass spectrometry.* Analyst, 2008. **133**(2): p. 226-32.

104. Sampson, J.S. and D.C. Muddiman, *Atmospheric pressure infrared (10.6 microm) laser desorption electrospray ionization (IR-LDESI) coupled to a LTQ Fourier transform ion cyclotron resonance mass spectrometer.* Rapid. Commun. Mass Spectrom., 2009. **23**(13): p. 1989-92.

105. Sampson, J.S., A.M. Hawkridge, and D.C. Muddiman, *Generation and detection of multiply-charged peptides and proteins by matrix-assisted laser desorption electrospray ionization (MALDESI) Fourier transform ion cyclotron resonance mass spectrometry.* J. Am. Soc. Mass. Spectrom., 2006. **17**(12): p. 1712-6.

106. Neidholdt, E.L. and J.L. Beauchamp, *Switched ferroelectric plasma ionizer (SwiFerr) for ambient mass spectrometry.* Anal. Chem., 2011. **83**(1): p. 38-43.

107. Schafer, K.C., et al., *In vivo, in situ tissue analysis using rapid evaporative ionization mass spectrometry.* Angew. Chem. Int. Ed. Engl., 2009. **48**(44): p. 8240-2.

108. Symonds, J.M., et al., *Microplasma discharge ionization source for ambient mass spectrometry.* Anal. Chem., 2010. **82**(2): p. 621-7.

109. Steeb, J., et al., *Beta electron-assisted direct chemical ionization (BADCI) probe for ambient mass spectrometry.* Chem. Commun., 2009(31): p. 4699-701.

110. Chen, H., et al., *Surface desorption atmospheric pressure chemical ionization mass spectrometry for direct ambient sample analysis without toxic chemical contamination.* J Mass Spectrom, 2007. **42**(8): p. 1045-56.

111. Haapala, M., et al., *Desorption atmospheric pressure photoionization.* Anal. Chem., 2007. **79**(20): p. 7867-72.

112. Cody, R.B., J.A. Laramee, and H.D. Durst, *Versatile new ion source for the analysis of materials in open air under ambient conditions.* Anal. Chem., 2005. **77**(8): p. 2297-302.

113. Na, N., et al., *Development of a dielectric barrier discharge ion source for ambient mass spectrometry.* J. Am. Soc. Mass. Spectrom., 2007. **18**(10): p. 1859-62.

114. Wang, H., et al., *Desorption corona beam ionization source for mass spectrometry.* Analyst, 2010. **135**(4): p. 688-95.

115. Forbes, T.P., T.M. Brewer, and G. Gillen, *Desorption electro-flow focusing ionization of explosives and narcotics for ambient pressure mass spectrometry.* Analyst, 2013. **138**(19): p. 5665-73.

116. Nyadong, L., A.S. Galhena, and F.M. Fernandez, *Desorption electrospray/metastable-induced ionization: a flexible multimode ambient ion generation technique.* Anal. Chem., 2009. **81**(18): p. 7788-94.

117. Chan, C.C., et al., *Desorption ionization by charge exchange (DICE) for sample analysis under ambient conditions by mass spectrometry.* J. Am. Soc. Mass. Spectrom., 2010. **21**(9): p. 1554-60.

118. Ozdemir, A. and C.H. Chen, *Electrode-assisted desorption electrospray ionization mass spectrometry.* J Mass Spectrom, 2010. **45**(10): p. 1203-11.

119. Haddad, R., R. Sparrapan, and M.N. Eberlin, *Desorption sonic spray ionization for (high) voltage-free ambient mass spectrometry.* Rapid. Commun. Mass Spectrom., 2006. **20**(19): p. 2901-5.

120. Shiea, J., et al., *Electrospray-assisted laser desorption/ionization mass spectrometry for direct ambient analysis of solids.* Rapid. Commun. Mass Spectrom., 2005. **19**(24): p. 3701-4.

121. Andrade, F.J., et al., *Atmospheric pressure chemical ionization source. 1. Ionization of compounds in the gas phase.* Anal. Chem., 2008. **80**(8): p. 2646-53.

122. Andrade, F.J., et al., *Atmospheric pressure chemical ionization source. 2. Desorption-ionization for the direct analysis of solid compounds.* Anal. Chem., 2008. **80**(8): p. 2654-63.

123. Galhena, A.S., et al., *Small molecule ambient mass spectrometry imaging by infrared laser ablation metastable-induced chemical ionization.* Anal. Chem., 2010. **82**(6): p. 2178-81.

124. Vaikkinen, A., et al., *Infrared Laser Ablation Atmospheric Pressure Photoionization Mass Spectrometry.* Anal. Chem., 2012. **84**(3): p. 1630-1636.

125. Nemes, P. and A. Vertes, *Laser Ablation Electrospray Ionization for Atmospheric Pressure, in Vivo, and Imaging Mass Spectrometry.* Anal. Chem., 2007. **79**(21): p. 8098-8106.

126. Gao, J., et al., *Laser-induced acoustic desorption/atmospheric pressure chemical ionization mass spectrometry.* J. Am. Soc. Mass. Spectrom., 2011. **22**(3): p. 531-8.

127. Hiraoka, K., et al., *Explosive Vaporization of a Liquid Water Beam by Irradiation with a 10.6 μm Infrared Laser.* Rapid Commun. Mass Spectrom., 1997. **11**(5): p. 474-478.

128. Ding, X.L., et al., *Microfabricated Glow Discharge Plasma (MFGDP) for Ambient Desorption/Ionization Mass Spectrometry.* Anal. Chem., 2013. **85**(19): p. 9013-9020.

129. Chen, H., A. Wortmann, and R. Zenobi, *Neutral desorption sampling coupled to extractive electrospray ionization mass spectrometry for rapid differentiation of biosamples by metabolomic fingerprinting.* J Mass Spectrom, 2007. **42**(9): p. 1123-35.

130. Chen, L.C., et al., *Rapid detection of drugs in biofluids using atmospheric pressure chemi/chemical ionization mass spectrometry.* Rapid. Commun. Mass Spectrom., 2009. **23**(3): p. 333-9.

131. Wang, H., et al., *Paper spray for direct analysis of complex mixtures using mass spectrometry.* Angew. Chem. Int. Ed. Engl., 2010. **49**(5): p. 877-80.

132. Heron, S.R., et al., *Surface acoustic wave nebulization of peptides as a microfluidic interface for mass spectrometry.* Anal. Chem., 2010. **82**(10): p. 3985-9.

133. Chipuk, J.E. and J.S. Brodbelt, *The influence of material and mesh characteristics on transmission mode desorption electrospray ionization.* J. Am. Soc. Mass. Spectrom., 2009. **20**(4): p. 584-92.

134. Wu, C., et al., *Mass spectrometry imaging under ambient conditions.* Mass Spectrom. Rev., 2012.

135. Kraft, M.L. and H.A. Klitzing, *Imaging lipids with secondary ion mass spectrometry.* Biochim Biophys Acta, 2014. **1841**(8): p. 1108-19.

136. Lanekoff, I., et al., *Automated platform for high-resolution tissue imaging using nanospray desorption electrospray ionization mass spectrometry.* Anal. Chem., 2012. **84**(19): p. 8351-6.

137. Scientific, T. *LTQ Orbitrap XL ETD Hybrid Ion Trap-Orbitrap Mass spectrometer*. 2016 17/01/16]; Available from: http://www.thermoscientific.com/en/product/ltq-orbitrap-xl-etd-hybrid-ion-trap-orbitrap-mass-spectrometer.html.

138. Waters. *Waters: The Science of What's Possible - Synapt*. 2016 17/01/16]; Available from: http://www.waters.com/waters/en_US/SYNAPT/nav.htm?cid=10131968&locale=101.

139. Mamyrin, B.A., et al., *The mass-reflectron, a new nonmagnetic time of flight mass spectrometer with high resolution.* J. Exp. Theor. Phys., 1973. **37**(1): p. 45-48.

140. Glish, G.L. and R.W. Vachet, *The basics of mass spectrometry in the twenty-first century.* Nat Rev Drug Discov, 2003. **2**(2): p. 140-50.

141. Miller, P.E. and M.B. Denton, *The quadrupole mass filter: Basic operating conepts.* J. Chem. Edu., 1986. **63**(7): p. 617.

142. Douglas, D.J., A.J. Frank, and D. Mao, *Linear ion traps in mass spectrometry.* Mass Spectrom. Rev., 2005. **24**(1): p. 1-29.

143. Makarov, A., *Electrostatic Axially Harmonic Orbital Trapping: A High-Performance Technique of Mass Analysis.* Anal. Chem., 2000. **72**(6): p. 1156-1162.

144. Hu, Q., et al., *The Orbitrap: a new mass spectrometer.* J. Mass Spectrom., 2005. **40**(4): p. 430-443.

145. Makarov, A., et al., *Performance Evaluation of a Hybrid Linear Ion Trap/Orbitrap Mass Spectrometer.* Anal. Chem., 2006. **78**(7): p. 2113-2120.

146. Ishihama, Y., *Proteomic LC–MS systems using nanoscale liquid chromatography with tandem mass spectrometry.* J. Chromatog. A, 2005. **1067**(1–2): p. 73-83.

147. Sundqvist, G., et al., *A general, robust method for the quality control of intact proteins using LC–ESI-MS.* J. Chromatog. B, 2007. **852**(1): p. 188-194.

148. Schlatterer, J. and D.E. Breithaupt, *Xanthophylls in Commercial Egg Yolks: Quantification and Identification by HPLC and LC-(APCI)MS Using a C30 Phase.* J Agr Food Chem, 2006. **54**(6): p. 2267-2273.

149. Snyder, L.R., J.J. Kirkland, and J.W. Dolan, *Introduction to modern liquid chromatography*. 2011: John Wiley & Sons.

150. Howard, G.A. and A.J.P. Martin, *The Separation of the C-12-C-18 Fatty Acids by Reversed-Phase Partition Chromatograhy.* Biochem. J., 1950. **46**(5): p. 532-538.

151. Boersema, P.J., S. Mohammed, and A.J. Heck, *Hydrophilic interaction liquid chromatography (HILIC) in proteomics.* Anal. Bioanal. Chem., 2008. **391**(1): p. 151-9.

152. Martire, D.E. and R.E. Boehm, *Unified theory of retention and selectivity in liquid chromatography. 2. Reversed-phase liquid chromatography with chemically bonded phases.* J. Phys. Chem., 1983. **87**(6): p. 1045-1062.

153. Delahunty, C. and J.R. Yates Iii, *Protein identification using 2D-LC-MS/MS.* Methods, 2005. **35**(3): p. 248-255.

154. Shen, Y., et al., *High-efficiency nanoscale liquid chromatography coupled on-line with mass spectrometry using nanoelectrospray ionization for proteomics.* Anal. Chem., 2002. **74**(16): p. 4235-49.

155. Abian, J., A.J. Oosterkamp, and E. Gelpí, *Comparison of conventional, narrow-bore and capillary liquid chromatography/mass spectrometry for electrospray ionization mass spectrometry: practical considerations.* J. Mass Spectrom., 1999. **34**(4): p. 244-254.

156. Shvartsburg, A.A. and R.D. Smith, *Fundamentals of traveling wave ion mobility spectrometry.* Anal. Chem., 2008. **80**(24): p. 9689-99.

157. Giles, K., et al., *Applications of a travelling wave-based radio-frequencyonly stacked ring ion guide.* Rapid Commun. Mass Spectrom., 2004. **18**(20): p. 2401-2414.

158. Tolmachev, A.V., et al., *Simulation-based optimization of the electrodynamic ion funnel for high sensitivity electrospray ionization mass spectrometry.* Int. J. Mass Spectrom., 2000. **203**(1–3): p. 31-47.

159. Salbo, R., et al., *Traveling-wave ion mobility mass spectrometry of protein complexes: accurate calibrated collision cross-sections of human insulin oligomers.* Rapid. Commun. Mass Spectrom., 2012. **26**(10): p. 1181-93.

160. Knapman, T.W., et al., *Considerations in experimental and theoretical collision cross-section measurements of small molecules using travelling wave ion mobility spectrometry-mass spectrometry.* Int. J. Mass Spectrom., 2010. **298**(1-3): p. 17-23.

161. Shvartsburg, A.A., et al., *Ultrafast differential ion mobility spectrometry at extreme electric fields in multichannel microchips.* Anal. Chem., 2009. **81**(15): p. 6489-95.

162. Shvartsburg, A.A., et al., *Ultrafast differential ion mobility spectrometry at extreme electric fields coupled to mass spectrometry.* Anal. Chem., 2009. **81**(19): p. 8048-53.

163. Brown, L.J., et al., *Miniaturized ultra high field asymmetric waveform ion mobility spectrometry combined with mass spectrometry for peptide analysis.* Anal. Chem., 2010. **82**(23): p. 9827-34.

164. Brown, L.J., et al., *Enhanced analyte detection using in-source fragmentation of field asymmetric waveform ion mobility spectrometry-selected ions in combination with time-of-flight mass spectrometry.* Anal. Chem., 2012. **84**(9): p. 4095-103.

165. Medzihradszky, K.F. and R.J. Chalkley, *Lessons in de novo peptide sequencing by tandem mass spectrometry.* Mass Spectrom. Rev., 2015. **34**(1): p. 43-63.

166. Jonscher, K.R. and J.R. Yates Iii, *The Quadrupole Ion Trap Mass Spectrometer—A Small Solution to a Big Challenge.* Anal. Biochem., 1997. **244**(1): p. 1-15.

167. Sleno, L. and D.A. Volmer, *Ion activation methods for tandem mass spectrometry.* J. Mass Spectrom., 2004. **39**(10): p. 1091-1112.

168. Olsen, J.V., et al., *Higher-energy C-trap dissociation for peptide modification analysis.* Nat Methods, 2007. **4**(9): p. 709-12.

169. Frese, C.K., et al., *Improved Peptide Identification by Targeted Fragmentation Using CID, HCD and ETD on an LTQ-Orbitrap Velos.* J. Proteome Res., 2011. **10**(5): p. 2377-2388.

170. Syka, J.E.P., et al., *Peptide and protein sequence analysis by electron transfer dissociation mass spectrometry.* Proceedings of the National Academy of Sciences of the United States of America, 2004. **101**(26): p. 9528-9533.

171. Thermo. *Planet Orbitrap*. 2015 [cited 2015 2015 May 19]; Available from: http://planetorbitrap.com/orbitrap-velos-pro - tab:schematic.

172. Waters. *SYNAPT G2-S HDMS Mass Spectrometer Overview and Maintenance Guide 715003892/Revision D*. 2014 2015 May 19]; Available from: http://www.waters.com/webassets/cms/support/docs/715003892rd.pdf.

173. Thermo. *TSQ Vantage*. 2007 2015 May 19]; Available from: http://www.antpedia.com/attachments/2012/11/8585_201211271721071.jpg.

174. Das, K. and P. Kar, *Non-Alcoholic Steatohepatitis.* J Assoc Physicians India, 2005. **53**: p. 195-199.

175. Obika, M. and H. Noguchi, *Diagnosis and Evaluation of Nonalcoholic Fatty Liver Disease.* Exp. Diabetes Res., 2012. **2012**: p. 1-12.

176. Pratt, D.S. and M.M. Kaplan, *Evaluation of abnormal liver-enzyme results in asymptomatic patients.* N. Engl. J. Med., 2000. **342**(17): p. 1266-71.

177. Furuhashi, M. and G.S. Hotamisligil, *Fatty acid-binding proteins: role in metabolic diseases and potential as drug targets.* Nat Rev Drug Discov, 2008. **7**(6): p. 489-503.

178. Chen, A., et al., *Liver fatty acid binding protein (L-Fabp) modulates murine stellate cell activation and diet-induced nonalcoholic fatty liver disease.* Hepatology, 2013. **57**(6): p. 2202-12.

179. Storch, J. and A.E. Thumser, *Tissue-specific functions in the fatty acid-binding protein family.* J. Biol. Chem., 2010. **285**(43): p. 32679-83.

180. Storch, J. and A.E. Thumser, *The fatty acid transport function of fatty acid-binding proteins.* Biochim. Biophys. Acta, 2000. **1486**(1): p. 28-44.

181. Peng, X.E., et al., *Two genetic variants in FABP1 and susceptibility to non-alcohol fatty liver disease in a Chinese population.* Gene, 2012. **500**(1): p. 54-8.

182. Fahy, E., et al., *Update of the LIPID MAPS comprehensive classification system for lipids.* J. Lipid Res., 2009. **50**: p. S9-14.

183. Rabinovich, A.L. and P.O. Ripatti, *On the conformational, physical properties and functions of polyunsaturated acyl chains.* BBA Lipids Lipid Met., 1991. **1085**(1): p. 53-62.

184. Levitsky, D. and V. Skulachev, *Carnitine: the carrier transporting fatty acyls into mitochondria by means of an electrochemical gradient of H+.* BBA Bioenerg., 1972. **275**(1): p. 33-50.

185. Reue, K. and D.N. Brindley, *Thematic Review Series: Glycerolipids. Multiple roles for lipins/phosphatidate phosphatase enzymes in lipid metabolism.* J. Lipid Res, 2008. **49**(12): p. 2493-2503.

186. Ghosh, S., J.C. Strum, and R.M. Bell, *Lipid biochemistry: functions of glycerolipids and sphingolipids in cellular signaling.* The FASEB J., 1997. **11**(1): p. 45-50.

187. Farooqui, A.A., L.A. Horrocks, and T. Farooqui, *Glycerophospholipids in brain: their metabolism, incorporation into membranes, functions, and involvement in neurological disorders.* Chem. Phys. Lipids, 2000. **106**(1): p. 1-29.

188. McDaniel, R., C. Hutchinson, and C. Khosla, *Engineered biosynthesis of novel polyketides: analysis of tcmN function in tetracenomycin biosynthesis.* J. Am. Chem. Soc., 1995. **117**(26): p. 6805-6810.

189. Lísa, M., E. Cífková, and M. Holčapek, *Lipidomic profiling of biological tissues using off-line two-dimensional high-performance liquid chromatography–mass spectrometry.* J. Chromatog. A, 2011. **1218**(31): p. 5146-5156.

190. Raetz, C.R.H., et al., *Discovery of new biosynthetic pathways: the lipid A story.* J. Lipid Res, 2009. **50**(Supplement): p. S103-S108.

191. Wewer, V., et al., *Quantification of sterol lipids in plants by quadrupole time-of-flight mass spectrometry.* J. Lipid Res, 2011. **52**(5): p. 1039-1054.

192. Astigarraga, E., et al., *Profiling and Imaging of Lipids on Brain and Liver Tissue by Matrix-Assisted Laser Desorption/Ionization Mass Spectrometry Using 2-Mercaptobenzothiazole as a Matrix.* Anal. Chem., 2008. **80**(23): p. 9105-9114.

193. Brown, S.H.J., et al., *Automated surface sampling of lipids from worn contact lenses coupled with tandem mass spectrometry.* Analyst, 2013. **138**(5): p. 1316-1320.

194. Heck, A.J., *Native mass spectrometry: a bridge between interactomics and structural biology.* Nat Methods, 2008. **5**(11): p. 927-33.

195. Karas, M., D. Bachmann, and F. Hillenkamp, *Influence of the wavelength in high-irradiance ultraviolet laser desorption mass spectrometry of organic molecules.* Anal. Chem., 1985. **57**(14): p. 2935-2939.

196. Zamdborg, L., et al., *ProSight PTM 2.0: improved protein identification and characterization for top down mass spectrometry.* Nucleic Acids Res., 2007. **35**(Web Server issue): p. W701-6.

197. Edwards, R.L., et al., *Compound heterozygotes and beta-thalassemia: top-down mass spectrometry for detection of hemoglobinopathies.* Proteomics, 2014. **14**(10): p. 1232-8.

198. Van Berkel, G.J. and V. Kertesz, *Continuous-flow liquid microjunction surface sampling probe connected on-line with high-performance liquid chromatography/mass spectrometry for spatially resolved analysis of small molecules and proteins.* Rapid Commun. Mass Spectrom., 2013. **27**(12): p. 1329-1334.

199. Schey, K.L., D.M. Anderson, and K.L. Rose, *Spatially-Directed Protein Identification from Tissue Sections by Top-Down LC-MS/MS with Electron Transfer Dissociation.* Anal. Chem., 2013. **85**(14): p. 6767-74.

200. Olsen, J.V., S.E. Ong, and M. Mann, *Trypsin cleaves exclusively C-terminal to arginine and lysine residues.* Mol. Cell Proteomics, 2004. **3**(6): p. 608-14.

201. Quanico, J., et al., *Development of liquid microjunction extraction strategy for improving protein identification from tissue sections.* J. Proteomics, 2013. **79**: p. 200-218.

202. Wisztorski, M., et al., *Microproteomics by Liquid Extraction Surface Analysis: Application to FFPE tissue to study the Fimbria region of tubo,Äêovarian cancer.* Proteomics Clin. Appl., 2013.

203. Rao, W., et al., *Ambient DESI and LESA-MS Analysis of Proteins Adsorbed to a Biomaterial Surface Using In-Situ Surface Tryptic Digestion.* J. Am. Soc. Mass. Spectrom., 2013. **24**: p. 1927-1936.

204. Harris, H., *On the rapid conversion of haematoxylin into haematein in staining reactions.* J. appl. Microsc., 1900. **3**: p. 777-780.

205. Avwioro, G., *Histochemical uses of haematoxylin – a review.* JPCS, 2011. **1**: p. 24-34.

206. Chambers, A.G. and J.M. Ramsey, *Microfluidic dual emitter electrospray ionization source for accurate mass measurements.* Anal. Chem., 2012. **84**(3): p. 1446-51.

207. Chambers, M.C., et al., *A cross-platform toolkit for mass spectrometry and proteomics.* Nat. Biotechnol., 2012. **30**(10): p. 918-20.

208. Race, A.M., I.B. Styles, and J. Bunch, *Inclusive sharing of mass spectrometry imaging data requires a converter for all.* J. Proteomics, 2012. **75**(16): p. 5111-5112.

209. Hsu, F.F. and J. Turk, *Electrospray ionization/tandem quadrupole mass spectrometric studies on phosphatidylcholines: the fragmentation processes.* J. Am. Soc. Mass. Spectrom., 2003. **14**(4): p. 352-63.

210. Griffiths, R.L. and J. Bunch. *Matrix Additives for enhanced Imaging of lipids by MALDI--MSI*. in *Ourence Conference on Imaging Mass Spectomety*. 2012. Ourence, Spain: Proteomass.

211. Dynesonline. *Viscosity, Surface Tension, Specific Density and Molecular Weight of Selected Liquids*. 2015 [23/06/15]]; Available from: https://www.dynesonline.com/visc_table.html.

212. Chaurand, P., et al., *New Developments in Profiling and Imaging of Proteins from Tissue Sections by MALDI Mass Spectrometry.* J. Proteome Res., 2006. **5**(11): p. 2889-2900.

213. Lemaire, R., et al., *MALDI-MS direct tissue analysis of proteins: Improving signal sensitivity using organic treatments.* Anal. Chem., 2006. **78**(20): p. 7145-53.

214. Schwartz, S.A., M.L. Reyzer, and R.M. Caprioli, *Direct tissue analysis using matrix-assisted laser desorption/ionization mass spectrometry: practical aspects of sample preparation.* J. Mass Spectrom., 2003. **38**(7): p. 699-708.

215. Bateman, K.P., et al., *Quantitative-Qualitative Data Acquisition Using a Benchtop Orbitrap Mass Spectrometer.* J. AM. Soc. Mass Spectrom., 2009. **20**(8): p. 1441-1450.

216. Southam, A.D., et al., *Dynamic Range and Mass Accuracy of Wide-Scan Direct Infusion Nanoelectrospray Fourier Transform Ion Cyclotron Resonance Mass Spectrometry-Based Metabolomics Increased by the Spectral Stitching Method.* Anal. Chem., 2007. **79**(12): p. 4595-4602.

217. Wu, C., et al., *Molecular imaging of adrenal gland by desorption electrospray ionization mass spectrometry.* Analyst, 2010. **135**(1): p. 28-32.

218. Bodzon‐Kulakowska, A., et al., *Desorption electrospray ionisation (DESI) for beginners–how to adjust settings for tissue imaging*. Rapid Commun. Mass Spectrom., 2014. **28**(1): p. 1-9.

219. Laskin, J., et al., *Tissue imaging using nanospray desorption electrospray ionization mass spectrometry.* Anal. Chem., 2012. **84**(1): p. 141-8.

220. Girod, M., et al., *Desorption electrospray ionization imaging mass spectrometry of lipids in rat spinal cord.* J. Am. Soc. Mass. Spectrom., 2010. **21**(7): p. 1177-89.

221. Eberlin, L.S., et al., *Desorption electrospray ionization then MALDI mass spectrometry imaging of lipid and protein distributions in single tissue sections.* Anal. Chem., 2011. **83**(22): p. 8366-71.

222. Gerbig, S., et al., *Analysis of colorectal adenocarcinoma tissue by desorption electrospray ionization mass spectrometric imaging.* Anal. Bioanal. Chem., 2012. **403**(8): p. 2315-25.

223. Brenton, A.G. and A.R. Godfrey, *Electro-focusing liquid extractive surface analysis (EF-LESA) coupled to mass spectrometry.* Anal. Chem., 2014. **86**(7): p. 3323-9.

224. Sarsby, J., et al., *Top-down and bottom-up identification of proteins by liquid extraction surface analysis mass spectrometry of healthy and diseased human liver tissue.* J. Am. Soc. Mass. Spectrom., 2014. **25**(11): p. 1953-61.

225. Rivera, C.A., *Risk factors and mechanisms of non-alcoholic steatohepatitis.* Pathophysiology, 2008. **15**(2): p. 109-14.

226. Promega. *Technical bulletin: Trypson Gold, mass spectrometry grade*. 2015 3 Sep 2015]; Available from: http://www.promega.com/~/media/files/resources/protocols/technical bulletins/101/trypsin gold mass spectrometry grade protocol.pdf.

227. Emory, J.F., et al., *Direct analysis of reversed-phase high-performance thin layer chromatography separated tryptic protein digests using a liquid microjunction surface sampling probe/electrospray ionization mass spectrometry system.* EJMS (Chichester, England), 2010. **16**(1): p. 21-33.

228. Shvartsburg, A.A. and R.D. Smith, *Protein analyses using differential ion mobility microchips with mass spectrometry.* Anal. Chem., 2012. **84**(17): p. 7297-300.

229. H. Lodish, A. Berk, and S. Zipursky, *Molecular Cell Biology* 4th ed. The Action Potential and Conduction of Electric Impulses, ed. W.H. Freeman. 2000, New York: NCBI.

230. Siegel, G., B. Agranoff, and R. Albers, *Basic Neurochemistry: Molecular, Cellular and Medical Aspects*. 6th ed. The Myelin Sheath., ed. P. Morell and R. Quarles. 1999, Philadelphia: Lippincott-Raven.

231. van den Pol, Anthony N., *Neuropeptide Transmission in Brain Circuits.* Neuron, 2012. **76**(1): p. 98-115.

232. Davis, T.P., T.J. Abbruscato, and R.D. Egleton, *Peptides at the blood brain barrier: Knowing me knowing you*. Peptides, 2015.

233. Banks, W.A., *Peptides and the blood-brain barrier.* Peptides, 2015.

234. Hsu, F.-F. and J. Turk, *Structural determination of glycosphingolipids as lithiated adducts by electrospray ionization mass spectrometry using low-energy collisional-activated dissociation on a triple stage quadrupole instrument.* J. Am. Soc. Mass Spectrom., 2001. **12**(1): p. 61-79.

235. Griffiths, R.L. and J. Bunch, *A survey of useful salt additives in matrix-assisted laser desorption/ionization mass spectrometry and tandem mass spectrometry of lipids: introducing nitrates for improved analysis.* Rapid Commun. Mass Spectrom., 2012. **26**(13): p. 1557-1566.

236. Thavarajah, R., et al., *Chemical and physical basics of routine formaldehyde fixation.* JOMFP, 2012. **16**(3): p. 400-405.

237. Han, X. and R.W. Gross, *Electrospray ionization mass spectroscopic analysis of human erythrocyte plasma membrane phospholipids.* PNAS, 1994. **91**(22): p. 10635-10639.

238. Hsu, F.-F., A. Bohrer, and J. Turk, *Formation of Lithiated Adducts of Glycerophosphocholine Lipids Facilitates their Identification by Electrospray Ionization Tandem Mass Spectrometry.* J. Am. Soc. Mass Spectrom., 1998. **9**(5): p. 516-526.

239. Milne, S., et al., *Lipidomics: An analysis of cellular lipids by ESI-MS.* Methods, 2006. **39**(2): p. 92-103.

240. Stubiger, G., E. Pittenauer, and G. Allmaier, *MALDI seamless postsource decay fragment ion analysis of sodiated and lithiated phospholipids.* Anal. Chem., 2008. **80**(5): p. 1664-78.

241. Tatituri, R.V., et al., *Characterization of polar lipids of Listeria monocytogenes by HCD and low-energy CAD linear ion-trap mass spectrometry with electrospray ionization.* Anal. Bioanal. Chem., 2015. **407**(9): p. 2519-2528.

242. Hsu, F.F. and J. Turk, *Distinction among isomeric unsaturated fatty acids as lithiated adducts by electrospray ionization mass spectrometry using low energy collisionally activated dissociation on a triple stage quadrupole instrument.* J. Am. Soc. Mass Spectrom., 1999. **10**(7): p. 600-612.

243. Castro-Perez, J., et al., *Localization of fatty acyl and double bond positions in phosphatidylcholines using a dual stage CID fragmentation coupled with ion mobility mass spectrometry.* J. Am. Soc. Mass. Spectrom., 2011. **22**(9): p. 1552-67.

244. Yagnik, G.B., A.R. Korte, and Y.J. Lee, *Multiplex mass spectrometry imaging for latent fingerprints.* J Mass Spectrom, 2013. **48**(1): p. 100-4.

245. Garrett, T.J., et al., *Imaging of small molecules in tissue sections with a new intermediate-pressure MALDI linear ion trap mass spectrometer.* Int. J. Mass Spectrom., 2007. **260**(2,Äì3): p. 166-176.

246. Martin, N.J., et al., *Native Liquid Extraction Surface Analysis Mass Spectrometry: Analysis of Noncovalent Protein Complexes Directly from Dried Substrates.* J. Am. Soc. Mass. Spectrom., 2015. **26**(8): p. 1320-7.

247. Carter, C., C. McLeod, and J. Bunch, *Imaging of Phospholipids in Formalin Fixed Rat Brain Sections by Matrix Assisted Laser Desorption/Ionization Mass Spectrometry.* J. Am. Soc. Mass Spectrom., 2011. **22**(11): p. 1991-1998.

248. Cerruti, C.D., et al., *MALDI imaging mass spectrometry of lipids by adding lithium salts to the matrix solution.* Anal. Bioanal. Chem., 2011. **401**(1): p. 75-87.

249. Hart, P.J., et al., *MALDI-MS imaging of lipids in ex vivo human skin.* Anal. Bioanal. Chem., 2011. **401**(1): p. 115-125.

250. Prideaux, B., et al., *High-sensitivity MALDI-MRM-MS imaging of moxifloxacin distribution in tuberculosis-infected rabbit lungs and granulomatous lesions.* Anal. Chem., 2011. **83**(6): p. 2112-8.

251. Khatib-Shahidi, S., et al., *Direct molecular analysis of whole-body animal tissue sections by imaging MALDI mass spectrometry.* Anal. Chem., 2006. **78**(18): p. 6448-56.

252. Prentice, B.M., C.W. Chumbley, and R.M. Caprioli, *High-speed MALDI MS/MS imaging mass spectrometry using continuous raster sampling.* J Mass Spectrom, 2015. **50**(4): p. 703-10.

253. Bennett, R.V., et al., *Contrast-enhanced differential mobility-desorption electrospray ionization-mass spectrometry imaging of biological tissues.* Anal. Chem., 2014. **86**(8): p. 3756-63.

254. Xu, L., et al., *Profiling and Imaging Ion Mobility-Mass Spectrometry Analysis of Cholesterol and 7-Dehydrocholesterol in Cells Via Sputtered Silver MALDI.* J. Am. Soc. Mass. Spectrom., 2015. **26**(6): p. 924-33.

255. Blatherwick, E.Q., et al., *Localisation of adenine nucleotides in heat-stabilised mouse brains using ion mobility enabled MALDI imaging.* Int. J. Mass Spectrom., 2013. **345–347**(0): p. 19-27.

256. Jackson, S.N., et al., *MALDI-Ion Mobility Mass Spectrometry of Lipids in Negative Ion Mode.* Anal Methods, 2014. **6**(14): p. 5001-5007.

257. Hart, P., et al., *Matrix assisted laser desorption ionisation ion mobility separation mass spectrometry imaging of ex-vivo human skin.* Int. J. Ion Mobil. Spec., 2013. **16**(2): p. 71-83.

258. Li, H., et al., *Ambient molecular imaging by laser ablation electrospray ionization mass spectrometry with ion mobility separation.* Int. J. Mass Spectrom., 2015. **377**(0): p. 681-689.

259. Chan, K.C. and H.J. Issaq, *Fractionation of peptides by strong cation-exchange liquid chromatography.* Methods Mol Biol, 2013. **1002**: p. 311-5.

260. Race, A.M., et al., *Memory Efficient Principal Component Analysis for the Dimensionality Reduction of Large Mass Spectrometry Imaging Datasets.* Anal. Chem., 2013.

261. McDonnell, L.A., et al., *Imaging mass spectrometry data reduction: automated feature identification and extraction.* J. Am. Soc. Mass Spectrom., 2010. **21**(12): p. 1969-1978.

262. Palmer, A.D., J. Bunch, and I.B. Styles, *Randomized approximation methods for the efficient compression and analysis of hyperspectral data.* Anal. Chem., 2013. **85**(10): p. 5078-86.

263. Lowe, J.B., et al., *Human-Liver Fatty-Acid Binding-Protein - Isolation of a Full Length cDNA and Comparative Sequence Analyses of Orthologous and Paralogous Proteins.* J. Bol. Chem., 1985. **260**(6): p. 3413-3417.

264. Gordon, J.I., et al., *Isolation of a Full Length Cdna-Encoding Human-Liver Fatty-Acid Binding-Protein - Comparative Sequence Analyses of Orthologous and Paralogous Proteins.* Gastroenterology, 1985. **88**(5): p. 1400-1400.